

Charge Transfer through thin Dielectric Films: Organic Molecules on MgO(001)/Ag(001)

Dissertation

submitted for the academic degree of

Dr. rer. nat.

of

Michael Hollerer



University of Graz, Austria
Institute of Physics

Supervisor:
Univ.-Prof. Martin Sterrer

Graz, March 2019

Abstract

The investigation of epitaxially grown, ultra-thin dielectric films on metal substrates is of great interest in the fields of catalysis and organic electronics. Within this thesis we explore the energy alignment of adsorbates on top of dielectric/metal systems and their resulting charge state. Finally, the impact of charge transfer on fundamental physical and chemical processes is demonstrated. Organic and inorganic adsorbates are therefore systematically investigated on pristine silver ($\text{Ag}(001)$) single crystals and on $\text{Ag}(001)$ supported magnesium oxide (MgO) ultra-thin films.

We demonstrate integer charge transfer to the Lowest Unoccupied Molecular Orbital (LUMO) of pentacene (5A) adsorbed on $\text{MgO}(001)/\text{Ag}(001)$ and observe the resulting Singly Occupied MO below E_F and the respective Singly Unoccupied MO above E_F . On pristine $\text{Ag}(001)$ fractional charge transfer with an occupation of 0.7 electrons per molecule is observed. Additionally, we determine the individual contributions to the energy level alignment that lead to charge transfer and put quantitative estimates on them. Moreover, we study the transition from Fermi-level pinning to Vacuum-level alignment for 5A, by tuning of the initial $\text{MgO}(001)/\text{Ag}(001)$ substrate workfunction. The equilibration mechanism to the constant, final workfunction is achieved within the monolayer by a variation of the ratio of charged to uncharged 5A molecules. A similar mechanism occurs for a variation of the dielectric thickness of MgO . The resulting charge transfer dipole can be well described by a simple capacitor model.

Charge transfer to 2-dimensional gold (Au) islands on $\text{MgO}(001)/\text{Ag}(001)$ enables the catalytic formation of oxalates from carbon-dioxides [1]. In the presented work, we investigate the catalytic reactivity in dependence on the morphology of the Au islands and their charge state. We find a morphological transition for Au, when deposited at 77 K, from 2D to 3D Au-islands upon annealing to 500 K or higher (STM), which coincides with a significant decrease of oxalate formation (IRAS). We conclude that the catalytic reactivity is facilitated by excess charges (Auger-parameter analysis) located on the rim of 2-dimensional Au-islands. Finally, a recipe for an optimized morphology, namely 2D Au islands with a high perimeter to area ratio, is proposed to yield the maximum reactivity by the deposition of Au at 77 K and subsequent annealing to 260 K. In a related topic, we demonstrate that charge transfer controls the self-metalation reaction of free-base porphyrin (2H-TPP) to Mg-TPP on $\text{MgO}(001)/\text{Ag}(001)$. This is achieved by tuning of the initial substrate workfunction to either enable or inhibit charge transfer, and verified via monitoring of the N 1s XPS signal of the porphyrins.

Finally, we present the first STM-images of ordered water-monolayers on $\text{MgO}(001)/\text{Ag}(001)$ and relate them to the established p(3x2) and c(4x2) phase [2]. We find no dependence of the water growth on the dielectric thickness. Furthermore, a growth study of Para-Sexiyphenyl (6P) on $\text{Ag}(001)$ is presented. The development of the wetting-layer is shown to involve two molecular reorientations, facilitated by an increased interaction between neighbouring molecules via intra-molecular twisting of the phenyl-rings. This wetting layer is further demonstrated to act as a template for the growth of a well-ordered bulk film with a (2 1 -3)-related contact plane with respect to the $\text{Ag}(001)$ surface.

Zusammenfassung

NEUE VERSION NOCH NICHT ÜBSERSETZT

Die Untersuchung von epitaktisch gewachsenen, ultra-dünnen dielektrischen Schichten auf Metallsubstraten ist von großem Interesse für die Forschungsfelder der Katalyse sowie der organischen Elektronik. Während dielektrische Schichten ursprünglich als passivierende Abstandshalter betrachtet wurden, welche für die Untersuchung von elektronischen Eigenschaften von Adsorbaten nützlich sind, zeigte sich kürzlich, dass sie auch eine aktive Rolle in der Verstärkung von Ladungstransfer spielen können. In dieser Dissertation wird die Rolle von dielektrischen Schichten in der Energieanpassung von metallischen und organischen Adsorbaten auf Oberflächen anhand derer Ladungszustände untersucht. Schlussendlich wird der Einfluss von Ladungstransfer auf fundamentale physikalische und chemische Prozesse untersucht. In dieser Arbeit untersuchen wir Magnesiumoxid (MgO) welches im Ultra-Hoch Vakuum (UHV) epitaktisch auf einen Silber Einkristall ($Ag(001)$) in atomar dicken Schichten aufgebracht wird. Auf diesem Modellsystem werden organische (Pentacen, Sexyphenyl, Tetraphenylporphyrin, Wasser) und metallische (Gold) Adsorbate systematisch mit ausgewählten Methoden der Oberflächenphysik (STM, TPD, LEED, ARPES, XPS, IRAS) sowie theoretischen Methoden (DFT) untersucht. Um den Einfluss der dielektrischen Schicht herauszuarbeiten werden komplementäre Messungen auf reinem $Ag(001)$ durchgeführt.

Diese Dissertation ist in zwei Teile gegliedert. In der ersten wird über die theoretische und experimentelle Entdeckung von Ladungstransfer durch ultra-dünne dielektrische Schichten für das Modellsystem Gold (Au) auf $MgO/Ag(001)$ berichtet. Das Auftreten von katalytischen Reaktion an geladenen Au -Inseln ist bekannt und wird in den gruppenübergreifenden Publikation *Supports and modified nano-particles for designing model catalysts* sowie *Model systems in heterogeneous catalysis: towards the design and understanding of structure and electronic properties* genauer untersucht. In einem anderen Projekt wird die Bildung von geordneten Strukturen von Wassermolekülen auf dieser Oberfläche in *Imaging the $c(4\times 2)$ and $p(3\times 2)$ superstructures of water on $MgO/Ag(001)$* betrachtet.

Im zweiten Teil wird die Betrachtung auf große organische Moleküle ausgeweitet. Dieser Teil beginnt mit einer ausführlichen Diskussion der Energieanpassung von Adsorbat/Substrat Systemen, wobei der Fokus auf den intrinsischen Eigenschaften der Adsorbate (Elektronenaffinität (EA) und Ionisationsenergie (IE)) und des Substrats (Austrittsarbeit ϕ) liegt. Die einzelnen Beiträge zur Energieanpassung nach heutigem Erkenntnisstand werden aufgeschlüsselt und die möglichen Ladungstransfer-Mechanismen diskutiert. Dieser konzeptionelle Zugang zum Ladungstransfer ist auch Teil unserer Untersuchung am Modellsystem Pentacen auf $MgO/Ag(001)$, und wird in der Arbeit *Charge Transfer and Orbital Level Alignment at Inorganic/Organic Interfaces: The Role of Dielectric Interlayers* erläutert. Dieser Teil endet mit einer Diskussion über die organisch/metallische Grenzfläche bei anwendungs-relevanten Schichtdicken aus der Arbeit *Growth study of para-sexiphenyl on $Ag(001)$: From single molecule to crystalline film*.

*Meinen Eltern,
die mir alles ermöglicht haben!*

Contents

1	Introduction	3
2	Fundamentals	7
2.1	Scanning Tunneling Microscopy	7
2.1.1	Theoretical Approach	9
2.1.2	Scanning Tunneling Spectroscopy	10
2.1.3	STM/STS of Organic Molecules	11
2.2	Temperature Programmed Desorption	13
3	Experimental Implementation	15
3.1	LT-STM chamber	15
3.2	TPD chamber	16
3.3	Sample Preparation	17
3.4	Physical Vapor Deposition (PVD)	20
4	Topics	23
4.1	Ultra-thin dielectric films	23
4.1.1	Water on MgO	30
4.2	Energy Alignment	34
4.2.1	Energy Alignment Mechanisms	36
4.2.2	Integer Charge Transfer Model	41
4.2.3	Related Publications	44
4.2.4	Organic Film Growth	49
4.3	Appendix	52
5	Conclusion	55
6	Published work	57
6.1	Supports and modified nano-particles for designing model catalysts . . .	57
6.2	Model systems in heterogeneous catalysis: towards the design and understanding of structure and electronic properties	71
6.3	Scanning Tunneling Microscopy of the Ordered Water Monolayer on MgO(001)/Ag(001) Ultrathin Films	93
6.4	Charge Transfer and Orbital Level Alignment at Inorganic/Organic Interfaces: The Role of Dielectric Interlayers	110
6.5	Growth study of para-sexiphenyl on Ag(001): From single molecule to crystalline film	127
7	Scientific Contributions	147

Contents

8 Acknowledgment

149

1 Introduction

The controlled epitaxial growth of atomically defined thin-films on metal supports in Ultra-High Vacuum (UHV) has received much attention in recent years. The *in-situ* fabrication allows not only the examination of different surfaces on one single crystal substrate, but also the investigation of *per se* insulating surfaces with electron-based methods. This is possible because charge-accumulation is impeded by tunneling of electrons through the thin dielectric layer. As a consequence, the electronic alignment of adsorbates on insulating films can be investigated. This is of great importance for the understanding of various applications such as catalysis or electronics and naturally occurring effects such as corrosion or decomposition processes. Metal-oxides are of a particular importance because of their vast abundance in bulk-form in nature. Furthermore, they occur (often unnoticed) as thin-films in the machining of metal surfaces (e.g. in electronic applications). The fundamental understanding of electronic level-alignment on oxide surfaces is therefore of great interest to a manifold of scientific fields and technical applications.

Magnesium Oxide (MgO) has been extensively studied in the last two decades and several recipes addressing the epitaxial growth on square-lattice substrates such as on Ag(001) or Mo(001) have been published [3, 4]. A pioneering theoretical study by *Pacchioni et al.* [5] demonstrated the possibility of inducing charge transfer from the metal support to metal atoms adsorbed on top of the MgO(001) thin films. It was soon realized that both the electronic properties of the adsorbate [6] (Electron Affinity (EA) and Ionization Energy (IE)) and substrate [7] (workfunction ϕ) play a crucial role in this process. Soon after, experimental evidence for this phenomena was presented for the system of Au on MgO(001)/Ag(001) [8]. Moreover, it was shown that charge transfer could also induce a transition in the growth behavior of Au agglomerates from three- to two-dimensional islands. This was demonstrated both theoretically [9] and experimentally [10]. In turn, this led to a series of related investigations such as the localization of excess charges within two-dimensional Au islands [11] and finally to the direct association of a catalytic reaction with charged Au^- species on the surface [1]. This realization encouraged further studies on the dependence of this model catalyst on charge transfer and adsorbate morphology. A corresponding investigation examining temperature and MgO film thickness dependencies is discussed in detail in chapter 4.1. Another, more fundamental, question concerns the level-alignment mechanisms and the resulting charge transfer. To further explore this question it is necessary to obtain a quantification of the charge transfer for well-defined adsorbate/substrate systems. Although such a quantification was already explored for Au islands on MgO(001)/Ag(001) [12] the small extension of single Au atoms and their high susceptibility to local substrate defects only allow for a vague estimation. Therefore, we consider the charge transfer to extended organic molecules on MgO(001)/Ag(001). In this study pentacene

(5A) is chosen as an example of a well-investigated organic semiconductor, which is frequently applied in the fundamental investigation of Organic Thin-Film Transistor (OTFT) devices. In this application it is the energy alignment of the semiconducting molecule with the (often oxidized) metal electrodes and with the gate dielectric that crucially determines the performance [13]. For the investigation of this system a combination of Scanning Tunneling Microscopy (STM) and Spectroscopy (STS) with Angle Resolved Photo-Emission Spectroscopy (ARPES) is applied with the support of Density Function Theory (DFT) and ARPES simulations following the plane-wave approximation [14]. With this set of methods the frontier orbitals of the molecule can be imaged both in real and in reciprocal space and their energetic positions can be assigned with two independent methods. As such, we can determine the electronic alignment of this model system and observe a charge transfer of one electron per molecule on MgO(001)/Ag(001) with the previous Lowest Unoccupied Molecular Orbital (LUMO) being split into the Singly Occupied and the Singly Unoccupied Molecular Orbital (SOMO/SUMO). A corresponding determination for 5A on pristine Ag(001) yields a significantly lower charge transfer of 0.7 electrons per molecule, indicating that the insertion of the dielectric layer promotes charge transfer. With the direct comparison between molecules adsorbed on a metal with a dielectric interlayer and molecules adsorbed directly on the metal we can draw conclusions concerning the individual contributions of the molecular energy alignment. A detailed discussion of this topic is presented in chapter 4.2.

In the past decades several scientific contributions have outlined the mechanisms behind the energy alignment, defining what is known as the *vacuum level alignment* and the *Fermi level pinning* regime [15, 16]. Dielectric thin films are well suited for a corresponding study because of the imposed integer charge transfer and the saturated push-back effect. Although recent systematic studies on thick amorphous films of varying adsorbate/substrate systems could reproduce the predicted trend of the integer charge transfer model [17], no insight could be provided on an atomic/molecular level. Within our follow-up study by Hurdax *et al.*¹ a more general approach is chosen. Motivated by a recent theoretical study [18] the workfunction of the MgO(001)/Ag(001) substrate was found to be experimentally tunable via its interface defects. This presents the chance to study the transition from *vacuum level alignment* to *Fermi level pinning* for a single, atomically controlled and well studied system.

Finally, this model system is used to test whether the occurrence of charge transfer induces structural or chemical modifications of adsorbate molecules. As an exemplary system we consider the metalation reaction of the *free-base* tetraphenylporphyrin (2H-TPP), in which two protons are extracted and substituted by one metal atom. Such metalation reactions were recently reported to occur for 2H-TPP at room temperature both on MgO nano-cubes exhibiting MgO(001) surfaces [19] and on MgO thin films epitaxially grown on Ag(001) [20]. In both cases the metalation reaction into Mg-TPP was attributed to the presence of defect-sites (step-edges) on the MgO surfaces. However, a metalation reaction might also be facilitated by the presence of excess charges via charge transfer from the metal substrate. As mentioned before, we can

¹Publication in preparation.

now tune the MgO(001)/Ag(001) workfunction to effectively control the charge state of the adsorbate 2H-TPP molecules. As a result we observe a direct correlation of the metalation of molecules with the presence of charge transfer².

Within this work we analyze the occurrence of charge transfer through an insulating layer as a general energy alignment mechanism. With a complementary set of techniques we unambiguously demonstrate the presence of excess charges localized within the adsorbate structures on an atomic/molecular level. Finally, we demonstrate the impact of charge transfer in two relevant examples, emphasizing the general importance of our findings for a more profound understanding of the involved physical and chemical processes.

²This project is conducted in collaboration with the group of *Mike Ramsey* from the University of Graz. All UPS and XPS measurements were performed by *Larissa Egger* who will further pursue this work in her PhD thesis.

2 Fundamentals

Within the work presented in this thesis a series of complementary experimental techniques were applied in order to address specific scientific problems. Detailed descriptions of standard experimental techniques can be found in any textbook on surface science. Therefore, only a brief description of the main techniques is given in the following section. As the majority of this work was conducted on a low-temperature STM setup (see chapter 3.1) with complementary TPD measurements performed on a separate UHV-setup (see chapter 3.2), both techniques will be briefly discussed.

2.1 Scanning Tunneling Microscopy

The first Scanning Tunneling Microscope (STM) was demonstrated in 1981 by Gerd Binning and Heinrich Rohrer [21] who were awarded with the Nobel prize in 1986 for its development. STM, a comparatively young technique, was immediately embraced by surface scientists for its ability to locally resolve a conductive surface with atomic resolution. Furthermore, it also enables the controlled manipulation of atoms and molecules and yields information on the electronic structure of a surface or adsorbate. It since became one of the most popular techniques in modern surface science. With the development of the tuning fork sensor in 1996 [22] and the accompanying improved resolution of Atomic Force Microscopes (AFM), the focus of development has slowly shifted to combined AFM/STM setups in recent years. Because of the similar technical implementation and the possibility of merging the two techniques they are nowadays often collectively referred to as Scanning Probe Microscopy (SPM).

The working principle of an STM is based on the quantum-mechanical phenomenon of *tunneling*. This phenomenon describes the possibility of a particle to surpass a potential barrier which would be deemed to be insurmountable from a classical point of view. In an STM this idea is projected on the possibility of an electron to tunnel from a sharp metallic tip through vacuum (representing the tunneling barrier) into a conductive sample surface, which is subject of investigation. By applying a voltage (potential difference) between tip and sample the tunneling probability can be altered, resulting in a directional transport of electrons, the *tunneling current*. It is then possible to obtain a map of the surface by laterally measuring the tunneling current line by line. As the magnitude of this tunneling current is extremely sensitive to the distance between tip and sample a vertical resolution in the sub-Å range can be achieved. This is sufficient to resolve the electronic corrugation of individual atoms within a suitable substrate when carefully choosing the measurement parameters. Typical values for an STM operating in UHV are tip-sample distances of 5 Å to 20 Å, tunneling currents ranging from 10 pA to 1000 pA and applied voltages between −4 V and +4 V.

To understand the tunnel current, its direction and magnitude, it is necessary to consider the electronic structure of both a metallic tip and a metallic substrate. A schematic energy diagram for a tip-sample tunneling junction is depicted in figure 2.1. When brought into electrical (tunneling) contact the Fermi energies of the two materials will align (Figure 2.1.a). This will result in an equilibration of the respective Fermi energies. The contact potential $\Delta\phi$ arises from the work function difference of the components. As the system is in equilibrium the probability for tunneling from one contact to the other is equal and the net current flow will be zero. Upon applying a positive bias voltage to the sample (Figure 2.1.b) the E_F of the sample is pushed downwards with respect to E_F of the tip. The filled states of the tip are now opposing empty states of the sample, into which electrons can tunnel through the potential barrier (blue). Consequently, an increased probability for tunneling arises resulting in an observable tunneling current, which is dependent on the height and width of the potential barrier $U(z)$. As such, it is possible to create a map via scanning the surface at a given bias voltage and recording the tip height $z(x, y)$, while maintaining a constant tunneling current (constant current mode). But what does the resulting 3D model of the surface actually represent?

In a first consideration a constant current image would map the surface corrugation as a contour of constant charge density. An interpretation as an actual surface topography is therefore reasonable. However, one could argue that the tunneling current is mainly constituted of electrons with energy E_F , since they experience the lowest potential barrier (see figure 2.1.b). This would imply a certain dependence of the tunneling current on the electronic structure of the surface. To understand the observed image contrast in STM we must therefore consider the Local Charge Density (LDOS) of both the tip and the surface as well as the spatial distribution of the electronic orbitals. A

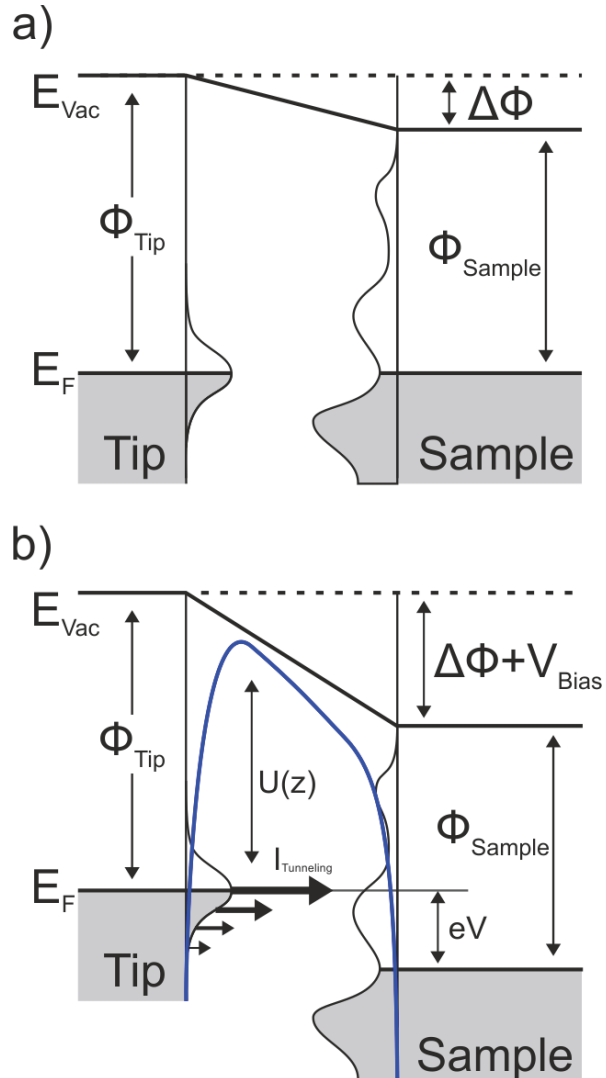


Figure 2.1: Schematic energy diagram of a tip-sample configuration without (a) and with (b) a positive Bias voltage V_{Bias} applied to the sample. Filled states in gray and potential barrier in blue.

thorough theoretical description is hence indispensable for the correct interpretation of STM imaging.

2.1.1 Theoretical Approach

In a first approach the tunneling probability is considered for a *Bloch* wave imposed on a constant, one-dimensional potential barrier. When employing the time-independent *Schrödinger* equation we find a transmission probability T for a particle with an energy E , much smaller than the potential barrier of

$$T \propto e^{-2 \cdot d \sqrt{\frac{2 \cdot m \cdot (U - E)}{\hbar^2}}} \quad (2.1)$$

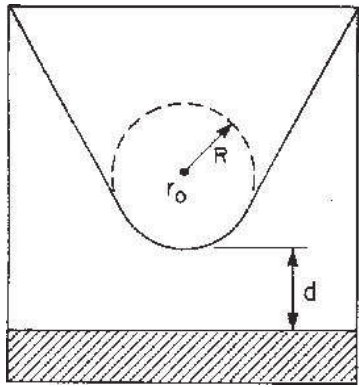


Figure 2.2: Schematic of the tunneling geometry assumed by Tersoff and Hamann. [23]

dependent Schrödinger equation with first-order perturbation theory on a geometry of planar electrodes separated by an insulating barrier (*Transfer-Hamiltonian approach*):

$$I = \frac{2\pi e}{\hbar} \sum_{\mu\nu} f(E_\mu) [1 - f(E_\nu) + eV] |M_{\mu\nu}|^2 \delta(E_\mu - E_\nu) \quad (2.2)$$

with the state distribution functions of tip $f(E_\mu)$ and sample $f(E_\nu)$, the Dirac-Delta function $\delta(E_\mu - E_\nu)$, which only allows for elastic tunneling into states of the same energy and $M_{\mu\nu}$ the probability matrix for the transition of the electron from state μ (within the tip) to ν (within the sample):

$$M_{\mu\nu} = \frac{\hbar^2}{2m} \int (\psi_\mu^\star \vec{\nabla} \psi_\nu - \psi_\nu^\star \vec{\nabla} \psi_\mu) d\vec{S} \quad (2.3)$$

Explicit wave-functions have to be chosen to obtain a solution for the probability matrix $M_{\mu\nu}$. Tersoff and Hamann therefore considered a tip with a radius of curvature of R which is centered at r_0 and terminates with an s-type orbital of spherical symmetry (Figure 2.2). It is placed in a distance d above the substrate surface. The tip wave function ψ_μ is interacting with a surface wave function ψ_ν , which is represented by

Bloch-waves that are expanded in a Fourier series and decay exponentially into the vacuum ($\psi_\nu \propto e^{-kz}$). To avoid the evaluation of the Fermi-distributions the calculation is limited to low temperatures and low bias voltages. Several assumptions are made in order to obtain a self-consistent solution, such as an electrochemical equilibrium, similar workfunctions and negligible electron-electron interactions. Finally, an expression for the tunneling current according to the Tersoff-Hamann model can be expressed:

$$I \propto V_{Bias} \cdot \rho_S(E_F) \cdot R^2 k^{-4} \cdot e^{2kR} \cdot \sum_\nu |\psi_\nu(\vec{r}_0)|^2 \delta(E_\nu - E_F) \quad (2.4)$$

with the bias voltage V_{Bias} , the DOS of the tip ρ_S at E_F , and the Bloch wave $k = \sqrt{2m\phi/\hbar^2}$ within the potential barrier, where ϕ is the workfunction. The sum over ψ_ν can be identified as the LDOS of the surface at E_F . The tunneling current is thus proportional to the LDOS at E_F . By writing out the square of the surface wavefunction we obtain an exponential decay with tip-sample distance and the square root of the potential height: $I \propto e^{-2 \cdot d \sqrt{\frac{2m\phi}{\hbar^2}}}$, similar as within the static one-dimensional model in equation 2.1.

According to this theoretical approach to the tunneling process we can now interpret constant current STM images as topographic maps that, apart from reproducing topographical heights (steps, adsorbates), images the contour of the constant LDOS of the surface at E_F . The presented Tersoff-Hamann approximation was the first tool to theoretically predict and compute STM images, allowing for a sound interpretation of experimentally obtained data. The model has since been adapted for various tip geometries (like p and d -orbitals) and approximations (e.g. to bypass the limitation for small voltages) [25]. Ultimately, the accuracy of this approach is always limited by the choice of the approximate wavefunctions of tip and surface.

So far the discussion was limited to low bias voltages because of the difficulty to model the effect of high electrical fields on the wavefunction. But in order to correctly interpret constant current maps at voltages of ± 1 V or higher we need to investigate the LDOS-dependence in a wider range around E_F . This is especially important when trying to obtain electronic spectra of the surface.

2.1.2 Scanning Tunneling Spectroscopy

Historically, Scanning Tunneling Spectroscopy (STS) was already well established for non-local measurements of planar electrodes before the invention of STM. But the development and improvement of reliable STMs has resulted in a renewed interest into locally probing the electronic structure of the surface. In the experimental setup the tip is kept at a fixed position (x,y,z) above the surface while measuring the tunneling current as a function of voltage. More specifically, the sample bias (DC-component) is ramped over a certain range while it is modulated with a sinusoidal signal (AC-component). The resulting current is recorded with a lock-in amplifier, yielding the differential signal of the tunneling current $\frac{\partial I}{\partial V_{Bias}}$ as the in-phase component of the modulation frequency. The so-obtained differential signal is then typically plotted versus the applied voltage. The interpretation of such spectra is, however, everything but straightforward. As the previously discussed Tersoff-Hamann approach is limited to low bias-voltages *Selloni et*

al. [26] suggested a simplification to derive an expression that is valid for a wider voltage regime. With the assumption of zero-temperature and a constant, voltage-independent DOS of the tip they obtain

$$\frac{\partial I}{\partial V_{Bias}} \propto \rho_S(\vec{r}, V) T(V) \quad (2.5)$$

with $\rho_S(\vec{r}, V)$, the LDOS of the sample at the position beneath the tip and at an energy $E = E_F + V$. $T(V)$ represents a \vec{k} -independent correction factor describing the voltage drop across the vacuum region. Although they explicitly state that the assumption of a constant tip DOS may not be realistic, they conclude a strong relation between tunneling current and the LDOS of the sample. The concept is more easily understood when considering the energy diagram in figure 2.1.b. When ramping the tip-sample voltage we continuously shift the sample LDOS with respect to E_F of the tip. We therefore obtain a current signal that is (as derived) proportional to the actual LDOS and reveals information on the electronic structure of the surface. A similar conclusion can be drawn for the interpretation of constant current images obtained for increased biases. Namely, that the constant LDOS of the sample should be shifted by the applied bias voltage. This means that by varying the applied bias voltage we can conceretely map the filled and empty states (constant LDOS map) of the surface via applying a positive or negative bias, respectively. This corrugation dependence on the applied bias was first observed and investigated for the system of Si(111)-(7x7) (see [27]).

The strong dependence on the (mostly unknown) shape and composition of the tip together with the difficulty of modeling the electric field dependence of substrate wavefunctions within the tunneling junction still constitute the challenge of correctly interpreting STS spectra or bias dependent STM images up to today.

2.1.3 STM/STS of Organic Molecules

So far we have discussed the theoretical description of the tunneling current for a simple tip/sample system. We will now extend the discussion to molecular adsorbates both on pristine metal substrates and insulator-metal hetero-structures. The electronic structure of a single molecule is defined by discrete electronic levels, known as Molecular Orbitals (MO). Related to the electronic orbitals of single atoms they can be described by the Linear Combination of Atomic Orbitals (LCAO) theory. Of special interest are the frontier orbitals, the Highest Occupied Molecular Orbital (HOMO) and the Lowest Unoccupied Molecular Orbital (LUMO), which can be considered the analogue to a classical semiconductors valence- and conduction band. However, the actual physical significance of the concept of molecular orbitals is still debated today. The ambiguity and controversy present in modern literature is best summarized by this quotation of a recent publication:

"Can Orbitals Really Be Observed in Scanning Tunneling Microscopy Experiments?"
"Molecular Orbitals are not unique and are not observable... orbitals are simply mathematical constructs used to build the (approximate) wave function and then the density

... " [28]

Nevertheless, contemporary literature has adapted the nomenclature of observing molecular orbitals rather than its associated probability densities. In the following paragraph an attempt to describe the physics beneath the tunneling process involving molecular electronic states is given.

Figure 2.3 depicts the energetic alignment of an organic molecule adsorbed on a metallic (right part, left side) and on an insulator/metal (right part, right side) sample. Both systems are aligned with the DOS of an idealized metal tip. In the aforementioned models the sample was considered to exhibit a flat electronic corrugation of a continuous LDOS. This is certainly not the case for a spatially defined molecule adsorbed on a metal-substrate. One would assume that the molecular orbitals of the molecule hybridize with

the electronic states of the substrate, leading to mixed wavefunctions and, therefore, an altered electronic corrugation. Scanning tunneling theory would then predict resonant tunneling into the new LDOS across the vacuum (and adsorbate) potential barrier. Indeed, good agreement was observed for first theoretical calculations with experimental data even when assuming unperturbed gas-phase molecules [29]. Interestingly, molecular features are also observed within the HOMO-LUMO gap. This is also true on dielectrics (see figure 4.1) where no substrate states are present to be effected by the molecule (Figure 2.3). Apparently, the presence of the molecule constitutes a local charge distribution that influences the tunneling process. This in turn begs the question whether resonant tunneling is still a valid assumption.

We now consider the tunneling process from a metallic tip to a molecular orbital on top of an insulator/metal hetero-structure (Figure 2.3, right side). One could imaging that besides resonant tunneling also a step-wise *hopping* process could occur. An electron *hopping* from the tip to the molecule M would then result in a temporarily charged species M^- , before tunneling through the insulating barrier into the metal substrate. Depending on whether the time constant of such a process allows for thermal

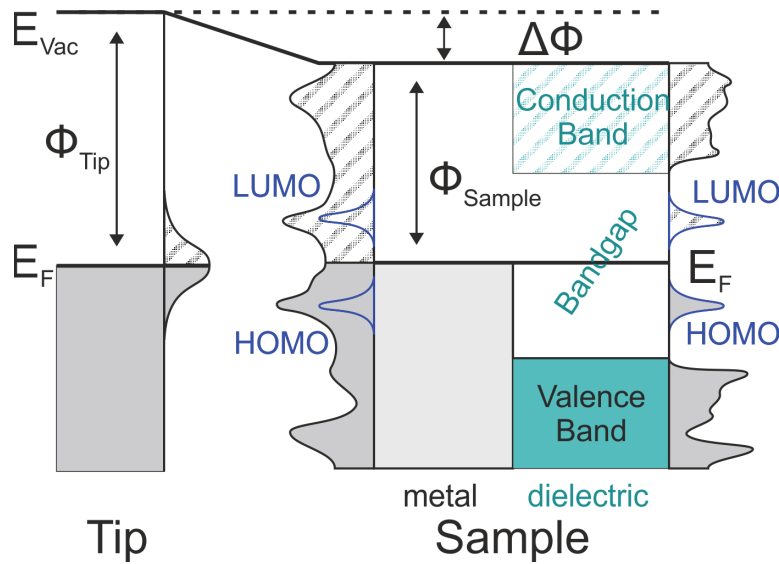


Figure 2.3: Energy diagram of the tunneling junction. Filled (gray) and empty (shaded) states of tip (left) and sample (right). The electronic states of the metal substrate are given in light gray, of the insulator/metal substrate in turquoise and of the molecular states in blue.

relaxation or not it is called a real or transient oxidation/reduction process, respectively. The latter would be the equivalent of a UPS photo-emission process and is also referred to as an adiabatic transition. So far, each of these processes has been ascribed to several experimental observations on different systems [30]. However, each process is based on different assumptions, resulting in fundamentally different interpretations of the energies observed for the electronic states of adsorbed molecules.

A detailed discussion for the evaluation of STS on organic adlayers (resonant tunneling) is given in [31] and a report on the influence of the immediate molecular surrounding is given in [32]. Because of the already vague mathematical description and the here-mentioned ambiguities the interpretation of Orbital Mediated Tunneling Spectroscopy (OMTS) remains a challenging task until today [30].

2.2 Temperature Programmed Desorption

Temperature Programmed Desorption (TPD), also often referred to as Thermal Desorption Spectroscopy (TDS), is a powerful tool to study molecular adsorbates on solid substrates. For this technique a sample is heated with a constant rate β (K/s) in front of a Quadrupole Mass Spectrometer (QMS). The desorption intensity of the molecular adsorbate is then monitored as a function of the temperature $I(T)$. A mathematical description of the desorption process is given with the *Polanyi-Wigner* equation [33]:

$$R_{des} = -\frac{d\Theta}{dT}\beta = \nu(\Theta, T) \cdot \Theta^n \cdot e^{\frac{-E_{des}(\Theta, T)}{kT}} \quad (2.6)$$

with the desorption rate R_{des} , the coverage Θ , the order of desorption n , the temperature T , the frequency factor N , the desorption energy E_{des} and Boltzmann's constant k . The desorption rate is directly proportional to the experimentally observed intensity. In figure 2.4 R_{des} is modelled for the integer (0,1,2) orders of desorption which are characteristic for specific substrate/adsorbate interactions.

As apparent from the equation, 0-order desorption describes a coverage-independent process, manifesting in an exponential increase of intensity with temperature until the adsorbate is completely desorbed. Originally, this was associated with the sublimation of single compound system. As the uppermost atoms desorb they reveal another atomic layer with identic adsorption energies. An analogous interpretation holds for a molecular multilayer on top of a solid substrate. The outermost molecules of a molecular island desorb layer by layer, always revealing molecules of similar desorption energies, until the entire island is gone. This results in a desorption rate that increases exponentially with the supplied thermal energy (temperature). In a coverage series the maximum of the desorption peak thus shifts with the coverage. In contrast, in 1st order desorption the maximum desorption rate is coverage independent and occurs at a constant temperature. It is most commonly observed for large molecules on top of a solid substrate. Desorption occurs once the thermal energy exceeds the binding energy of the prevalent molecular species. This energy does not depend on whether the surface is fully, or only partially covered by the adsorbate molecules.

Finally, the 2nd order desorption rate exhibits a square dependence on the coverage. Here, the maximum desorption peak shifts to lower temperatures with increasing

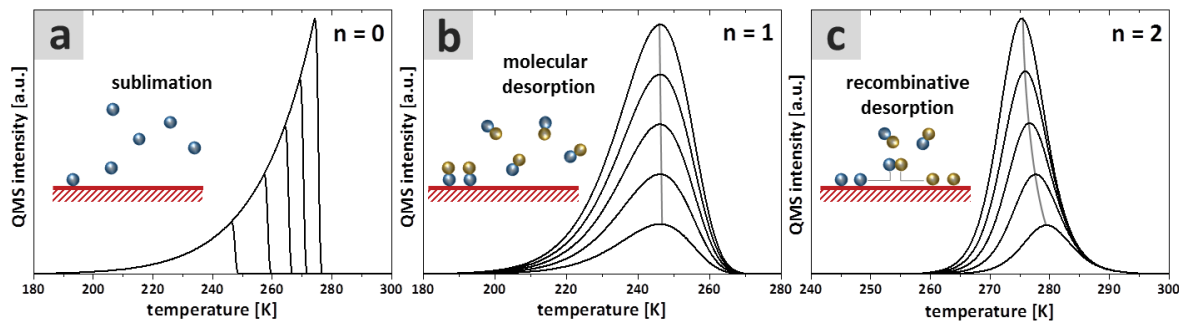


Figure 2.4: Simulated TPD curves for the most common reaction orders of $n = 0, 1, 2$ (a,b,c, respectively). Different lines are given for increasing initial coverages Θ . (Figure taken from [34])

coverage. It is characteristic for recombinative desorption. So far the reaction orders were stated as integers, but it should be noted that also fractional numbers are common ($0 < n < 1$) and observed, when, e.g. cluster formation or edge-of-island desorption occurs. Additionally, information about other surface processes, such as dewetting, repulsive behavior or transition-states can sometimes be extracted from TPD data.

Within this thesis mainly large organic molecules are investigated. Organic film growth usually involves the formation of a wetting layer, followed by the evolution of molecular islands (multilayer). TPD is therefore a powerful tool that allows for the discrimination of the molecular multilayer and the often complex wetting layer just by their appearance in a desorption series. Furthermore, it is also possible to obtain information on the molecular desorption energies and the corresponding frequency factor. To this aim several approaches have been introduced in the past, such as the *Redhead method* [35] or the *Leading Edge method* [36]. While the physical meaning of the desorption energy is evident, the frequency factor, or pre-exponential factor, is less clear. In simple terms, it is associated with the vibrational frequency of a molecule in the direction of desorption. A modern definition is given via a statistical rate approach [37] or transition state theory [38]. Even for a given molecular species the numerical value of the frequency factor strongly varies with the immediate surrounding of the molecule (multilayer to monolayer from $1 \times 10^{12} \text{ s}^{-1}$ to $1 \times 10^{19} \text{ s}^{-1}$ [39]). Given the varying theoretical approaches and the accompanying assumptions it is evident that great care has to be taken in the analysis of TPD data. Nevertheless, it represents a quick and powerful method for the characterization of organic thin-film formation.

3 Experimental Implementation

Within this chapter the principally utilized experimental setups are briefly described and the theoretical background of the employed techniques is given. Furthermore, the specific sample preparation procedures are stated and the material specifications and supplying sources are listed.

3.1 LT-STM chamber

The majority of the experimental work within this thesis was conducted on a Low-Temperature Scanning Tunneling Microscope (LT-STM) setup. It is partitioned into three separable compartments, the Fast Entry (FE), the Preparation Chamber (PC) and the Measurement Chamber (MC) (see figure 3.1(a)). The system is evacuated with a scroll pump and a *Pfeiffer TMU 261 P* turbo-molecular pump via the FE. The PC is additionally equipped with a *VARIAN VacIon 150* ion pump and a *VAB Elmshorn* titanium sublimation pump, achieving a base pressure of 1×10^{-10} mbar at room temperature. When cooled with liquid He a base pressure in the mid 10^{-11} mbar regime is achieved.

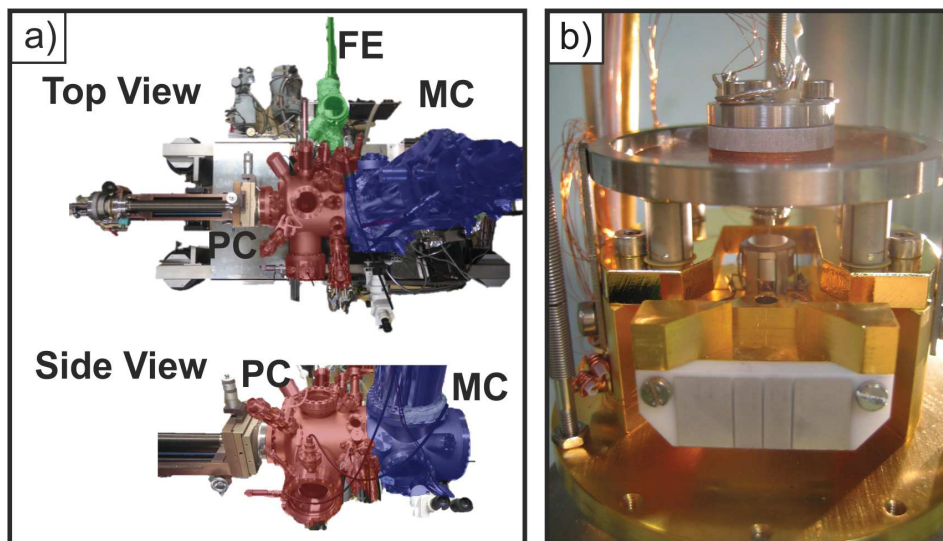


Figure 3.1: LT-STM chamber (a) Top and Side View of the UHV chamber. The three compartments that can be separated with UHV-valves are color-coded. (b) View of the actual STM. A Ag crystal is mounted onto a sample-holder which is inserted into the STM.

The system is equipped with a *BALZERS QMA200* Quadrupole Mass Spectrometer (QMS), a 4-grid *Specs ErLEED 1000-A* Low Energy Electron Diffraction (LEED) device

3 Experimental Implementation

and a *CREATEC* Low-Temperature Scanning Tunneling Microscope (LT-STM), which is fixed to a two-shell cryostat and placed within two radiation shields to achieve working temperatures down to 7 K. The LT-STM is of a *Besocke Beetle* type and vibrational damping is achieved by a coupled spring system.

The circular sample itself (standard size of $\phi=10\text{ mm} \times 2\text{ mm}$) is mounted onto a *Heatwaves Labs, Inc* button heater which is fastened to the sample holder depicted in figure 3.1(b). When clamped to the manipulator a wide temperature range of 20 K to 900 K can be achieved via resistive heating of the button heater or cooling of the manipulator with liquid He or N₂, respectively. A *Creekside Technologies* sputtergun is installed for sample cleaning via Ar⁺ ion bombardment. For the controlled deposition of metallic as well as organic adsorbates by Physical Vapor Deposition (PVD) an *Omicron EFM 3T* triple e-beam evaporator and a home-built triple Knudsen cell (Al-housing with resistive heating) are installed. The nominal deposition thickness is monitored by a Quartz-Crystal Microbalance (QCM) with sub Å precision. For a detailed description of the LT-STM consult [40].

3.2 TPD chamber

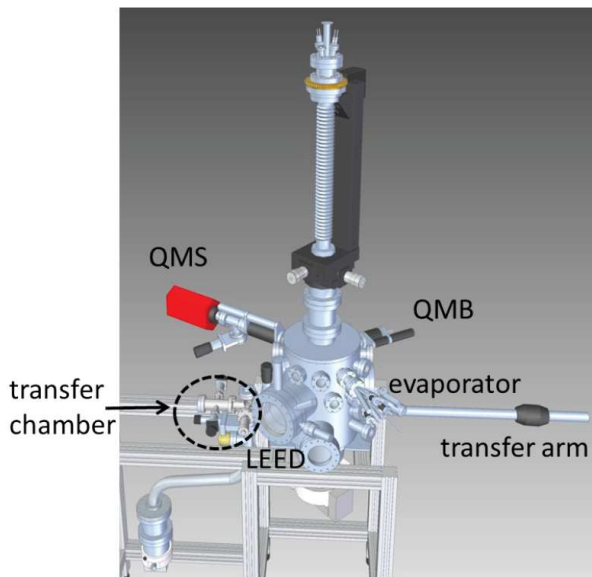


Figure 3.2: Engineering drawing of the TPD chamber. The setup is designed for quick sample transfer for additional *ex-situ* sample characterization or preparation. It is equipped with standard surface science preparation and characterization techniques as well as a separately pumped QMS for TPD measurements.

An additional UHV-chamber was utilized to obtain complementary Temperature Programmed Desorption (TPD) measurements. The chamber consists of the main Preparation Chamber (PC) as well as a Fast Entry (FE) for rapid sample transfer. Both chambers are equipped with a turbo-molecular pump which are connected to a pre-vacuum rotary-vane pump, achieving base-pressure in the 10⁻¹⁰ mbar range within

the PC and in the 10^{-8} mbar range within the FE. An additional turbo-molecular pump is attached to the QMS setup. Furthermore, a rotary-vane pump is installed for a set of gas-line dosing valves.

Attached to the PC is a *Pfeiffer QMG 220* QMS, which is used to conduct TPD measurements. For controlled desorption experiments the QMS is placed inside a separately pumped metal cylinder which tapers to a $\varnothing=0.8$ mm inlet. For more details on the TPD setup and measurements see chap. 2.2. Similar to the LT-STM setup an *Omicron EFM 3T* triple e-beam evaporator and a home-built triple Knudsen cell are installed for PVD of metallic and organic materials. A QCM is utilized to monitor the deposition rate. Furthermore, a *SPECS IQE 11* sputtergun is attached for sample cleaning and a *Specs LEED Er3000-D* device is used to check the sample cleanliness. The circular sample is mounted on a Molybdenum plate with isolated connectors for a thermo-couple. The sample holder can be inserted into the manipulator footing, which features an electric connection to the sample for the application of high voltage (HV) as well as an electrically isolated tungsten filament of $\varnothing=0.3$ mm. As such the sample can be heated via electron-bombardment with rates of >3 K/s. Additionally, the manipulator can be cooled with LN₂ allowing for a wide temperature control of 90 K to 1300 K. For more details on the experimental setup consult [41]. Note that the setup was adapted to hold a new sample-holder design.

3.3 Sample Preparation

Substrate

All experiments were performed on a Silver (Ag) single crystal. Ag is of a face centered cubic (fcc) crystal structure (Figure 3.3 (a)) with a lattice constant of $a = 4.079$ Å [42]. The crystal is cut along the Ag(001) plane resulting in a square surface lattice (Figure 3.3 (b)). Within this work three different Ag(001) crystals of $\varnothing=10$ mm with thicknesses of 2 mm, 2 mm and 10 mm were utilized. All crystals feature a nominal alignment accuracy of $<0.1^\circ$. The crystals were cleaned under UHV conditions by cycles of Ar⁺ sputtering (800 V, and 3 µA to 10 µA, depending on the system) and annealing to 500 °C for 2 min. Cleanliness and ordering of the substrate surface was then verified by obtaining perfectly defined (1x1) spots by LEED (Figure 3.3 (c)). During the last cleaning cycle prior to metal/organic adsorption a cooling rate of <30 K/min was applied in order to obtain large terraces.

Magnesium Oxide

Magnesium oxide crystallizes in a similar fcc structure as Ag(001) with a slightly larger lattice constant of 4.21 Å [43]. The small lattice mismatch of only 3.2 % enables epitaxial growth of MgO(001) on a Ag(001) substrate (see figure 3.3 (d,e)) resulting in little strain within the film [44]. Please note that for the ensuing discussion one atomic layer (half a unit cell) will be referred to as a monolayer (ML). In order to obtain large extended islands and layer-by-layer growth MgO is prepared based on the recipe pub-

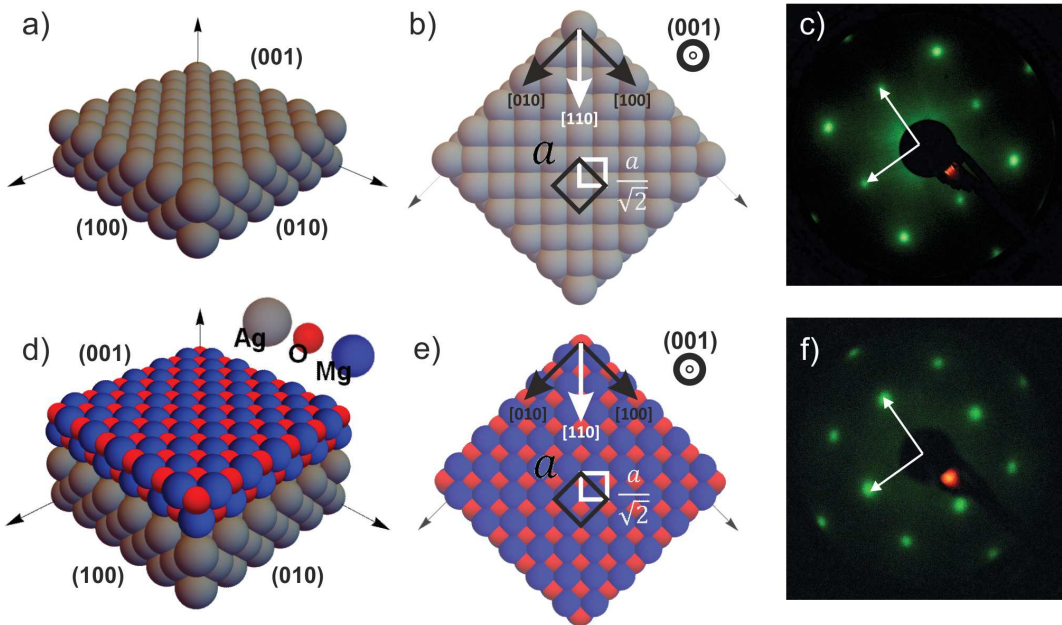


Figure 3.3: a) Schematic of a fcc Ag single crystal cut along the (001) plane. b) Top View of the Ag(001) surface. Note that the fcc(001) structure results in atomic nearest neighbors along the $<110>$ directions. Consequently the reduced surface unit cell results in a lattice constant of $\frac{a}{\sqrt{2}}$. c) LEED pattern of a clean Ag(001) crystal ($E_{el} = 145$ eV). d) Schematic of two atomic layers of MgO(001) on top of three atomic layers of Ag(001). e) Top View of the MgO(001) surface. Note that O adsorbs on top of the Ag atoms while Mg adsorbs on the hollow sites. f) LEED pattern of a nominally 2.6 ML thick MgO(100) film on Ag(001) ($E_{el} = 145$ eV).

lished by *J. Pal et al.* [45]. For the preparation of MgO, Mg¹ is evaporated using an *Omicron EFM 3T* E-beam evaporator and a home-made graphite crucible² onto atomically clean Ag(001). A deposition rate for bare Mg (see chap. 3.4) of about 1.5 Å/min is determined, resulting in an approximate ion flux of 100 nA. During the actual deposition onto the crystal an O₂ background pressure of 1×10^{-6} mbar is established and the desired amount of Mg is evaporated onto the sample which is kept at a temperature of 573 K. After deposition the crystal is slowly cooled down (2 K/min) to room temperature for characterization or further treatment. A representative LEED pattern of a 2.6 ML MgO film is shown in figure 3.3 (f). Because of the similar periodicity of MgO(001) and Ag(001) their LEED patterns are identical, but a spot-broadening can be observed with increasing MgO thickness due to surface roughening.

Organic molecules

Within the scope of this work three large organic molecules (5A, 6P, 2H-TPP) have been investigated which are depicted in figure 3.4. The stated molecular dimensions relate

¹Mg rod, $\varnothing = 6.35$ mm, Purity: >99.9 %, Supplier: chemPUR (Item-Nr.: 009252)

²Graphite rod, $\varnothing = 17$ mm, Purity: <5 ppm ash, Supplier: chemPUR (Item-Nr.: 901670)

to hydrogen-hydrogen distances according to the PubChem database [46]. The given molecules consist of rings of hydrocarbons in different sp^2 hybridizations, resulting in an alternating single- and double-bond configuration. Such conjugated systems exhibit, beside the formation of strong σ bonds, extended π orbitals perpendicular to the carbon backbone. A strong overlap of the π orbitals results in de-localized electron-states extending over the entire molecular backbone, which manifests in the appearance of semi-conducting properties.

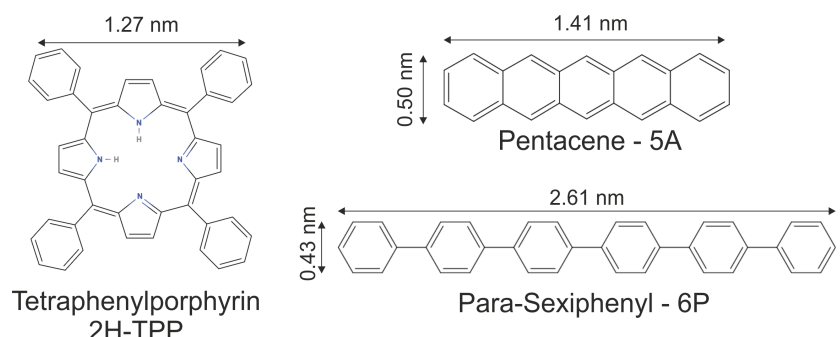


Figure 3.4: Molecules utilized within the scope of this PhD thesis. Structural formula and molecular dimensions taken from PubChem [46].

Pentacene

Pentacene³ (5A) consists of five linearly organized aromatic rings, each sharing 2 carbon atoms with its neighboring ring. It is easy to handle, UHV-stable, shows well-defined growth behavior [47] and exceptionally high charge carrier (hole) mobilities of $>1\text{ cm}^2/\text{Vs}$ [48]. It therefore advanced to be one of the most investigated organic molecules for the fundamental research on Organic Thin Film Transistors (OTFT). It is also one of the first molecules whose Highest Occupied Molecular Orbital (HOMO) and Lowest Unoccupied Molecular Orbital (LUMO) could be imaged with STM [49].

Para-Sexiphenyl

Para-sexiphenyl⁴ (6P) consists of six C-C bonded aromatic rings. Similar to pentacene it is easy to handle and UHV-stable. Due to the single C-C bonds connecting the phenyl rings it is much more flexible than 5A, as will be discussed in chapter 6.5. As it is an optically active molecule it can be utilized for the manufacturing of blue light emitting diodes [50].

³Pentacene, purified by sublimation, was obtained in powder form from *TCI chemicals* with a purity of 99.999 % (CAS 135-48-8).

⁴Para-Sexiphenyl was obtained in powder form from *TCI chemicals* (No purity stated, CAS 4499-83-6).

Meso-Tetraphenylporphyrin

Meso-Tetraphenylporphyrin⁵ (TPP) is a synthesized molecule that consists of four phenyl rings that are attached to the *meso* positions of the porphyrin. The *free-base* TPP has two hydrogen atoms bound to the nitrogen in its center (2H-TPP) which can be substituted by a metal atom such as Mg, Fe, Zn or Co. Porphyrin-based molecules play a major role in human and botanical metabolisms, such as the Fe-porphyrin based Hemoglobin or the Mg-porphyrin based Chlorophyll. As the natural forms often occur in complex molecular environments, 2H-TPP and its metalated forms have become model systems for basic research due to their simple synthesis and UHV-compatibility. Additional interest has developed for TPP in potential applications for single-molecule electronics or catalysis. Hence, numerous studies have been conducted. A comprehensive overview of these studies is given in the review articles of *Otsuki* [51] and *Gottfried* [52].

3.4 Physical Vapor Deposition (PVD)

A crucial issue when investigating adsorbates on an atomic/molecular scale is the controlled deposition of sub-monolayer amounts of the desired adsorbate. Sublimation of UHV-compatible solid material is simply achieved by thermal evaporation, carried out either via resistive heating or electron bombardment. The resulting atomic/molecular vapor is then mechanically focused by one or multiple apertures. The flux of the resulting beam can be accurately adjusted via tuning of the heating current and thus the vapor pressure. Such a setup is simply realized in a *Knudsen* cell, consisting of a closed cylinder filled with the desired material, surrounded by a heating wire and a pinhole. To quantify the amount of deposited material a Quartz-Crystal Microbalance (QCM) is placed within the profile of beam. The deposited mass is measured using the change of the eigenfrequency of the quartz-crystal disc. The relationship of the frequency-shift with the deposition thickness is given by the *Sauerbrey* equation [53]:

$$d = -\frac{\sqrt{\mu_{Qu}\rho_{Qu}}}{\rho_{ads}} \frac{\Delta f}{2f^2} \quad (3.1)$$

μ_{Qu} ... Shear modulus of quartz crystal, $2.947 \times 10^{11} \text{ g/cm s}^2$

ρ_{Qu} ... Density of quartz crystal, 2.643 g/cm^3

ρ_{ads} ... Density of adsorbate, 1 g/cm^3 for H_2O

f ... Eigenfrequency of quartz crystal, 5.94 MHz

Δf ... Frequency shift of QCM with adsorbate

d ... Adsorbate film thickness

In general the inner structure of very thin molecular films will differ from their bulk phases and it is therefore misleading to judge film thicknesses with respect to bulk-density values. A redefinition of the film thickness to a monolayer of a defined commensurate adsorbate structure is hence desirable. For this purpose the *Sauerbrey* equation can be rewritten to a monolayer of a hypothetic thickness of $x \text{ \AA}$ measured for a unity

⁵Meso-Tetraphenylporphyrin was obtained in powder form from *porphyrin systems* with a purity of 98% (CAS 917-23-7).

density of $\rho_{dig} = 1 \text{ g/cm}^3$. (The thickness reading of 1 \AA assuming $\rho_{dig} = 1 \text{ g/cm}^3$ is also often referred to as 1 digit, as an actual \AA reading wrongly suggests the knowledge of a monolayers height.) The areal density of the primitive unit cell ρ_{ads} is than defined by the atomic weight of an adsorbate m_{ads} per unit-cell area A_{ads} . Consequently, the frequency shift can be related to a full ML coverage of a defined adsorbate structure:

$$\Delta f = x [\text{\AA}] \cdot \rho_{dig} \cdot C = 1 \text{ML} \cdot \rho_{ads} \cdot C = 1 \text{ML} \frac{m_{ads}}{A_{ads}} \cdot C \quad (3.2)$$

with $C = -\frac{\sqrt{\mu_{Qu}\rho_{Qu}}}{2f^2}$, for $f >> \Delta f$. We can now express the nominal thickness x for 1 ML as:

$$x [\text{\AA}] \stackrel{!}{=} 1 \text{ML} \frac{m_{ads}}{A_{ads}} \frac{1}{\rho_{dig}} = \frac{m_{ads}}{A_{ads}} \frac{[\text{amu}]}{[\text{\AA}^2]} \cdot 1.6605 \cdot 10^{-24} \frac{[g]}{[\text{amu}]} \cdot \frac{[\text{cm}^3]}{[\text{g}]} \cdot 10^{24} \frac{[\text{\AA}^3]}{[\text{cm}^3]} \quad (3.3)$$

Considering the deposition of an atomic monolayer of MgO the nominal amount of deposited \AA can now be calculated. If only Mg adsorption is measured with the QCM and oxygen is freely supplied during deposition, as is discussed in chapter 3.3, we obtain a nominal thickness 4.55 \AA by only considering 1 Mg atom per unit cell (24.305 amu per 8.86 \AA^2). Assuming an equivalent sticking coefficient on the QCM as on the sample with similar geometry as well as an Mg flux unaltered by the oxygen, the deposition of 4.55 \AA of Mg onto the sample thus amounts to the deposition of a nominal ML of MgO and will hence be referred to as such. A nominal ML for molecular deposition can be likewise defined applying the experimentally obtained areal molecular density and the atomic weight of the molecule.

4 Topics

4.1 Ultra-thin dielectric films

The recent progress in the development of ultra-thin insulating layers has opened up a variety of exciting new fields of investigation. The possibility of manufacturing atomically controlled insulating layers of few monolayers thickness allows for the analysis of *insulating* samples with standard surface-science techniques based on electron interaction¹. Hence, a manifold of techniques such as Low Energy Electron Diffraction (LEED), Scanning Tunneling Microscopy (STM), High-Resolution Electron Energy Loss Spectroscopy (HREELS) and Ultraviolet Photoemission Spectroscopy (UPS) can now be utilized to characterize insulating materials in more detail.

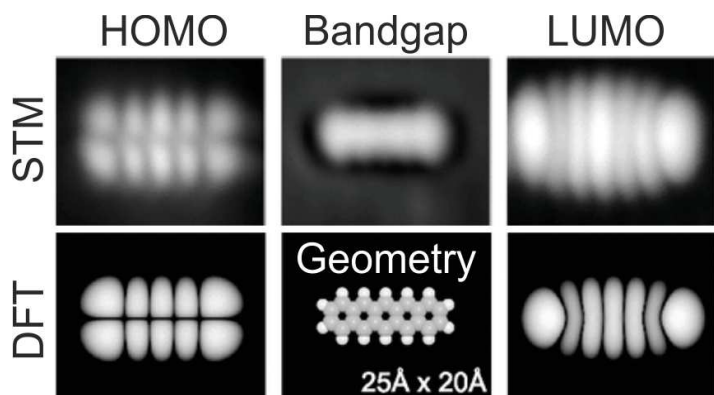


Figure 4.1: STM images of pentacene on ultra-thin NaCl on Cu(111). Top row: STM images of (left to right) the Highest Occupied Molecular Orbital (HOMO), within the bandgap, the Lowest Unoccupied Molecular Orbital (LUMO). Bottom row depicts corresponding STM simulations for the gas-phase molecule. [49]

molecules, which is useful for the investigation of the molecular electronic structure (Figure 4.1) [49]. However, it was recently shown that thin dielectric layers must not necessarily be of a passivating nature, but may actually be active in the promotion of charge transfer from the substrate to the adsorbate [5]. Such an influence on an adsorbates electronic structure has an impact on the energy alignment of hybrid organic/inorganic interfaces and can even enable catalytic activity or induce structural change (metalation). This awareness is even more important, as thin oxide layers can

Another interesting aspect is the investigation of the dielectric properties for decreasing insulator thicknesses, even down to a monolayer. As modern transistor technology rapidly approaches this miniaturization limit [54] this is of great interest for industrial application. In other fields thin dielectric films are utilized as a support for catalytically active metal particles [55] or to stabilize atomic magnetic moments [56]. Furthermore, dielectric thin films have been reported to act as decoupling layers for adsorbate

¹Electron-based methods accumulate charge on the surfaces of insulating materials. For very thin insulators the electrons can tunnel into the support, circumventing this charging

form unnoticed on reactive metal surfaces in industrial application in the presence of oxygen (even in low to mid-range vacuum). As such it is of crucial importance not only to understand the characteristics of hybrid structures with thin dielectric layers, but also to study their growth and development in detail.

For the fundamental investigation of thin dielectric/metal systems it is necessary to realize flat, well-ordered dielectric layers on top of metal-single crystals. To this end three major techniques have evolved within the last decades, namely the *epitaxial growth* of dielectric layers by evaporation [57], the controlled *thermal oxidation* of metal surfaces [58] and the *mechanical transfer* from sheet-like materials (or epitaxially grown films) onto various substrates [59]. For the *epitaxial growth* the dielectric material is evaporated in UHV-conditions onto the substrate. Mixed compounds (e.g. oxides) can also be realized by evaporation of a solid in a specific atmosphere (background dosing or post-oxidation). A good match of substrate and adsorbate lattice structure is essential, as lattice misfits of >5 % either completely inhibit the epitaxial evolution of a dielectric film or induce strong islanding, de-wetting or polycrystallinity in the thin film. As such the variety of suitable systems is limited. In recent years various recipes have been developed for the successful and reproducible production of dielectric/metal systems, such as CeO₂ on Pt(111) or NaCl, KCl, CoO and MgO on Ag(001) to name just a few... [3].

When exposed to oxygen, many single-crystal metal surfaces form thin oxide layers at the surface [60]. To achieve thicker metal-oxide films with *thermal oxidation*, metal crystals can be heated in an oxygen-rich atmosphere. Thus, the topmost atomic layers of the substrate can restructure into an oxide film. Such thermally grown oxides are typically amorphous or only poorly aligned with the substrate [61]. This procedure is commonly applied in semiconductor technology for the formation of gate oxides (SiO₂).

Finally, the *mechanical transfer* of sheet-like materials got popular with the discovery of stable graphene sheets and the mechanical exfoliation technique [62]. It was since adapted to various other 2D materials such as boron nitride or silica films [63, 64, 59]. With this technique material is transferred from a substrate onto the desired support. Therefore, lattice-match constraints do not apply, allowing for a great variety of adsorbate/substrate combinations.

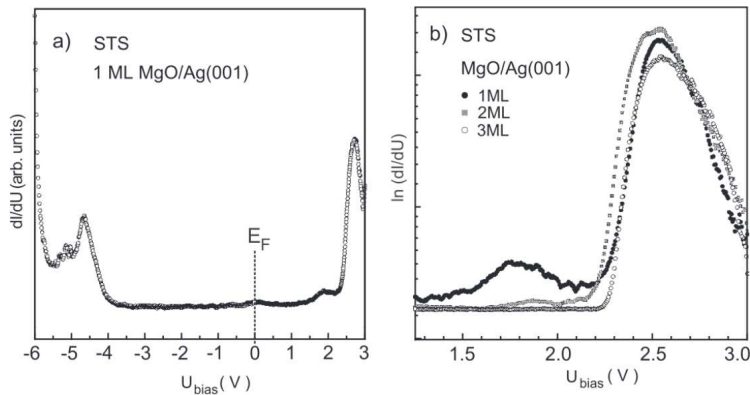


Figure 4.2: Scanning Tunneling Spectroscopy (STS) measurements of (a) 1 atomic Monolayer (ML) of MgO and (b) 1-3 ML of MgO epitaxially grown on Ag(001). Peaks at -4.2 eV, 1.7 eV and 2.5 eV are identified as MgO valence band, MgO/Ag interface state and MgO surface band, respectively. [3]

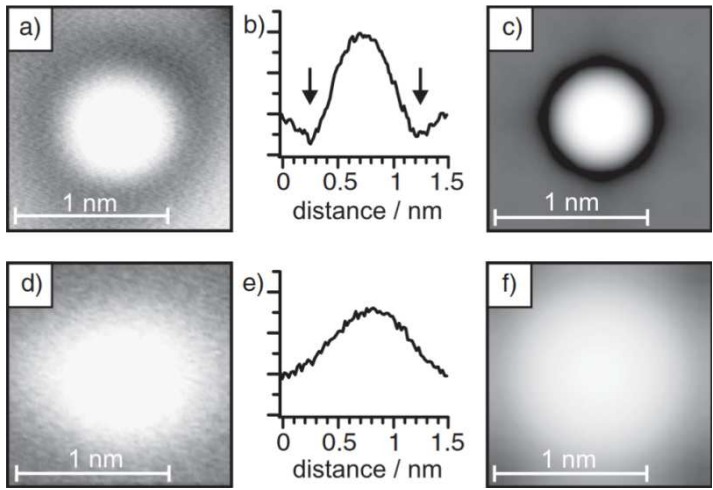


Figure 4.3: (a,b) STM image and height profile for a single Au atom and (d,e) a single Pd atom on 3 ML of MgO/Ag(001). Simulated STM images are depicted for (c) a singly charged Au atom and (f) a neutral Pd atom . [8]

cannot be straightforwardly adapted for thin-film systems. It is therefore important to address the intrinsic properties of ultra-thin films with respect to their bulk-like counterparts. A detailed characterization for ultra-thin MgO on Ag(001) is given in the review article by Schintke and Schneider [3]. As we regard thin MgO films on a metal substrate, Scanning Tunneling Spectroscopy (STS) can be applied to probe the electronic structure. Figure 4.2(a) depicts a dI/dV spectra of 1 ML of MgO on Ag(001). A peak evolves at -4 eV which is ascribed to the MgO valence band. Similarly, a peak is emerging at $+2.5\text{ eV}$, which is attributed to the MgO conduction band at the MgO(001) surface [65]. Between these states, a reduced tunneling current is observed and associated with tunneling through the MgO into underlying Ag states. An additional feature observed at 1.7 eV , associated with MgO/Ag interface states, diminishes with increasing layer thickness (Figure 4.2(b)). At a thickness of 3 atomic layers it disappears, resulting in an overall bandgap of 6 eV (6.5 eV peak-to-peak). Bulk MgO, as an insulating material, exhibits a wide-bandgap of 7.8 eV [66, 67], which is reduced by 2.3 eV to 5.5 eV (absorption threshold) by the before mentioned MgO surface states. This fits to the thin-film bandgap of 6 eV obtained for the 3 ML MgO/Ag(001) STS spectra. It is therefore concluded that ultra-thin MgO layers exhibit insulating properties already starting with the formation of the first atomic layer, while adapting a fully bulk-like electronic structure for 3 or more MgO monolayers. [3]

Bulk magnesium oxide, as many other oxides, is often considered as a support for catalytically active metal clusters. In 2005, Yoon *et al.* [69] demonstrated that Au_8 clusters were catalytically active for CO oxidation only when adsorbed on a defect-rich MgO support. They further related this activity to charging of Au clusters adsorbed on F-centers (also referred to as color centers), which are oxygen vacancies with 2 trapped electrons.

Within this thesis we employ the model system of MgO on Ag(001). Thin films exhibiting bulk-like geometry and stoichiometry are epitaxially grown with thicknesses ranging from 1 to 10 monolayer (ML). Details of the film preparation and crystal structure are found in chapter 3.3. However, thin films might exhibit different properties than their bulk-counterparts. Since material properties are usually obtained for its bulk form and theoretically calculated for infinite unit-cells (e.g. solid-state theory) they

This conclusion was further corroborated by STM and Electron Paramagnetic Resonance (EPR) measurements observing negatively charged Au atoms, dimers or trimers adsorbed on F-centers of MgO/Ag(001) [70]. Therefore, the catalytic activity is strongly limited by the defect concentration of the chosen support. However, at the same time a theoretical study predicted charging of Au atoms on defect-free ultra-thin MgO layers adsorbed on Mo(100) [5] or Ag(001) [6] to occur via direct tunneling from the substrate. For Pd, which exhibits a much lower Electron Affinity (EA) than Au a neutral charge state is predicted. Shortly after, this was experimentally confirmed for Au on MgO/Ag(001) by *Sterrer et al.* [8]. Within their work single Au and Pd atoms were deposited at low temperatures onto 3 ML of MgO on Ag(001). In figure 4.3 the adsorbed Au atom (a,b) appears as a bright circular protrusion surrounded by a dark depression whereas the Pd atom (d,e) appears just as a small continuous elevation. Corresponding DFT calculations provide simulated STM images which perfectly compare to the experimental data, as shown in (c) for a singly charged Au atom and (f) for a neutral Pd atom. An additional analysis of the radial pair-distance distribution of the atoms, whether random or equally spaced, corroborates the finding of charged Au and neutral Pd atoms.

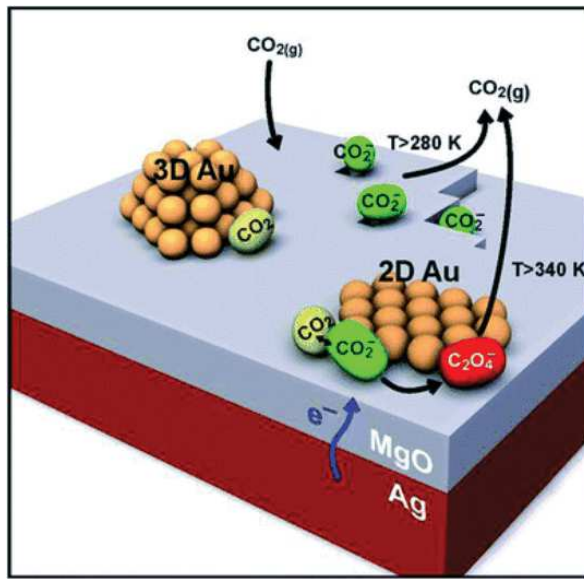


Figure 4.4: Morphology-sensitive catalytic reaction of carbon dioxide. Neutral CO₂ species (yellow) chemisorb on negatively charged 2D Au islands, absorb the charge (CO₂⁻, green) and finally combine to form oxalate C₂O₄²⁻ (red). At 3-dimensional Au islands this reaction is inhibited with the disappearance of the active sites. [68]

A consequence of the observed charge transfer is an altered growth behavior of Au deposits. For Au on bulk MgO, where no charge transfer occurs, the formation of 3D nano crystallites is energetically most favorable. But according to *Ricci et al.* [9] ultra-thin MgO on Ag(001) can induce the growth of stable 2D islands. The charge transfer leads to enhanced adhesion, which stabilizes the 2D-islands. This was experimentally investigated and confirmed by *Sterrer et al.* for Au deposited at low temperatures on MgO/Ag(001) [10]. It was further found that the excess electrons, tunneling from the substrate to the Au, preferably accommodate in the perimeter atoms of such Au islands [11]. This seems natural, as the Coulomb repulsion of the excess electrons would result in a maximization of the distance between them. *Calaza et al.* [1] demonstrated that such localized charges can activate molecules for catalytic reactions. In figure 4.4 a schematic depicts the formation of oxalates on Au/MgO/Ag(001). When CO₂ adsorbs at the rim of an island it can accept the localized electrons and form CO₂⁻. It can then further react with an additional CO₂ to form oxalate (C₂O₄²⁻). Within

their work, Calaza *et al.* could then observe such oxalate species with a combined Infrared Reflection Absorption Spectroscopy (IRAS) and STM study, supported by DFT calculations.

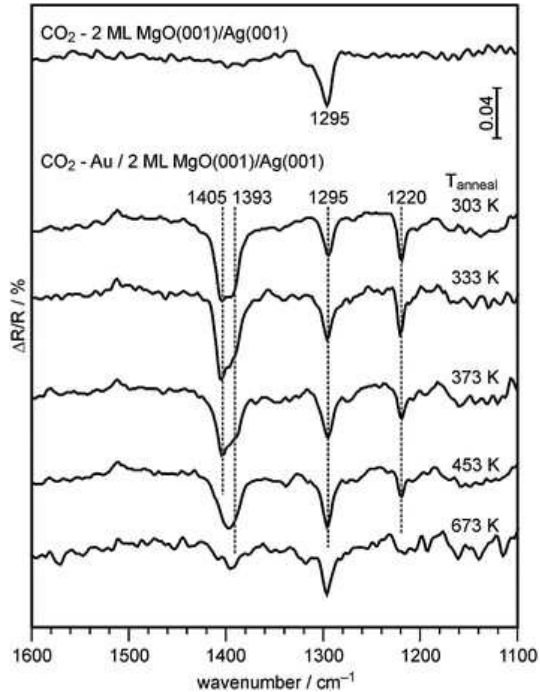


Figure 4.5: IRAS temperature series of a saturation dosage of CO_2 at 223 K on $\text{Au}/\text{MgO}/\text{Ag}(001)$. The top spectra shows a reference measurement on a substrate without Au islands, exhibiting no sign of oxalate formation. [68]

obtained spectra are depicted in figure 4.5. Three distinct bands are visible, which were previously associated to the vibrational bands of CO_2^- on MgO (1295 cm^{-1}) and oxalate on MgO (1220 cm^{-1} and 1398 cm^{-1}) [1]. While both species are present at substrate annealing temperatures of up to 453 K, only CO_2^- prevails for the 673 K preparation, indicating a sudden decay of the catalytic activity of the template. To relate the drastically reduced oxalate formation with the sample morphology, STM measurements for Au deposition at 77 K and successive annealing were performed. We observe a sudden change in the morphology of the Au islands for annealing temperatures of 500 K or higher. Starting from flat, roundish islands a transition into well-defined nanocrystallites of increased height is observed (Figure 4.4 and 4.7). Apparently, a crossover from a 2-dimensional to a 3-dimensional growth occurs, indicating that the thermal energy is sufficiently high for the Au atoms in the 2D clusters to overcome diffusion barriers. We can now assume that the decreased catalytic activity is related to the morphological change of the metal clusters. As charge transfer to a Au island scales with its contact area, significantly less charge per atom is transferred to a 3D island and, consequently,

Au islands on thin $\text{MgO}(001)/\text{Ag}(001)$ therefore represent a perfect model for further investigations of catalytic reactions. It is widely accepted that a catalysts performance is strongly determined by its metal/oxide interface [55]. Influencing factors are often associated with the size, shape or faceting of the metal particles on the oxide support. All these properties are rather susceptible to change with temperature. It is therefore of great interest to study the effects of thermal treatments on this model system.

This is subject of the publication presented in chapter 6.1: "Supports and modified nano-particles for designing model catalysts". To assess the catalytic activity an IRAS series was performed to observe the possible occurrence of oxalate species. The model catalyst was prepared by epitaxially growing 2 ML of MgO on top of a $\text{Ag}(001)$ single crystal (see chapter 3.3). Au was then deposited at 100 K and consecutively annealed to a set of increasing temperatures. These samples were then exposed to a saturation dosage of CO_2 at 223 K and studied with IRAS. The ob-

less CO_2^- is formed. We, therefore, conclude that the disappearance of oxalate species at elevated temperatures is caused by the morphological transition from 2D to 3D Au islands.

These results raise the question whether the growth parameters for the model catalyst can be tuned to an optimized island distribution and, therefore, catalytic activity. Another pending question concerns the quantification of charge transfer and its relation to island morphology. Although several STM/DFT studies have addressed this issue on a local level no quantitative analysis on a macroscopic scale was at hand.

These questions are addressed in our follow-up study presented in chapter 6.2: "Model systems in heterogeneous catalysis: towards the design and understanding of structure and electronic properties". To gain insight on the charge states of the Au islands a *modified* Auger parameter analysis was performed [72].

For that purpose the modified Auger-parameter β of an atomic species (e.g.: Au island) is determined as the difference of the Auger kinetic energy (KE) and the XPS binding energy (BE) for specific core-levels and Auger transitions. Both, KE and BE, are measured with respect to a bulk standard (e.g. β of Au(111)), yielding the Auger-parameter shift $\Delta\beta$. From this value the initial- and final-state contributions $\Delta E_{B,\text{initial}}$ and $\Delta E_{B,\text{final}}$ of the XPS core-level can be deduced (for more information consult [73, 72, 74]). While $\Delta E_{B,\text{final}}$ reflects the screening of the final-state hole (particle size), $\Delta E_{B,\text{initial}}$ can directly be related to the charge of the particle; i.e. negative values indicating the presence of excess charge and vice versa. In figure 4.6 the obtained values are graphically depicted for Au islands on thin and thick MgO films for increasing annealing temperatures. XPS spectra after Au deposition at 100 K require a fit of 2 species. While positively charged Au species are clearly observed for thin and thick films (left bar) only the thin film exhibits a distinct signal for negatively charged Au species (right bar). After annealing to 300 K there is only one species left. On the thin film, this species is negatively charged, whereas on the thick film, Au is essentially neutral. Finally, after annealing to 573 K, only little negative charge remains on the Au clusters on the thin MgO film. This is in perfect agreement with the observed morphological transition from 2D to 3D islands at this temperature and the accompanying reduction of charge transfer per Au atom. For thick MgO films on Ag(001) no significant charge transfer is observed independent of the annealing temperature,

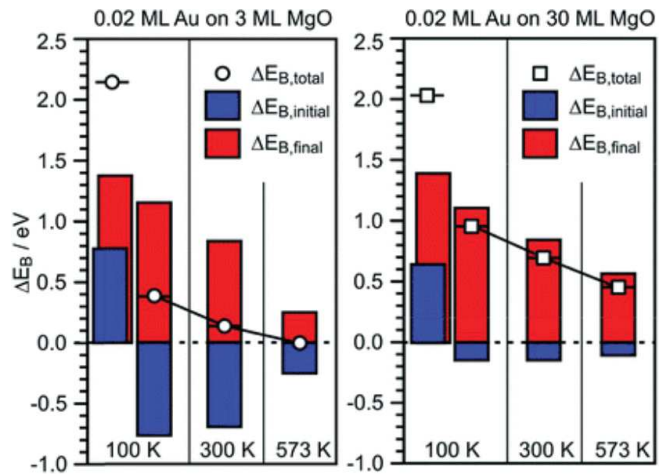


Figure 4.6: Binding energy shifts derived from Auger parameter analysis for Au on thin (left) and thick (right) MgO films on Ag(001) with respect to a Au(111) single crystal. Results are shown after deposition at 100 K (two Au species) and after annealing to 300 K and 573 K (1 species). [71]

corroborating previous results that significant charge transfer through the insulator is only observed for ultra-thin dielectric layers.

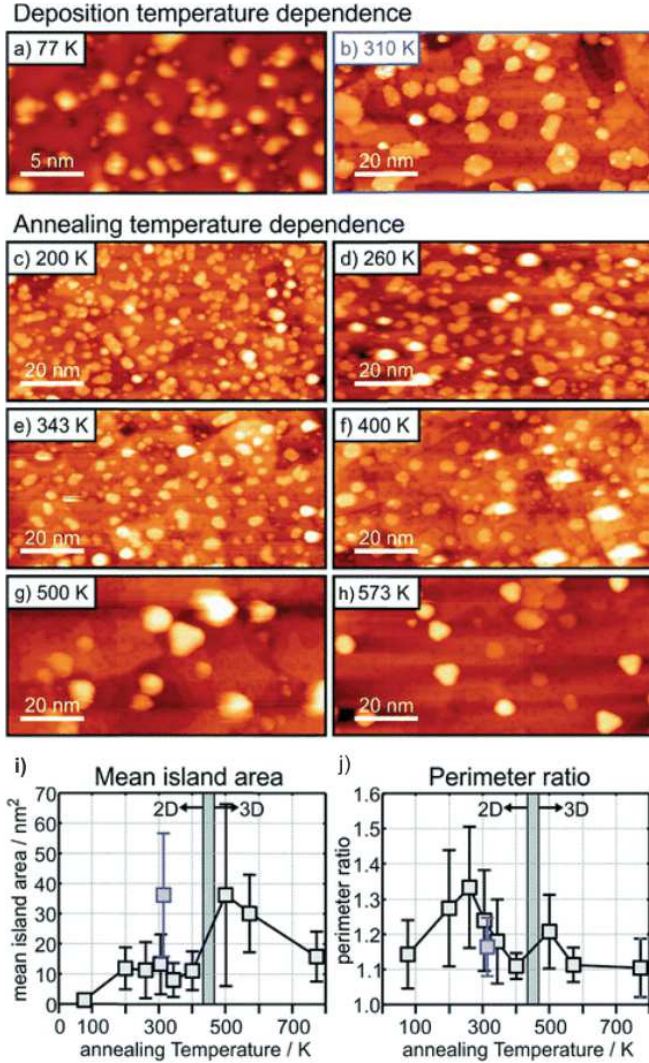


Figure 4.7: STM images of 0.1 ML of Au deposited at 77 K on 2 ML of MgO on Ag(001) and annealed to the temperatures (specified in the inlays in a, c-f). (b) Au deposited at 310 K. In g) and h), mean island area and perimeter ratio (defined in text) are plotted versus temperature, respectively. [71]

is plotted versus the annealing temperature. A distinct transition from gold clusters (77 K) to 2D islands (200 K). Further annealing results in little change until a sudden increase at 500 K indicates the formation of 3D-islands. Note that, although image artifacts induce an increased errorbar for the 500 K preparation, the presence of larger 2D islands and hexagonal 3D islands is still apparent from the STM image. Further increasing the annealing temperature results in a continuous de-

A detailed evaluation of the morphological development of Au on thin MgO films on Ag(001) is presented in figure 4.7. STM images were obtained for the following preparations: (a) Au on MgO/Ag(001) deposited at 77 K and (c-f) after successive annealing steps of 3 min each to elevated temperatures. The images show randomly distributed Au atoms and clusters for deposition at 77 K. After annealing to 200 K the clusters have nucleated to elongated islands with an apparent height of 0.3 nm to 0.4 nm (2D-islands). Upon annealing to temperatures of 500 K or higher, hexagonal crystallites of 1 nm to 2 nm apparent height (3D-islands) appear together with some remaining 2D-islands, in agreement with the previously mentioned 2D-3D transition.

To gain more quantitative information on the morphological development, a statistic analysis of the island distribution and morphology was performed for each preparation. In figure 4.7(i) the mean island area

rise occurs with the transition from gold clusters (77 K) to 2D islands (200 K).

crease of mean island area as the remaining large area 2D islands transform into 3D structures. A control experiment for Au deposition directly at room temperature (blue box, STM image in figure 4.7 (b)) exhibits a significantly increased island area, hinting towards altered diffusion barriers and nucleation properties. As the island rim was shown to play an active role in catalysis, an analysis of the island perimeter development is given in figure 4.7(j). We define the *perimeter ratio* as the ratio between the measured perimeter of an island and its ideal circular counterpart of the same area. This parameter is, thus, a measure for the deviation of circular island shape. Single atoms and small clusters exhibit circular shape and show a ratio of almost one. Although the mean island area between 200 K and 400 K (Figure 4.7(i)) is almost constant, a peculiar progression with a peak at an annealing temperature of 260 K is visible in the perimeter ratio. This is consistent with the elongated shape of islands observed in the respective STM images. With the transition to 3D-islands at 500 K the ratio converges to 1 again. Note that the room temperature preparation (blue square) exhibits a slightly lower ratio (and higher area) compared to its annealed counterpart, indicative for an increased diffusion length. Following the argument of activation at an islands rim the best catalytic performance is predicted for the 260 K preparation.

4.1.1 Water on MgO

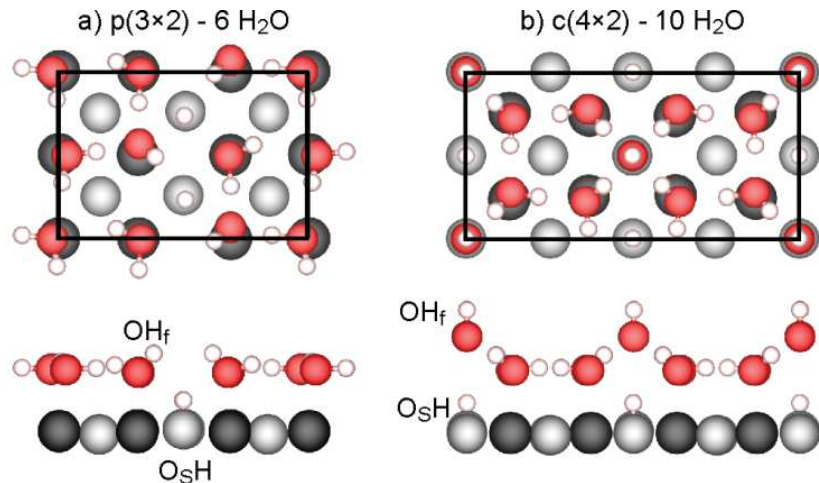


Figure 4.8: Monolayer phases of water on MgO. (a) The $p(3\times 2)$ unit-cell consists of 6 water molecules of which 2 are dissociated into OH_f and O_SH groups. (b) The $c(4\times 2)$ unit-cell consists of 10 water molecules, again including 2 dissociated molecules in OH_f and O_SH groups. Note the two structurally elevated OH_f groups which are not present in the $p(3\times 2)$ phase.

As already discussed in the previous section, metal-oxides play a major role in a manifold of catalytic processes as a support for metal nanoparticles or as the active material itself [55]. It was recently shown that the presence of molecular or dissociated water can both promote [75] or inhibit [76] catalytic reactions by blocking the active sites (metal cations). It is therefore crucial to understand the adsorption behavior of water on metal-oxide surfaces on a molecular level. Furthermore, a variety of fundamen-

tal processes of great interest for technological application require water/metal-oxide systems, such as photo-catalytic water-splitting, electro-chemistry and corrosion. For this reason a manifold of adsorption studies have been presented in the past decades [77, 78]. However, the complexity of water-substrate interactions often inhibited a full understanding of these systems on an atomic and molecular level. Hence, the focus shifted towards a surface science approach based on the investigation of single-crystal metal-oxide surfaces supported by DFT calculations. It was found that both intact and dissociated water molecules were stable on oxide surfaces, although the relative stability is difficult to determine, even on the simplest oxide surface. In the case of TiO₂(110) only a minor difference in binding energy of 35 meV was found [79]. The interaction between intact and dissociated species can have an additional, stabilizing effect on the dissociated products (hydroxyl-groups). Consequently, also mixed superstructures of intact and dissociated water molecules on metal-oxide surfaces can be expected to occur on oxide surfaces. Indeed, various recent publications demonstrated the coexistence of intact and dissociated water molecules in ordered 1-dimensional ([80]) and 2-dimensional ([81], [82]) structures. Interestingly, a 1-dimensional growth was found for water on CaO(001) [83] whereas the very related system of water on MgO(001) was found to produce a 2-dimensional superstructure [2].

The first experimental data for water on MgO(001) single crystal surfaces revealed the symmetry and size of two commensurate monolayer phases exhibiting a p(3x2) and a c(4x2) symmetry with diffraction methods [84, 85]. In corresponding TPD measurements the multilayer was found to desorb at 150 K revealing (mostly) the c(4x2) phase [86, 87]. With increasing temperature the monolayer exhibits a weakly pronounced transition to the p(3x2) phase until monolayer desorption at 190 K. However, it took until 2011 to fully resolve the molecular arrangement of the ordered water monolayer phases [2], which are depicted in figure 4.8. This was accomplished via a series of complementary experimental techniques (IRAS, XPS, TPD) as well as ab-initio DFT calculations in combination with structure search using genetic algorithm. Nevertheless, no locally resolved images of the discussed monolayer phases of water on MgO(001) were presented so far.

Within our work "Scanning Tunneling Microscopy of the Ordered Water Monolayer on MgO(001)/Ag(001) Ultrathin Films" in chapter 6.3 we present the first locally resolved STM images of an ordered water monolayer on MgO(001) epitaxially grown on a Ag(001) support.

It was recently shown that thin-films of MgO on Ag(001) exhibit significantly altered adsorption energies for water and its dissociation (and transition) products [88]. To investigate whether this influences the composition of the water monolayer spectroscopic measurements were performed. The two phases of ordered water monolayers on MgO(001), presented in figure 4.8, can be easily distinguished with spectroscopic measurements (IRAS). Good agreement has been found for the different stretching frequencies of the hydroxyl and water species and corresponding DFT deduced values [2]. Thus, water was deposited on thick (12 ML) and thin (2 ML) MgO films on Ag(001) and investigated with IRAS (according to [88] 3 ML or higher already represents bulk-like behavior). Within the measurement series, the temperature was step-wise increased to monitor the occurrence of the ordered monolayer phases. However, no significant deviation was observed for bulk-like and thin MgO films and the water adsorption was concluded to be similar in both cases.

An STM image of water adsorbed at 160 K on 2 ML of MgO on Ag(001) with a superimposed model of the c(4x2) phase is shown in figure 4.9(a). The bright protrusions fit perfectly to the OH_f groups found in the DFT calculations. Given the structural height of the OH_f groups in the calculated unit cell and the presence of only 1 bright spot per unit cell area this assignment seems reasonable. To demonstrate the presence of a long-range order a large scale image is shown in figure 4.9(b). Parallel stripes of protrusions extending over several nanometers can be seen. The stripes run along the [310] substrate direction and have a perpendicular spacing of 5.2 Å according to the STM linescan. This is in perfect agreement with the direction of the diagonal of the c(4x2) unit cell (Figure 4.8(b)) and the perpendicular spacing between the diagonals of neighboring unit cells. We therefore conclude that the striped superstructure represents the long-range ordered

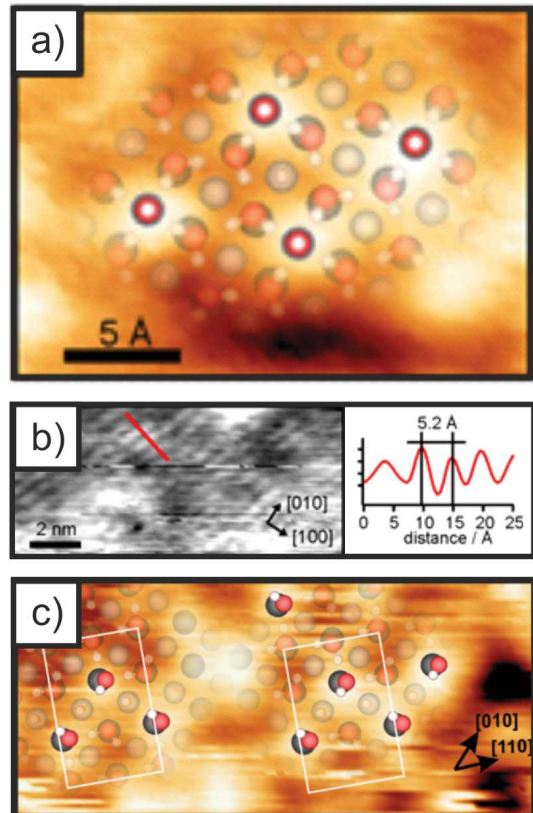


Figure 4.9: STM images of a monolayer of water on 2 ML of MgO/Ag(001). (a) Model of c(4x2)-phase superimposed on an STM image detail. (b) Large scale appearance of a c(4x2)-phase. (c) STM detail of a sample area which exhibits strong similarities to the p(3x2)-phase (model superimposed).

c(4x2) phase. As water deposition was conducted just above the multilayer desorption temperature (150 K) the c(4x2)-phase is indeed expected to prevail.

In addition to the aforementioned images of the c(4x2) phase, STM images exhibiting a different structure could also be locally resolved. An example is shown in figure 4.8(c). Within this image, no apparent long-range order is visible and fewer protrusions suggest a lower density of water molecules. However, a certain tendency for the formation of zig-zag structures is apparent with an alignment along the $\langle 110 \rangle$ direction. Superimposing the ionic sub-lattice on the STM image further reveals that the protrusions are separated only by nearest neighbor distances in the $\langle 100 \rangle$ direction. Both, the zig-zag orientation and the nearest neighbor distance also occur in the p(3x2) monolayer phase. Indeed, superposition of the p(3x2) unit cell in figure 4.8(c) shows good agreement between the STM-image and the model. This interpretation is further supported by simulated STM-images for the applied tunneling conditions (data not shown).

4.2 Energy Alignment

Within the work presented so far, charge transfer through thin dielectric layers was predicted, verified and related to the activity of a model catalyst. However, the driving forces behind charge transfer and in what quantity it occurs is still subject of ongoing discussion. Though in principle an electron can only be transferred through a tunneling barrier as a whole or not, many DFT calculations mostly yield fractional values. This may, however, simply be due to the known limitations of the calculations regarding the chosen functional and size of the surface unit cell. For example, many functionals overestimate electron delocalization [89], leading to fractional charge transfer. Additionally, if only one molecule per unit cell is considered, integer charge transfer can lead to a large dipole, that destabilizes the system, which DFT compensates by backdonation, hence, fractional charge transfer [90]. Finally, it should be noted that charge quantification in DFT, such as Bader charge analysis, is generally problematic because of the definition of the observed volume.

However, also experimental results on integer charge transfer through thin, dielectric layers were reported. *Lin et al.* [12, 11] observed local Au clusters and two-dimensional Au islands on MgO(001)/Ag(001). With a combined STM and DFT approach they demonstrated integer charge transfer to the Au adsorbates and found that the number of transferred electrons increases with the island size. In a different study UPS measurements were performed on a monolayer of large organic molecules (fullerenes) on a dielectric/metal substrate. Charge transfer was concluded to occur to only 5 % of the molecules within the monolayer [91]. In our study we aim to provide a quantitative study for a well-defined adsorbate where charge transfer to a distinct, observable electronic state occurs. We find such criteria to be fulfilled by large organic molecules exhibiting discrete states in extended molecular orbitals.

But in order to discuss the aspects of charge transfer in more detail, the basic concepts of energy level alignment have to be introduced. The energetic alignment of organic molecules on inorganic substrates is of great importance in the industrial sectors of organic electronics. It is therefore subject of many scientific studies [15, 16].

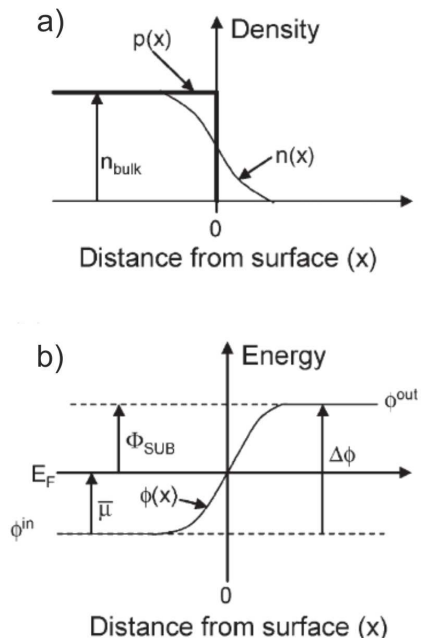


Figure 4.10: a) Positive $p(x)$ and negative $n(x)$ charge density distribution across a metal surface. b) Electrostatic potential increase from bulk to outer potential. The bulk chemical potential $\bar{\mu}$ together with the occurring dipole $\Delta\phi$ define the substrate workfunction ϕ_{SUB} with respect to the Fermi edge E_F . (Figure taken from [16])

Because of the interest in technological applications many studies have been presented on working macroscopic devices with poorly defined interfaces on a molecular or atomic level. With the recent development and advanced control of ultra-thin dielectric films on metal substrates, subject of the previous chapter, new possibilities arise in the investigation of this phenomenon. Within this chapter a picture of the energy alignment mechanisms of molecules with metallic or dielectric/metal substrates is provided. For this purpose some physical key quantities are introduced before the general alignment mechanism is discussed.

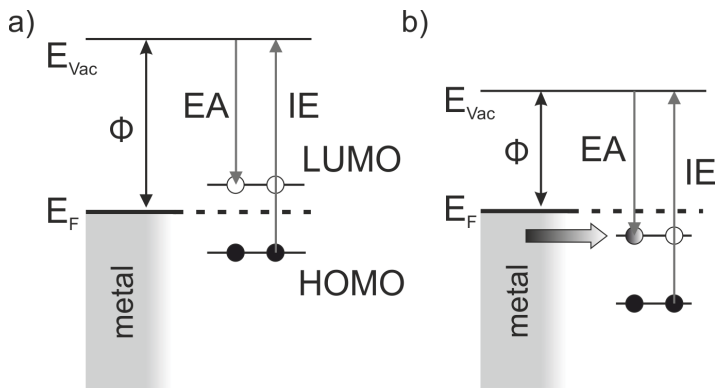


Figure 4.11: Energetic alignment of a given molecule at infinite distance for a) a high workfunction substrate and b) a low workfunction substrate.

between the local workfunction, defined by the local structure of the crystal (e.g. surface facets, reconstructions, lattice position, defects) and the global workfunction of a crystal surface. Note that at adequately large distances local workfunction contributions are averaged and one obtains a global work-function! For a single crystal, typically utilized in surface science, only one crystal facet is present which, apart from defects, mostly defines the global workfunction.

The workfunction can be mathematically defined when introducing the vacuum level E_V as the energy level at an infinite distance from the surface and the Fermi level E_F , which is the energy of the highest occupied electronic state in equilibrium at 0 K according to the Fermi distribution.

$$\phi = E_{Vac} - E_F \quad (4.1)$$

This definition is valid even if no electronic states are actually present at the surface around E_F , as is the case for thin insulating films on metals (see chapter 4.1). For a given (metal-) substrate the workfunction is defined by the bulk chemical potential $\bar{\mu}$ and the electrostatic potential across the surface $\Delta\phi$. The latter is based on the spill-out of electrons beyond the metal surface, resulting in a net-negative charge outside of, and a net-positive charge within the crystal as depicted in figure 4.10(a) and first described with the *Jellium model* [92]. Such a dipole increases the energy necessary to extract an electron from a crystal and as such its workfunction. In figure 4.10(b) the increase of the electrostatic potential caused by the electronic spill-out is

The principally considered quantity is the workfunction ϕ , which simply speaking is the energy needed to take an electron from within a solid through its surface to the outside of the solid. It can also be defined as the energy difference between the equilibrium systems of an N electron and an $N - 1$ electron system with the extracted electron being far from the surface and without kinetic energy. Furthermore, one has to distinguish

depicted in 1D across the surface. [16]

In contrast to a metal bulk with an electronic band structure, single molecules exhibit discrete energy levels. Figure 4.11 schematically depicts the level alignment of a molecule/substrate system with respect to the common Vacuum level prior to adsorption. The molecules Electron Affinity (EA) depicts the energy gain of bringing an electron from the Vacuum level to the Lowest Unoccupied Molecular Orbital (LUMO) while the Ionisation Energy (IE) depicts the energy to bring an electron from the Highest Occupied Molecular Orbital (HOMO) up to the Vacuum level. In (a) the level alignment is such that the EA is smaller and the IE is larger than the substrate workfunction, suggesting that the molecule will adsorb in a neutral charge state (neglecting adsorption induced effects for a moment). In (b) the initial workfunction has been reduced which places the initially unoccupied orbital, the LUMO, now below E_F . According to quantum-statistics all states below E_F within a closed system should be occupied, resulting in a charge transfer from metal to molecule upon adsorption in this system.

However, it is generally not possible to predict whether or not charge transfer will occur, from the known values of the substrate workfunction and the gas-phase EA and IE of the molecules, since adsorption induced effects can significantly alter the level position in a given adsorbate system. In the following an overview of the mechanisms involved in the level alignment for molecular adsorption on (dielectric-) metal systems based on our recent work is given.

4.2.1 Energy Alignment Mechanisms

Starting from a neutral molecule in the gas-phase the energetic alignment with respect to the Vacuum level is defined by its IE_{gas} and EA_{gas} as already discussed earlier. As the Vacuum level represents an absolute energetic level unperturbed by matter and corresponding electrostatic or electrodynamic effects it is applicable for both substrate and molecule and can serve as a reference level. Aligning the energetic levels of adsorbate and substrate with respect to the Vacuum level (Figure 4.11) is referred to as Vacuum level alignment. Once a molecule approaches the surface a series of effects (see figure 4.12) will then alter the relative positions of substrate and molecular electronic states. Finally, the adsorbed molecule relaxes to an energetic position with its (now possibly different) frontier orbitals defining the IE_{ads} and EA_{ads} , respectively. In the following, a breakdown of the major alignment-effects is given and sketched in figure 4.12 for organic/metal systems and figure 4.13 for organic/dielectric/metal systems. Note that although all contributions are depicted as a sequence of effects they occur simultaneously and can therefore influence each other.

Push-Back

As already mentioned, electron density spills out into the vacuum region on metal surfaces. Upon adsorption of large organic molecules, as in this work, *Pauli Repulsion* will lead to a *push-back* of electron density into the metal. This *push-back* or *pillow effect* reduces the electrostatic dipole and as such the workfunction of the system [93]. Hence, the Vacuum level is shifted down with respect to the metals E_F and consequently

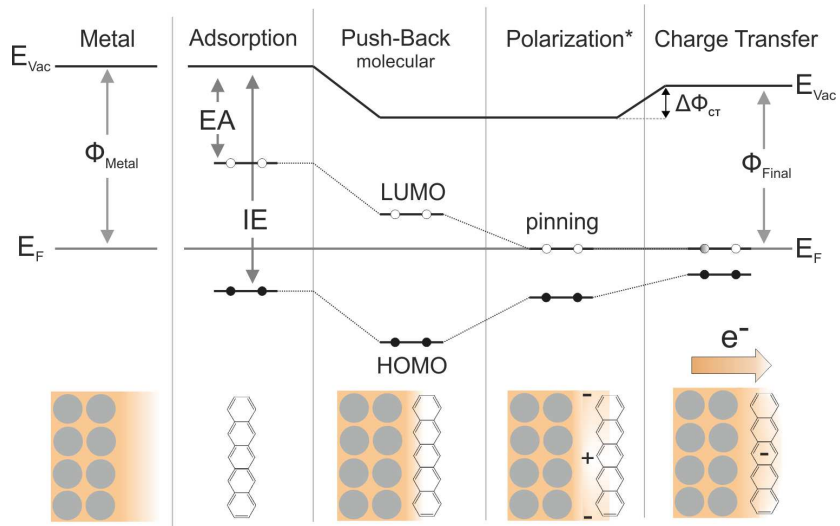


Figure 4.12: Development of the energetic alignment of an organic molecule adsorbing on a metal substrate. The model starts with Vacuum level alignment of a pristine substrate and a gas-phase molecule. For better visibility the entire diagram is aligned at the substrates E_F . A simplified illustration of the evolution of the charge density at the surface is given at the bottom of the figure. (*Structural relaxation is not sketched separately but is included in the polarization contribution.)

so are the molecules electronic states as shown in figure 4.12. This effect can also occur when thin dielectric films are deposited on metal surfaces (for more information on thin dielectric films see chapter 4.1).

Polarization

Furthermore, a decrease of the molecular HOMO-LUMO gap occurs upon adsorption on a substrate. In literature various denotations are found for the same phenomena such as *polarisation*, *gap re-normalization*, *dynamic polarizability*, or even *screening*². This effect is caused by the polarizability of the substrate and relates to *non-local correlation* effects. The gap reduction was found to scale with the Density Of States (DOS) at E_F for metal substrates and with the bandgap-width of semiconductors. [94, 95]

This polarization effect can be viewed as the response of substrate states to the presence of an extended polarizable object. Charge rearrangements in the substrate manifest in attractive interaction with unoccupied states (i.e. lowering the LUMO closer to E_F) and repulsive interactions with the occupied states of the molecule (i.e. lowering the binding energy of the HOMO and drawing it to E_F). This effect is more naturally grasped when considering a molecular crystal, which always features a reduced HOMO-LUMO gap as compared to its gas-phase value. In that case it is not the substrate but the molecular neighbours that respond to the presence of the molecule. For molecules adsorbed on surfaces the polarization contribution was shown to scale

²Note that this screening has to be distinguished from the final-state screening of holes in photo-emission processes

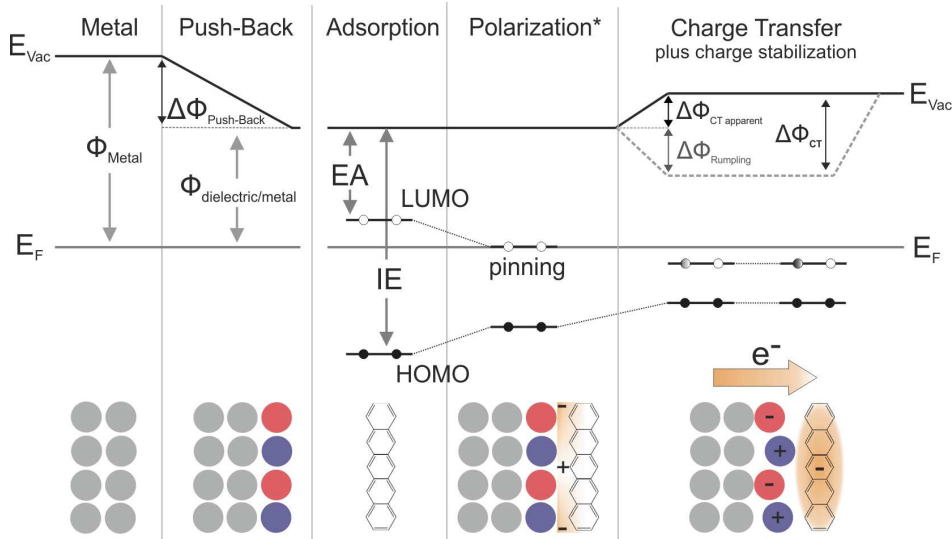


Figure 4.13: Development of the energetic alignment of a molecule and a dielectric/metal substrate. In contrast to the organic/metal system in figure 4.12 the push-back effect inherent is entirely fulfilled by the dielectric. Inhere, vacuum level alignment of the dielectric/metal substrate with the gas-phase molecule is given as the starting position. (*Structural relaxation is not sketched separately but is included in the polarization contribution.)

with the number of molecular neighbours, their polarizability (i.e. extension of the orbitals) and the distance of the molecule to the substrate surface [32]. Note that this effect considers the neutral molecule and effectively reduces the charging energies of frontier states. The polarization of the substrate does not create an overall dipole perpendicular to the surface and thus, the workfunction of the substrate, i.e. the metals E_F and E_V , remain unchanged. Additional changes of the molecular levels may also be induced by structural relaxation of the molecule upon adsorption, possibly interwoven with the formerly mentioned polarization. However, calculations yield rather small energetic shifts induced by relaxation (max. 0.10 eV [96]), which means that especially for planar, rigid molecules structural relaxation is only of minor importance for the level alignment. According to literature, polarization can contribute to HOMO-LUMO gap reductions in the range of 1 eV to 3 eV [94, 95].

Charge Transfer

If, by a combination of the aforementioned effects, the LUMO is shifted to or below E_F , as depicted in figure 4.12 and 4.13, charge will be transferred from the occupied substrate states to the unoccupied molecular states. The mechanism of this charge transfer can vary for different adsorbate systems. Inhere, we will only consider large, stable, π -conjugated molecules without intrinsic dipoles and/or functional groups. In other words, we strive to describe the interaction of extended molecular orbitals with delocalized substrate states and not site-specific covalent bonding. We start with the description of molecular adsorbates on unreactive metal substrates as depicted in figure 4.12. In simple terms a metal consists of a well-defined positive ion-grid with its valence

electrons forming a delocalized electron-gas. By definition, its density of states is continuous at E_F with no bandgap present. These metal states can hybridize with molecular states, meaning that the overlapping wave-function of the molecular orbital mixes with the wavefunction of the corresponding substrate state [97]. For the situation described above, this means that the molecular LUMO mixes with a substrate state and as such becomes partially occupied. Within this mechanistic description the amount of charge transferred to the molecule can vary continuously and this mechanism is generally referred to as *Fractional Charge Transfer (FCT)*.

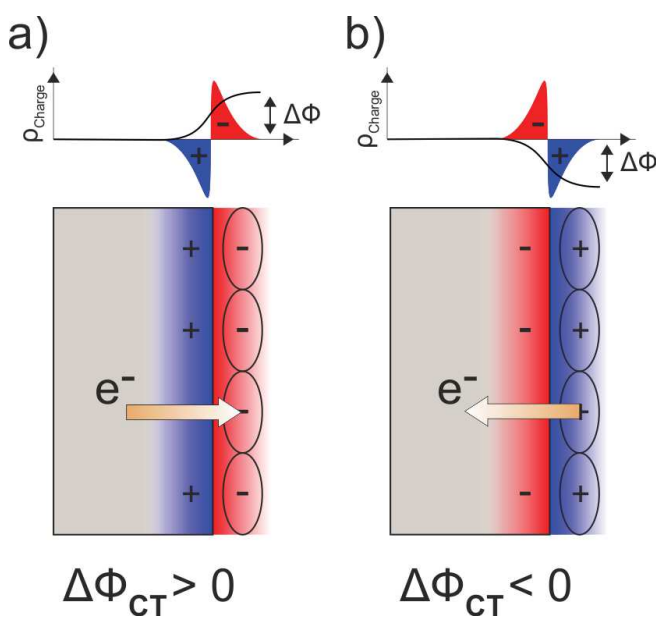


Figure 4.14: Electrostatic dipole induced by charge transfer. (a) Electrons are transferred from the substrate to a molecular orbital. The change in the charge density distribution, given in the graph above, results in a dipole potential of positive sign. The workfunction increases. (b) Charge transfer from the molecule to the substrate results in a decrease of the workfunction.

tion and small molecular IE will lead to charge transfer in opposite direction, namely from the HOMO into the substrate.

Charge transfer naturally results in the rearrangement of charge densities. In the case of charge transfer to the LUMO an electrostatic dipole is built up which results in an increase of the workfunction as depicted in 4.14(a). As the molecule gains negative charge, electrostatic repulsion also decreases the binding of lower lying orbitals and as a consequence all occupied orbitals are pushed up towards E_F . The LUMO itself should also be affected by the electrostatic repulsion, but can not be pushed above E_F , as it would then not experience charging in the first place. It is therefore *pinned* to (or below) E_F . This self-regulatory process determines the amount of transferred charge and will be discussed in detail later. If charge transfer occurs in the opposite direction,

In the case of a dielectric/metal system, as depicted in figure 4.13, no substrate states are available for hybridization, because the dielectric layer has a bandgap around E_F . The molecular LUMO is pushed below E_F and it is energetically favourable to occupy it. In this case electrons of the metal substrate tunnel through the thin dielectric layer and occupy the LUMO. Following this mechanism, only integer electron charges can be transferred to the molecule and it is therefore referred to as *Integer Charge Transfer (ICT)*. At this point it should be mentioned that localized charges from defects [70] or dopants [98] can also partake in the charge transfer, but (as a negligible factor within our studies) will not be part of the discussion. Apart from the depicted alignment in figure 4.12 and 4.13 a high initial workfunc-

i.e. from the HOMO to the substrate (Figure 4.14(b)), the workfunction decreases and the HOMO is pinned to E_F .

Charge Stabilization by Polaronic Distortion

Polaronic distortion describes the structural relaxation of an ionic-lattice upon interaction with a charged adsorbate [99]. If, for example, a negatively charged molecule adsorbs on an ionic lattice, attractive forces will act towards the cations while the anions will experience repulsive forces. Consequently, a structural relaxation of the ionic lattice via a polaronic distortion of the surface occurs. In literature, reports already claimed a non-negligible effect induced by rumpling for oxide mono- [100] and bi-layer [101] even in the absence of a charged adsorbate, which is induced by interface charge-transfer. Considering an extended molecular orbital in which charge transfer occurs, a collective rearrangement of the ions can induce an additional dipole across the entire surface. Recent DFT calculations for 5A/MgO/Ag (see chapter 4.3) predict a dipole potential resulting in a workfunction decrease of 1.3 eV, almost independent of dielectric film thickness (2-8 ML). The predicted ionic rearrangements are in the sub-Å range and mostly localized in the topmost atomic layer. Note that theory also predicts a rumpling of the interface layer, resulting in a dipole of opposite direction, that is present even without charged adsorbates. The corresponding DFT results and a more detailed discussion are given in the Appendix 4.3.

As discussed in the previous section, charge transfer to a given molecule with given EA will occur if the substrate workfunction is low enough. The charge-induced electrostatic dipole would then increase the workfunction, but at the same time the polaronic distortion will significantly reduce the workfunction. The ionic rearrangement is therefore essential for the *stabilization* of the transferred charges. A similar effect of opposite sign for charge transfer from the HOMO to the substrate might also occur, but has not yet been investigated.

Experimental evidence for this phenomenon is rather difficult to obtain as the structural relaxation is expected to occur rather localized beneath the charged molecular species and simultaneously with charging. Although it is possible to experimentally obtain the workfunction change $\Delta\phi$ induced by the deposition of a molecular monolayer on a dielectric/metal substrate, this value is composed of two counteracting contributions, namely the positive charge transfer dipole $\Delta\phi_{CT}$ and the negative dipole induced by the polaronic distortion $\Delta\phi_{PD}$ (for CT to the LUMO):

$$\Delta\phi = \Delta\phi_{CT} + \Delta\phi_{PD} \quad (4.2)$$

Both workfunction contributions are linearly dependent on the number of charged molecules. The *apparent* CT dipole is hence strongly underestimated if the rumpling of the surface and the corresponding polaronic distortion dipole is not considered. This effect is also schematically depicted in the alignment diagram in figure 4.13). For a more detailed discussion and DFT calculations on this phenomena see the appendix in chapter 4.3.

4.2.2 Integer Charge Transfer Model

With the fundamental processes of level alignment established, we can now discuss a more general concept of energy alignment. As already stated, charge transfer will occur if the substrate workfunction is small enough to place the LUMO below E_F . The transferred charges then result in a dipole that pushes the LUMO towards E_F . Thus, we encounter a self-regulatory process where charge-transfer will occur until a threshold or *pinning* workfunction is reached. The energetic alignment of molecules adsorbed on top of an (ideal) substrate can therefore be generalized within the *Integer Charge Transfer (ICT) model* (see figure 4.15) [16].

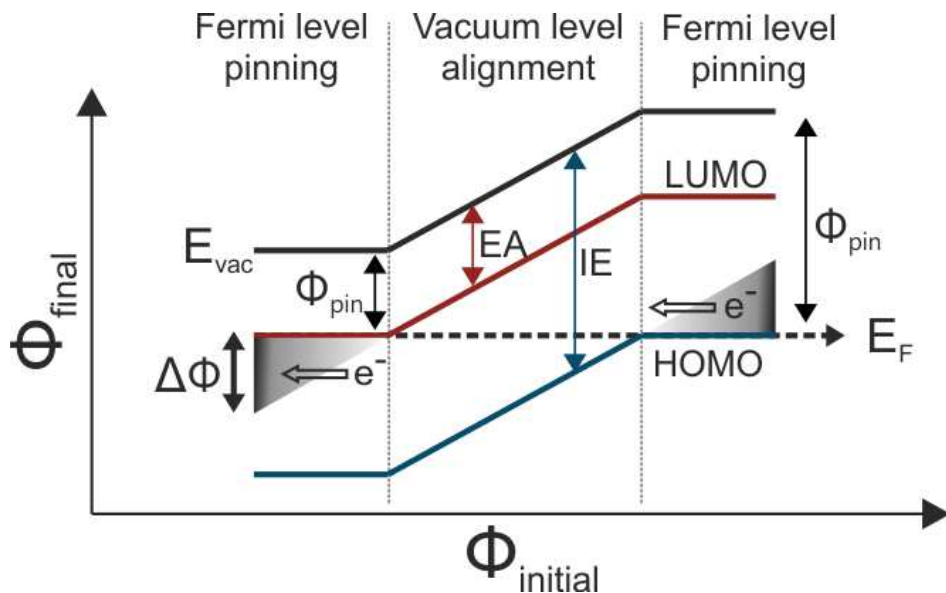


Figure 4.15: *Mark of Zorro* dependence: Final workfunction ϕ_{final} of a molecular monolayer adsorbed on the substrate vs. the initial *idealistic* substrate workfunction $\phi_{initial}$.

Within this model we consider a full coverage (monolayer) of a molecule with a given EA and IE on top of a substrate of an initial workfunction $\phi_{initial}$. Note, that $\phi_{initial}$ is in this case not the workfunction of the clean substrate, but includes already the aforementioned contributions to the workfunction change upon molecular adsorption, except the charge transfer dipole. In experiment it is therefore better applicable to dielectric/metal systems, where the push-back effect is fully achieved by the dielectric and no more push-back contributions are added by the molecular adsorption. In the middle section of figure 4.15 the empty LUMO appears above and the filled HOMO appears below E_F . When reducing the initial workfunction (moving to the left in the figure), the LUMO approaches E_F while the HOMO moves further down to higher binding energies. No charge transfer and hence no workfunction change occurs, resulting in a linear relationship between final and initial workfunction. The molecular states align with E_{vac} and consequently shift with the substrate workfunction. Once the LUMO hits E_F charge transfer to the molecule occurs and ϕ_{final} will stay constant. The bigger the discrepancy between the linear dependence of $\phi_{initial}$ and ϕ_{final} ($\Delta\phi$ in figure 4.15), the more charge will be transferred from the substrate to the molecule and hence, the

charge transfer dipole increases. The molecular states are now *pinned* relative to E_F , independent of the initial substrate workfunction. A similar mechanism is given for high initial workfunctions (right side of the graph), with charge now transferring from the HOMO to the substrate. This results in a dipole of opposite sign. In case of integer charge transfer through thin dielectric films the dipole potential can be approximated by a simple capacitor model:

$$\Delta\phi = e^- \cdot \frac{Q_A \cdot d_{Ox}}{\epsilon_0 \epsilon_r} \quad (4.3)$$

with e^- the electron charge, Q_A the charge per unit area, d_{Ox} the oxide thickness and ϵ_0 , ϵ_r vacuum and relative dielectric constant, respectively. Following this equation for a given system of thickness d_{Ox} a large dipole potential will result in a higher charge density per unit area, or an increased number of charged molecules on the surface. In principle this conceptual model can also be applied for simple organic/metal systems with the dielectric being a vacuum layer.

As pointed out in the previous section, the experimental quantification of the individual contributions of the charge transfer dipole is not possible. Usually only the initial workfunction before and the final workfunction after the adsorption of a molecular monolayer are experimentally accessible. This includes already effects such as push-back and relaxation on metal surfaces. But even when regarding dielectric/metal systems the previously stated polaronic distortion induced by negatively charged molecules can lead to dipole changes of -1.3 eV and thus to a vast underestimation of a charge transfer induced $\Delta\phi$ (see chapter 4.3).

Charge transfer mechanisms

The mechanism of charge transfer is subject to a number of studies due to its importance in organic electronics [102, 103]. Charge transfer in organic/metal systems (fractional CT) is realized by a hybridization between molecular and substrate states, which is rather challenging to characterize experimentally. In the following discussion we therefore focus on organic/dielectric/metal systems which exhibit integer charge transfer. These systems further have the advantage that the push-back effect due to the molecules is negligible which yields a more realistic, measurable $\phi_{initial}$.

In their work, leading up to the ICT model *Salaneck and co-workers* have investigated polymers and large organic molecules (e.g. F4-TCNQ) on atomically defined metal substrates [104, 16]. Furthermore, the ICT model was also studied more extensively on a macroscopic level. *Greiner et al.* investigated three different molecules on an extensive set of various polycrystalline, thermally oxidized metal substrates [17]. They find a good experimental reproduction of the *mark of zorro* dependence, even for these rather poorly defined dielectric/metal systems. Though there are various studies on the actual pinning workfunction and whether it is substrate or just molecule dependent [93, 96, 105] no conclusive picture is drawn so far. Hence, we aim to provide a detailed study on atomically defined dielectric/metal systems to gain further insight on this phenomenon.

A pending question in this context is how the charge distribution within a molecular film is established for varying initial workfunctions within the Fermi level pinning

regime. According to the capacitor model in eq. 4.3 a workfunction shift for a given dielectric thickness results in a change of the areal charge density. While for organic/metal systems fractional charging will continuously compensate an initial workfunction change, dielectric/metal systems are limited by integer charge transfer. Within the ICT description and in the Fermi level pinning regime, a continuous variation of the CT dipole with varying initial workfunction can only be achieved by changing the ratio of charged and uncharged molecules in the molecular layer. While previous DFT studies always found fractional CT, a more recent approach by *Hofmann et al.*, utilizing large unit cells and a higher degree of localization, could reproduce the expected presence of charged and uncharged species [90]. Within their work they considered TCNE molecules on NaCl/Cu(100). Figure 4.16(a-c) shows the development of the surface potential when subsequently placing one (a), two (b) and three (c) molecules on the surface (gray molecules depict placeholders for where other molecules would be at full coverage). Red color marks potential energies where a newly placed molecule would get charged while it would remain neutral in blue colored areas. In (c) the three molecules placed in the unit cell experience charging. The resulting surface potential decreases in the entire unit cell so that additional molecules, independent on where they adsorb, will remain neutral. Such a mix of charged and uncharged molecules limits the dipole compensation to a rational number. A more continuous compensation might be achieved by additional variation of the molecular monolayer density as well as the adsorption height of the molecules. In our recent work we could indeed find experimental evidence for the co-existence of charged and uncharged species with a combination of ARPES and STM measurements (see chapter 4.2.3).

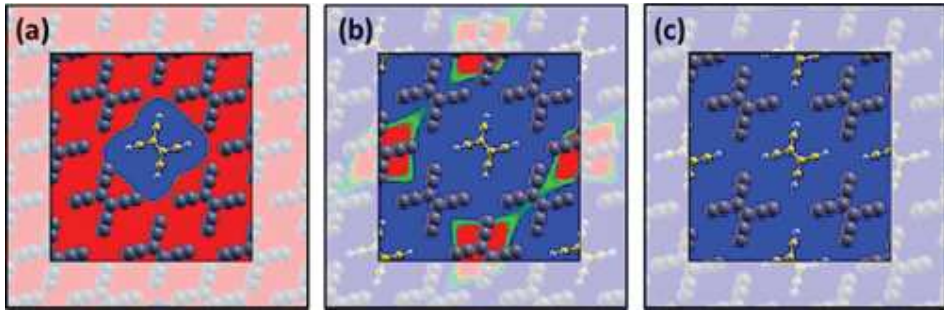


Figure 4.16: In their theoretical studies on FCT vs. ICT of organic adsorbates on dielectric/metal systems *Hofmann et al.* demonstrated density-limited charging of individual molecules. (Figure taken from [90])

In summary, this chapter aimed to describe the major known parameters that govern the energy level alignment which determines, whether or not, charge transfer can occur. However, some open questions still remain, regarding, for example, the energetic positions of the newly charged species and how this is connected to the potential induced by polaronic distortions. Another open question concerns the transition from a singly into a doubly occupied molecular orbital through charging within the Fermi level pinning regime.

4.2.3 Related Publications

The nature of the charge transfer through dielectric interlayers is subject of our publication: *"Charge Transfer and Orbital Level Alignment at Inorganic/Organic Interfaces: The Role of Dielectric Interlayers"*, in chapter 6.4. Within this study we employed MgO(001)/Ag(001) as a dielectric/metal model system and investigated the adsorption of pentacene (5A) with a combined STM/UPS approach. The experimental findings are further supported by DFT simulations.

In STM the molecule is imaged as an elongated feature consisting of 7 lobes both for negative and positive bias voltages. This appearance is in good agreement with the LUMO of the isolated (neutral) pentacene. Additional ST spectra reveal one empty and one filled state which can be associated with the aforementioned LUMO appearances (see figure 4.17). The observation of the LUMO as a filled, secluded state is a strong indication for integer charge transfer from the metal, through the dielectric, into the pentacene molecule. To avoid misinterpretation of the STS data (caused, e.g., by possible Coulomb-blockade effects) complementary UPS measurements were performed.

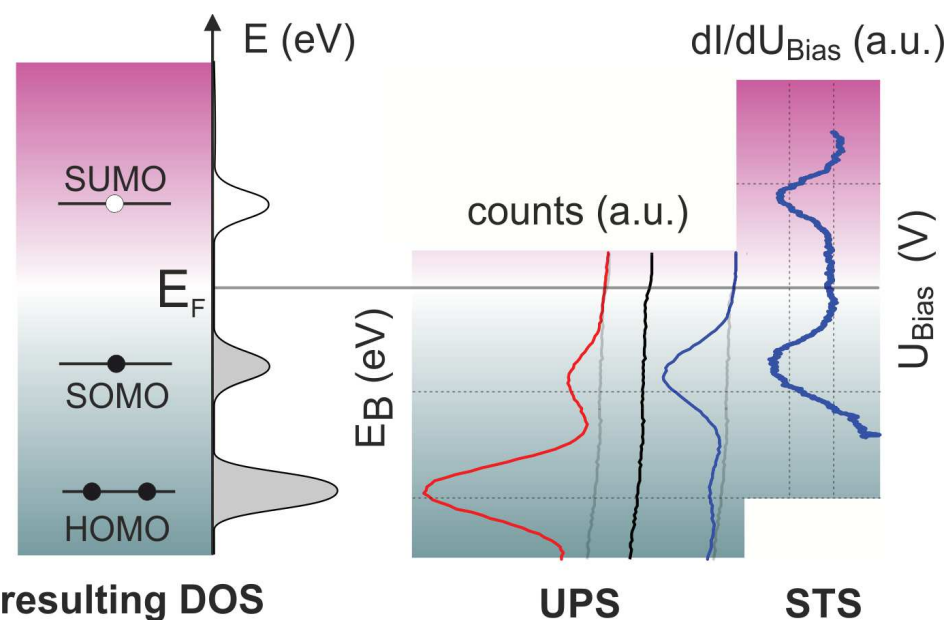


Figure 4.17: Correlation of spectroscopic UPS and STS data and resulting energy scheme for the system of 5A on MgO/Ag(001).

It was recently demonstrated that within the plane wave approximation the angle-resolved photo-emission distribution of molecular orbitals is related to the Fourier transform of the real space orbital [14]. We are therefore able to identify the emission feature associated with specific orbitals (e.g. the pentacene LUMO) in k-space in ARPES experiments. We find a perfect agreement of the energetic position of the LUMO in STM and UPS (see fig. 4.17). Moreover, by comparing the experimentally obtained emission features with the computed data, we obtain a quantitative estimate for the involved charge transfer of one electron per pentacene molecule on 2 ML of MgO on Ag(001). We hence identify the electronic state below E_F as the Singly Occupied Molecular Or-

bital (SOMO), formerly LUMO, and the state above E_F as the corresponding Singly Unoccupied Molecular Orbital (SOMO). With the identification of the molecular orbitals of pentacene in real space (STM/STS) and k-space (ARPES) we are also able to construct the level diagram around the Fermi edge, as schematically depicted in figure 4.17.

For the deposition of pentacene on pristine Ag(001), an electronic state associated with the LUMO is observed directly at E_F . The quantification of transferred charge yielded a value of 0.7 eV per molecule. Thus, this system shows fractional charge transfer because the molecular and substrate states hybridize. This is in contrast to pentacene on the MgO interlayer, where hybridization is inhibited by the dielectric and integer charge transfer is observed. Additionally, an attempt to quantify the individual contributions partaking in the energy alignment process is made both for the organic/metal as well as the organic/dielectric/metal system as shown in figure 4.18.

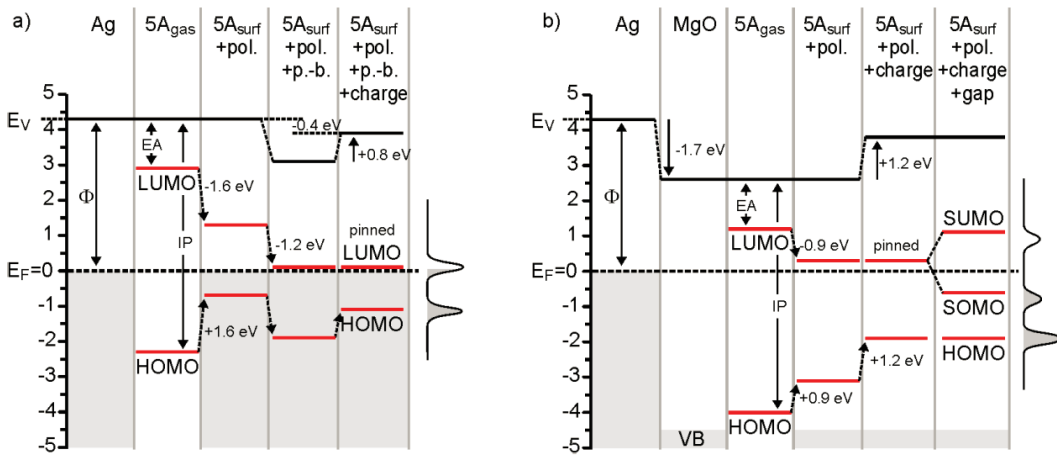


Figure 4.18: Partitioning of the energy level alignment for a) 5A/Ag(001) and b) 5A/MgO(001)/Ag(001). The orbital energy levels (LUMO, HOMO) of isolated pentacene (5A_{gas}) are aligned to the vacuum levels (EV) of Ag(001) and MgO(001)/Ag(001), and the contributions of polarization (pol.), push-back (p.-b.), charging (charge) and gap opening (gap, in b only) to the level alignment are added. The curves on the right side of each Figure represent the measured spectra.

So far this system represents a single data point within the ICT model, situated in the Fermi level pinning regime of the LUMO (see figure 4.15). This point is defined by the initial MgO(001)/Ag(001) substrate workfunction of 2.6 eV and the final work function of 3.8 eV after the deposition of 5A. To investigate the ICT model further, it is interesting to deliberately change the initial workfunction of the system. A recent experimental and theoretical study by *Jaouen et al.* [18] predicts a strong dependency of the initial MgO(001)/Ag(001) workfunction on interface defects. DFT simulations by *D. Lüftner and P. Puschnig* even predict a workfunction range of 2.3 eV to 3.7 eV, achieved via a variation of the amount of oxygen at the MgO(001)/Ag(001) interface. As such, the ICT model can be probed for a wide range of initial workfunctions for a single, well understood adsorbate/substrate system.

This is subject of our paper in preparation *Controlling the charge transfer across dielectric interlayers*. In this combined UPS/STM study, we probe the areal charge distribution of a monolayer of pentacene in dependence of the initial MgO(001)/Ag(001) substrate workfunction. All UPS measurements were conducted by *P. Hurdax*. Figure 4.19 depicts ARPES spectra of 5A monolayer preparations on MgO(001)/Ag(001) substrates of different initial workfunctions (y-axis offset). The chosen measurement geometry is set on the maximum photoemission intensity of the 5A LUMO. The corresponding emission features relate to the SOMO of charged 5A molecules and are marked with a purple line. It is immediately apparent that the peak intensity of the SOMO decreases with increasing initial substrate workfunction. Starting with a low initial-workfunction, we find a high SOMO intensity, indicating that almost all molecules are singly charged. The charge transfer decreases with the initial workfunction until no more SOMO intensity is detectable at $\phi_{Initial} = 3.65$ eV, indicating the absence of charged 5A molecules. Note, that this coincides with the *pinning workfunction* of 3.7 eV, which is similar for all preparations after the deposition of a monolayer of 5A. We can now relate the experimental findings to the ICT model depicted in figure 4.15. We find the final workfunction to be constant for initial workfunctions which are similar or lower than the pinning workfunction. This regime is thus the Fermi-level pinning regime. Furthermore, the decreasing SOMO intensity nicely follows the decrease in the charge transfer dipole (according to the capacitor model 4.3), which constitutes the theoretical explanation of the ICT model. Interestingly, the SOMO binding energy is constant, independent of the concentration of charged species. This indicates that the local potential is not affected by whether the neighboring molecules are charged or uncharged. This begs the question whether we can actually detect and image the neutral molecular species. To this end a series of STM experiments was conducted.

In figure 4.20 filled and empty state images are presented for a monolayer coverage of pentacene on MgO(001)/Ag(001). As the measurement of the workfunction with STM was not reliable the system was prepared according to recipes used in the UPS system. The initial preparation of 2 ML of MgO on Ag(001), according to chapter 3.3, represents a low initial-workfunction preparation. The corresponding STM images after deposition of 1 ML of 5A are given in the top panel of figure 4.20. Subsequently, the sample was annealed until the molecules desorbed and further heated in oxygen to increase the

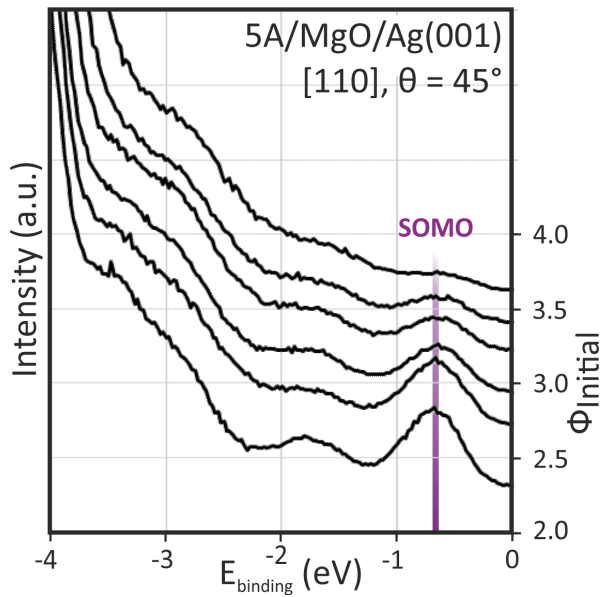


Figure 4.19: Photo-emission intensities of monolayers of 5A on MgO(001)/Ag(001) films of different initial workfunctions (right scale). Special thanks to Philipp Hurdax for the provided data.

local potential. The right side of the plot shows the initial workfunction $\Phi_{Initial}$ on a logarithmic scale from 2.0 to 4.0 eV. The left side of the plot shows the binding energy $E_{binding}$ in eV on a linear scale from -4 to 0. The title of the plot is "5A/MgO/Ag(001)" and the subtitle is "[110], $\theta = 45^\circ$ ". The y-axis is labeled "Intensity (a.u.)" and the x-axis is labeled " $E_{binding}$ (eV)". A purple vertical line is drawn at approximately $\Phi_{Initial} = 3.65$ eV, labeled "SOMO".

substrate workfunction. The corresponding STM images after deposition of a ML of 5A shown in the lower panel of figure 4.20 therefore represent a high initial-workfunction preparation. For the low workfunction preparation we observe 5A molecules exhibiting the characteristic 7-lobed LUMO appearance (see chapter 6.4) both in empty and in filled state images. Thus, we conclude that all molecules are charged with one electron, giving rise to a singly filled SOMO below, and the SUMO above E_F . For the high initial-workfunction preparation, we observe a similar 5A LUMO appearance in the empty state image, although with a slightly lower molecular density. However, two species can be differentiated in the filled state image. Firstly, we observe a species with the 7-lobed LUMO. This minority species is thus singly charged, similar to the molecules on the low-workfunction preparation. Secondly, we observe the majority species exhibiting 5 lobes and a central node. This appearance resembles the HOMO of the neutral molecule (see inset in figure 4.20). Therefore, it can be concluded that this species represents neutral molecules adsorbed on the substrate.

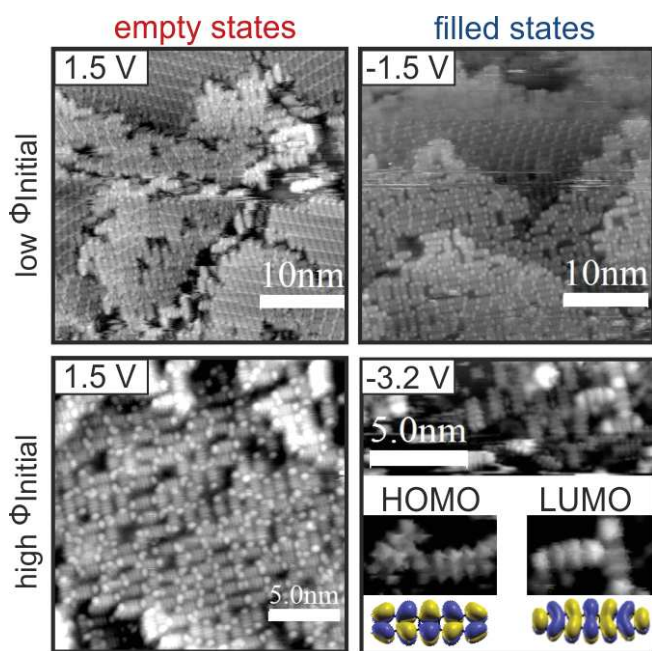


Figure 4.20: STM images of a ML of 5A on a low initial-workfunction (top panel) and a high initial-workfunction (bottom panel) MgO(001)/Ag(001) substrate.

we present a model system for the active control of charge transfer to adsorbate molecules. This enables the deliberate investigation of charge-state induced chemical and physical phenomena.

Within our follow-up project *Charge-state induced metalation reaction of porphyrins* we study the metalation of free-base tetraphenylporphyrin (2H-TPP) on our MgO(001)/Ag(001) model system. Although previous studies of 2H-TPP on MgO nanocubes [20] and on ultra-thin MgO(001)/Ag(001) films [19] could demonstrate the

In summary, we find that the mechanism of Fermi level pinning in this system is indeed constituted by the formation and presence of singly charged and uncharged molecules. The potential difference between initial and pinning workfunction is compensated by the charge transfer dipole and thus determines the number of charged molecular species. Further fine-tuning of the compensation dipole might be achieved by a variation of the molecular density of the monolayer. In conclusion, we could for the first time validate the ICT model for a single, controlled system on an atomic/molecular level. This paves the way for a more fundamental understanding of organic/inorganic energy alignment mechanisms. Furthermore,

self-metallation to Mg-TPP the underlying processes are still unclear. Both studies concluded a correlation of the metalation process with the presence of defects (step-edges) in the MgO surface. Following this interpretation the deprotonation and subsequent incorporation of Mg^{2+} is facilitated only at defect-sites because of the lower Mg^{2+} vacancy formation energy and the higher stability of the OH groups [106]. The premise of this project is the assumption that the metallation process can also be achieved by charge transfer.

For this purpose low and high workfunction substrates were prepared and subsequently covered with a monolayer of 2H-TPP. Figure 4.21 shows the monolayer phase of 2H-TPP on a standard, low initial-workfunction preparation of $MgO(001)/Ag(001)$. The STM image reveals a well-ordered monolayer with a square unit cell. Note that the bright protrusions correspond to the phenyl-rings of TPP, which is apparent from the shape of the vacancy in the STM image. The corresponding model depicts the unit cell and the molecular alignment with respect to the $MgO(001)$ substrate. The perfect agreement of the simulated pattern, according to the extracted unit cell, with the sharp LEED spots demonstrates that the model is representative for the macroscopic sample surface. Hence, we present one of the first reports on a well-ordered porphyrin monolayer evolving on an oxide surface.

Starting from the monolayer structure and the molecular alignment we now turn to spectroscopic investigations of this model system. All UPS and XPS measurements were conducted by *L. Egger*. Figure 4.22 shows results of UPS and XPS measurements of a 2H-TPP monolayer deposited on a high (turquoise) and low (green) initial-workfunction $MgO(001)/Ag(001)$ substrate, respectively. The angle-resolved UPS spectra were obtained for an experimental geometry that reveals emission features of both the 2H-TPP HOMO and LUMO. Note that only the low initial-workfunction preparation exhibits a peak associated with the LUMO. We, therefore, obtain charged molecules (Fermi level pinning) for the low, and neutral molecules (vacuum level alignment) for the high initial-workfunction preparation, in accordance with the aforementioned energy level alignment concept. Finally, the samples were analyzed with XPS to probe whether metallation has occurred. The free-base porphyrin has four nitrogen atoms in the center of which two are bound to hydrogen atoms. The different bonding results in a chemical shift and two distinguishable nitrogen 1s peaks. This is observed for 2H-TPP on the

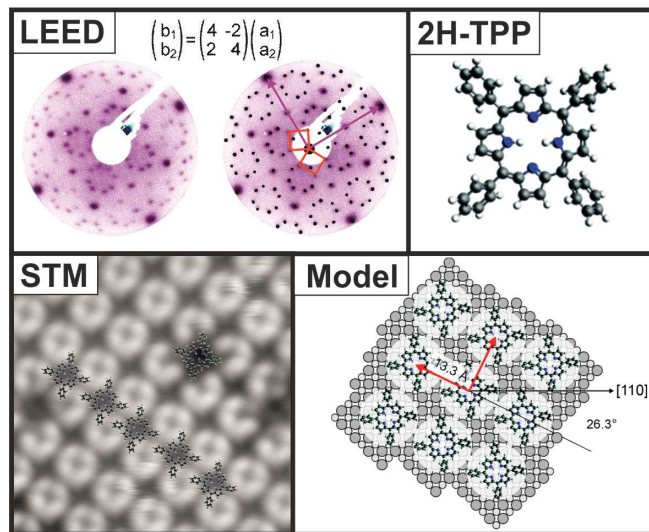


Figure 4.21: Monolayer of 2H-TPP adsorbed on 3 ML of $MgO(001)/Ag(001)$. The commensurable monolayer structure exhibits a square unit cell, long-range order and a single molecular alignment.

high initial-workfunction substrate. Hence, the molecules remain intact. However, only one N 1s peak is obtained for the 2H-TPP molecules on the low initial-workfunction substrate. A deprotonation of the molecules has occurred, followed by the incorporation of a substrate Mg^{2+} and the formation of a coordinated N-Mg bonds with similar N 1s binding energies [19]. Thus, we find that the molecules are metalated and that the metalation of the porphyrins can be controlled by the initial-workfunction of the substrate. Quite clearly, the presence of an excess charge facilitates the metalation process.

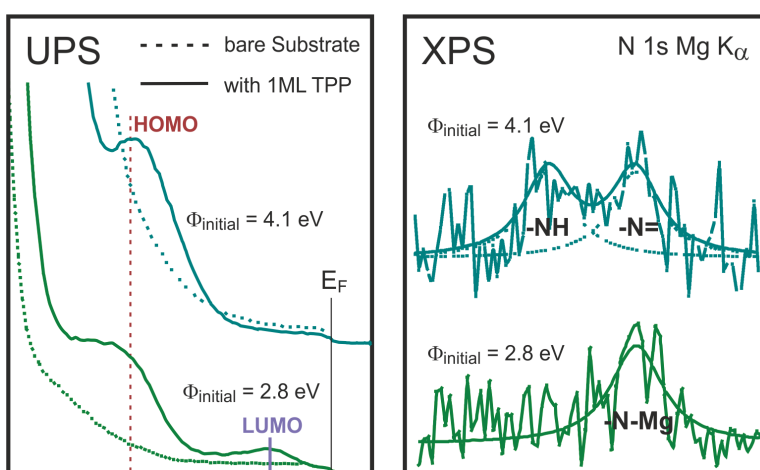


Figure 4.22: UPS and XPS spectra for a monolayer of 2H-TPP adsorbed on a high (turquoise) and a low (green) workfunction preparation of $MgO(001)/Ag(001)$. Special thanks to Larissa Egger for the provided data.

Our result resolves the apparent discrepancy of previously published data for 2H-TPP on MgO thin films and shows that metalation can occur also on regular terrace sites if the molecules are charged. A possible explanation for the enhanced metalation probability on regular terraces includes a shorter adsorption height of the macrocycle and a larger electric field at the adsorption site due to the presence of the excess charge.

4.2.4 Organic Film Growth

So far we have discussed the adsorption of organic molecules on metal and dielectric/metal surfaces from an energetic point of view. It is this alignment that determines the functionality and performance of any organic electronic application. However, also the geometric alignment of the molecule with the substrate as well as the structural conformation of the molecule have an impact on the energetic alignment. For the experimental characterization of such organic/metal systems, typically a saturated molecular monolayer is investigated. Nevertheless, actual organic electronic devices are composed of thin films of several molecular layers. As the molecular film evolves, additional intramolecular forces may influence the adsorption geometry [107, 108] of the contact layer and consequently the energetic alignment with the substrate. This in turn will also have an impact on the performance of real organic electronic devices.

Within our work *Growth study of para-sexiphenyl on Ag(001): From single molecule to crystalline film* in chapter 6.5, we present a detailed study of organic film formation starting from the first molecule up to the development of a bulk crystallite. The aim of the study is to connect the bulk structure of an epitaxially grown organic crystal to the actual organic/substrate interface. As it is extremely difficult to experimen-

tally obtain structural information on the organic/metal interface of a thick film one typically assumes the projected bulk-unit cell to constitute the interface layer or separately investigates the saturated monolayer. Para-Sexiphenyl (6P) was chosen as a representative for flexible, rod-like molecules with semiconducting properties [109] and application in light emitting diodes [50]. Ag(001) serves as a high-symmetry substrate of comparably weak interaction and easy UHV-handling.

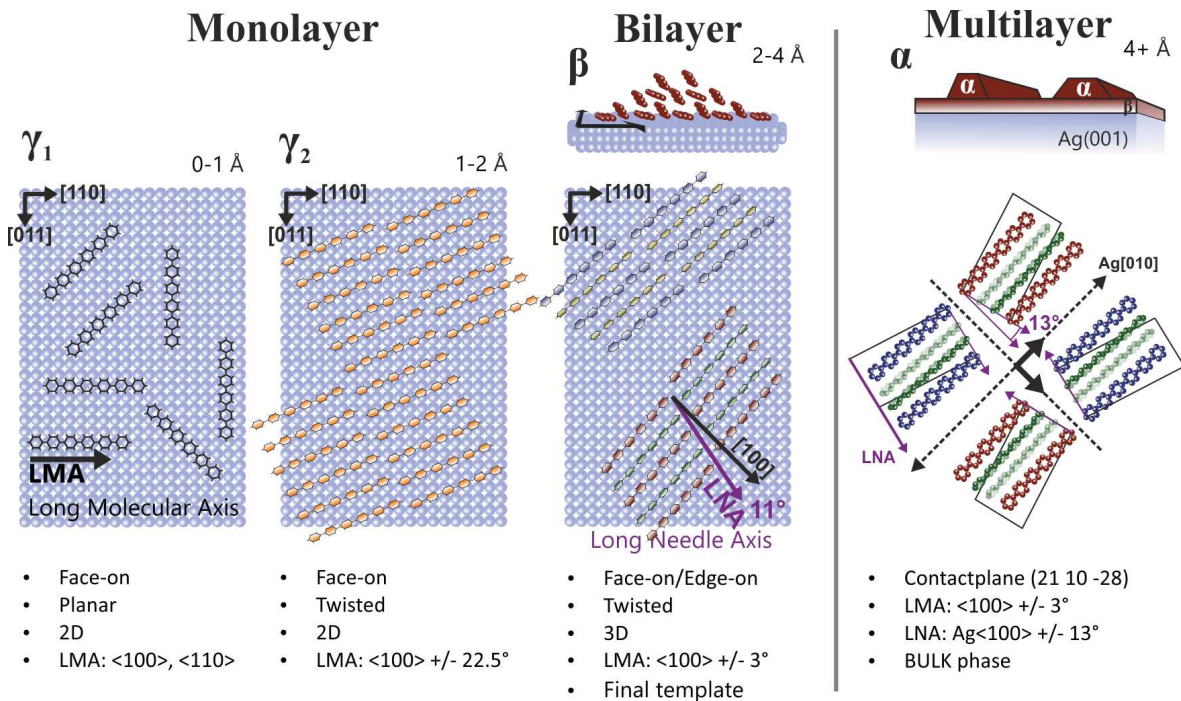


Figure 4.23: Schematic overview of the evolution of the 6P film growth on Ag(001). On the left part of the graphic the bilayer constitutes the wetting layer that acts as a template for the growth of macroscopic bulk crystallites.

We track the complex development of the wetting layer, from single molecule to the bilayer, with in-situ surface sensitive local (STM) and quantitative (LEED) methods and provide a continuous observation of the wetting-layer to bulk transition with Thermally Programmed Desorption (TPD) measurements. The resulting bulk structure is ex-situ morphologically (AFM) and structurally (XRD) characterized and related to the results obtained for the wetting layer. Thus we present a detailed study of the development of molecular crystallites for the model system of 6P on Ag(001).

Figure 4.23 depicts a schematic summary of the evolution of the organic crystal structure. The complex development of the wetting layer is found to consist of 3 distinctively different, well defined structures indicated as γ_1 - , γ_2 - and β - phase. Upon adsorption the molecules initially adopt a planar conformation with a specific substrate alignment. Although a neutral charge-state is adapted a repulsive behavior results in widely-spaced molecules which constitute this dilute monolayer γ_1 . When increasing the coverage the molecules are forced to overcome their initial repulsive behavior and respond with a conformational change. Because of attractive π - π interactions of phenyl-rings that face

each other [110] an alternating out-of-plane twist of the phenyl-ring is observed and calculated (DFT) to enclose 10 deg with the surface plane. Additionally, a 22.5 deg realignment of the LMA with respect to the substrate is observed and ascribed to the change in molecular conformation. This twisted and realigned phase γ_2 exhibits long-range order, is commensurable and 4-fold symmetric. A further increase in coverage induces the incorporation of edge-on molecules up to a critical ratio of 2:1 flat to edge-on molecules which constitutes the transition phase γ_2^* (not shown in figure 4.23). Finally, a second realignment of the Long Molecular Axis (LMA) with respect to the substrate occurs with the adsorption of second layer molecules. Interestingly, the transition appears promptly for entire domains upon exceeding the critical coverage of the γ_2^* -phase. At a saturation coverage this β -phase forms a 3D, pyramid-like ridge structure (see estimated side-view in 4.23), already exhibiting bulk-like characteristics. As a corresponding unit-cell consists of several molecules of undefined twist/tilt no DFT calculations could be performed. However, we suggest a similar rearrangement mechanism as for the γ_1 - γ_2 transition, facilitated by the increased intermolecular interactions of this 3D wetting layer.

Finally, structure and alignment of the multilayer (nominally 30 nm) were deduced via X-Ray Diffraction (XRD) measurements. Corresponding pole figures attest perfect crystalline order (despite a perplexing morphology) with a contact plane of (21 10 - 28), closely related to the frequently observed (2 1 -3) contact plane [111]. Comparing the deduced projected bulk unit-cell with the saturated wetting layer, we find perfect agreement of the molecular alignment (LMA) with respect to the substrate as well as a reasonable concordance of the Long Needle Axis (LNA). As such we conclude that the saturated bilayer indeed acts as the template for the evolution of the organic crystal.

For the weakly interacting system of the flexible oligo-phenyl 6P on Ag(001) we observed two molecular realignments as well as conformational changes to precede the epitaxial growth of the final organic crystallite. The first layer is hence not immutable to change and great care has to be taken when investigating the actual organic/substrate interface beneath an epitaxially grown crystal. This work also has an impact on the problem of designing and predicting the anisotropic growth of organic material, furthering the understanding of the delicate interplay between intermolecular and substrate-molecule interactions.

4.3 Appendix

Charge Stabilization

Charge stabilization is a phenomena observed for charged molecules on top of dielectric, ionic lattice substrates. Here, DFT calculations for the model system of pentacene on ultra-thin MgO on Ag(001) are presented for varying MgO film thicknesses³. DFT calculations were performed using the same unit cell and adsorption geometry as for the simulations of chapter 6.4. A slab of 5 atomic Ag layers was utilized to model the metallic substrate. All calculations were performed with the *Vienna Ab Initio Simulation Package (VASP)* using a PBE functional. Within this calculations the atomic positions were set as an optimization parameter and were thus allowed to structurally relax. In tab. 4.1 the workfunctions for various thicknesses of MgO are listed for the relaxed MgO/Ag(001) system, as obtained by DFT.

Table 4.1: DFT calculations for the relaxed MgO(001)/Ag(001) system with varying MgO layer thickness.

ML MgO...	considered MgO thickness in atomic layers
$\phi_{Ag(001)}^{bot} \dots$	Ag workfunction taken at the bottom of the MgO(001)/Ag(001) slab
$\phi_{MgO/Ag} \dots$	workfunction of the combined MgO(001)/Ag(001) slab (top)
$\Delta\phi \dots$	workfunction difference
$\Delta\phi_{PushBack} \dots$	contribution of Push-Back effect
$\Delta\phi_{MgO} \dots$	contribution of rumpling of the MgO (interface) layers
$\Delta\phi_{CTest} \dots$	$\phi_{5A/MgO/Ag} - \phi_{MgO/Ag}$

in (eV)	$\phi_{Ag(001)}^{bot}$	$\phi_{MgO/Ag(001)}$	$\Delta\phi$	$\Delta\phi_{PushBack}$	$\Delta\phi_{MgO}$	$\Delta\phi_{CTest}$
2 ML MgO	4.27	3.04	-1.23	-1.66	+0.43	+0.74
3 ML MgO	4.29	3.04	-1.25	-1.74	+0.52	
4 ML MgO	4.28	3.03	-1.25	-1.73	+0.52	+0.70
8 ML MgO	4.29	2.83	-1.46			+0.91

The values show good agreement with experimental data (see chapter 6.4) and little dependence on the dielectric film thickness. The average workfunction of Ag (4.3 eV) reduces by 1.3 eV to 3.0 eV for the combined MgO/Ag system. This reduction can be attributed to a large push-back effect reducing the workfunction by -1.7 eV and a counteracting dipole of 0.4 eV induced by a rumpling of the MgO layer, mostly localized at the Ag/MgO interface. As the final workfunction of MgO/Ag shows good agreement with experimental data it is assumed to represent the real system. As a first assumption the dipole induced by Charge Transfer (CT) to the molecule can now be estimated by subtracting the workfunction of the relaxed 5A/MgO/Ag system (see tab. 4.2) from the relaxed MgO/Ag system. The resulting dipole is then given by $\Delta\phi_{CTest}$ and amounts to 0.7 eV. Such an approach is equivalent to the actual experimental procedure of estimating the CT-induced dipole the difference of the measured MgO/Ag and 5A/MgO/Ag workfunctions.

³Many thanks to Daniel Lüftner for providing the data presented here.

Table 4.2: DFT calculations for the relaxed 5A/MgO(001)/Ag(001) with varying MgO layer thickness.

ML MgO...	considered MgO thickness in atomic layers
$\phi_{Ag(001)}^{bot} \dots$	Ag workfunction taken at the bottom of the MgO(001)/Ag(001) slab
$\phi_{MgO/Ag}^{\dagger} \dots$	calculated workfunction for the MgO/Ag(001) slab upon removal of 5A
$\Delta\phi \dots$	workfunction difference
$\Delta\phi_{PushBack} \dots$	contribution of PushBack effect
$\Delta\phi_{MgO}^{\dagger} \dots$	contribution of rumpling of (topmost) MgO layers
$\phi_{5A/MgO/Ag} \dots$	final workfunction for the 5A/MgO/Ag(001) system
$\Delta\phi_{CT} \dots$	$\phi_{5A/MgO/Ag} - \phi_{MgO/Ag}^{\dagger}$ (with charge stabilization)

in (eV)	$\phi_{Ag(001)}^{bot}$	$\phi_{MgO/Ag}^{\dagger}$	$\Delta\phi$	$\Delta\phi_{PushBack}$	$\Delta\phi_{MgO}^{\dagger}$	$\phi_{5A/MgO/Ag}$	$\Delta\phi_{CT}$
2 ML MgO	4.28	1.82	-2.46	-1.61	-0.84	3.78	+1.96
4 ML MgO	4.24	1.91	-2.33	-1.63	-0.76	3.73	+1.82
8 ML MgO	4.29	1.82	-2.74			3.74	+1.92

In tab. 4.2 the theoretically calculated values are listed for the relaxed 5A/MgO/Ag system, again obtaining a similar workfunction of 4.3 eV for Ag. As already demonstrated in chapter 6.4, DFT successfully reproduces integer charged molecules on top of a MgO(001)/Ag(001) substrate. It should be mentioned that fractional charging in DFT is realized via back-donation of lower lying orbitals, as discussed in chapter 4.2.1. As such it is only fully applicable for a net charge density of exactly integer charge per molecular cell⁴. However, an attenuated charge stabilization effect is also expected for lower charge densities. In order to estimate the interaction of charged pentacene on MgO/Ag, the atomic positions are frozen after the structural relaxation and the molecule is then removed from the system. It therefore represents a hypothetical MgO/Ag[†] structure with a significantly reduced workfunction of $\phi_{MgO/Ag}^{\dagger} = 1.8$ eV. Note that by definition this workfunction satisfies the constraints of $\phi_{initial}$, utilized in the Integer Charge Transfer model in chapter 4.2.1. Interestingly, the interaction with the charged molecule induces a rumpling, mostly localized in the topmost MgO layer, as a result of a slight push-back of the oxygen anions due to the presence of the charged pentacene. This structural rearrangement results in a dipole change of $\Delta\phi_{MgO}^{\dagger} = -0.8$ eV, opposite in sign compared to the bare MgO/Ag system of $\Delta\phi_{MgO} = +0.4$ eV. It is therefore the major contribution in the workfunction difference between $\phi_{MgO/Ag}^{\dagger}$ and $\phi_{MgO/Ag}$. Note that the calculated push-back contribution is almost similar for both systems. Finally, we can estimate the CT induced dipole change with respect to the relaxed MgO/Ag[†], or $\phi_{initial}$, and obtain a significantly increased value of 1.9 eV instead of 0.7 eV. In summary, we observe a structural substrate relaxation upon adsorption of a charged molecule that decreases the workfunction and as such increases the driving force for charge transfer. Therefore this mechanism is of a self-stabilizing nature. In principal this effect is expected to occur for all extended objects that charge upon adsorption on thin ionic-lattice/metal systems. The magnitude of this effect should scale with the areal charge density.

⁴Within the presented calculations the net charge transfer decreases with film thickness while still retaining 1e⁻ per molecule in the LUMO

5 Conclusion

This thesis provides a fundamental investigation of charge transfer on an atomic-/molecular level. The mechanism of charge transfer is discussed within the more general framework of energy alignment of substrate/adsorbate systems. Finally, the impact of charge transfer on fundamental physical and chemical processes is demonstrated.

For the system of pentacene (5A) on MgO(001)/Ag(001) charge transfer from the metal substrate to the adsorbed molecule is demonstrated by imaging of the filled molecular orbitals both in real and in reciprocal-space. Integer charge transfer of 1 electron per molecule results in the singular occupation of the previously empty LUMO and its splitting into SOMO and SUMO around the Fermi edge. On pristine Ag(001) a charge transfer of 0.7 electrons per molecule is observed. Furthermore, approximate numerical values for workfunction changes could be assigned to specific energy alignment contributions such as the molecular/dielectric push-back, the polarizability and the charge transfer dipole.

The concept of energy alignment according to the *integer charge transfer model* is demonstrated for pentacene by a variation of the initial MgO(001)/Ag(001) workfunction. Moreover, it is shown that the system can be prepared in a controlled manner to exhibit either only neutral or only singly charged molecules. Thus, a model system for further investigations on the impact of charge transfer on adsorbate structures could be established.¹

This is subsequently demonstrated for two exemplary systems. Firstly, the catalytic model system of Au nano-particles on MgO(001)/Ag(001) is considered. The formation of oxalate species from CO₂ is shown to be controlled by the morphology of Au islands which itself is dependent on thermal treatment. Catalytic activity is observed only for 2-dimensional Au islands, which are stabilized through the excess charges which are localized at the rim of the islands. An abrupt decrease in the catalytic activity is observed with annealing temperatures of 500 K and above. This is associated with the distinct morphological transition to 3-dimensional nano-crystallites. Furthermore, an analysis of the growth conditions resulted in an optimized perimeter ratio of the Au islands for deposition at 77 K and subsequent annealing to 260 K. This preparation is proposed to exhibit optimized catalytic performance.

Secondly, the metalation reaction of 2H-TPP to Mg-TPP on MgO(001)/Ag(001) surfaces is demonstrated to be directly related to the occurrence of charge transfer. This is achieved by controlling the charge state of the molecules via the initial substrate workfunction. A perfect correlation between charge transfer and metalated molecules is observed.²

Within a related project, ordered monolayer structures of water on MgO(001)/Ag(001)

¹Publication by Philipp Hurdax in preparation.

²Project in progress. UPS and XPS experiments by Larissa Egger.

5 Conclusion

were microscopically imaged for the first time. In agreement with previous reports [2], a long-range ordered c(4x2) phase as well as patches of short-range ordered p(3x2) phase could be imaged. Furthermore, the monolayer growth is concluded to be independent of the MgO film thickness (2 and 12 ML). Consequently, an independence of the monolayer growth on charge transfer is also probable.

Finally, a detailed growth study of Para-Sexiphenyl (6P) on Ag(001) is presented as an example for systems of flexible molecules on weakly interacting substrates. Two molecular reorientations occur with increasing coverage. They are ascribed to intra-molecular twisting of the phenyl rings, caused by an increasing inter-molecular interaction in 2 dimensions, and subsequently in 3 dimensions, which constitutes the final wetting layer. This is identified as the template for the evolution of a well aligned 6P bulk phase exhibiting a (2 1 -3)-related contact plane.

6 Published work

In this section selected publications are printed to which i could contribute in the course of my PhD thesis. As this thesis is designed as a cumulative work the following papers with my respective contributions represent the official requirement for the completion of my academic degree according to the Curriculum of the B 796 600 876 studies. (Curriculum für das Doktoratsstudium der Naturwissenschaften, 2011)

- Growth study of para-sexiphenyl on Ag(001): From single molecule to crystalline film.
Chapter: [6.5](#). I contributed more than 60 %.
- Charge Transfer and Orbital Level Alignment at Inorganic/Organic Interfaces: The Role of Dielectric Interlayers
Chapter: [6.4](#). I contributed more than 20 %.
- Scanning Tunneling Microscopy of the Ordered Water Monolayer on MgO(001)/Ag(001) Ultrathin Films
Chapter: [6.3](#). I contributed more than 20 %.

Because of copyright issues the presented papers are given in the formatting of the first submission. A full list of all scientific publications and contributions is given in chapter [7](#).

Supports and modified nano-particles for designing model catalysts

C. P. O'Brien,^a K.-H. Dostert,^b M. Hollerer,^c C. Stiehler,^b F. Calaza,^b S. Schauermann,^{bd} S. Shaikhutdinov,^b M. Sterrer^c and H.-J. Freund^{*b}

Received 9th October 2015, Accepted 21st October 2015

DOI: 10.1039/c5fd00143a

In order to design catalytic materials, we need to understand the essential causes for material properties resulting from its composite nature. In this paper we discuss two, at first sight, diverse aspects: (a) the effect of the oxide–metal interface on metal nanoparticle properties and (b) the consequences of metal particle modification after activation on the selectivity of hydrogenation reactions. However, these two aspects are intimately linked. The metal nanoparticle's electronic structure changes at the interface as a catalyst is brought to different reaction temperatures due to morphological modifications in the metal and, as we will discuss, these changes in the chemistry lead to changes in the reaction path. As the morphology of the particle varies, facets of different orientations and sizes are exposed, which may lead to a change in the surface chemistry as well. We use two specific reactions to address these issues in some detail. To the best of our knowledge, the present paper reports the first observations of this kind for well-defined model systems. The changes in the electronic structure of Au nanoparticles due to their size and interaction with a supporting oxide are revealed as a function of temperature using CO₂ activation as a probe. The presence of spectator species (oxopropyl), formed during an activation step of acrolein hydrogenation, strongly controls the selectivity of the reaction towards hydrogenation of the unsaturated C=O bond vs. the C=C bond on Pd(111) when compared with oxide-supported Pd nanoparticles.

Introduction

The properties of dispersed metal catalysts are dominated by two factors: the size, morphology, and chemical modification of the metal nanoparticles after having been activated, and the interaction of these nanoparticles, or small metal clusters, with the support, *i.e.* the metal–support interface. These two factors are strongly

^aUS Army Research Laboratory, USA

^bFritz Haber Institute of the Max Planck Society, Department of Chemical Physics, Faradayweg 4-6, 14195 Berlin, Germany. E-mail: freund@fhi-berlin.mpg.de

^cInstitute of Physics, University of Graz, Austria

^dInstitut für Physikalische Chemie, Christian-Albrechts-Universität zu Kiel, Germany

interlinked and need to be addressed in model studies if we want to understand their influence at the atomic level and find design principles for new catalytic materials. This is described in this paper and exemplified by investigating two, seemingly different, model systems.

There is no doubt that the metal–support interface is one of the determining factors in catalysis, as documented by many examples in the literature,¹ yet, it is not considered in most model studies. The electronic structure of the metal–support interface changes as the morphology of the metal particle may vary as a function of temperature, for example, due to sintering. This may lead to the formation of particles with a variety of facets, which, in turn, changes the surface chemistry.^{2–5}

Plausible explanations have been presented over the years for the “structure sensitivity”, defined early on by Michel Boudart in connection with the function of the catalyst. It mainly refers to the size of a metal nanoparticle and relates to the various possible terminations with different facets.^{4–6} This concept was taken as a basis for the surface science approach based on metal single crystal surfaces with respect to experiments,^{7,8} and theoretical slab calculations,⁹ with varying terminations, the result of which could be used by superposition to explain the observed catalytic behavior. While in this approach the support might be taken as the cause of the particular appearance of the nanoparticle, the support’s chemical nature and specific interaction with the nanoparticle are not taken into account in such approaches.¹⁰ The appearance of particles of different sizes and shapes may cause a modification of the catalyst during the activation process. A series of attempts has been made in the literature to consider material modification by the overgrowth of oxide films¹¹ or the incorporation of carbon in the surface² as well as subsurface areas, which only then is turned into an effective hydrogenation catalyst.¹² Robert Schlögl¹³ has recently presented a comprehensive review on the dynamic catalyst.

In the present paper we would like to address both the influence of the metal–oxide interface, as well as the influence of spectator species on selective hydrogenation, in an attempt to exemplify design principles for new catalytic materials. The present work is based on and is a substantial extension of previous work on CO₂ activation on supported Au nanoparticles and on the competitive, selective hydrogenation of C=C *vs.* C=O double bonds on oxide-supported Pd nanoparticles as a function of particle size. The paper is organized as follows: after a short description of the experiments, we present and discuss the new results in comparison to the results obtained so far. We conclude with a summary and an outlook to further experiments.

Experimental conditions

The experiments on supported Au nanoparticles on ultrathin MgO(100) films were carried out using different ultrahigh-vacuum (UHV) set-ups, all of them equipped with basic sample cleaning and preparation (sputtering, heating, evaporation, gas dosing) as well as characterization (low-energy electron diffraction, LEED) facilities. One of them had, in addition, a polarization modulation infrared reflection absorption spectroscopy (IRAS) and X-ray photoelectron spectroscopy (XPS) set-up attached. Infrared spectra were acquired with a Bruker IFS66v FTIR spectrometer using a liquid nitrogen cooled MCT detector. The XPS

spectrometer was a SPECS type hemispherical analyzer (Phoibos 150) with a dual anode (Mg/Al) X-ray source. Scanning tunneling microscopy (STM) experiments were carried out both at the Fritz Haber Institute using a home-built low-temperature STM operated at liquid helium temperature as well as in the Physics Department of the University of Graz using a CreaTec low-temperature STM operated at liquid nitrogen temperature. The surface of the Ag(100) crystal used as a support for the MgO(100) films was cleaned by repeated sputter (Ar^+ , 800 V, 5 μA)–anneal (700 K) cycles, and the cleanliness and surface quality was checked using LEED, as well as Auger spectroscopy and XPS. Preparation of the MgO films was carried out according to published methods by reactive deposition of Mg in an oxygen atmosphere (1×10^{-6} mbar).¹⁴ CO_2 was dosed from the background *via* a leak valve.

The experiments on acrolein hydrogenation on iron oxide supported Pd were performed with an ultra-high vacuum molecular beam machine that has been described in detail previously.¹⁵ Molecular beams of acrolein and H_2 were directed at the sample simultaneously while the sample was held at a constant temperature. The effusive molecular beams were produced by doubly differentially pumped multi-channel array sources. Acrolein (Sigma-Aldrich, 95% purity) was purified prior to each experiment by repeated freeze–pump–thaw cycles. During all reactivity experiments the flux of H_2 on the sample surface was 4.8×10^{15} molecules per cm^2 per s. The sample was exposed to H_2 for five minutes prior to acrolein exposure. The flux of acrolein on the sample surface was 1.5×10^{13} molecules per cm^2 per s. Gas-phase fragments $m/z = 56$, 57, and 58 were detected with a quadrupole mass spectrometer (QMS) (ABB Extrel). Acrolein and the hydrogenation products propenol and propanal were identified by their fragmentation patterns in the QMS. Acrolein generates signals at $m/z = 56$, 57, and 58 with an intensity distribution of 1 : 0.04 : 0.01. Propenol causes signals at $m/z = 57$ and 58 with an intensity ratio of 1 : 0.1, and propanal was identified by signals at the same masses with an intensity distribution of 0.3 : 1. Surface species were detected simultaneously with the gas-phase products using an infrared spectrometer (Bruker IFS 66v) with an MCT detector and a spectral resolution of 2 cm^{-1} .

A well-ordered ~ 10 nm thick Fe_3O_4 film was grown on a Pt(111) substrate (see ref. 16 and 17 for details), followed by Pd deposition onto the Fe_3O_4 film at 120 K by physical vapor deposition of Pd (Goodfellow, >99.9%) using a commercial evaporator (Focus EFM 3). After depositing Pd, the sample was annealed at 600 K and the Pd nanoparticles were stabilized by repeated cycles of oxidation and reduction at 500 K.¹⁸ The size of the Pd nanoparticles was controlled by the nominal thickness of the Pd film deposited onto the Fe_3O_4 substrate at 120 K, in comparison with the STM images reported previously (see ref. 19 for details). The Pd(111) crystal was cleaned by repeated cycles of Ar^+ sputtering at room temperature, annealing at 1000 K, and oxidation in 1×10^{-6} mbar O_2 at 750 K. The cleanliness of the Pd/ Fe_3O_4 and Pd(111) samples was verified prior to every experiment by infrared reflection absorption spectroscopy (IRAS) of adsorbed CO.

Results and discussion

Activation of carbon dioxide^{20,21}

In a previous study²¹ we observed a scenario schematically represented in Fig. 1. A two-layer MgO film was grown on an Ag(100) substrate, and Au was deposited

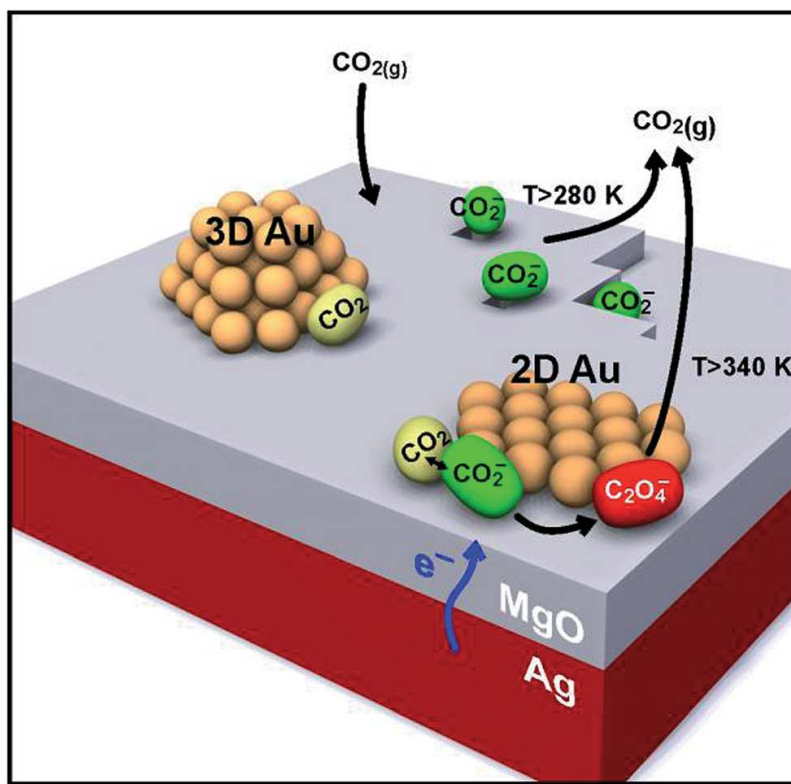


Fig. 1 Schematic showing the individual steps of oxalate formation upon chemisorption of CO_2 on the rim of 2D Au islands on thin $\text{MgO}(001)/\text{Ag}(001)$ films.²¹ Carboxylate species (green) are formed both on defect sites of the MgO film and on the rim of the 2D Au islands by electron transfer. Only on the latter, is additional CO_2 (yellow) able to solvate the carboxylate species, yielding a $(\text{CO}_2)_2^-$ dimer ion, which, after an additional electron transfer, results in adsorbed oxalate $\text{C}_2\text{O}_4^{2-}$ (red). This reaction does not occur on 3D Au particles.

from an Au evaporator at 77 K, and annealed consecutively at 300 K. It was noticed previously that deposition at a low temperature led to the two-dimensional growth of Au nanoparticles and islands,²² as suggested by theoretical calculations.²³ The driving force for this unusual wetting of the oxide surface is an electron transfer from the Ag substrate through the film and collected by the Au islands due to the large electron affinity of Au.²³ STM investigations, together with model calculations, suggested that the charge in this metal–insulator–metal (MIM) system localizes at the rim of the nanoparticles, *i.e.* at the nanoparticle–oxide interface.²⁴ Having noticed this phenomenon, a study of the molecular adsorption was started. The first attempt was made using CO.²⁵ However, it turned out that direct imaging of the molecules was not possible, but inelastic spatially resolved electron tunneling spectra of the CO hindered translation at 45 meV provided evidence that these molecules do interact exclusively with the rim of the nanoparticle. It is interesting to note that the CO molecules do not exhibit an appreciable IR intensity.²⁵ This is indicative of a geometry leading to a small dipole moment perpendicular to the surface. Following up on this, we investigated the adsorption of a bigger molecule, isophorone, promising easier constant current imaging. It was possible to image the molecule at the rim, and, in addition, to study the consequences of adsorption on the quantum well states of the nanoparticle, which develop due to its finite size.²⁶ In fact, the energetic position of the quantum well states of the same nanoparticle was compared with those of the

particle interacting with isophorone. Isophorone, as revealed by infrared spectroscopy, physisorbs on Au nanoparticles. This leads to a characteristic enhancement of the effective electron mass of the Au electrons, in line with physisorption. While this is important to understand the details of the molecule–nanoparticle interaction, these observations do not provide evidence for a reaction. This came from studies of CO₂ adsorption on these systems.²¹ When CO₂ adsorbs on the surface, it is located at the rim of the clusters and it transforms to CO₂⁻ (see Fig. 1) by electron transfer from the Au nanoparticle. While this process is energetically uphill by 0.6 eV, the presence of additional CO₂, able to “solvate” the carboxylate to a (CO₂)₂⁻ dimer ion, leads to a 1.6 eV downhill process. Spectroscopic studies, further elaborated and extended on below, suggest, together with model calculations, that this finally results in an oxalate ion by a second electron transfer, all happening at the rim of the nanoparticle.

Fig. 2 shows a set of infrared spectra of the surface as a function of annealing temperature. First, we concentrate on the trace recorded at the lowest temperature. The peak at 1295 cm⁻¹ is due to CO₂ adsorption on the oxide support forming a carboxylate, *i.e.* not a carbonate(!), at specific sites on the MgO film. The two bands at 1220 cm⁻¹ and 1440 cm⁻¹ have been identified as being due to the oxalate species. This spectrum is entirely consistent with the spectra recorded before.²¹ The other spectra in Fig. 2 have been recorded after annealing the Au

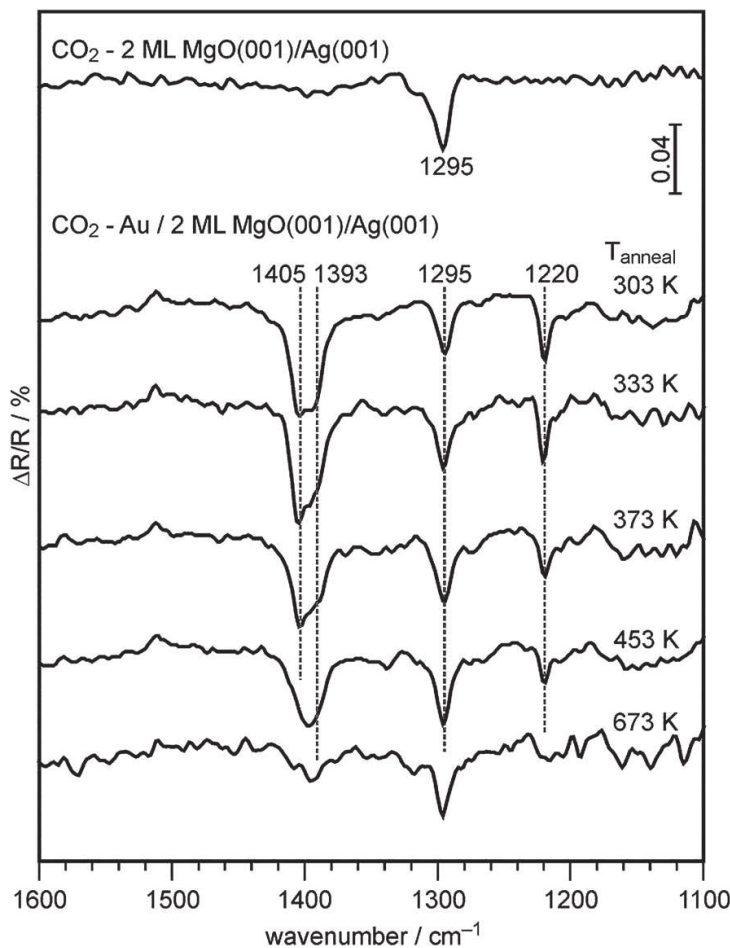


Fig. 2 IRA spectra of bare (top) and Au-loaded 2 monolayer (ML) thick MgO(001)/Ag(001) samples recorded after a saturation dose of CO₂ at 223 K. Au was deposited at 100 K and the samples were subsequently annealed at the indicated temperature prior to CO₂ adsorption.

deposits at higher temperatures. Obviously, annealing at a higher temperature does not influence the intensities in the infrared spectra massively, unless the system is annealed at or higher than 500 K. This is also consistent with our previous findings using temperature programmed desorption, where oxalate dissociation into two CO₂ molecules started to occur well below this temperature. If one annealed not quite at this temperature, then the process of oxalate formation was entirely reversible. This hinted towards a kinetically controlled process that changes the system.

Ricci *et al.*,²³ in a landmark paper, demonstrated that for nanoparticles on ultrathin oxide films, the electron transfer through the film depends strongly on the dimensionality of the Au particle on the oxide. Clearly, a two-dimensional particle was prone to accepting more electronic charge than a three-dimensional particle, and it also depended considerably on the contact area of the particle. Given this scenario, one might envision that by increasing the mobility of the Au atoms on the oxide film through annealing at a higher temperature, three-dimensional particles start to grow on the film. These particles would exhibit a small enough charge transfer that the chemical potential for forming the CO₂ anion and the oxalate is impossible. This would establish the first proof of a morphology driven change in a reaction at the oxide metal interface. In order to see whether this would be a valid interpretation, we performed and present here a STM study that is summarized in Fig. 3. This figure shows a set of STM images taken at different annealing temperatures. Fig. 3a has been recorded at 77 K and reveals Au adsorbed as single atoms or small clusters. Annealing at room temperature or slightly above (Fig. 3b) causes two-dimensional islands to form all over the surface. Their average size varies between 3 and 5 nm with a variation in shape ranging from roundish (hexagonal) islands to more rectangular (raft-like) ones. This is consistent with our previous findings.²² Increasing the temperature to 400 K increases the average island diameter to 4–8 nm but does not change the growth mode (Fig. 3c). A drastic change occurs if the annealing temperature is raised to 500 K (Fig. 3d). We find a cross-over to three-dimensional growth with particle diameters between 5 and 10 nm, and heights of 1–2 nm. There are still a few two-dimensional islands observed, but most of the Au is contained in 3D particles.

Using this information we may now return to a discussion of Fig. 2, and try to understand the changes in the oxalate signals as a function of temperature. As stated above, the lowest temperature trace represents the oxalate species at the rim of the 2D nanoparticles, as proven in previous reports.²¹ The infrared spectra start to attenuate and significantly change after the system has been either prepared at temperatures higher than approx. 500 K, or annealed for a sufficiently long time at that temperature. We know from the above STM study that this is concomitant with the change from 2D to 3D morphology. As referred to above, the formation of the 3D particles reduces the electron transfer from the Ag substrate, and, we conclude, must be the reason for the reduced ability to form oxalate species. Note that the species due to adsorption on the MgO film at 1295 cm⁻¹ is not influenced by the change in growth mode.

At the present time, theoretical modeling of the process, which would be highly desirable, is not possible. Hannu Häkkinen and his group have greatly contributed to our understanding of the oxalate formation, as documented in ref. 21. However, a full, detailed description involving nanoparticles of the size observed experimentally seems to be out of range at present. Schematically, as

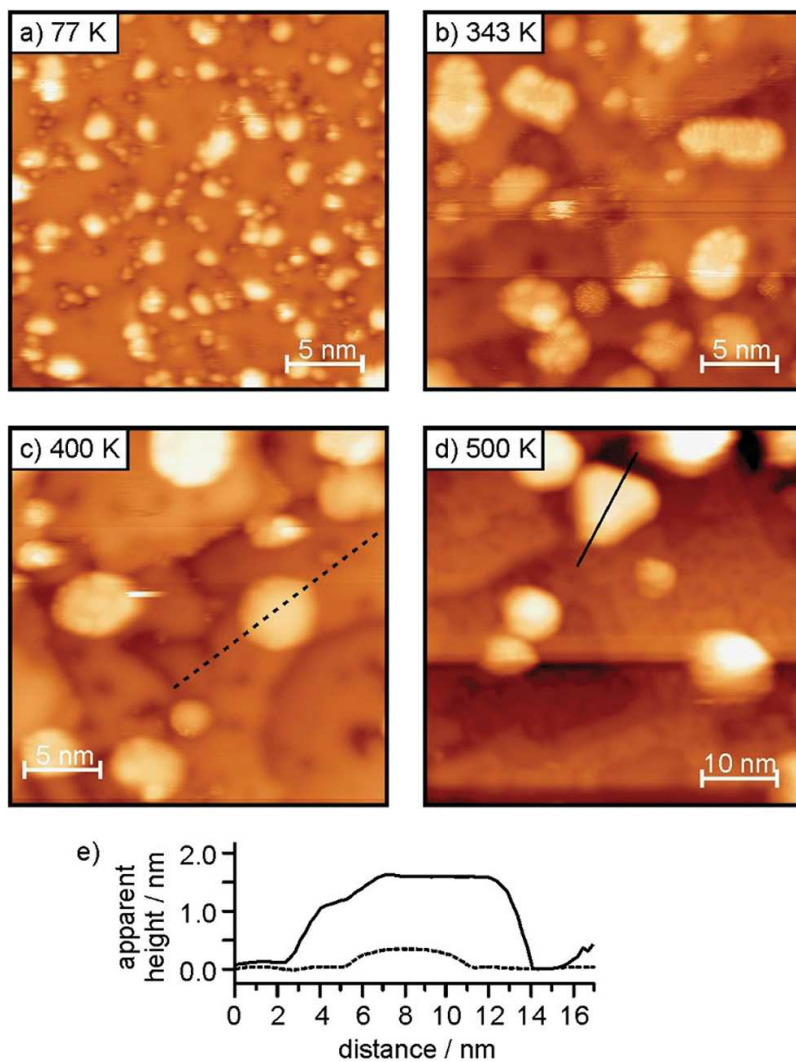


Fig. 3 STM images of (a) Au deposited on 2 ML MgO(001)/Ag(001) at 77 K, and after subsequent annealing of the system at 343 K (b), 400 K (c) and 500 K (d). All images were taken at 77 K. Scan area: (a)–(c) 25 nm × 25 nm; (d) 50 nm × 50 nm. $U_{\text{bias}} = + (0.5 - 0.75)$ V. $I_t = 30$ pA. (e) Height profiles of representative islands/particles from the 400 K (dashed line) and 500 K (solid line) annealed samples, highlighting the transition from 2D to 3D geometries.

depicted in Fig. 1, this means a change from reacting CO₂ at nanoparticles (2D) towards unreactive particles with a 3D morphology. To the best of our knowledge, this is the first clear experimental indication for such behavior.²⁷

In order to relate the findings reported in this paper to the design of real powder-based catalysts, we refer to our study showing doping of bulk oxides with transition metals,²⁸ which provide an electron source to trigger a similar control of morphology as the Ag support of the ultrathin film. It will be a future task to experimentally establish this in model systems and in powder samples. However, based on the findings reported here, one may envision the control and design of CO₂ activation catalysts by doping induced charge transfer, and thus this establishes a design principle for supported Au catalysts.

Hydrogenation of acrolein²⁹

Hydrogenation of C=C double bonds has been shown to depend on the presence of hydrogen atoms absorbed inside the metal nanoparticles.² The absorbed

hydrogen provides a pool to sustain catalytic activity. Carbon and/or carbonaceous deposits adsorbed at the particle's corners and edges control the diffusion of the hydrogen necessary for hydrogenation from below the surface to the surface of the particle. The selective, competitive hydrogenation of acrolein, *i.e.* the hydrogenation of a C=C double bond *versus* the hydrogenation of a C=O double bond, represents an even more ambitious situation.²⁹

In a previous study,²⁹ we investigated the selectivity of the partial hydrogenation of acrolein on a Pd(111) single crystal and on Pd/Fe₃O₄ model catalysts by isothermal molecular beam experiments under well-defined UHV conditions. The formation of gas-phase products was detected by quadrupole mass spectrometry (QMS); simultaneously, the evolution of surface species was investigated by infrared reflection absorption spectroscopy (IRAS) studies. Pd(111) and Pd/Fe₃O₄ showed very different selectivities in the partial hydrogenation of acrolein. Over Pd/Fe₃O₄, selective conversion of acrolein to propanal occurs, while over a Pd(111) single crystal, propenol is formed with near 100% selectivity. IRAS studies on the surface turning over showed that the selectivity for propenol formation on Pd(111) critically depends on the presence of a dense overlayer of an oxopropyl species formed at an initial stage of acrolein and hydrogen exposure. On the modified Pd(111) surface, acrolein is adsorbed *via* the C=O bond and reacts with propenol. On Pd/Fe₃O₄, however, significantly different surface chemistry occurs under identical experimental conditions. Instead of forming an oxopropyl layer, a fraction of the acrolein molecules decomposes, forming CO molecules and C_xH_y fragments that eventually block all Pd sites, while the propanal formation rate decreases to zero. Most likely, low-coordinated surface sites and (100) facets of the Pd clusters are responsible for the rapid acrolein decarbonylation. The reason for the significantly different surface chemistry on Pd/Fe₃O₄ and Pd(111), however, needs further investigation. In particular, a detailed kinetic analysis of all possible reaction pathways on the different Pd surfaces would be required. Nevertheless, our investigations unambiguously show that the modification of the Pd(111) surface with a dense oxopropyl overlayer correlates with a change in selectivity from propanal to propenol formation. Moreover, the absence of the oxopropyl layer on Pd/Fe₃O₄ seems to be related to the decarbonylation of acrolein.

Based on our previous results, we have addressed the question of whether it is possible to also produce propenol on Pd/Fe₃O₄ model catalysts. We could think about a large number of different approaches, such as modifying the Pd clusters prior to acrolein conversion, *e.g.* by pre-adsorbed CO or hydrocarbons or by C modification of low-coordinated Pd sites. In the present study, however, we focus on the effect of Pd particle size. We have investigated the hydrogenation of acrolein on 7 nm and 12 nm Pd particles using molecular beam techniques under isothermal conditions. The formation of the gas-phase products has been detected by QMS and the surface composition has been simultaneously investigated by IRAS. In all experiments, the surface was pre-exposed to 4.8×10^{15} H₂ per cm² per s for 300 s before the acrolein beam with 1.5×10^{13} molecules per cm² per s was switched on.

Fig. 4 shows the formation rates of the partial hydrogenation products on Fe₃O₄-supported 7 nm and 12 nm Pd particles detected in the gas phase. With both particles sizes, similar propanal formation rates are observed, which pass through a maximum after about 30 s and then decrease to zero. On the 12 nm

particles, however, a small amount of propenol is also detected. The propenol production rate rapidly increases after about 40 s, when the propanal formation has almost stopped, passes through a maximum after about 60 s and finally decreases to zero. In general, both partial hydrogenation products have been identified by their characteristic fragmentation patterns in QMS. The clearly different time dependence of the two product formation rates in this study, however, provides an additional possibility to unambiguously distinguish between propanal and propenol. Nevertheless, the total amount of propenol that is formed on the 12 nm particles is much smaller than on a Pd(111) single crystal. It should be noted that the formation of gas-phase propenol has only been detected in a narrow temperature range near 250 K. It was not observed in our previous studies on Pd particles under slightly different conditions, such as a lower or higher surface temperature or when using a pulsed acrolein beam instead of continuous exposure.

Fig. 5 illustrates the correlation between the evolution of propenol in the gas phase detected by QMS and the formation of surface species on the 12 nm Pd particles turning over, as studied by IRAS. A time-dependent series of IR spectra obtained with a time resolution of 45 s is shown in Fig. 5a. IR absorption features appear near 1855 cm^{-1} , 1755 cm^{-1} , and 1670 cm^{-1} . The vibration at 1670 cm^{-1} is most likely associated with the C=O stretching in molecularly adsorbed acrolein. It has been assigned to acrolein adsorbed on a Pd(111) single crystal in a previous study.²⁹ The adsorbate giving rise to the IR absorption near 1755 cm^{-1} accumulates at the beginning of the acrolein exposure and saturates during the first 45 s. Interestingly, this band has previously been related to the oxopropyl species modifying the Pd(111) surface for propenol production. The IR vibration at 1855 cm^{-1} most likely shows CO adsorbed on the Pd(111) facets. The slowly increasing IR absorption intensity indicates a rather slow accumulation of CO, most likely from acrolein decarbonylation. Hence, the decarbonylation of acrolein is significantly less efficient at 250 K compared to our previous studies at 270 K. Fig. 5b illustrates the simultaneously recorded propenol evolution in the gas phase. A

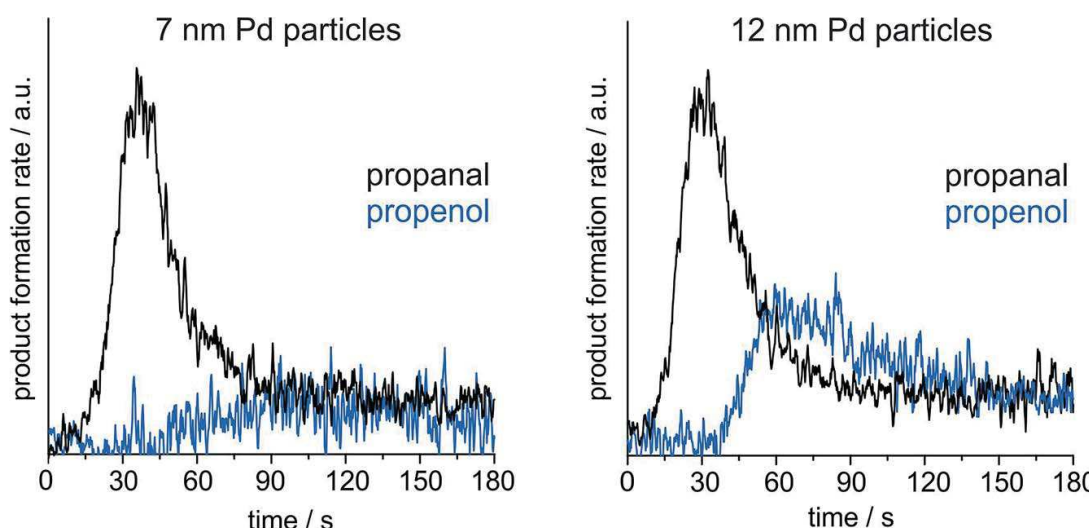


Fig. 4 Formation rates of propanal (black lines) and propenol (blue lines) over Fe_3O_4 -supported Pd particles with diameters of 7 nm (left) and 12 nm (right) at 250 K, detected by QMS.

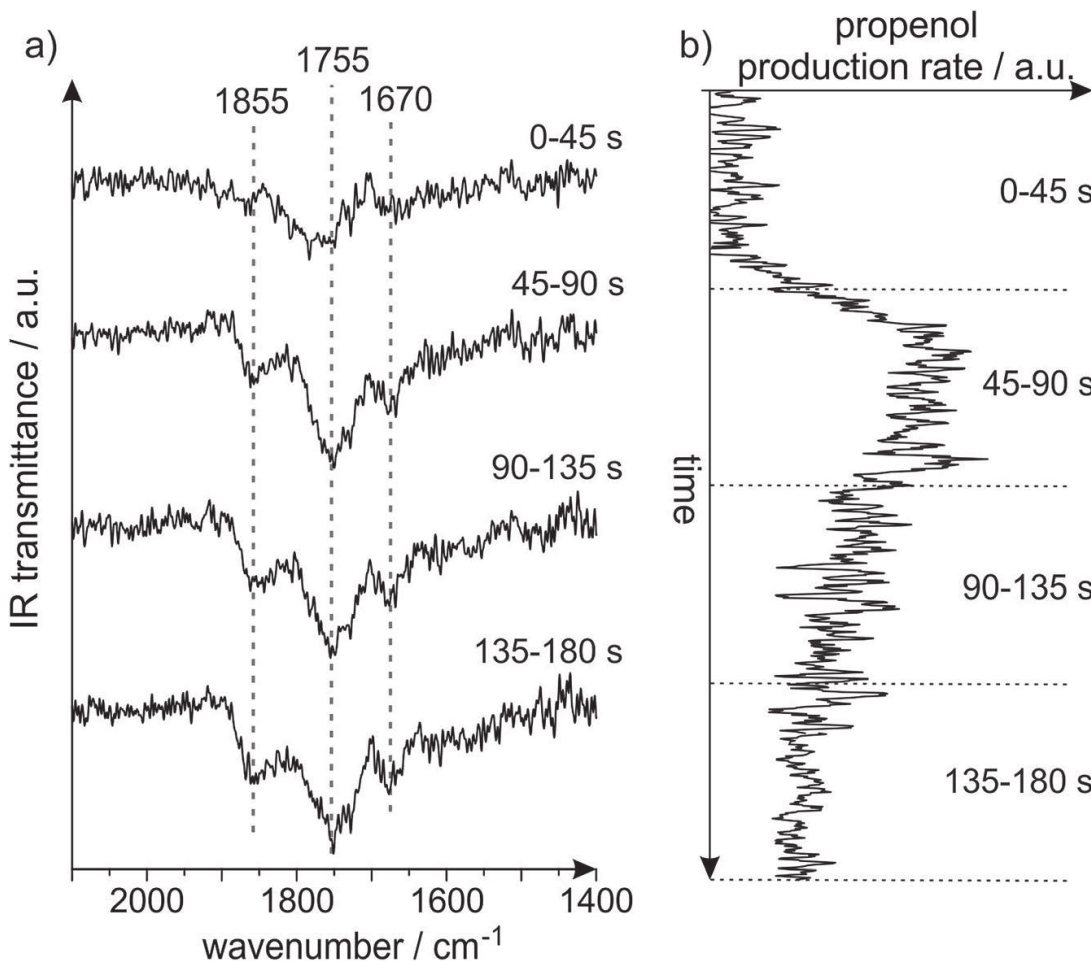


Fig. 5 (a) Time-resolved IR spectra monitoring the evolution of surface species on the 12 nm Pd particles turning over and (b) QMS measurements showing the formation rate of propenol in the gas phase.

clear onset is observed after about 40 s, which is approximately when the oxopropyl species saturates.

The simultaneously performed IRAS and QMS studies on the 12 nm Pd particles turning over at 250 K give detailed insights into the mechanism of the acrolein conversion. On the one hand, our results strongly reveal that on the 12 nm particles a modification of the surface by an oxopropyl layer triggers the propenol production. In contrast to Pd(111), however, the additional presence of acrolein and CO on the surface reveals that the oxopropyl species is not covering the whole Pd surface with a dense layer. On the other hand, it is again indicated that the decarbonylation of acrolein has to be avoided to form propenol on Pd particles. By reducing the surface temperature from 270 K to 250 K, the decarbonylation of acrolein is largely suppressed, while the temperature is still high enough to form a small amount of propenol. It seems that the temperature needs to be carefully chosen to keep the decarbonylation reaction rate as low as possible, while the propenol formation rate should still be sufficiently high.

Our studies show a significant particle size dependence of the selectivity in the partial hydrogenation of acrolein over Pd model catalysts at 250 K. On both 7 nm and 12 nm Pd particles, a similar amount of propanal is formed. Hydrogenation of acrolein to propenol, in contrast, appears possible only on 12 nm particles. The clearly different time dependence of propanal and propenol evolution agrees well

with our previous findings, showing propanal formation as long as pristine Pd is available and propenol production, in contrast, after a dense oxopropyl overlayer is formed. It seems that the selectivity towards propenol formation increases with increasing Pd cluster size from 0% on 7 nm Pd particles and a small amount over 12 nm Pd particles to approximately 100% on a Pd(111) single crystal. Possibly, the formation of an oxopropyl layer on sufficiently large domains is necessary to produce propenol, which is more likely to happen on larger Pd clusters having larger (111) facets and a lower concentration of low-coordinated sites. Low-coordinated sites, such as edges, corners, and defects, may catalyze acrolein decarbonylation.

Synopsis

The present study clearly points to two important factors influencing the catalytic activity of supported metal nanoparticles, which influence the design of new catalytic materials:

- The interaction with the support controls the size and shape of the nanoparticle, and, in particular, the charge exchange and transfer at the oxide–metal interface. Specifically designed model systems allow us to isolate details of the problem and study them at the atomic level. Here, the surface science approach turns out to be the method of choice to image and characterize molecules interacting with the metal particle at the metal–oxide interface using a combination of scanning probe and spectroscopic techniques. This has allowed, for the first time, the direct identification of the consequence of molecular adsorption and reaction on the electronic structure of a metal nanoparticle. Temperature is decisive in determining the mobility of metal atoms and particles on supports. We show in this paper that a change in particle morphology controls the reactivity of the system at the oxide–metal interface, as the transition from two-dimensional Au particles at a lower temperature to three-dimensional growth at a higher temperature reduces the charge transfer from the support to the metal nanoparticle.

- Adsorbed species formed during a reaction, which are not turned over, have been identified as being able to modify a supported metal nanoparticle, and *via* this modification, control the selectivity of a hydrogenation reaction. The selective hydrogenation of acrolein has been studied as an example. In particular, an oxopropyl species formed from adsorbed acrolein modifies the surface in such a way that acrolein hydrogenation leads to propenol and the hydrogenation of the C=C double bond is avoided. We have demonstrated before that Pd(111) single crystals selectively hydrogenate the C=O bond in acrolein, while supported Pd nanoparticles exclusively hydrogenate the C=C bond. We show in this paper that there is a particle size effect. The particle needs to have a certain size in order to expose (111) facets of a sufficient size to favor the effect. If particles are smaller, presumably the presence of edges, corners and irregularities in the particles favor the formation of CO, which poisons the oxopropyl effect.

The knowledge derived from both of these observations can be used to design catalytic materials and control catalytic reactions.

Acknowledgements

We are grateful to the German Science Foundation through the cluster of Excellence Unicast (administered by the TU Berlin) as well as the Fonds der

Chemischen Industrie for financial support. F. Calaza thanks the Alexander von Humboldt foundation for a Georg Forster Research Fellowship. C. Stiehler thanks the Studienstiftung des Deutschen Volkes for a fellowship. S. Schauermann is grateful to the European Research Council for a Starting Grant “Enantioselective Reactions on Model Chirally Modified Surfaces”. M. Sterrer acknowledges support from the European Research Council through Grant Agreement No. 280070 (STRUBOLI).

References

- 1 H. K. G. Ertl, F. Schüth and J. Weitkamp, *Handbook of Heterogeneous Catalysis*, VCH, Wiley-VCH, Weinheim, compl. rev. and enlarged ed. edn., 2008.
- 2 M. Wilde, K. Fukutani, W. Ludwig, B. Brandt, J.-H. Fischer, S. Schauermann and H. J. Freund, *Angew. Chem., Int. Ed.*, 2008, **47**, 9289–9293.
- 3 S. J. Thomson and G. Webb, *J. Chem. Soc., Chem. Commun.*, 1976, 526–527.
- 4 G. C. Bond, *Metal-Catalysed Reactions of Hydrocarbons*, Springer, US, New York, 2005.
- 5 J. Sauer and H.-J. Freund, *Catal. Lett.*, 2015, **145**, 109–125.
- 6 M. Boudart and G. Djéga-Mariadassou, *La cinétique des réactions en catalyse hétérogène*, Masson, Paris, New York, 1982.
- 7 G. Ertl, *Angew. Chem., Int. Ed.*, 2008, **47**, 3524–3535.
- 8 G. Ertl and H. J. Freund, *Phys. Today*, 1999, **52**, 32–38.
- 9 J. Sauer, *Chem. Rev.*, 1989, **89**, 199–255.
- 10 H. J. Freund, N. Nilius, T. Risse and S. Schauermann, *Phys. Chem. Chem. Phys.*, 2014, **16**, 8148–8167.
- 11 S. Shaikhutdinov and H.-J. Freund, *Annu. Rev. Phys. Chem.*, 2012, **63**, 619–633.
- 12 D. Teschner, J. Borsodi, A. Woitsch, Z. Révay, M. Hävecker, A. Knop-Gericke, S. D. Jackson and R. Schlögl, *Science*, 2008, **320**, 86–89.
- 13 R. Schlögl, *Angew. Chem., Int. Ed.*, 2015, **54**, 3465–3520.
- 14 J. Pal, M. Smerieri, E. Celasco, L. Savio, L. Vattuone and M. Rocca, *Phys. Rev. Lett.*, 2014, **112**, 126102.
- 15 J. Libuda, I. Meusel, J. Hartmann and H.-J. Freund, *Rev. Sci. Instrum.*, 2000, **71**, 4395.
- 16 W. Weiss and W. Ranke, *Prog. Surf. Sci.*, 2002, **70**, 1–151.
- 17 C. Lemire, R. Meyer, V. E. Henrich, S. Shaikhutdinov and H. J. Freund, *Surf. Sci.*, 2004, **572**, 103.
- 18 T. Schalow, B. Brandt, D. Starr, M. Laurin, S. Schauermann, S. Shaikhutdinov, J. Libuda and H. J. Freund, *Catal. Lett.*, 2006, **107**, 189–196.
- 19 T. Schalow, B. Brandt, D. E. Starr, M. Laurin, S. K. Shaikhutdinov, S. Schauermann, J. Libuda and H. J. Freund, *Phys. Chem. Chem. Phys.*, 2007, **9**, 1347–1361.
- 20 H.-J. Freund and M. W. Roberts, *Surf. Sci. Rep.*, 1996, **25**, 225–273.
- 21 F. Calaza, C. Stiehler, Y. Fujimori, M. Sterrer, S. Beeg, M. Ruiz-Oses, N. Nilius, M. Heyde, T. Parviaainen, K. Honkala, H. Häkkinen and H.-J. Freund, *Angew. Chem., Int. Ed.*, 2015, **54**, 12484.
- 22 M. Sterrer, T. Risse, U. Martinez Pozzoni, L. Giordano, M. Heyde, H.-P. Rust, G. Pacchioni and H.-J. Freund, *Phys. Rev. Lett.*, 2007, **98**, 096107.
- 23 D. Ricci, A. Bongiorno, G. Pacchioni and U. Landman, *Phys. Rev. Lett.*, 2006, **97**, 036106.

- 24 X. Lin, N. Nilius, M. Sterrer, P. Koskinen, H. Haekkinen and H.-J. Freund, *Phys. Rev. B: Condens. Matter Mater. Phys.*, 2010, **81**, 153406.
- 25 X. Lin, B. Yang, H. M. Benia, P. Myrach, M. Yulikov, A. Aumer, M. Brown, M. Sterrer, O. Bondarchuk, E. Kieseritzky, J. Rocker, T. Risse, H. Gao, N. Nilius and H. J. Freund, *J. Am. Chem. Soc.*, 2010, **132**, 7745–7749.
- 26 C. Stiehler, F. Calaza, W.-D. Schneider, N. Nilius and H.-J. Freund, *Phys. Rev. Lett.*, 2015, **115**, 036804.
- 27 M. Chen and D. W. Goodman, *Chem. Soc. Rev.*, 2008, **37**, 1860–1870.
- 28 X. Shao, S. Prada, L. Giordano, G. Pacchioni, N. Nilius and H.-J. Freund, *Angew. Chem., Int. Ed.*, 2011, **50**, 11525–11527.
- 29 K.-H. Dostert, C. P. O'Brien, F. Ivars-Barcelo, S. Schauermann and H.-J. Freund, *J. Am. Chem. Soc.*, 2015, **137**, 13496–13502.

Model Systems in Heterogeneous Catalysis:
Towards designing and understanding of structure and electronic properties

Q. Pan¹, L. Li¹, S. Shaikhutdinov¹, Y. Fujimori¹, M. Hollerer², M. Sterrer², H.-J. Freund¹

¹ Fritz-Haber-Institute of the Max-Planck Society, Department of Chemical Physics,
Faradayweg 16, 14195 Berlin, Germany.

² University of Graz, Institute of Physics, NAWI Graz, Universitätsplatz 5, 8010 Graz,
Austria.

Abstract

We discuss in this paper two case studies related to nano-particle catalyst systems: one concerns a model system for the Cr/SiO₂ Phillips catalyst for ethylene polymerization. Here we present XPS data to complement the previously published TPD, IRAS and reactivity studies to elucidate the electronic structure of the system in some detail. The second case study provides additional information on Au nano-particles supported on ultrathin MgO(100)/Ag(100) films where we had observed a specific activity of the particles rim at the metal-oxide interface with respect to CO₂ activation and oxalate formation, obviously connected to electron transfer through the MgO film from the metal substrate underneath. Here we present XPS and Auger data which allow a detailed analysis of the observed chemical shifts. This analysis corroborates previous findings deduced via STM.

Introduction

Catalysts are complex materials! Take heterogeneous catalysis, which is the topic of the present paper, as an example: A reaction between gaseous components proceeds at the surface of a solid material usually containing several components. In order to identify the active part of the catalyst we need to be able to study a very small amount of starting material and of products at the surface of the complex material, and we need to be simultaneously able to differentiate the surface of the material from its bulk. This requires the development of specific, surface sensitive techniques and, in order to isolate the action of the various material components, a

systematic variation in the complexity of the studied material.¹ This variation has to proceed from the most simple to the more complex, and not vice versa. Only by adding complexity will we be able to finally approach the final real system. In this sense, we set up model systems in catalysis, which may be characterized at the atomic level. In addition, we note, that progress in the spirit of understanding phenomena at the atomic level will only be achieved by experiment and theory going hand-in-hand.²

Since the complex structure of real, supported metal catalysts often hampers the attempt to connect macroscopic effects with the microscopic processes taking place on the surface, an increasing number of model studies have been conducted so far to tackle these questions. For studies of that kind, planar substrates, instead of the technically used porous materials, are needed in order to take full advantage of modern surface spectroscopic and microscopic techniques.^{3, 4} Vapor deposition of metals⁵⁻⁷ or deposition of metal clusters from the gas phase⁸ under ultrahigh vacuum (UHV) conditions have been preferred in experiments keyed to more fundamental questions about the correlation between structure and properties of small metal particles.

In these cases, well-ordered substrates are desirable, just to know where the atoms are. The most straightforward choice in this context is a single crystal sample, of course. Studies of bulk oxides, however, can be connected with severe experimental problems. Their insulating character can restrict or even prevent electron and ion spectroscopic, as well as low-energy electron diffraction (LEED) and scanning tunneling microscopic (STM) measurements. Only in cases where the oxide can be made sufficiently bulk conducting (e.g. TiO₂), this limitation may not apply.^{9, 10} Other difficulties encountered are related to sample mounting and cleaning (adjustment of surface stoichiometry) or arise from the poor thermal conductivity associated with oxide materials. In this context, ultra-thin oxide films grown on a metallic substrate are an excellent alternative in order to circumvent all these problems^{6, 7, 11, 12}. It has been shown that even films with a thickness of just a few Angstroms may exhibit physical properties characteristic of the bulk material¹³. The traditional method to prepare such films is the oxidation of the native metal¹³ or an alloy¹⁴⁻¹⁷, although this often results in amorphous or polycrystalline overlayers (e.g. Al oxide on Al¹⁸⁻²¹, or Si oxide on Si^{22, 23}) or films with a rather

high defect density. This is due to the large mismatch which usually exists between the metal and the oxide lattice (e.g. NiO(100)/Ni(100)²⁴). There are a few examples where well-ordered crystalline films can be obtained in this way (e.g. Cr₂O₃(111) on Cr(110)²⁵⁻²⁷ or Al₂O₃ on NiAl(110)^{14, 15} and Ni₃Al(111)^{16, 17}). Therefore, other routes have been proposed. Goodman et al., for example, extensively explored preparation techniques based on the evaporation of a metal (or non-metal) onto a host crystal, mostly a refractory metal, in an ambient oxygen atmosphere ^{11, 12, 28}. This approach allows one to vary the oxide film thickness, and explore whether the oxide film-metal support interface influences the properties of the supported particles. In fact, the oxide film metal interface may be used to control charge transfer from the interface to the supported metal particle.

In this discussion we elaborate on two systems, which we have worked on recently. The first is the design of a model system for the Phillips catalyst (Cr/SiO₂) for ethylene polymerization, the second one is the design of a system that allows us to study the action of the oxide-metal nanoparticle interface at the atomic level, i.e. Au nano-particles on MgO(100)/Ag(100).

a) Model for the Phillips Catalyst

The Phillips catalyst (Cr/SiO₂) is used in the large-scale production of polyethylene and has attracted considerable attention in the catalytic community over the last sixty years.²⁹⁻³² However, the atomic structure of the active site(s) and the reaction mechanism remain controversial, in particular due to the structural complexity and surface heterogeneity of the amorphous silica.³³⁻³⁹ However, recently developed thin silica films grown on metals as a well-defined silica support offers the opportunity to investigate mechanistic aspects of the reaction at the atomic scale.⁴⁰⁻⁴³ The so-called “bilayer” film grown on Ru(0001) consists of two silicate layers, each being formed by corner sharing of SiO₄ tetrahedra like in sheet silicates, and the film is weakly bonded to the metal surface.^{44, 45} Figure 1a displays high-resolution microscopy images of the film surface, obtained in our own laboratories, which are superimposed with a network of N-membered silica rings. Being terminated by fully saturated siloxane bonds and hence essentially hydrophobic, the silica surface could, however, be hydroxylated with the help of low energy electron radiation.⁴⁶ It was thought that surface hydroxyls will be acting as

anchors for chromium species deposited from certain precursors, ultimately resulting in a well-defined planar model system, schematically shown in Fig. 1b. These systems could, in principle, be characterized with atomic resolution using STM in combination with other spectroscopic techniques employed in surface science.

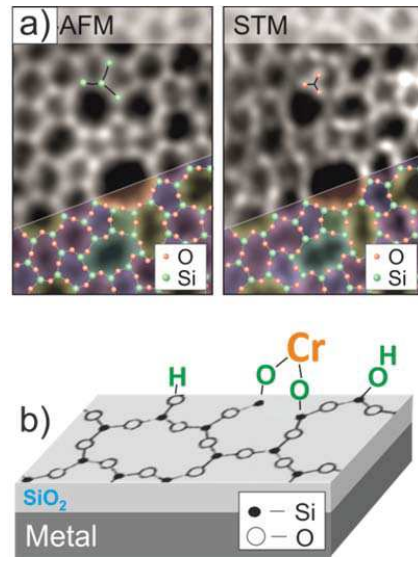


Figure 1. a) Atomic force microscopy (AFM) and STM images of amorphous bilayer silica film grown on Ru(0001), which are superimposed with a silica network. b) Schematic view of a planar model system for the Phillips catalyst, where Cr species are anchored onto an atomically flat hydroxylated silicate film. (Reprinted with permission from ref. 43. Copyright (2017) Elsevier.)

In a previous infrared reflection-absorption spectroscopy (IRAS) and temperature programmed desorption (TPD) study, we used Cr physical vapor deposition ⁴³ that led to reaction of Cr with silanol (Si-OH) species as evidenced by disappearance of the corresponding IRA band. Adsorption of CO as a probe molecule showed a broad IRA signal at 2055 cm^{-1} and a weak band at 2160 cm^{-1} , which were assigned to CO adsorbed on “naked” Cr sites and on Cr=O species, respectively. On the basis of TPD results, the amount of chromyl species is found to be relatively small. The system is fairly stable as no spectral changes were observed upon heating to 400 K in UHV. In oxygen ambient at elevated temperatures, Cr species become oxidized, thus forming more mono-chromyl species (and their aggregates) and probably di-oxo chromyl species which do not coordinate CO.

Ethylene adsorption experiments on our model systems were conducted under UHV conditions at low temperature. The observed IRA bands at 2960 and 2874 cm⁻¹, and 1462 and 1381 cm⁻¹ are characteristic for stretching $\nu(\text{C-H})$ and bending $\delta(\text{C-H})$ vibrations, respectively, in R-CH₃ groups. Accordingly, the bands at 2931 and 2862 cm⁻¹, and 1462 cm⁻¹ are assigned to C-H vibrations in R-CH₂-R.⁴⁷ Combined with IRAS results, TPD spectra suggested the formation and desorption of butene even at 110 K, probably from butadiyl species.⁴⁸ The desorption signals at ~120 K were assigned to a mixture of ethylene and butane. This formation of C4 molecules at low temperatures would be consistent with the two-steps initiation mechanism proposed by Scott and co-workers, in which n-butane is formed.³³ It has recently been suggested that butene formation results from ethylene oligomerization.^{49, 50}

To shed more light on the structure of our model system, we performed XPS measurements. The O 1s signal in the pristine films on Ru(0001) contains a main signal at 531.6 eV, assigned to oxygen atoms in the various Si-O-Si bonds in the film, and a shoulder at 529.4 eV, assigned to chemisorbed O atoms on Ru(0001) (Figure 2a), in agreement with previous studies.^{40, 51-53}

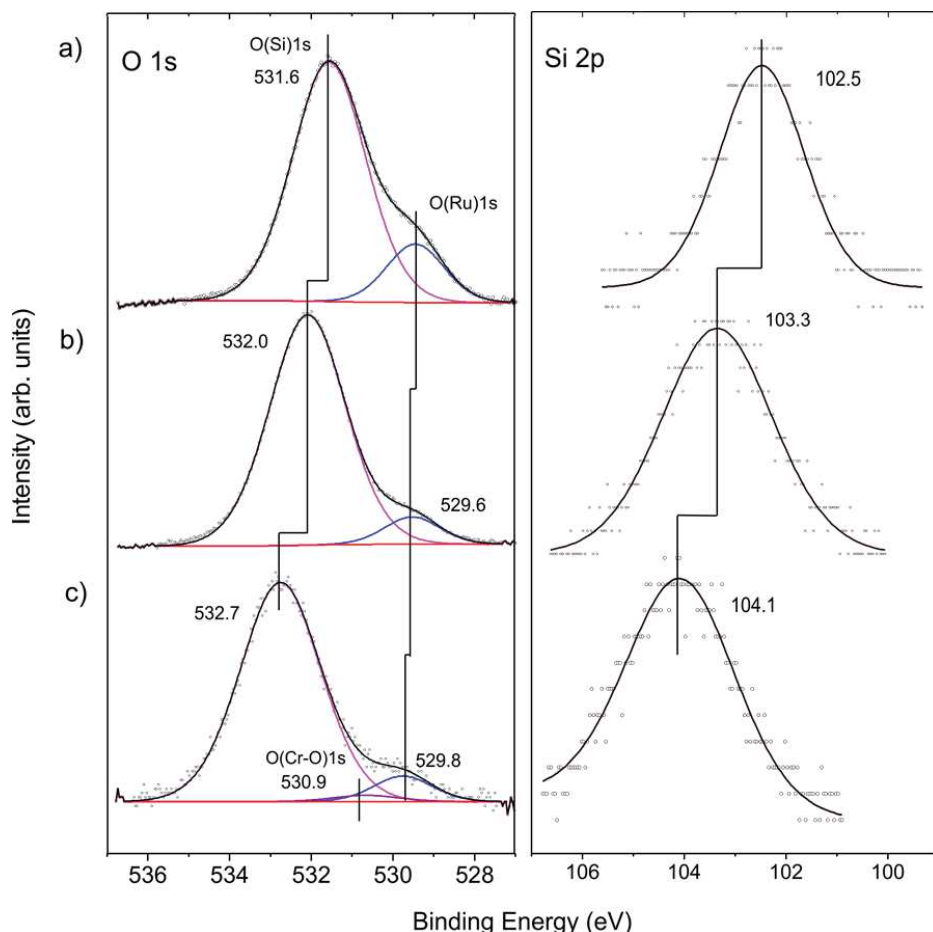


Figure 2. The O 1s and Si 2p regions of XP spectra measured at normal electron emissions on: (a) bilayer silicate film; (b) hydroxylated silicate film; and (c) hydroxylated silicate film after chromium deposition. The deconvolution envelope is shown in black.

For hydroxylation of the silica surface, the film was pre-covered by a thin “ice” layer formed upon water adsorption at 100 K and subsequently irradiated with low energy (200 eV) electrons, as described in detail in ref.⁴⁶. The sample was then flashed to 300 K to ensure desorption of molecular water. Electron bombardment greatly enhances the degree of hydroxylation without destroying the principal structure of the bilayer film as judged by IRAS and also by STM, although atomic resolution had not been achieved. Apparently, the hydroxylation occurs through the breaking of siloxane bonds in the silica network.^{43, 54} In the course of XPS studies, we found certain beam damaging effects which are manifested by a lowering of the intensity of the silanol bands in IRAS after XPS measurements. However, the silanols can be fully recovered by subsequent re-adsorption of water at 100 K and heating to

300 K. In order to minimize such effects, we used a lower number of scans for recording the Si 2p region, which, in contrast to the O 1s level, shows only one component. This explains a relatively low signal-to-noise ratio in the Si 2p spectra presented in Fig. 2.

Upon hydroxylation, the O(Ru) component (Figure 2b) considerably attenuates and slightly shifts by about 0.2 eV, that is within the spectral resolution of our spectrometer (200 meV). However, the O(Si) and the Si 2p signals exhibit an obvious shift (0.4 eV and 0.8 eV, respectively) towards higher binding energies. In principle, the shifts could be explained by the loss of oxygen at the Ru-silica interface and respective changes in the work function of the substrate underneath the silica.⁵¹⁻⁵³ Since the shift in the O(Si) core level is substantially different from the Si 2p one (0.4 vs 0.8 eV), it is more plausible, however, that the observed shifts are, to a large extent, due to chemical changes in the silica framework caused by the formation of silanol bonds.^{43, 46}

Cr deposition onto hydroxylated films was carried out at low temperatures in order to prevent migration of adsorbed metal atoms to the silica/support interface as previously observed for Pd.⁵⁵ Also, to minimize the above-mentioned beam damaging effects, the XP spectra were recorded with only two scans both for O 1s and Si 2p regions. Figure 2c shows that the Si 2p level further shifts to higher energies by ~ 0.8 eV. Concomitantly, a similar shift (~ 0.7 eV) is found for the O(Si) component. In addition, a very weak signal around ~530.9 eV is observed upon spectral deconvolution. The latter can, in principle, be attributed to the formation of Cr-O bonds, in agreement with IRAS results.⁴³ The formation of Cr-O-Si bonds can also well explain the shift of oxygen and silica signal towards higher binding energies.

To examine whether Cr migrates to the silica/Ru interface in our conditions, XP spectra were additionally measured at various electron emission angles (between 25 and 90° with respect to the surface plane). Due to the intentionally low amounts of chromium deposited and because of the strong overlap of the most intense Cr 2p signals and the Ru 3s core level, the binding energies of chromium could not precisely be determined. The deconvolution of the spectra (Figure 3a) shows, however, that there are, at least, two Cr components (Cr_A and Cr_B). This would be consistent with the presence of “naked” Cr and Cr=O species observed by titration with CO. The peak area ratios between the Cr 2p and Si 2p signals are plotted in Figure

3b as a function of the detection angle. The almost constant value of the peak area ratio suggests that most of the chromium species are located at the surface. Indeed, it is difficult to imagine that CO will penetrate through a silicate film at low temperature used (85K) and adsorb on chromium species underneath, if such exist. Therefore, we may conclude that the shift of both O 1s signals and Si 2p signals upon Cr deposition reflects the bonding of Cr at the silica surface, which, in turn, modified the chemical environment of the atoms involved.

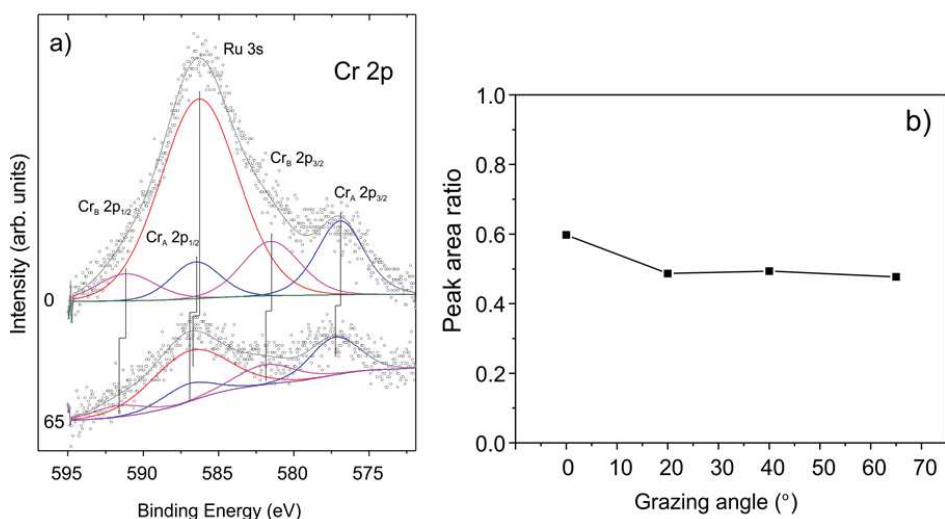


Figure 3. (a) The deconvoluted Cr 2p signals in XP spectra and (b) the peak area ratios of Cr 2p and Si 2p signals measured as a function of electron emissions.

In summary, the XPS data presented in this paper nicely corroborate our previous results on the structure of the Phillips catalyst model system studied by IRAS and TPD. Further investigations, in particular with high resolution STM, are in progress to ultimately determine the atomic structure of the model catalysts.

b) The Oxide-Nanoparticle Interface

In order to design a model catalyst system that allows us to experimentally study the issues addressed above, a number of pre-requisites have to be fulfilled. Firstly, and foremost, the system has to represent oxide supported metal nano-particles as they are found in disperse metal catalysts.⁵⁶ A model is schematically shown in Fig. 5.

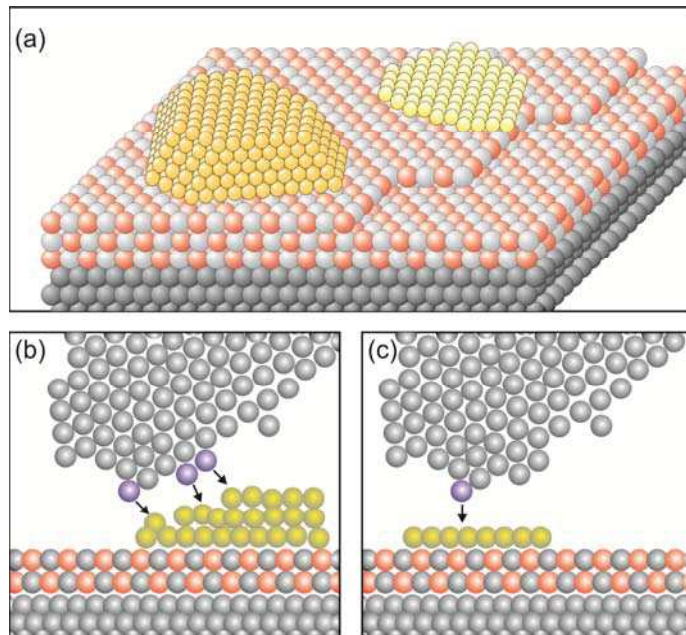


Figure 5. Schematic atomistic diagrams of two typical model catalyst systems (yellow: metal clusters, light grey and red: oxide film, gray: metal support. (a) Two nano-particles with different morphologies (left: 3-dimensional cluster, right: 2-dimensional raft) supported on a thin oxide film, (b) scanning tunneling microscope (STM) tip (grey atoms) approaching from above the rim of the nano-particle. The three atoms in blue at the front end and the side of the tip are responsible for the tunnel current. The black arrows indicate the tip surface interactions. Consequently, an atomically resolved topographic image of the 3D-cluster rim is difficult to obtain. (c) In contrast, the tunneling process to a well-defined 2D flat cluster is determined predominantly by the “last” atom of the tip (blue) which is closest to the flat surface. This situation allows us to obtain atomically resolved images of the whole cluster, and specifically of the cluster rim on a metal supported thin oxide film system. Reprinted with permission from ref. ⁵⁶)

Two nano-particles are placed on a thin, epitaxially grown oxide film on a metal support.⁴ The particles have different morphologies, i.e., one is a three-dimensional (3D) nano-particle, the other one assumes a two-dimensional (2D) raft morphology. Depending on the materials combination, electrons may tunnel from the metal support underneath the insulating oxide film to the nano-particle supported on top of it. This process is governed by the energy it takes to remove an electron from the interface between the metal support and the thin oxide film (ionization potential of the interface), as well as by the energy released by placing one (or several) electron(s) onto the metal nano-particle on top of the oxide film (electron affinity of the metal nano-particle).^{57,58} The idea is that scanning tunneling microscopy and spectroscopy (STM, STS) should be well suited to detect this process. In particular, inelastic electron

tunneling spectroscopy (IETS) would then – under specific conditions - provide evidence for the number of electrons involved in the transfer process. Furthermore, due to the ability to spatially resolve the local electron density we should be in a position to locate also where the electrons reside on the particle. Here the morphology of the nano-particle plays an important role. Consider the morphology of the nano-particle with respect to the size of the tunneling tip as schematically indicated in Fig. 1. It is obvious that a 3D particle may not be imaged in its entirety at atomic resolution. STM can in principle reveal only the exact arrangement of all atoms in a nano-particle if it is planar. For 3D nano-particles only the positions of the surface atoms can be mapped whereas the atomic arrangement on the lateral facets is in most cases difficult to obtain.

Only very recently Calaza et al.⁵⁹ were able to record and image CO₂ reactivity at the rim of two-dimensional Au rafts on MgO(100). As depicted in Fig. 6, in this study advantage was taken of two important factors: On the one hand we exploit the morphology (flat raft) of the pristine nano-particle (Fig. 13 (a)), which allows us to access the perimeter in detail, and on the other hand we make use of the pronounced electron transfer towards the Au atoms residing at the perimeter, which may be used to induce chemical reactions.⁶⁰⁻⁶³ In the present case CO₂ has been used as a reactant. Figure 6 (b) shows the Au-nano-particle decorated with CO₂ at its perimeter, while the differential conductance spectroscopic image shown in Fig. 6 (c) clearly reveals the increased electron density at the nano-particle rim (ref 58). CO₂ is a thermodynamically very stable molecule if no electrons are present. In the presence of electrons CO₂ is activated by electron transfer. The energy cost to transfer an electron to CO₂ is about 0.6 eV, but if one deals with a CO₂ aggregate of at least two molecules the electron transfer becomes energetically favorable. For a dimer, in particular, the gain is 0.9 eV as determined by molecular beam experiments in the gas phase.⁶⁴⁻⁶⁶

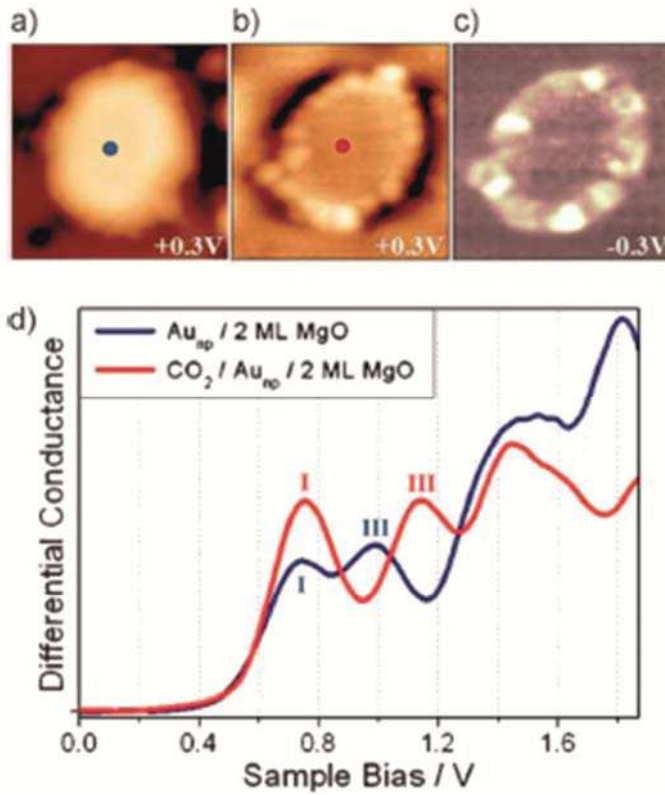


Figure 6. (a) STM topographic images of (a) a pristine planar Au cluster and (b) after exposure to CO_2 , (scan size $8.0 \times 8.0 \text{ nm}^2$, 50 pA). The Au clusters were prepared by evaporating Au on MgO mono- or bilayer films at 300 K . Subsequently the sample was exposed to $10 - 15 \text{ L } \text{CO}_2$ in a temperature range from 220 to 250 K . Molecules at the cluster perimeter in (b) become visible only when scanning at bias voltages between -0.5 and $+0.5 \text{ V}$. (c) Corresponding dI/dV map, displaying the high localization of electron density at the negatively charged cluster rim. (d) dI/dV spectra taken at the center of the clusters shown in (a) (blue) and (b) (red). The positions of the first (I) and third (III) quantum well state in both spectra are indicated. Note the energy shift towards higher energy of the internal energy scale of the cluster which is compatible with a CO_2 induced decrease of the electron potential well formed by the Au island. From Ref. ⁵⁹

Since the reaction of a CO_2 dimer to an oxalate ($\text{C}_2\text{O}_4^{2-}$) molecule has been observed on metal surfaces, which had been electron enriched by alkali adsorption⁶⁷, it is not surprising that the electron-rich supported Au nano-particles induce the formation of oxalate molecules at its perimeter where the extra electrons are localized. According to the STM studies the reaction is confined to the rim of the particles and the nature of the created species is confirmed by ensemble averaging infrared reflection absorption spectroscopy (IRAS), including isotopic labeling studies. When one investigates the distribution of oxalate molecules along the perimeter one finds inhomogeneities, that may be connected to the above mentioned

inhomogeneous distribution of extra electrons along the perimeter. To look deeper into this problem we will perform IETS measurements, which will allow us to investigate the exact nature of individual molecular species and its formation. Here we present XPS and Auger data to evaluate the charge on the particles and point out the importance to separate initial and final state effects. To address this issue empirically, Wagner established the Auger parameter (α)⁶⁸, which consists of the difference between the kinetic energies (KEs) of XPS and Auger peaks from the same atom in a given material.⁶⁹

The change noted in this value ($\Delta\alpha$) when comparing the same spectra for a given atom in different environments has been shown to relate to changes exclusively in the final state of core-level photoemission processes via the following equation:

$$\Delta\alpha = \Delta(BE_{XPS} + KE_{Auger}) = 2\Delta R, \quad (\text{Eq. 1})$$

where R is defined as the relaxation contribution to the final state of a core-level BE.

A central assumption of this general approach is that ΔBE ($-\Delta\varepsilon_n - \Delta R_n$) will be equal for all electrons, regardless of orbital n . This, however, is empirically false⁷⁰, especially when comparing changes in valence and deeper core levels⁷¹, which many continue to do by incorporating easily accessed core-valence-valence Auger measurements into their α experiments. To circumvent this problem associated with the original definition put forth by Wagner, a modified Auger parameter (β) was created⁷² in which the following (more specific) relationship was proposed:

$$\Delta\beta = \Delta[2E_B(i) - E_B(j) + E_{Kin}(jii)] = 2\Delta R_i. \quad (\text{Eq. 2})$$

In this case β represents a combination of three experimentally measured values that are chosen in a way that no longer requires the assumptions of equality for all orbital energy differences $\Delta\varepsilon$ and relaxation energy differences ΔR .⁷³ If, for practical reasons, $E_B(j)$ is not accessible in experiment, a modified version of Eq. 2 can be used:

$$\Delta\beta = \Delta[E_B(i) + E_{Kin}(jii)] = 2\Delta R_i. \quad (\text{Eq. 3})$$

Since $\Delta R_i = 1/2\Delta\beta$ and $\Delta E_B = -\Delta\varepsilon_i - \Delta R_i$, the initial-state orbital energy shift $\Delta\varepsilon_i$ can straightforwardly be calculated. The initial- and final-state contributions to the core-level XPS BE shift are then obtained by $\Delta E_{B,\text{initial}} = -\Delta\varepsilon_i$ and $\Delta E_{B,\text{final}} = -\Delta R_i$, since, by convention, $\Delta\varepsilon$ and ΔR refer to orbital energies and $\text{BE}(i) = -\varepsilon(i)$. For the present discussion of Au nanoparticles on MgO thin film substrates a negative $\Delta E_{B,\text{final}}$, when referenced to atoms in a bulk-like environment, is then indicative of the presence of negatively charged species, and vice versa.

The XPS (Au4f) and Auger spectra (AuM₅N₆₇N₆₇) of a clean Au(111) single crystal are shown in Fig. 7 and serve as bulk reference for $\Delta\beta$ determination in the present study. Spectral fitting gives a BE of 84.0 eV for the Au 4f_{7/2} component, as expected. The M₅N₆₇N₆₇ Auger transition consists of three microstates, of which the most intense (¹I₆, two holes in the 4f, $l=+3$ orbital) at 2015.5 eV KE was used for analysis.

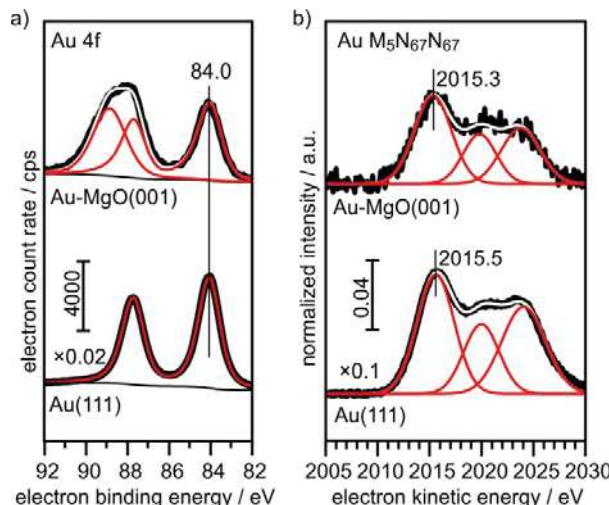


Figure 7. XPS und x-ray excited Auger reference spectra of Au(111) and 0.4 ML Au on 30 ML MgO(001)/(Ag(001)).

For comparison, we show in Fig. 7 the spectra obtained from large, 3-dimensional Au nanoparticles supported on a thick (30 ML) MgO(001) film grown on Ag(001), which have been prepared by deposition of 0.4 MLE Au at room temperature and subsequent annealing at 573 K. The second component in the Au4f spectra of Au on MgO(001) is due to Mg2s ionization. There is basically no observable shift between the pure metal substrate and the nano-particulate system in the XPS and Auger spectra, confirming that most of the atoms in the large Au nano-

particles are in a bulk-like environment. These spectra need to be compared with those from 0.02 monolayers of Au on a three layer MgO film and on a thirty layer MgO film, taken directly after deposition at 100 K and after annealing at 300 K and 573 K, respectively (Fig. 8). Due to the low Au concentration the spectra are considerably noisier, but they may be clearly fitted by the equivalent components used to fit the spectra in Fig. 7. Note, that the spectra obtained directly after deposition at 100K can only be fitted by inclusion of two Au species, with one species featuring a considerably higher binding and smaller electron kinetic energy. We will see below that this is compatible with positively charged Au particles even for the ultrathin film.

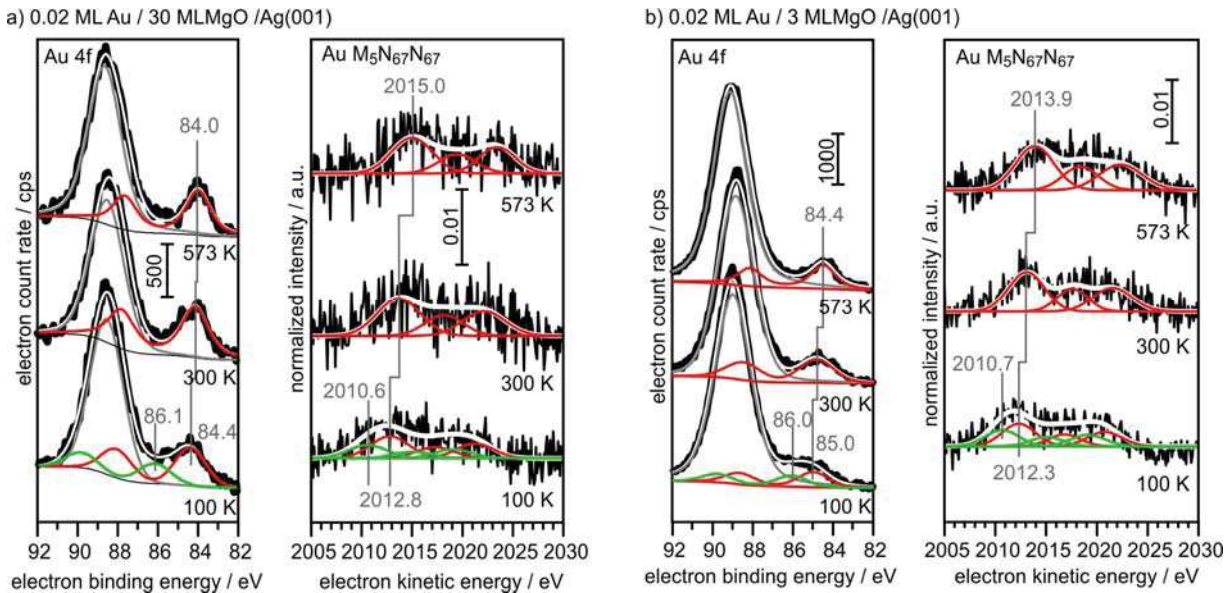


Figure 8. XPS and x-ray excited Auger spectra of 0.02 ML Au/30 ML MgO (a) and 0.02 ML Au/3 ML MgO (b) for different annealing temperatures (bottom: 100 K; middle: 300 K; top: 573 K).

Via combination of XPS binding energy shifts and kinetic energy shifts in Auger spectra we are in a position to calculate the modified Auger parameter, which allows a separation of initial state effects, directly connecting to the charge of the particle, and the final state effects due to the screening of the final hole-state. Table 1 summarizes the XPS and Auger data as well as the initial and final state contributions according to the modified Auger parameter (β). Fig. 9 shows a graphical representation of the various shifts. At 100K, before the system has been equilibrated, there are positively charged Au species, possibly caused by the deposition process or the nucleation of gold on defect sites, present on both the ultrathin and the thick MgO(001)

films. Their presence is consistent with the results of previous XPS and IRAS studies of Au deposited on MgO(001)/Ag(001) thin films.⁷⁴ After heating to 300K the system equilibrates, the positively charged species have disappeared, and the shifts change considerably. In the following we only discuss the situation after equilibration. In the case of the thick MgO film the initial state shifts of the main component are small and negative, indicating only minor charge transfer across the Au/MgO interface, and the BE shifts observed in XPS are dominated by final-state contributions. The decrease of $\Delta E_{\text{B,final}}$ with increasing annealing temperature, which reflects the enhanced possibility of the Au6s electrons to screen the hole, is consistent with thermally induced particle coarsening.

	T K	Au 4f eV	Au M ₅ N ₆₇ N ₆₇ eV	ΔE_{B} eV	ΔE_{kin} eV	$\Delta E_{\text{B,final}}$ eV	$\Delta E_{\text{B,initial}}$ eV
Au(111)	300	84.0	2015.5				
0.4 ML Au / 30 ML MgO	573	84.0	2015.3	0	-0.2	0.1	-0.1
0.02 ML Au / 3 ML MgO	100	84.39	2012.8	0.39	-2.70	1.155	-0.765
		86.15	2010.6	2.15	-4.90	1.375	0.775
	300	84.14	2013.69	0.14	-1.81	0.835	-0.695
	573	84.0	2015	0	-0.50	0.25	-0.25
0.02 ML Au / 30 ML MgO	100	84.96	2012.32	0.96	-3.18	1.11	-0.15
		86.04	2010.67	2.04	-4.83	1.395	0.645
	300	84.70	2013.1	0.7	-2.40	0.85	-0.15
	573	84.46	2013.9	0.46	-1.60	0.57	-0.11

Table 1. XPS and x-ray excited Auger data and initial-state as well as final-state-contributions to the total-BE-shift via modified Auger-Parameter (β)-analysis.

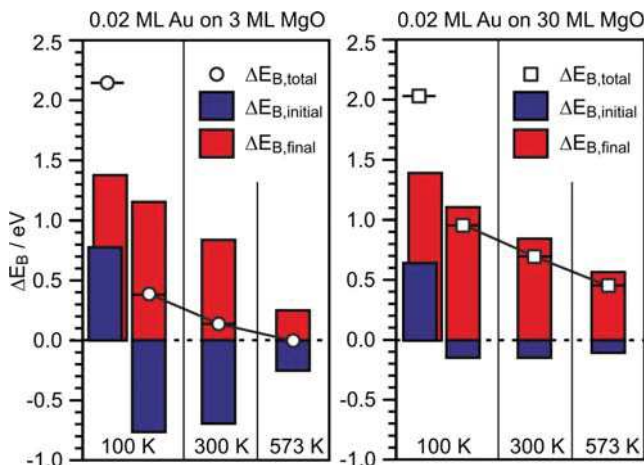


Figure 9. Graphical representation of the E_B -shifts derived from $\Delta\beta$ measurements for 0.02 ML Au on 3 ML MgO(001)/Ag(001) (left) and 0.2 ML Au on 30 ML MgO(001)/Ag(001) (right) with reference to Au(111) from Table 1.

The situation is different for the ultrathin MgO films: Here the initial state shifts are considerably bigger and negative indicating negatively charged Au particles. In particular, we note that, while the final state shifts follow a similar trend for Au on the ultrathin and the thick MgO films, the $\Delta E_{B,\text{initial}}$ contribution remains large after annealing at 300 K and gets considerably reduced only after heating to 573 K. The latter finding is consistent with a strong reduction of the number of negatively charged, interfacial Au atoms and indicates a change of the Au particle morphology. This is corroborated by inspection of the STM images of Au deposited on ultrathin (2 ML) MgO(001) films shown in Fig. 10 where the particle sizes and their distributions are represented for different Au deposition temperatures (Fig. 10a) and 10b)) and sample annealing temperatures (Fig. 10c)-10f)). Some of these images have been published in a previous study,⁷⁵ where we had indicated that in a temperature range around 450 K the particles change from a 2-dimensional to a 3-dimensional morphology. Here, we include results for a larger set of annealing temperature and, in light of the discussion about CO₂ activation noted at the beginning of this chapter, focus in particular on the evaluation of the images with respect to mean particle area and length of the particles perimeter (Fig. 10g) and 10h)).

Fig. 10a) and 10b) (a: 25 nm × 13 nm, b: 100 nm × 50 nm) have been taken directly after deposition at 77 K and 310 K respectively. At 77 K very small islands and individual atoms are observed, and we know from previous studies that this leads to positively charged species.⁷⁴ At

deposition at room temperature larger flat islands are formed. Fig. 10c) to 10f) are images taken after heating to the given temperatures starting from the 77K preparation.

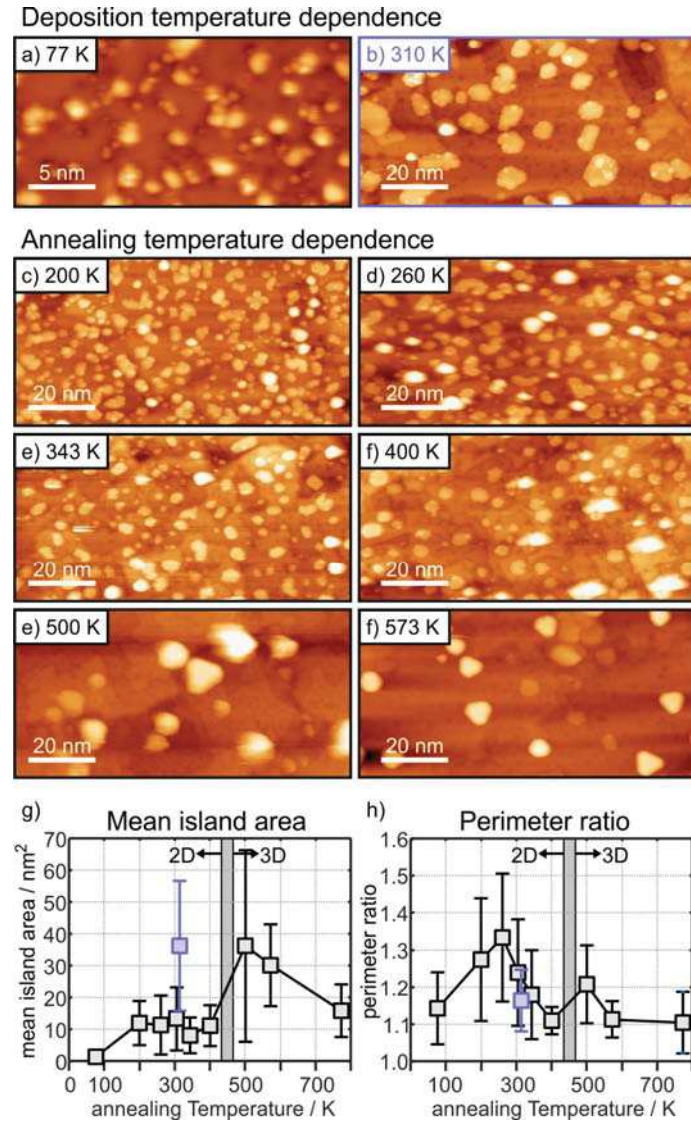


Figure 10. STM images taken at LN₂ temperature of Au islands and nanoparticles on 2 monolayers MgO(001)/Ag(001) formed after deposition at 77K (a), 25 nm × 13 nm, and 310K (b), 100 nm × 50 nm, and after annealing the sample shown in a) at progressively higher temperature, c)-f), 100 nm × 50 nm. Tunneling conditions: $U_{bias} = +(0.5-0.75)$ V, $I_t = 30$ pA. The mean Au island area and perimeter ratio (see text) are plotted as a function of annealing temperature in g) and h). (Note: the large error bar of the data point at 500 K results from the poor image quality due to a bad STM tip).

It is clear from Fig. 10g) that after an initial particle agglomeration between 100 K and 200 K the mean particle area remains rather constant between 200K and 400K, in the temperature range

where 2-dimensional Au particles are stable. After crossing the 2D-to-3D transition, the mean particle area first increases, but decreases again at higher annealing temperature due mainly to approaching a more favorable spherical particle shape. Note that 2-dimensional Au particles prepared by deposition at room temperature have a much larger mean particle area than those obtained by annealing the low-temperature deposits to a similar temperature (compare Fig. 10b) and 10e) and see the blue mark in Fig. 10g)), which hints at different nucleation properties and diffusion barriers at the different deposition and annealing temperatures. Most important for the present discussion is the morphological change of the 2-dimensional particles at annealing temperatures between 200 K and 400 K. While the particles display rather arbitrary shapes below 300 K (Fig. 10c) and 10d)), they exhibit a more regular circular shape, and hence a reduced fraction of perimeter atoms, at higher temperature (Fig. 10e) and 10f)). To put this observation in a more quantitative term we plot in Fig.10h) the perimeter ratio, which is defined as the ratio of the observed perimeter length of an island in relation to the perimeter length of a circular island with the same area, as a function of temperature. It is clear that there is a maximum at 260K. Since between 200K and 400K the island size remains constant one may conclude that the activity might be highest for a sample prepared by annealing to 260 K because the number of perimeter atoms is largest in this case. This conclusion is based on the discussion concerning CO₂ -activation discussed at the beginning of this chapter. This is a prediction that needs to be verified through future experiments.

Summarizing this part we notice that the detailed analysis of the XPS and Auger data corroborates the conclusions based on the analysis of the STM data in previous work, that the Au particles carry a negative charge, which is responsible for the observed reactivity of the rim of the particles towards the formation of oxalate species.

Conclusions

We have discussed two different case studies of oxide supported metal catalysts using a model approach. Here we presented mainly XPS data in order to complement results gained by a number of other techniques used in previous studies on the same systems. Since x-ray

photoelectron spectroscopy is a generally applied technique, it is important to discuss those results in perspective to the available information. The case studies demonstrate that the simplest interpretation just using the observed shifts in binding energy would be misleading and that a more careful analysis based on a more sophisticated analysis allows us to retrieve information that corroborates results derived from a combination of complementary techniques.

Acknowledgement

We thank the German Science Foundation (DFG) through the Cluster of Excellence UniCat and the Fonds der Chemischen Industrie for financial support.

References

1. H.-J. Freund, N. Nilius, T. Risse, S. Schauermann and T. Schmidt, *ChemPhysChem*, 2011, **12**, 79-87.
2. J. Sauer and H.-J. Freund, *Catal. Lett.*, 2015, **145**, 109-125.
3. M. Bäumer and H.-J. Freund, *Prog. Surf. Sci.*, 1999, **61**, 127-198.
4. H.-J. Freund, *J. Am. Chem. Soc.*, 2016, **138**, 8985-8996.
5. C. T. Campbell, *Surf. Sci. Rep.*, 1997, **27**, 1-111.
6. H. J. Freund, *Angew. Chem. Int. Ed.*, 1997, **36**, 452-475.
7. M. Bäumer, J. Libuda and H.-J. Freund, in *Chemisorption and Reactivity on Supported Clusters and Thin Films*, eds. R. M. Lambert and G. Pacchioni, Kluwer Academic Publishers Dordrecht, 1997, vol. 331, pp. 61-104.
8. U. Heiz, F. Vanolli, L. Trento and W. D. Schneider, *Rev. Sci. Instrum.*, 1997, **68**, 1986.
9. U. Diebold, J.-M. Pan and T. E. Madey, *Surf. Sci.*, 1995, **331-333**, 845.
10. R. Persaud and T. E. Madey, in *The Chemical Physics of Solid Surfaces*, eds. D. A. King and D. P. Woodruff, Elsevier, 1997, vol. Volume 8, pp. 407-447.
11. D. W. Goodman, *Surf. Rev. Lett.*, 1995, **2**, 9-24.
12. D. W. Goodman, *Surf. Sci.*, 1994, **299–300**, 837-848.
13. H.-J. Freund, *Phys. Status Solidi b*, 1995, **192**, 407-440.
14. R. M. Jaeger, H. Kuhlenbeck, H. J. Freund, M. Wuttig, W. Hoffmann, R. Franchy and H. Ibach, *Surf. Sci.*, 1991, **259**, 235-252.
15. J. Libuda, F. Winkelmann, M. Bäumer, H.-J. Freund, T. Bertrams, H. Neddermeyer and K. Müller, *Surf. Sci.*, 1994, **318**, 61-73.
16. U. Bardi, A. Atrei and G. Rovida, *Surf. Sci.*, 1992, **268**, 87-97.
17. C. Becker, J. Kandler, H. Raaf, R. Linke, T. Pelster, M. Dräger, M. Tanemura and K. Wandelt, *J. Vac. Sci. Technol. A*, 1998, **16**, 1000-1005.
18. J. G. Chen, J. E. Crowell and J. T. Yates Jr, *Surf. Sci.*, 1987, **185**, 373-393.
19. D. N. Belton and S. J. Schmieg, *Surf. Sci.*, 1988, **199**, 518-536.
20. J. G. Chen, M. L. Colaianni, W. H. Weinberg and J. T. Yates Jr, *Surf. Sci.*, 1992, **279**, 223-232.

21. D. N. Belton and S. J. Schmieg, *Surf. Sci.*, 1988, **202**, 238-254.
22. F. Rochet, S. Rigo, M. Froment, C. d'Anterroches, C. Maillot, H. Roulet and G. Dufour, *Adv. Phys.*, 1986, **35**, 237-274.
23. S. T. Pantelides, ed., *The Physics of SiO₂ and its Interfaces*, in *Proceedings of the International Topical Conference on the Physics of SiO₂ and Its Interfaces Held at the IBM Thomas J. Watson Research Center, Yorktown Heights, New York, March 22-24, 1978*, Pergamon Press, 1978.
24. M. Bäumer, D. Cappus, H. Kuhlenbeck, H. J. Freund, G. Wilhelm, A. Brodde and H. Neddermeyer, *Surf. Sci.*, 1991, **253**, 116.
25. H. Kuhlenbeck, C. Xu, B. Dillmann, M. Haßel, B. Adam, D. Ehrlich, S. Wohlrab, H.-J. Freund, U. A. Ditzinger, H. Neddermeyer, M. Neuber and M. Neumann, *Ber. Bunsenges. Phys. Chem.*, 1992, **96**, 15.
26. F. Rohr, M. Bäumer, H. J. Freund, J. A. Mejias, V. Staemmler, S. Müller, L. Hammer and K. Heinz, *Surf. Sci.*, 1997, **372**, L291-L297.
27. R. Rohr, M. Bäumer, H. J. Freund, J. A. Mejias, V. Staemmler, S. Müller, L. Hammer and K. Heinz, *Surf. Sci.*, 1997, **389**, 391-391.
28. D. W. Goodman, *J. Vac. Sci. Technol. A*, 1996, **14**, 1526.
29. J. P. Hogan, *J. Polym. Sci., Part A: Polym. Chem.*, 1970, **8**, 2637-2652.
30. E. Groppo, C. Lamberti, S. Bordiga, G. Spoto and A. Zecchina, *Chem. Rev.*, 2005, **105**, 115-184.
31. B. M. Weckhuysen, R. A. Schoonheydt, J. M. Jehng, I. E. Wachs, S. J. Cho, R. Ryoo, S. Kijlstra and E. Poels, *J. Chem. Soc., Faraday Trans.*, 1995, **91**, 3245-3253.
32. M. P. McDaniel, in *Adv. Catal.*, eds. C. G. Bruce and K. Helmut, Academic Press, 2010, vol. Volume 53, pp. 123-606.
33. C. Brown, J. Krzystek, R. Achey, A. Lita, R. Fu, R. W. Meulenberg, M. Polinski, N. Peek, Y. Wang, L. J. van de Burgt, S. Profeta, A. E. Stiegman and S. L. Scott, *ACS Catal.*, 2015, **5**, 5574-5583.
34. E. Groppo, C. Lamberti, S. Bordiga, G. Spoto and A. Zecchina, *J. Catal.*, 2006, **240**, 172-181.
35. E. L. Lee and I. E. Wachs, *J. Phys. Chem. C*, 2007, **111**, 14410-14425.
36. M. P. Conley, M. F. Delley, G. Siddiqi, G. Lapadula, S. Norsic, V. Monteil, O. V. Safanova and C. Copéret, *Angew. Chem. Int. Ed.*, 2014, **53**, 1872-1876.
37. M. F. Delley, F. Núñez-Zarur, M. P. Conley, A. Comas-Vives, G. Siddiqi, S. Norsic, V. Monteil, O. V. Safanova and C. Copéret, *Proc. Natl. Acad. Sci. U.S.A.*, 2014, **111**, 11624-11629.
38. P. C. Thüne, J. Loos, A. M. de Jong, P. J. Lemstra and J. W. Niemantsverdriet, *Top. Catal.*, 2000, **13**, 67-74.
39. P. C. Thüne, J. Loos, X. Chen, E. M. E. van Kimmenade, B. Kong and J. W. Niemantsverdriet, *Top. Catal.*, 2007, **46**, 239-245.
40. B. Yang, W. E. Kaden, X. Yu, J. A. Boscoboinik, Y. Martynova, L. Lichtenstein, M. Heyde, M. Sterrer, R. Włodarczyk, M. Sierka, J. Sauer, S. Shaikhutdinov and H.-J. Freund, *Phys. Chem. Chem. Phys.*, 2012, **14**, 11344-11351.
41. S. Shaikhutdinov and H.-J. Freund, *J. Phys.: Condens. Matter*, 2015, **27**, 443001.
42. C. Büchner, L. Lichtenstein, X. Yu, J. A. Boscoboinik, B. Yang, W. E. Kaden, M. Heyde, S. K. Shaikhutdinov, R. Włodarczyk, M. Sierka, J. Sauer and H.-J. Freund, *Chem. Eur. J.*, 2014, **20**, 9176-9183.
43. Q. Pan, L. Li, S. Shaikhutdinov and H.-J. Freund, *J. Catal.*, 2017, accepted.
44. L. Lichtenstein, C. Büchner, B. Yang, S. Shaikhutdinov, M. Heyde, M. Sierka, R. Włodarczyk, J. Sauer and H.-J. Freund, *Angew. Chem. Int. Ed.*, 2012, **51**, 404-407.
45. L. Lichtenstein, M. Heyde and H.-J. Freund, *J. Phys. Chem. C*, 2012, **116**, 20426-20432.
46. X. Yu, E. Emmez, Q. Pan, B. Yang, S. Pomp, W. E. Kaden, M. Sterrer, S. Shaikhutdinov, H.-J. Freund, I. Goikoetxea, R. Włodarczyk and J. Sauer, *Phys. Chem. Chem. Phys.*, 2016, **18**, 3755-3764.

47. P. Larkin, in *Infrared and Raman Spectroscopy*, Elsevier, Oxford, 2011, DOI: <https://doi.org/10.1016/B978-0-12-386984-5.10004-7>, pp. 55-62.
48. I. Lee and F. Zaera, *J. Phys. Chem. B*, 2005, **109**, 2745-2753.
49. M. F. Delley, G. Lapadula, F. Núñez-Zarur, A. Comas-Vives, V. Kalendra, G. Jeschke, D. Baabe, M. D. Walter, A. J. Rossini, A. Lesage, L. Emsley, O. Maury and C. Copéret, *J. Am. Chem. Soc.*, 2017, **139**, 8855-8867.
50. A. Fong, Y. Yuan, S. L. Ivry, S. L. Scott and B. Peters, *ACS Catal.*, 2015, **5**, 3360-3374.
51. R. Włodarczyk, M. Sierka, J. Sauer, D. Löffler, J. J. Uhlrich, X. Yu, B. Yang, I. M. N. Groot, S. Shaikhutdinov and H.-J. Freund, *Phys. Rev. B*, 2012, **85**, 085403.
52. M. Wang, J.-Q. Zhong, J. Kestell, I. Waluyo, D. J. Stacchiola, J. A. Boscoboinik and D. Lu, *Top. Catal.*, 2017, **60**, 481-491.
53. D. Löffler, J. J. Uhlrich, M. Baron, B. Yang, X. Yu, L. Lichtenstein, L. Heinke, C. Büchner, M. Heyde, S. Shaikhutdinov, H.-J. Freund, R. Włodarczyk, M. Sierka and J. Sauer, *Phys. Rev. Lett.*, 2010, **105**, 146104.
54. W. E. Kaden, S. Pomp, M. Sterrer and H.-J. Freund, *Top. Catal.*, 2016, DOI **10.1007/s11244-016-0715-7**.
55. C. Büchner, L. Lichtenstein, S. Stuckenholz, M. Heyde, F. Ringleb, M. Sterrer, W. E. Kaden, L. Giordano, G. Pacchioni and H.-J. Freund, *J. Phys. Chem. C*, 2014, **118**, 20959-20969.
56. H.-J. Freund, W.-D. Schneider and M. Heyde, *Chem. Eur. J.*, 2017, accepted.
57. D. Ricci, A. Bongiorno, G. Pacchioni and U. Landman, *Phys. Rev. Lett.*, 2006, **97**, 036106.
58. M. Sterrer, T. Risze, M. Heyde, H.-P. Rust and H.-J. Freund, *Phys. Rev. Lett.*, 2007, **98**, 206103.
59. F. Calaza, C. Stiehler, Y. Fujimori, M. Sterrer, S. Beeg, M. Ruiz-Oses, N. Nilius, M. Heyde, T. Parviaainen, K. Honkala, H. Häkkinen and H.-J. Freund, *Angew. Chem. Int. Ed.*, 2015, **54**, 12484-12487.
60. C. Stiehler, F. Calaza, W.-D. Schneider, N. Nilius and H.-J. Freund, *Phys. Rev. Lett.*, 2015, **115**, 036804.
61. X. Lin, N. Nilius, M. Sterrer, P. Koskinen, H. Häkkinen and H.-J. Freund, *Phys. Rev. B*, 2010, **81**, 153406.
62. X. Lin, N. Nilius, H. J. Freund, M. Walter, P. Frondelius, K. Honkala and H. Häkkinen, *Phys. Rev. Lett.*, 2009, **102**, 206801.
63. C. Stiehler, Y. Pan, W.-D. Schneider, P. Koskinen, H. Häkkinen, N. Nilius and H.-J. Freund, *Phys. Rev. B*, 2013, **88**, 115415.
64. A. Stamatovic, K. Stephan and T. D. Märk, *Int. J. Mass Spectrom. Ion Processes*, 1985, **63**, 37-47.
65. E. L. Quitevis and D. R. Herschbach, *J. Phys. Chem.*, 1989, **93**, 1136-1139.
66. R. N. Compton, P. W. Reinhardt and C. D. Cooper, *J. Chem. Phys.*, 1975, **63**, 3821-3827.
67. F. M. Hoffmann, M. D. Weisel and J. A. K. Paul, in *Carbon Dioxide Chemistry*, Woodhead Publishing, 1994, DOI: <https://doi.org/10.1016/B978-1-85573-799-0.50011-X>, pp. 55-63.
68. C. D. Wagner, *Faraday Disc. Chem. Soc.*, 1975, **60**, 291-300.
69. C. D. Wagner and A. Joshi, *J. Electron Spectrosc. Relat. Phenom.*, 1988, **47**, 283-313.
70. R. N. Sodhi and R. G. Cavell, *J. Electron Spectrosc. Relat. Phenom.*, 1983, **32**, 283-312.
71. P. S. Bagus, A. Wieckowski and H. Freund, *Chem. Phys. Lett.*, 2006, **420**, 42-46.
72. G. Hohlneicher, H. Pulm and H.-J. Freund, *J. Electron Spectrosc. Relat. Phenom.*, 1985, **37**, 209-224.
73. W. E. Kaden, C. Büchner, L. Lichtenstein, S. Stuckenholz, F. Ringleb, M. Heyde, M. Sterrer, H.-J. Freund, L. Giordano, G. Pacchioni, C. J. Nelin and P. S. Bagus, *Phys. Rev. B*, 2014, **89**, 115436.
74. M. A. Brown, F. Ringleb, Y. Fujimori, M. Sterrer, H.-J. Freund, G. Preda and G. Pacchioni, *J. Phys. Chem. C*, 2011, **115**, 10114-10124.

75. C. P. O'Brien, K. H. Dostert, M. Hollerer, C. Stiehler, F. Calaza, S. Schauermann, S. Shaikhutdinov, M. Sterrer and H. J. Freund, *Faraday Discuss.*, 2016, **188**, 309-321.

Scanning Tunneling Microscopy of the Ordered Water Monolayer on MgO(001)/Ag(001) Ultrathin Films

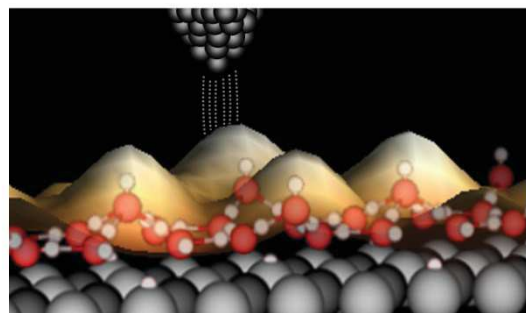
Michael Hollerer,¹ David Prochinig,¹ Peter Puschnig,¹ Esther Carrasco,² Hans-Joachim Freund,³ Martin Sterrer^{1,*}

¹University of Graz, Institute of Physics, NAWI Graz, Universitätsplatz 5, 8010 Graz, Austria

² IMDEA Nanoscience, Ciudad Universitaria de Cantoblanco, 28049 Madrid, Spain

³ Fritz Haber Institut der Max-Planck-Gesellschaft, Faradayweg 4-6, 14195 Berlin, Germany

* Corresponding author: E-mail martin.sterrer@uni-graz.at



Abstract

The two-dimensionally ordered monolayers of water on MgO(001) have been extensively studied in the past using diffraction, spectroscopic and computational methods, but direct microscopic imaging of the structures is still missing. Here, we present a scanning tunneling microscopy (STM) study, supported by infrared and X-ray photoelectron spectroscopy, of the c(4×2)-10H₂O and p(3×2)-6H₂O structures prepared on ultrathin MgO(001)/Ag(001) films. With the tunneling conditions applied, the contrast in the STM images originates from the hydroxyl groups resulting from water dissociation within the monolayer. The observed periodicities perfectly match the structures for the energetically most favorable c(4×2) and p(3×2) monolayer phases obtained from density functional calculations. Although the molecular water species within the monolayers, which are essential for the stabilization of the hydroxyl groups, could not be resolved, the STM results presented in this study provide further confirmation of the predicted structural models of the c(4×2)-10H₂O and p(3×2)-6H₂O monolayers.

1 Introduction

The understanding of water interaction with oxide surfaces has strongly progressed over the last years. This is partly driven by the enormous importance of water-oxide systems in a number of technologically important processes, but also because of the fundamental interest in the general principles that govern the adsorption mode and structures of water at interfaces.¹ For water on oxides both, the nature of adsorption (molecular or dissociative) and the possibility to arrange, via hydrogen bond interaction, in two-dimensionally ordered superstructures, depend on the chemical properties of the oxides (acid-base properties), the lattice parameter, and the surface orientation and termination.²⁻⁴ Because of the inherent complexity of the systems, it is generally not straightforward to predict how water structures evolve on a given oxide surface. Nevertheless, with the help of computational modeling and sophisticated surface science experimental investigations, detailed insight into the properties of water at selected oxide surfaces could be gained. These studies revealed, e.g., the adsorption and dissociation of single water molecules,^{5,6} dimerization and the formation of water clusters and agglomerates,^{7,8} and the structures of 1- and 2-dimensional superstructures.⁹⁻¹²

Water adsorption on the oxides of the alkaline earth metals (MgO, CaO, SrO) represents a particularly interesting case. They have the same crystal structure and differ only in terms of lattice constant and basicity. Hence, the influence of the latter parameters on the dissociation probability of water and the ability to form long-range ordered superstructures can be studied systematically. It is well established that a single water molecule adsorbs intact on the MgO(001) surface, whereas dissociation occurs on both CaO(001) and SrO(001) because of their higher basicity. An interesting trend is seen when the water coverage is increased. Computational studies have shown that 2-dimensional ordered superstructures are most stable on MgO(001), while 1-dimensional chain structures prevail on CaO(001), and isolated and dissociated monomer and dimer species represent the energetically most stable state of water on SrO(001).¹³ This trend can be well explained by the differences in the interaction strength between water and the oxides, and the ability to establish intermolecular hydrogen bonding. Recent scanning tunneling microscopy (STM) studies have confirmed the presence of 1-dimensional chain structures of water on CaO(001),¹³ and of monomer and dimer species on an SrO(001)-terminated Sr₃Ru₂O₇ surface,⁶ at room temperature. Direct microscopic observation of the 2-dimensional water structures on MgO(001) is, however, still missing. Herein, we report on a first attempt to resolve the 2D ordered monolayer structures formed on MgO(001) by STM.

In Figure 1 we present models of the two most stable water monolayer structures on MgO(001), the high-coverage $c(4\times 2)-10\text{ H}_2\text{O}$ and the low-coverage $p(3\times 2)-6\text{ H}_2\text{O}$. Early experiments with MgO(001) single crystal surfaces using diffraction methods^{12,14} have revealed the symmetries and sizes of the unit cells of these structures and thermal desorption experiments¹⁵ have shown that the water monolayer is stable up to 210 K in UHV. The phase transition between the $c(4\times 2)$ and the less-dense $p(3\times 2)$ phase occurs at around 180 K. The molecular-level details of the arrangement of individual water/hydroxyl

species within these structures could, however, only be obtained with the help of calculations using DFT. While the early structural proposal for the $p(3\times 2)$ - $6\text{H}_2\text{O}$ by Giordano et al.¹⁶ (Figure 1a) is still accepted, many different models of the $c(4\times 2)$ structure have been suggested over the years, but a conclusive structural model of the $c(4\times 2)$ (Figure 1b) has only been obtained after extensive structural search using DFT in combination with infrared spectroscopic experiments.¹⁷ A common feature of the monolayer structures is that they contain both molecularly and dissociatively adsorbed water, i.e. they are mixed water/hydroxyl phases. The dissociation products give rise to two inequivalent hydroxyl groups, the “surface OH” ($\text{O}_{\text{S}}\text{H}$) resulting from the binding of the proton to a lattice oxygen, and the “free OH” (OH_{f}). As shown in Figure 1, the OH_{f} groups are stabilized by hydrogen-bond interaction with the surrounding H_2O molecules. For the $c(4\times 2)$ - $10\text{H}_2\text{O}$ in particular, the stabilized OH_{f} groups strongly protrude out of the monolayer plane consisting of nearly horizontally aligned H_2O molecules.¹⁷

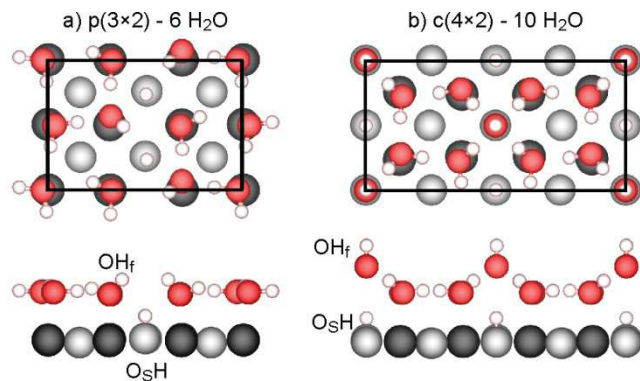


Figure 1. Top and side views of the most stable (3×2) and (4×2) water structure models on $\text{MgO}(001)$. a) $p(3\times 2)$ - $6\text{H}_2\text{O}$; b) $c(4\times 2)$ - $10\text{H}_2\text{O}$. (Mg dark gray; O light grey and red; H white)

Because of the insulating nature of bulk MgO , STM investigations are limited to ultrathin $\text{MgO}(001)$ films grown on a metallic substrate, e.g. $\text{Ag}(001)$ or $\text{Mo}(001)$. The properties and reaction paths of adsorbates on oxide surfaces may, however, be significantly different when the oxide is prepared in the form of a metal-supported ultrathin film compared to bulk.¹⁸ In particular, $\text{MgO}(001)$ ultrathin films have evolved to the prototypical system for studying charge-transfer processes between the metal substrate and adsorbates through a wide band-gap dielectric interlayer.¹⁹ Various adsorbates with moderate to high electron affinity, including Au ,^{20,21} O_2 ,²² NO_2 ,²³ and pentacene,²⁴ have been shown to be negatively charged on metal-supported $\text{MgO}(001)$ ultrathin films. Several experimental studies have also treated water adsorption on ultrathin $\text{MgO}(001)/\text{Ag}(001)$ films from the single-molecule level to hydroxylation at elevated water vapor pressure,²⁵⁻²⁸ and it was generally concluded that water dissociation is enhanced on ultrathin MgO films compared to bulk-like $\text{MgO}(001)$. Shin et al and Cabailh et al. studied water adsorption and dissociation on monolayer and submonolayer $\text{MgO}(001)/\text{Ag}(001)$ films with STM.^{25,28} It was found that intact water molecules adsorb at low temperature (10 K) without any tendency to form ordered

structures on regular MgO(001) terraces. STM tip-induced dissociation results in adsorbed hydroxyl species, which appear in STM with much less contrast than molecular water.^{28,29} On the other hand, water dissociation occurs spontaneously at the borders of submonolayer MgO islands, resulting in their decoration with hydroxyl groups that are easily observed in STM.²⁵ According to DFT calculations, the water monomer adsorption on ultrathin MgO(001) films is not particularly affected by the presence of the Ag(001) support, and dissociation of the water monomer, although energetically more preferred than on bulk MgO(001), is still slightly endothermic.³⁰ The situation changes when water dimers are considered. On 1 ML MgO(001)/Ag(001) the dissociation of one water molecule in the dimer is energetically favorable and the dissociated state is stabilized compared to bulk MgO(001) because of the polaronic distortion of the thin film induced by the charged fragments.³¹ In addition, the calculated adsorption energy of the dissociated dimer is only slightly smaller than that of a full p(3x2) monolayer ($E_{ads} = 0.75$ eV for the dissociated dimer on 1ML MgO(001)/Ag(001)³¹ vs. $E_{ads} = 0.81$ eV for the p(3x2)-6H₂O on 2 ML MgO(001)/Ag(001)³⁰), and hence, the propensity to form long-range ordered water structures might be affected on ultrathin MgO(001) films.

In this work, we study water adsorption on ultrathin MgO(001) films supported on Ag(001) with emphasis on the formation and structure of long-range ordered water monolayer phases, using infrared reflection absorption spectroscopy (IRAS), X-ray photoelectron spectroscopy (XPS) and low-temperature scanning tunneling microscopy (STM). Our IRAS and XPS results confirm that water monolayer phases exhibit the same properties on ultrathin (2 ML) and more bulk-like (12 ML) MgO films and with STM we are able to image both known stable water monolayer phases on MgO(001). STM image simulations using the Tersoff-Hamann approach support our experimental observations.

2 Experimental and computational methods

Experiments were conducted in two separate UHV-setups. The first set-up was mainly used for spectroscopic studies and has in addition to the standard components for sample preparation and characterization a *Bruker IFS 66v* infrared spectrometer for infrared reflection absorption spectroscopy (IRAS) studies and a dual-anode (Mg/Al) X-ray source together with a hemispherical electron analyzer (*SPECS Phoibos 150*) for X-ray photoemission spectroscopy (XPS) experiments attached. Low-temperature scanning tunneling microscopy (STM) experiments were performed in a separate UHV set-up consisting of a preparation chamber and a *Createc* low-temperature STM operated at liquid N₂ or liquid He temperature.

Magnesium oxide (MgO) was epitaxially grown in varying thicknesses on a supporting Ag(001) crystal. The Ag(001) was cleaned by repeated cycles of Ar⁺ sputtering (800 V, ~5 μA) and annealing (773 K) until defined (1x1) spots were observed in low energy electron diffraction (LEED). MgO(001) thin films were grown by evaporation of Mg on Ag(001) at 573 K in an oxygen background pressure of 1×10^{-6} mbar (rate 0.67 ML / min). To obtain wide terraces the sample was slowly cooled to room temperature after film growth.³² Order and cleanliness of the MgO(001)/Ag(001) thin film was checked with LEED and XPS. Water (H₂O

and D₂O) was dosed via a precision valve from a glass vial attached to the UHV chamber and properly degassed before dosing by repeated freeze-pump-thaw cycles. For spectroscopic measurements a multilayer of water was first adsorbed via background-dosing of D₂O at a substrate temperature of 100 K. IR spectra were then collected for the stated annealing temperatures with a resolution of 4 cm⁻¹ by accumulation of 1000 scans. A spectrum obtained after high-temperature annealing of the MgO(001)/Ag(001) sample after the water adsorption experiments was used for background correction. XPS data was obtained with an Al K α X-ray source ($h\nu = 1486.6$ eV, 100 W) at a photoelectron takeoff angle of 60°. To obtain a defined water monolayer for STM measurements the substrate was kept at 155-160 K during water dosing. After water adsorption the sample was quickly transferred to the STM where it was cooled to 5 K.

Density functional calculations were performed for the p(3×2)-6H₂O and c(4×2)-10H₂O structural models shown in Figure 1 a) and b), respectively. Starting from the adsorption geometry reported in Ref. (17) and using the repeated slab approach, we have computed the relaxed geometry for the p(3×2)-6H₂O and c(4×2)-10H₂O structures on 2ML of MgO(001) on Ag(001) where the latter has been modelled by five atomic Ag layers. Utilizing the VASP code,^{33,34} the generalized gradient approximation (GGA)³⁵ is used for exchange-correlation effects and van-der-Waals corrections according to the DFT-D3 method of Grimme have been added.³⁶ Using the projector augmented wave (PAW) method, a plane-wave cutoff of 400 eV is employed, and for k-point sampling, a Monkhorst-Pack grid of 6x9x1 points is used with a first-order Methfessel-Paxton smearing of 0.1 eV for Brillouin zone integrations. The STM simulations are performed within the framework of the Tersoff-Hamann approximation³⁷ by computing the local density of states in an energy window from the Fermi energy to either 2 above or 2 eV below, respectively. Non-contact atomic force microscopy (nc-AFM) images have been simulated by applying the probe-particle model³⁸ and using a CO molecule as probe-particle with an effective charge of -0.05.

3 Results and discussion

3.1 Spectroscopic characterization of ordered water phases on 2 ML MgO(001)/Ag(001)

Spectroscopically, the two ordered monolayer phases of water on MgO(001) can be distinguished based on the different stretching frequencies of the hydroxyl and water species. Figure 2 (bottom) shows the experimental IRA spectrum for the water monolayer prepared on a 12 ML thick, bulk-like MgO(001)/Ag(001) film at 163 K. (Note that the experiments were performed with D₂O instead of H₂O.) The spectrum shows narrow bands in the range 2600-2750 cm⁻¹ and broad absorptions between 2000 cm⁻¹ and 2500 cm⁻¹. The individual spectral contributions can be assigned based on the good agreement between the experimentally observed IR bands and the calculated OD stretching frequencies of the most stable structures shown in Figure 1a and 1b.¹⁷ While the OD_f groups in both structures have similar stretching frequencies at 2720 cm⁻¹, the O_sD groups are slightly different, 2638 cm⁻¹ for c(4x2)-10H₂O and 2595 cm⁻¹ for p(3x2)-6H₂O. Due to the metal surface selection rule, the molecular water species, which are oriented almost parallel to the surface in both structures, give rise to only weak absorption signals. In fact, they do not contribute to the IR

spectrum of the p(3×2) structure. In the case of the c(4×2) structure, combinations of the symmetric and anti-symmetric D₂O stretching vibrations lead to signal contributions in the 2100 – 2450 cm⁻¹ spectral range, which are detected in the experiment as broad bands. The additional absorption at around 2532 cm⁻¹ in the spectrum of D₂O on 12 ML MgO(001)/Ag(001) is not related to the ordered monolayer phases. Its origin will be discussed in the next paragraph when the IRAS results for D₂O on an ultrathin MgO(001)/Ag(001) film are presented.

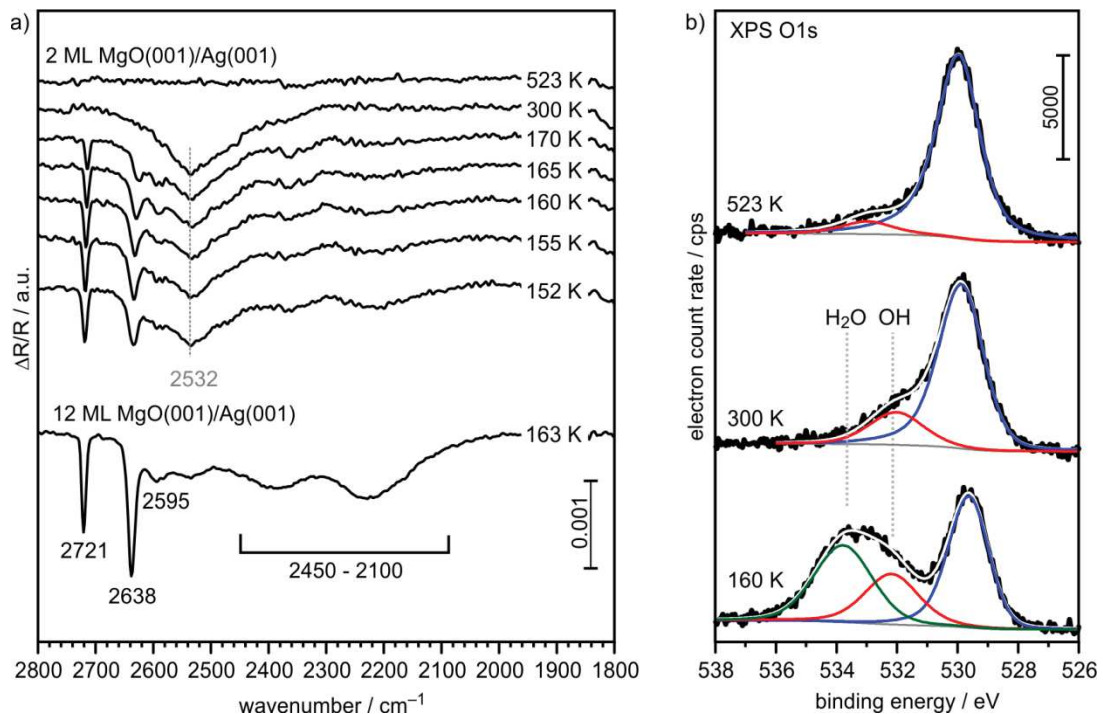


Figure 2. a) IRA spectra of water (D₂O) monolayer on 12 ML MgO(001)/Ag(001) (bottom) and 2 ML MgO(001)/Ag(001) (top). D₂O was dosed at 100 K and spectra were recorded after heating to the temperature indicated in the figure. b) XP spectra (O1s region) of 2 ML MgO(001)/Ag(001) after initial adsorption of D₂O at 100 K and subsequent heating to the indicated temperature.

A series of IRA and XP spectra of 2ML MgO(001)/Ag(001) recorded after initial adsorption of water (D₂O) multilayers at 100 K and subsequent heating to the indicated temperatures in vacuum is shown in Figure 2a(top) and 2b. Since multilayer desorption occurs at 150 K the observed spectral features can be attributed to monolayer water species. The XP spectrum presented in Figure 2b reveals, in addition to the oxide O 1s peak at 529.6 eV binding energy (BE), the presence of a hydroxyl species with 532.4 eV BE and molecular water with 533.9 eV BE, confirming the mixed molecular/dissociated nature of the monolayer phase. The smaller intensities of the OD and D₂O vibrations in the IRA spectrum of the ultrathin film compared to the 12 ML thick film observed experimentally is in agreement with the prediction from DFT.³⁰ The positions of the O_SD and O_Df signals are the same on both substrates, as shown earlier.²⁶

The evolution of the water monolayer-related vibrations with increasing temperature (Figure 2a, 152 K - 170 K) observed in the present study for the ultrathin MgO film follows the same trend as previously reported for a 12 ML thick MgO(001)/Ag(001) film, suggesting the predominance of the c(4×2) phase at lower temperature and a partial transition c(4×2) → p(3×2) at increasing temperature.¹⁷ Because of the smaller intensities of the water monolayer-related vibrations, the previously mentioned broad band at 2532 cm⁻¹ appears more prominent in the spectra of the 2 ML MgO(001)/Ag(001) sample. This band remains present upon heating to 300 K but disappears after annealing at 523 K. The corresponding XP spectrum of the film heated to 300 K shows noticeable intensity of the hydroxyl O 1s species (about 20 % of the full monolayer, Figure 2b). In agreement with previous studies, we attribute these hydroxyl species to water adsorption and dissociation at the non-polar [100] step sites of MgO.^{25,39} Steps are indeed the most abundant defects on the thin film sample and exhibit higher reactivity towards water dissociation than the (100) terrace sites.⁴⁰ The disappearance of the IRAS signal at 2532 cm⁻¹ and the hydroxyl O 1s XPS signal after heating to 523 K nicely agrees with the reported stability of hydroxyl species at steps obtained from DFT calculations.³⁹

3.2 STM of the ordered water phases on 2 ML MgO(001)/Ag(001)

The spectroscopic results presented above confirm that the water monolayer phases exhibit the same properties and structures on an ultrathin MgO(001) film and on bulk-like MgO(001). For the STM investigations presented in the following, we have therefore grown MgO(001) films with a nominal thickness (2 ML) similar to that used in the spectroscopic investigations. An STM image of the clean surface of a MgO(001)/Ag(001) film is shown in Figure 3a. It exhibits flat terraces of up to 70 nm width, sufficiently large to enable the formation of long-range ordered superstructures. For preparation of the water monolayer, we used a slightly different water dosing procedure compared to the spectroscopy measurements. Instead of water multilayer adsorption at 100 K and subsequent heating, we saturated the MgO surface with water directly at a sample temperature of 155 K - 160 K, which is slightly above the multilayer desorption temperature but well below monolayer desorption, and then quickly cooled the sample to liquid Helium temperature inside the STM compartment. By using this procedure and according to the infrared results presented in Figure 2a, we expect to predominantly form the c(4×2) phase under these conditions.

A larger scale STM image of such a preparation is shown in Figure 3b, which presents a water covered MgO(001) terrace separated from neighboring terraces by monolayer (on the left-hand side) and bilayer (on the right-hand side) steps. Since the step edges of the MgO islands run along the non-polar ⟨100⟩ directions, the high-symmetry axes of the substrate can be straightforwardly identified. We note that the island terrace is not flat, but exhibits a distinct periodic corrugation that points to the presence of a superstructure formed by the adsorbed water. In Figure 4a, where a detail of the MgO(001) terrace is shown with enhanced contrast, the superstructure is identified as parallel stripes with a perpendicular separation of about 5.3 Å (see line profile in Figure 4a). In addition, the stripes appear not to be aligned along a high-symmetry axis of the substrate.

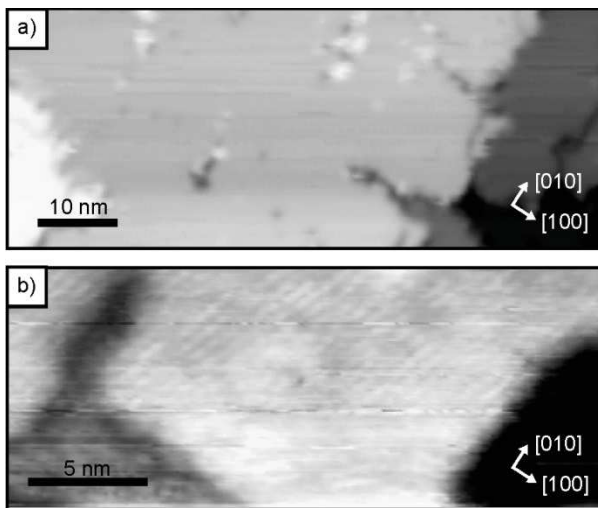


Figure 3. STM images of 2 ML MgO(001)/Ag(001) before (a) and after (b) adsorption of D₂O at 160 K. (a) 75 nm × 30 nm, V_s = + 3.0 V, i_t = 100 pA, (b) 25 nm × 10 nm, V_s = -0.72 V, i_t = 30 pA.

To confirm the substrate orientation and determine the stripe direction exactly, we have obtained from the same preparation an atomically resolved image of the MgO(001) substrate (see inset in Figure 4a). Typically, only one ionic sublattice is resolved, most likely representing the positions of the oxygen ions.⁴¹ From Figure 4a we have extracted the stripe orientation and overlaid it onto the ionic lattice. The stripes are rotated from the [110] direction by 26.5°. Close inspection of Figure 4a reveals that neighboring stripes are separated by 2 lattice constants in [110] direction and 1 lattice constant in [1̄10] direction. Thus, the stripes form a commensurate superstructure with respect to the underlying MgO lattice. The stripe direction can be identified as the [310] substrate direction (Figure 4a). Coming back to the models of the ordered water overlayers shown in Figure 1, we note that the [310] direction is the diagonal of the conventional c(4×2) unit cell and represents the direction of the principle lattice vector of the corresponding primitive rhombic unit cell, which in matrix notation reads $\begin{pmatrix} 2 & -1 \\ 2 & 1 \end{pmatrix}$. To better illustrate this, we present in Figure 4b a model of the c(4×2)-10H₂O phase with the conventional unit cell marked by the rectangle and the corresponding primitive unit cell represented by the gray area. The unit cell vectors of the primitive unit cell have a length of 6.66 Å (assuming a bulk lattice constant of MgO, a = 2.98 Å) and each encloses an angle of 26.57° with the [110] substrate direction. Note that the perpendicular distance between the parallel sides of the rhombus is 5.3 Å, similar to the experimentally observed stripe separation in Figure 4a. Combining all this information provides strong support for the conclusion that the stripe superstructure imaged in Figure 3b represents the ordered c(4×2) water monolayer phase on MgO(001).

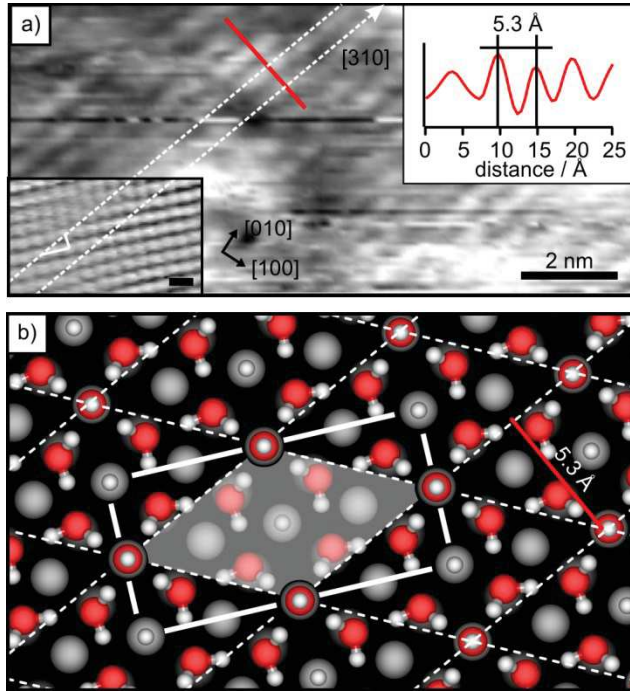


Figure 4. a) Detail ($13 \text{ nm} \times 6 \text{ nm}$) of the STM image shown in Figure 3b. The inset is an atomically resolved image of the MgO(001) surface obtained from the same sample. The stripes in the STM image run along the [310] substrate direction (dashed white lines). Neighboring stripes exhibit a perpendicular separation of 5.3 \AA (see line scan). b) Model of the $c(4 \times 2)$ - $10\text{H}_2\text{O}$ structure with the conventional rectangular $c(4 \times 2)$ unit cell and corresponding primitive rhombic unit cell. (Mg dark gray; O light grey and red; H white)

Attempts to better resolve the $c(4 \times 2)$ phase with STM were often not successful because of the presence of many mobile adsorbates on the surface, which led to unstable tip conditions and streaky or blurred image appearance. An STM image of a water-covered MgO(001) terrace with stripe superstructure, which exhibits some areas where better resolution has been obtained, is shown in Figure 5a. The [310] stripe direction is indicated by an arrow and areas where individual protrusions can be recognized are encircled. In these areas, the protrusions are arranged in a rhombic lattice spanned by the $\langle 310 \rangle$ family of substrate directions. A detail of Figure 5a showing 4 protrusions arranged in rhombic form is presented in Figure 5b. The side length and enclosed angles of the rhombus perfectly fit the dimension and angles of the primitive unit cell of the $c(4 \times 2)$ structure. What remains to be determined is the identity of the protrusions. We note that the primitive unit cell contains 5 water molecules, out of which 4 are molecular water and 1 is dissociated. Since we image only one protrusion per primitive unit cell, we exclude molecular water and assign the protrusions to the OH_f groups of the $c(4 \times 2)$ - $10\text{H}_2\text{O}$ structure, because they are the most obvious protruding element of this structure from a geometrical point of view (Figure 1b). To support this assignment, we compare our experimental STM images with simulated images of the $c(4 \times 2)$ -

$10\text{H}_2\text{O}$ structure, which have been obtained by applying the Tersoff-Hamann approximation (Figure 5c). Because of the absence of molecular states for water and hydroxyl groups at bias voltages around the Fermi level, the contrast in the simulated image is entirely geometric in nature and determined by the protruding OH_f groups, thus confirming our assignment.

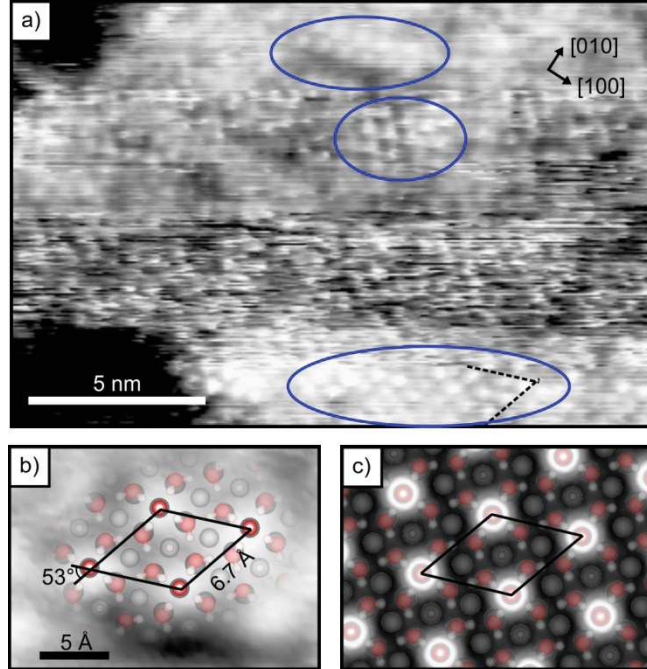


Figure 5. STM image ($18\text{ nm} \times 12\text{ nm}$, $V_s = -1.1\text{ V}$, $i_t = 50\text{ pA}$) of the water monolayer on 2 ML $\text{MgO}(001)/\text{Ag}(001)$. Encircled are regions where protrusions arranged in a rhombic lattice are resolved. The dashed lines represent the $[310]$ substrate directions. b) Detail ($2.2\text{ nm} \times 1.6\text{ nm}$) of a) with overlaid model of the $c(4\times 2)\text{-}10\text{H}_2\text{O}$ structure. c) Simulated STM image ($V_{\text{bias}} = -1\text{ V}$) of the $c(4\times 2)\text{-}10\text{H}_2\text{O}$ structure.

In addition to regions on the surface of the $\text{MgO}(001)/\text{Ag}(001)$ thin film, where the long-range ordered $c(4\times 2)\text{-}10\text{H}_2\text{O}$ phase grows on larger $\text{MgO}(001)$ terraces in a single rotational domain (see Figure 3b), we also found areas, such as the one shown in the STM image of Figure 6a, that appear to exhibit, as judged by the number of protrusions observed, less water coverage and less order. Indeed, the appearance of Figure 6a strongly resembles that of STM images for individual water molecules on MgO thin films reported earlier by Shin et al.²⁸ However, a closer inspection of this image reveals that the protrusions are not randomly spread over the surface area, but arranged in groups that exhibit the general structural motif of the $c(4\times 2)\text{-}10\text{H}_2\text{O}$ phase. To illustrate this point, we have overlaid an ionic sublattice of the $\text{MgO}(001)$ surface onto the STM image and centered one lattice point on one of the protrusions. As shown in Figure 6b, all observed protrusions are perfectly aligned with the ionic sublattice. In addition, nearest neighbor distances and position vectors appear mainly in two groups, the next nearest neighbors in the $\langle 110 \rangle$ directions and the nearest neighbors in the $\langle 310 \rangle$ directions, thus representing the lattice directions and points of the

c(4×2) structure in the two possible rotational domains. We, therefore, assign the protrusions to the protruding OH_f groups of the c(4×2)-10H₂O structure.

In Figure 6b we have connected neighboring protrusions with differently colored lines according to their domain alignment. From this representation it becomes clear that in this particular image area the water molecules and hydroxyl groups are arranged in clusters where short-range order is maintained. Within the clusters, small units of the (4×2) structure, most often not extending to a complete (4×2) unit cell size, are directly linked with small units aligned along the other, 90°-rotated domain.

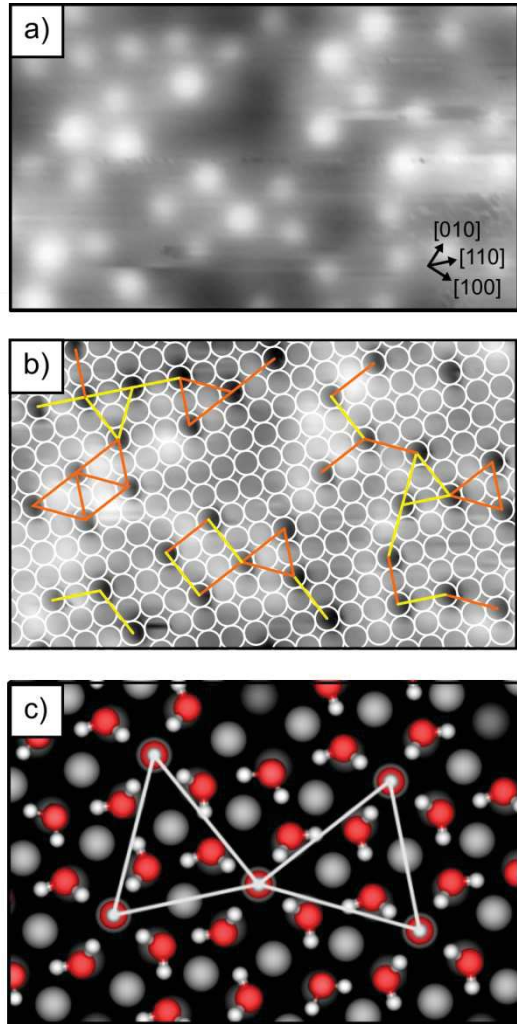


Figure 6. a) STM image ($6.1 \text{ nm} \times 3.7 \text{ nm}$, $V_s = -0.26 \text{ V}$, $i_t = 50 \text{ pA}$) of water on 2 ML MgO(001)/Ag(001). b) Same area as in a) but with inverted image contrast and overlaid ionic sublattice of MgO(001). All protrusions shown in a) are located at the same kind of lattice site. The lines connect nearest neighbor protrusions and the different colors represent the two different rotational domain alignments. c) Model for the cluster formed by two corner-sharing triangular structures (middle-right in b) constructed with the basic structural unit of the c(4×2)-10H₂O structure. (Mg dark gray; O light grey and red; H white)

At this point it is interesting to think about how the water molecules in the overlayer have to rearrange, or if they have to rearrange at all, to form the observed clusters. From previous DFT calculations, which have dealt with the water coverage dependent formation of ordered (3×2) and (4×2) phases on the MgO(001) surface, it is known that protruding OH_f groups also exist in structures with slightly lower coverage than the c(4×2)-10 H₂O, namely p(4×2)-9 H₂O and p(3×2)-7 H₂O.¹⁷ These structures are, however, energetically slightly less favorable than the c(4×2)-10 H₂O phase. Nevertheless, these studies show that the factors that govern the formation and stability of the protruding OH_f are, apart from the molecule-adsorbate interaction, the hydrogen-bond interaction of OH_f with the hydrogen atoms of the four water molecules in the first coordination sphere (see Figure 1b). Hence, it is tempting to construct a molecular model for the structures observed in Figure 6a using this principal structural unit of the c(4×2)-10H₂O. As an example, we show in Figure 6c our model for the two corner-sharing triangular structures, where each triangle represents half of the primitive c(4×2) unit cell in the respective domain. Only one water molecule in the first coordination sphere of the central OH_f group has to be rotated to establish a continuous hydrogen bonding network over the two 90° rotated domains. While other arrangements of water molecules around the OH_f groups are probably conceivable, this simple analysis demonstrates that, if at all, only very minor geometrical rearrangements compared to the original c(4×2) structural motif are necessary to be able to construct molecular models of the short-range ordered water/hydroxyl clusters present on the surface. The energetic cost for the necessary rearrangements are expected to be minute, which explains why the structures are stable and do not relax into the energetically more unfavorable lower coverage structures at the temperature of the experiment.

According to the IRAS data presented in Figure 2a and considering the experimental conditions for water monolayer preparation (160 K adsorption temperature), we may, however, also find the lower coverage p(3×2)-6H₂O phase. In comparison with the c(4×2)-10H₂O, the p(3×2)-6H₂O structure is much less corrugated and the two OH_f groups in the unit cell protrude only slightly out of the otherwise flat water layer (Figure 1a). Identification of the p(3×2)-6H₂O structure by STM is hence likely to be more difficult. In Figure 7a we show a detail of an STM image, where protrusions do not form a rhombic lattice but instead are arranged in zig-zag lines along the ⟨110⟩ direction with neighboring protrusions connected along ⟨100⟩. Overlaying a grid representing an ionic sublattice of the MgO(001) surface reveals that the protrusions are indeed separated by only nearest neighbor distances in ⟨100⟩ directions (Figure 7b), which corresponds to the arrangement of the OH_f groups in the p(3×2)-6H₂O unit cell. We note that a theoretically proposed p(3×2) structure with 8 water molecules per unit cell, with two dissociated molecules and OH_f groups that protrude out of the water layer similar as in the c(4×2)-10H₂O structure, would give rise to a similar zig-zag appearance.¹⁷ However, this structure is energetically very unfavorable. Therefore, we attribute the features in Figure 7a to the small water clusters that contain the basic structural motif of the p(3×2)-6H₂O (Figure 7c). Again, our interpretation is supported by

comparison of the experimental image with the simulated STM image in Figure 7d, where the slightly upward tilted OH_f groups give rise to the contrast. Note that in the STM image simulations the distinct OH_f contrast is only obtained for empty state images (see also Figure 8b), whereas in filled state images also molecular water is visible.

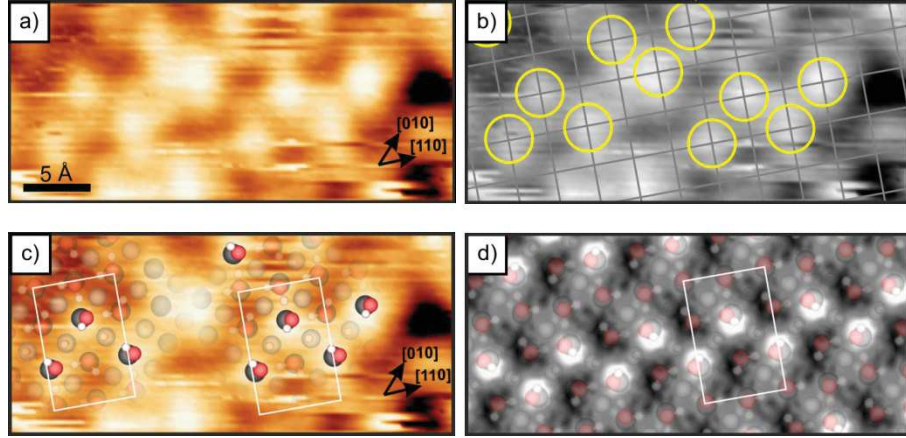


Figure 7. a) STM image ($3.3 \text{ nm} \times 1.5 \text{ nm}$, $V_s = -0.53 \text{ V}$, $i_t = 50 \text{ pA}$) of water on 2 ML MgO(001)/Ag(001). As shown in b), the protrusions are arranged in zig-zag lines with a nearest neighbor separation of one lattice constant in [100] directions. (The grid represents a sublattice of the MgO(001) substrate.) c) Same STM image as in a) with overlaid model of the p(3×2)-6H₂O structure. The protrusions observed in the STM image fit to the expected lattice position of the OH_f groups. d) Simulated STM image ($V_{\text{bias}} = +1 \text{ V}$) of the p(3×2)-6H₂O structure.

Our STM results on the structure of the water monolayer on MgO(001) are in agreement with the models of the c(4×2)-10H₂O and p(3×2)-6H₂O previously proposed from DFT calculations. At the tunneling conditions applied in this study the STM image contrast is determined by the protruding OH_f groups, and the observed periodicities are in agreement with those expected for the arrangement of the OH_f groups in the c(4×2)-10H₂O and p(3×2)-6H₂O structures. Further confirmation of the structural models would require a simultaneous, or at least consecutive, imaging of OH_f's and the surrounding molecular water. STM image simulations reveal that the vertically aligned OH_f's determine the image contrast of the c(4×2)-10H₂O structure in a wide range of bias voltages because of geometrical reasons (Figure 8a). In contrast, the neighboring molecular water species in the p(3×2) structure, which form stripes along the [110] directions, are predicted to be more dominant than the OH_f's in filled-state imaging (Figure 8b). This might, however, be due to a slight overestimation of the contribution of the HOMO of molecular water in the GGA calculations. Generally, we expect the image contrast around the Fermi level, because of the absence of molecular states, to be mainly determined by the geometrical factors. Ultimately, non-contact atomic force microscopy (nc-AFM) with CO-functionalized tips could provide the required information on molecular water species within the 2D phases. nc-AFM

has recently been applied to the investigation of water clusters on, e.g., thin NaCl(100) films and Fe₃O₄(001) surfaces.^{8,42} As an outlook for future nc-AFM studies of the water monolayers on MgO(001), we present in Figure 8c and Figure 8d simulated nc-AFM images of the c(4×2)-10H₂O and p(3×2)-6H₂O structures, obtained by applying the probe-particle model.³⁸ For c(4×2)-10H₂O (Figure 8c), these simulations reveal that at large tip-sample distance (Δz) the image contrast is determined by the OH_f groups, similar as in our STM studies. At slightly closer distance a complete contrast reversal occurs, and triangular features representing the water molecules appear, which may even allow the orientation of the water molecules to be determined. Interestingly, the model predicts a different Δz dependence for the p(3×2) structure (Figure 8d). Here, the OH_f's dominate at intermediate Δz , giving rise to a zig-zag appearance similar as in our STM images (Figure 7), whereas at larger distances also a zig-zag line appears, which, however, originates from the molecular water species. At closer approach the model predicts for both structures the observation of sharp lines and, finally, again a contrast inversion, which can be explained by Pauli repulsion and lateral relaxation of the probe particle.

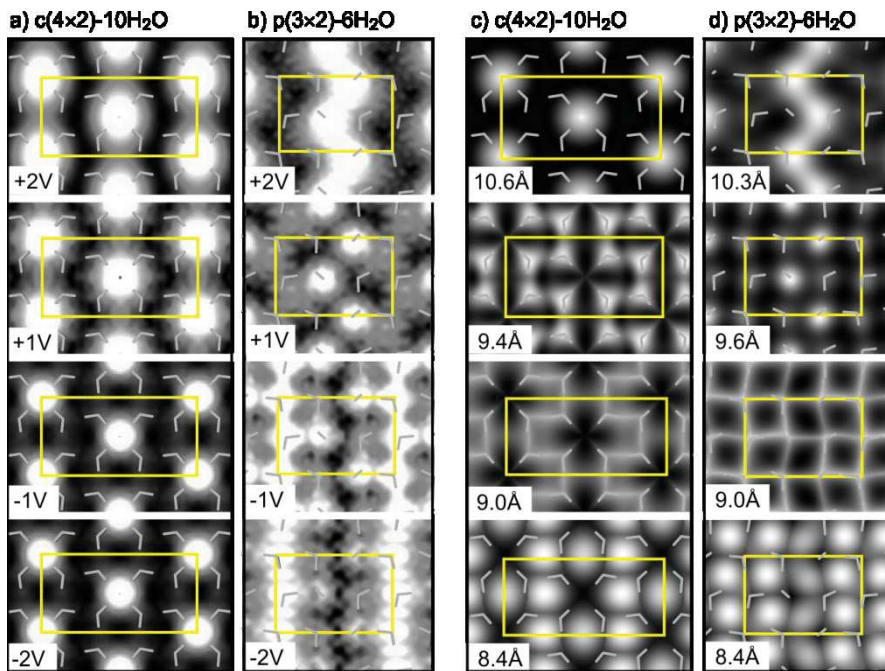


Figure 8. Simulated STM and nc-AFM images of the c(4×2)-10H₂O (a,c) and p(3×2)-6H₂O (b,d) structures. The images have been generated for the bias voltages (STM) and tip-sample distances Δz (nc-AFM) indicated in the figure. Δz is the distance between the surface MgO plane and the oxygen atom of the CO-tip. Yellow rectangles represent the unit cells of the structures and gray lines show the positions of the water molecules and hydroxyls.

Conclusions

In conclusion, our low-temperature scanning tunneling microscopy study of the water monolayers on ultrathin MgO(001)/Ag(001) thin films revealed morphological signatures that are in agreement with the models of the c(4×2)-10H₂O and p(3×2)-6H₂O structures

predicted for bulk MgO(001). The similarity of the monolayers on ultrathin and more bulk-like MgO(001) films was also proven by infrared reflection absorption spectroscopy. Thus, we conclude that the structural properties of the water monolayers are not seriously affected by the MgO film thickness and possible charge transfer through the film.

Our STM images show that the c(4×2)-10H₂O monolayer grows in single-domain orientation on large MgO(001) terraces. However, also metastable water/hydroxyl clusters have been found, which often consist of directly linked, 90°-rotated c(4×2) units. Our morphological characterization provides further proof of the water monolayer structures on MgO(001), in particular regarding the position and arrangement of the OH_f groups within the unit cells. Since nc-AFM image simulations reveal distinct H₂O and OH⁻ contrast for different tip-sample distances, we suggest that additional information about the orientation of the molecular water within the monolayer could in the future be obtained by using nc-AFM with CO-functionalized tips.

Acknowledgment

Financial support from the Austrian Science Fund (FWF) project I3731 is acknowledged. The computational results presented have been achieved using the computing facilities of the University of Graz and the Vienna Scientific Cluster (VSC3).

References

- (1) Bjornehohn, E.; Hansen, M. H.; Hodgson, A.; Liu, L. M.; Limmer, D. T.; Michaelides, A.; Pedevilla, P.; Rossmeisl, J.; Shen, H.; Tocci, G.; Tyrode, E.; Walz, M. M.; Werner, J.; Bluhm, H. "Water at interfaces" *Chem. Rev.* **2016**, *116*, 7698-7726.
- (2) Hu, X. L.; Carrasco, J.; Klimes, J.; Michaelides, A. "Trends in water monomer adsorption and dissociation on flat insulating surfaces" *Phys. Chem. Chem. Phys.* **2011**, *13*, 12447-12453.
- (3) Rao, R. R.; Kolb, M. J.; Hwang, J.; Pedersen, A. F.; Mehta, A.; You, H.; Stoerzinger, K. A.; Feng, Z. X.; Zhou, H.; Bluhm, H.; Giordano, L.; Stephens, I. E. L.; Shao-Horn, Y. "Surface orientation dependent water dissociation on rutile ruthenium dioxide" *J. Phys. Chem. C* **2018**, *122*, 17802-17811.
- (4) Schwarz, M.; Faisal, F.; Mohr, S.; Hohner, C.; Werner, K.; Xu, T.; Skala, T.; Tsud, N.; Prince, K. C.; Matolin, V.; Lykhach, Y.; Libuda, J. "Structure-Dependent Dissociation of Water on Cobalt Oxide" *J. Phys. Chem. Lett.* **2018**, *9*, 2763-2769.
- (5) Brookes, I. M.; Muryn, C. A.; Thornton, G. "Imaging Water Dissociation on TiO₂(110)" *Phys. Rev. Lett.* **2001**, *87*, 266103.
- (6) Halwidl, D.; Stöger, B.; Mayr-Schmöller, W.; Pavlec, J.; Fobes, D.; Peng, J.; Mao, Z. Q.; Parkinson, G. S.; Schmid, M.; Mittendorfer, F.; Redinger, J.; Diebold, U. "Adsorption of water at the SrO surface of ruthenates" *Nat. Mater.* **2016**, *15*, 450-455.
- (7) Merte, L. R.; Bechstein, R.; Peng, G.; Rieboldt, F.; Farberow, C. A.; Zeuthen, H.; Knudsen, J.; Lægsgaard, E.; Wendt, S.; Mavrikakis, M.; Besenbacher, F. "Water clustering on nanostructured iron oxide films" *Nat. Commun.* **2014**, *5*, 4193.
- (8) Meier, M.; Hulva, J.; Jakub, Z.; Pavlec, J.; Setvin, M.; Bliem, R.; Schmid, M.; Diebold, U.; Franchini, C.; Parkinson, G. S. "Water agglomerates on Fe₃O₄(001)" *Proc. Natl. Acad. Sci.* **2018**, *115*, E5642-E5650.

- (9) Mu, R. T.; Zhao, Z. J.; Dohnalek, Z.; Gong, J. L. "Structural motifs of water on metal oxide surfaces" *Chem. Soc. Rev.* **2017**, *46*, 1785-1806.
- (10) Mirabella, F.; Zaki, E.; Ivars-Barcelo, F.; Li, X.; Paier, J.; Sauer, J.; Shaikhutdinov, S.; Freund, H.-J. "Cooperative formation of long-range ordering in water ad-layers on Fe₃O₄(111)" *Angew. Chem. Int. Ed.* **2017**, *57*, 1409-1413
- (11) Meyer, B.; Marx, D.; Dulub, O.; Diebold, U.; Kunat, M.; Langenberg, D.; Woll, C. "Partial dissociation of water leads to stable superstructures on the surface of zinc oxide" *Angew. Chem. Int. Ed.* **2004**, *43*, 6642-6645.
- (12) Heidberg, J.; Redlich, B.; Wetter, D. "Adsorption of water vapor on the MgO(100) single-crystal surface" *Ber. Bunsen-Ges. Phys. Chem. Chem. Phys.* **1995**, *99*, 1333-1337.
- (13) Zhao, X.; Shao, X.; Fujimori, Y.; Bhattacharya, S.; Ghiringhelli, L. M.; Freund, H.-J.; Sterrer, M.; Nilius, N.; Levchenko, S. V. "Formation of water chains on CaO(001): What drives the 1D growth?" *J. Phys. Chem. Lett.* **2015**, *6*, 1204-1208.
- (14) Ferry, D.; Glebov, A.; Senz, V.; Suzanne, J.; Toennies, J. P.; Weiss, H. "Observation of the second ordered phase of water on the MgO(100) surface: Low energy electron diffraction and helium atom scattering studies" *J. Chem. Phys.* **1996**, *105*, 1697-1701.
- (15) Stirniman, M. J.; Huang, C.; Smith, R. S.; Joyce, S. A.; Kay, B. D. "The adsorption and desorption of water on single crystal MgO(100): The role of surface defects" *J. Chem. Phys.* **1996**, *105*, 1295-1298.
- (16) Giordano, L.; Goniakowski, J.; Suzanne, J. "Partial dissociation of water molecules in the (3 x 2) water monolayer deposited on the MgO (100) surface" *Phys. Rev. Lett.* **1998**, *81*, 1271-1273.
- (17) Włodarczyk, R.; Sierka, M.; Kwapien, K.; Sauer, J.; Carrasco, E.; Aumer, A.; Gomes, J. F.; Sterrer, M.; Freund, H.-J. "Structures of the Ordered Water Monolayer on MgO(001)" *J. Phys. Chem. C* **2011**, *115*, 6764-6774.
- (18) *Oxide Ultrathin Films: Science and Technology*; Pacchioni, G.; Valeri, S., Eds.; Wiley-VCH: Weinheim, 2011.
- (19) Pacchioni, G.; Freund, H. "Electron Transfer at Oxide Surfaces. The MgO Paradigm: from Defects to Ultrathin Films" *Chem. Rev.* **2013**, *113*, 4035-4072.
- (20) Pacchioni, G.; Giordano, L.; Baistrocchi, M. "Charging of Metal Atoms on Ultrathin MgO/Mo(100) Films" *Phys. Rev. Lett.* **2005**, *94*, 226104.
- (21) Sterrer, M.; Risse, T.; Pozzoni, U. M.; Giordano, L.; Heyde, M.; Rust, H. P.; Pacchioni, G.; Freund, H.-J. "Control of the Charge State of Metal Atoms on Thin MgO Films" *Phys. Rev. Lett.* **2007**, *98*, 096107.
- (22) Gonchar, A.; Risse, T.; Freund, H. J.; Giordano, L.; Di Valentin, C.; Pacchioni, G. "Activation of Oxygen on MgO: O₂⁻ Radical Ion Formation on Thin, Metal-Supported MgO(001) Films" *Angew. Chem. Int. Ed.* **2011**, *50*, 2635-2638.
- (23) Starr, D. E.; Weis, C.; Yamamoto, S.; Nilsson, A.; Bluhm, H. "NO₂ Adsorption on Ag(100) Supported MgO(100) Thin Films: Controlling the Adsorption State with Film Thickness" *J. Phys. Chem. C* **2009**, *113*, 7355-7363.
- (24) Hollerer, M.; Lüftner, D.; Hurdax, P.; Ules, T.; Soubatch, S.; Tautz, F. S.; Koller, G.; Puschnig, P.; Sterrer, M.; Ramsey, M. G. "Charge Transfer and Orbital Level Alignment at Inorganic/Organic Interfaces: The Role of Dielectric Interlayers" *ACS Nano* **2017**, *11*, 6252-6260.
- (25) Cabailh, G.; Lazzari, R.; Cruguel, H.; Jupille, J.; Savio, L.; Smerieri, M.; Orzelli, A.; Vattuone, L.; Rocca, M. "Stoichiometry-Dependent Chemical Activity of Supported MgO(100) Films" *J. Phys. Chem. A* **2011**, *115*, 7161-7168.

- (26) Carrasco, E.; Brown, M. A.; Sterrer, M.; Freund, H. J.; Kwapien, K.; Sierka, M.; Sauer, J. "Thickness-Dependent Hydroxylation of MgO(001) Thin Films" *J. Phys. Chem. C* **2010**, *114*, 18207-18214.
- (27) Newberg, J. T.; Starr, D. E.; Yamamoto, S.; Kaya, S.; Kendelewicz, T.; Mysak, E. R.; Porsgaard, S.; Salmeron, M. B.; Brown, G. E.; Nisson, A.; Bluhm, H. "Autocatalytic Surface Hydroxylation of MgO(100) Terrace Sites Observed under Ambient Conditions" *J. Phys. Chem. C* **2011**, *115*, 12864-12872.
- (28) Shin, H. J.; Jung, J.; Motobayashi, K.; Yanagisawa, S.; Morikawa, Y.; Kim, Y.; Kawai, M. "State-selective dissociation of a single water molecule on an ultrathin MgO film" *Nat. Mater.* **2010**, *9*, 442-447.
- (29) Wang, Z. T.; Wang, Y. G.; Mu, R.; Yoon, Y. H.; Dahal, A.; Schenter, G. K.; Glezakou, V. A.; Rousseau, R.; Lyubinetsky, I.; Dohnalek, Z. "Probing equilibrium of molecular and deprotonated water on TiO₂(110)" *Proc. Natl. Acad. Sci.* **2017**, *114*, 1801-1805.
- (30) Honkala, K.; Hellman, A.; Gronbeck, H. "Water Dissociation on MgO/Ag(100): Support Induced Stabilization or Electron Pairing?" *J. Phys. Chem. C* **2010**, *114*, 7070-7075.
- (31) Giordano, L.; Ferrari, A. M. "Modified Ion Pair Interaction for Water Dimers on Supported MgO Ultrathin Films" *J. Phys. Chem. C* **2012**, *116*, 20349-20355.
- (32) Pal, J.; Smerieri, M.; Celasco, E.; Savio, L.; Vattuone, L.; Rocca, M. "Morphology of monolayer MgO films on Ag(100): Switching from corrugated islands to extended flat terraces" *Phys. Rev. Lett.* **2014**, *112*, 126102.
- (33) Kresse, G.; Hafner, J. "Ab-initio Molecular Dynamics for Liquid Metals" *Phys. Rev. B* **1993**, *47*, 558-561.
- (34) Kresse, G.; Joubert, D. "From Ultrasoft Pseudopotentials to the Projector Augmented-Wave Method" *Phys. Rev. B* **1999**, *59*, 1758-1775.
- (35) Perdew, J. P.; Burke, K.; Ernzerhof, M. "Generalized Gradient Approximation Made Simple" *Phys. Rev. Lett.* **1996**, *77*, 3865-3868.
- (36) Grimme, S.; Antony, J.; Ehrlich, S.; Krieg, H. "A consistent and accurate ab initio parametrization of density functional dispersion correction (DFT-D) for the 94 elements H-Pu" *J. Chem. Phys.* **2010**, *132*, 154104.
- (37) Tersoff, J.; Hamann, D. R. "Theory of the scanning tunneling microscope" *Phys. Rev. B* **1985**, *31*, 805-813.
- (38) Hapala, P.; Kichin, G.; Wagner, C.; Tautz, F. S.; Temirov, R.; Jelínek, P. "Mechanism of high-resolution STM/AFM imaging with functionalized tips" *Phys. Rev. B* **2014**, *90*, 085421.
- (39) Savio, L.; Smerieri, M.; Orzelli, A.; Vattuone, L.; Rocca, M.; Finocchi, F.; Jupille, J. "Common fingerprint of hydroxylated non-polar steps on MgO smoke and MgO films" *Surf. Sci.* **2010**, *604*, 252-257.
- (40) Scamehorn, C. A.; Harrison, N. M.; McCarthy, M. I. "Water chemistry on surface defect sites: Chemidissociation versus physisorption on MgO(001)" *J. Chem. Phys.* **1994**, *101*, 1547-1554.
- (41) Fernandes, E.; Donati, F.; Patthey, F.; Stavric, S.; Sljivancanin, Z.; Brune, H. "Adsorption sites of individual metal atoms on ultrathin MgO(100) films" *Phys. Rev. B* **2017**, *96*.
- (42) Peng, J.; Guo, J.; Hapala, P.; Cao, D.; Ma, R.; Cheng, B.; Xu, L.; Ondráček, M.; Jelínek, P.; Wang, E.; Jiang, Y. "Weakly perturbative imaging of interfacial water with submolecular resolution by atomic force microscopy" *Nat. Commun.* **2018**, *9*, 122.

Charge Transfer and Orbital Level Alignment at Inorganic/Organic Interfaces: The Role of Dielectric Interlayers

Michael Hollerer,¹ Daniel Lüftner,¹ Phillip Hurdax,¹ Thomas Ules,¹ Sergey Soubatch,^{2,3} F. Stefan Tautz,^{2,3} Georg Koller,¹ Peter Puschnig,¹ Martin Sterrer,^{1,*} Michael G. Ramsey¹

¹ Institute of Physics, University of Graz, NAWI Graz, Universitätsplatz 5, 8010 Graz, Austria

² Peter Grünberg Institut (PGI-3), Forschungszentrum Jülich, 52425 Jülich, Germany

³ Jülich Aachen Research Alliance (JARA), Fundamentals of Future Information Technology, 52425 Jülich, Germany.

Abstract

It is becoming accepted that ultrathin dielectric layers on metals are not merely passive decoupling layers, but can actively influence orbital energy level alignment and charge transfer at interfaces. As such, they can be important in applications ranging from catalysis to organic electronics. However, the details at the molecular level are still under debate. In this study, we present a comprehensive analysis of the phenomenon of charge transfer promoted by a dielectric interlayer with a comparative study of pentacene adsorbed on Ag(001) with and without an ultrathin MgO interlayer. Using scanning tunneling microscopy and photoemission tomography supported by density functional theory we are able to unambiguously identify the orbitals involved and quantify the degree of charge transfer in both cases. Fractional charge transfer occurs for pentacene adsorbed on Ag(001), while the presence of the ultrathin MgO interlayer promotes integer charge transfer with the LUMO transforming into a singly occupied and singly unoccupied state separated by a large gap around the Fermi energy. Our experimental approach allows a direct access to the individual factors governing the energy level alignment and charge transfer processes for molecular adsorbates on inorganic substrates.

Thin dielectric layers on metals form the basis for many applications such as semiconductor microelectronics, corrosion protection, or data read-out (magnetic tunnel junctions), but are also of interest in fundamental research. On the one hand, various potentially new phenomena can arise from the reduced thickness and the variability of composition and structure in the ultrathin regime, leading to drastically changed chemical and physical properties compared to the corresponding bulk-like analogs.¹⁻² On the other hand, the possibility to simply electronically decouple adsorbed species from the metallic substrate has allowed fundamental atomic and molecular properties, such as the imaging of orbitals and the charge state switching of atoms and molecules by scanning tunneling microscopy (STM),³⁻⁵ or the observation of giant magnetic anisotropy and long magnetization lifetime of single atom magnets,⁶ to be studied. However, thin dielectric layers on metal surfaces can play a far more active role than mere decoupling or passivating layers. Large changes in workfunction (WF) induced by the dielectric can change the electron energy level alignment for adsorbates such that charge transfer is promoted.⁷⁻⁸ This phenomenon can have important consequences in fields ranging from catalysis to organic electronics.⁹⁻¹³

The basic concepts of energy level alignment at, and of charge transfer across the interfaces are generally understood. As the interaction between adsorbates and (large band gap) dielectrics is in general weak, the dominant charge transfer mechanism from the substrate through the dielectric into the adsorbate is tunneling, in which case the transferred charge is expected to be integer. This has to be distinguished from fractional charge transfer, which occurs in strongly coupled (hybridized) systems, e.g. for adsorbates in direct contact with a metal. However, the quantification of transferred charge is challenging, both theoretically and experimentally. For instance, the degree of calculated charge transfer is strongly dependent on the functional used, and on the computational scheme employed to quantify charges in density functional theory (DFT) calculations.¹⁴ Experimentally, while the presence of charged species can be inferred from optical spectroscopy or STM,^{4, 15-16} it cannot be quantified. Ultraviolet-photoemission spectroscopy (UPS) can give direct access to charge transfer states. However, without unambiguous identification of emission features to orbitals, charge transfer is difficult to infer, and without an understanding of the photoemission angular distribution, until now impossible to quantify.¹⁷ Moreover, from the properties known for the isolated substrate and adsorbate, which typically are the work function of the substrate and the electron affinity (EA) and ionization potential (IP) of the adsorbate, one can generally not conclude whether or not charge transfer will occur. Additional contributions that govern the energetic position of the molecular orbitals upon adsorption, and usually come hand-in-hand, are the polarizability of the substrate, and Pauli repulsion (push-back effect).¹⁸ While the former reduces the gap between frontier orbitals (increasing EA and decreasing IP), the push-back effect reduces the work function of the system and thereby the overall energy level alignment.

In the present work, we aim at an experimental quantification of both, charge transfer across interfaces, and energy level alignment at interfaces characterized by strong and weak electronic coupling. To this end, we use as a model the organic semiconductor pentacene adsorbed on pristine Ag(001) and the same substrate covered by an ultrathin dielectric layer, respectively. The atomic structure and the shape of the frontier orbitals of adsorbed pentacene (5A, C₂₂H₁₄) (Figure 1a) have already been experimentally resolved with scanning force and scanning tunneling microscopy, respectively.^{3, 19-21} STM in particular allows the frontier orbitals to be identified. However, a prerequisite for this is that the molecule is electronically decoupled from the metallic substrate, which can be achieved, for example, by adsorbing 5A on ultrathin NaCl layers grown on Cu(111).³ This substrate system exhibits a comparably high WF and the molecule remains uncharged on the

surface. Herein, we study the integer charge transfer state of 5A, which is spontaneously formed by occupation of the lowest unoccupied molecular orbital (LUMO) of 5A on the electronically decoupling, low-workfunction substrate system of ultrathin MgO(001) films on Ag(001) (Figure 1b). We compare the charging behavior of 5A on this substrate with the charge transfer on 5A/Ag(001) without dielectric interlayer and will show that the presence of the dielectric, at first glance counterintuitively, promotes charge transfer to 5A. Moreover, we will present direct evidence for integer charge occupation of the LUMO by imaging orbitals in real and reciprocal space via scanning tunneling microscopy (STM) and photoemission tomography, respectively, which enables us to unambiguously identify the singly occupied (SOMO) and the associated unoccupied (SUMO) molecular orbital of the molecule.

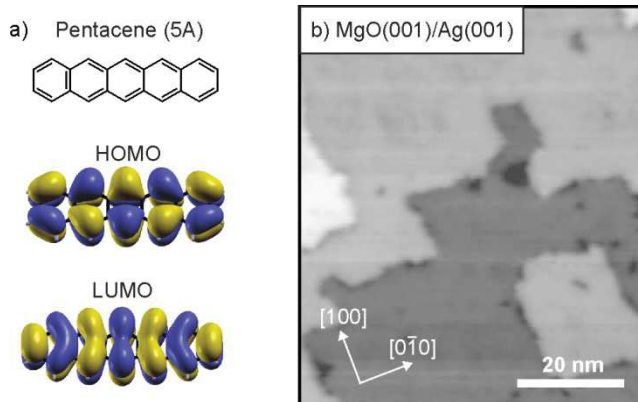


Figure 1. a) Chemical structure and shape of the frontier orbitals of pentacene, 5A. b) STM image ($75 \text{ nm} \times 65 \text{ nm}$) of 2-4 ML MgO(001)/Ag(001) ($U_{\text{bias}} = 3.2 \text{ V}$, $i_t = 100 \text{ pA}$).

Results and Discussion

Charge transfer into pentacene. As the WF prior to adsorption of the molecule is the principal driving force for the charge transfer to the molecule, and the final work function after adsorption depends on the degree of charge transfer to the molecule, an indication about the charge flow can be obtained from WF changes (Table 1). Upon adsorption of a full monolayer 5A, the WF of the bare Ag(001) surface, 4.3 eV, is decreased by 0.4 eV. This change arises from the reduction of the WF by the push-back of the electrons spilling out from the Ag(001) surface (Pauli repulsion), which is partly compensated by the dipole induced by charge transfer to the molecular layer.

Table 1. Experimental and calculated work functions Φ and work function changes $\Delta\Phi$ for adsorption of 5A on bare Ag(001) and 2 ML MgO(001)/Ag(001).

	$\Phi_{\text{exp}} (\Phi_{\text{theo}})/\text{eV}$	$\Delta\Phi_{\text{exp}} (\Delta\Phi_{\text{theo}})/\text{eV}$
Ag(001)	4.3(4.28)	-0.4(-0.37)
5A / Ag(001)	3.9(3.91)	
Ag(001)	4.3(4.28)	-1.7(-1.24)
2 ML MgO(001) / Ag(001)	2.6(3.04)	+1.2(+0.74)
5A / 2 ML MgO(001) / Ag(001)	3.8(3.78)	

For MgO films on Ag(001) our measurements confirm previous theoretical and experimental results,²²⁻²⁴ showing a 1.7 eV reduction of the WF upon dielectric film formation. The large reduction in WF is due to the push-back, which is uncompensated as there is no significant net charge transfer to the MgO layer. Subsequent adsorption of a full monolayer of 5A on MgO(001)/Ag(001) leads to an increase of the WF by 1.2 eV. This increase can be explained by charge transfer and the corresponding induced dipole caused by the presence of negatively charged molecules on the MgO

surface. Note that the final WF of 5A/Ag(001) and 5A/MgO(001)/Ag(001) are essentially the same, suggesting Fermi level pinning in both cases.²⁵

The observed WF changes (Table 1) support the idea of spontaneous charging of 5A and occupation of 5A's LUMO upon adsorption on MgO(001)/Ag(001). To gain molecular information about the adsorption and charging of 5A on Ag(001) and MgO(001)/Ag(001), the systems were analyzed with STM. Figure 2a shows a representative STM image of a submonolayer coverage of 5A on bare Ag(001). The 5A molecules are in general very mobile on the metallic substrate at 77K, as indicated by the noisy appearance of the image. Only occasionally clusters of stable, immobile molecules were found on flat Ag(001) terraces (e.g. 4 molecules forming the cross on the upper right corner, and the cluster of 6 molecules on the left side in Figure 1d) and at step edges. Upon increasing the coverage of 5A on Ag(001) to a full monolayer, the molecules are immobilized in ordered domains with their long molecular axis aligned parallel to the principal [110]/[1-10] directions (Figure 2b). Note that the molecules appear as rod-like protrusions in both filled and empty-state images and, as expected for a system with strong overlap between molecular and metallic states, do not show any orbital-like features.

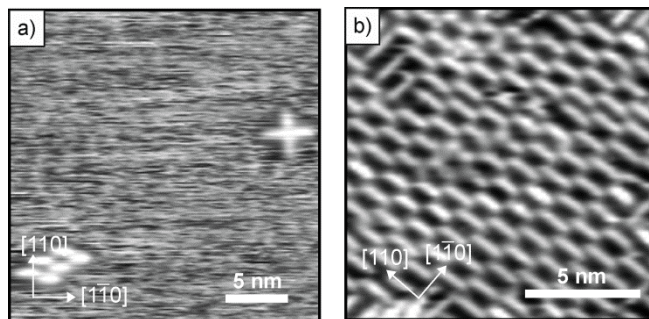


Figure 2. STM of a) submonolayer coverage and b) monolayer coverage of 5A on Ag(001). a) $U_{\text{bias}} = -0.8$ V, $i_t = 90$ pA, 25 nm \times 25 nm; (b) $U_{\text{bias}} = -0.6$ V, $i_t = 50$ pA, 13.5 nm \times 13.5 nm.

STM images of submonolayer coverages of 5A molecules on MgO(001)/Ag(001) thin films with a nominal MgO thickness of 2-4 ML are shown in Figure 3a and 3b, respectively. In contrast to clean Ag(001), the molecules are immobile, even at submonolayer coverage. They are again aligned, because of the [100]/[100] epitaxial relationship between Ag(001) and MgO(001), with their long axis parallel to the principal [110]/[1-10] directions, i.e. along the closed-packed Mg/O rows of the film. The molecules display a distinct orbital-like structure at the bias voltages applied. All 5A molecules feature a 7-lobe structure, clearly resembling the LUMO of isolated 5A (Figure 1a),³ when imaged at $U_{\text{bias}} \approx 1$ V both below (Figure 3a) and above E_F (Figure 3b). Representative STS spectra (Figure 3c) reveal the presence of two states at $U_{\text{bias}} = -0.8$ V and $U_{\text{bias}} = +0.9$ V, which both have, according to the images shown in Figure 3a and Figure 3b, LUMO-like character. Observation of the LUMO shape below E_F suggests charge transfer into the 5A molecules, while the appearance of the LUMO above E_F indicates that the LUMO is not fully occupied. One would naturally conclude from this result that the two states observed in STS correspond, respectively, to the singly occupied (SOMO, below E_F) and its associated unoccupied (SUMO, above E_F) molecular orbital state of the molecule. At this point we have to mention that qualitatively comparable results have been reported for a neutral Au - 5A complex created on 3 ML NaCl/Cu(111), where similar submolecular structures are observed above and below E_F . However, there the splitting was attributed to temporary charging and discharging of the neutral molecule by the STM tip.²⁶

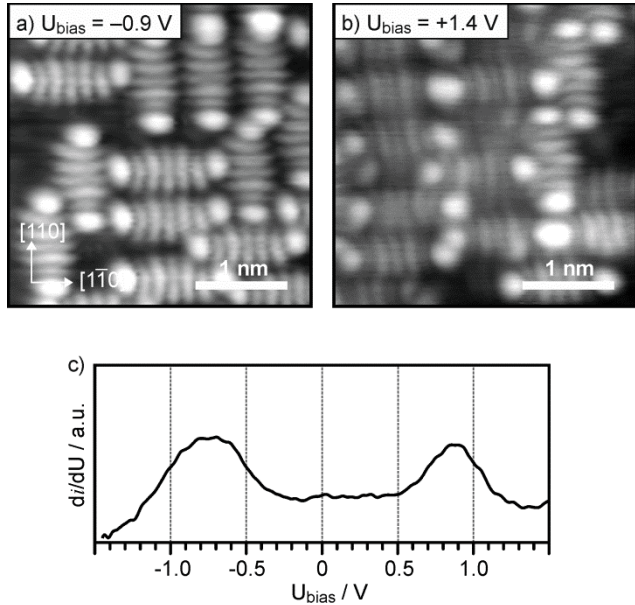


Figure 3. STM ($3.3 \text{ nm} \times 3.3 \text{ nm}$, $i_t = 20 \text{ pA}$) of submonolayer coverage of 5A on 2 ML MgO(001)/Ag(001). a) Filled state and b) empty state images obtained at a sample bias of -0.9 V and $+1.4 \text{ V}$, respectively. c) STS spectrum of 5A on 2 ML MgO(001)/Ag(001).

Since STM alone does obviously not allow to unambiguously conclude about the electronic structure of the system, we performed ab initio calculations within the framework of density functional theory (DFT) and additional photoemission imaging and spectroscopy experiments to gain further insight into the charge rearrangement, electronic structure and energy level alignment of the 5A/MgO(001)/Ag(001) (and 5A/Ag(001)) interface.

DFT calculations. Two types of calculations were considered, one for 5A adsorbed on Ag(001) and MgO(001)/Ag(001), both utilizing the VASP code,²⁷⁻²⁸ and another one for gas-phase 5A, using the NWChem package.²⁹

On both surfaces, the calculations confirm the experimental findings of the molecules being aligned along the [110]/[1-10] substrate directions and of charge transfer into the molecules. First consider the situation for 5A adsorbed on clean Ag(001). The 5A molecule adsorbs on-top of the closed-packed Ag row with the central benzene unit centered on an Ag atom (Figure 4a) and a calculated adsorption energy of 2.65 eV per molecule. Information about charge transfer and charge rearrangement upon adsorption is gained from the charge density differences shown in Figure 4b and the projected density of states (PDOS) plotted in Figure 4c. Similar as for 5A adsorbed on Ag(110),³⁰ the energetic position of the molecular LUMO falls onto E_F (Figure 4c), indicating charge transfer into 5A and partial occupation of the LUMO. This can also directly be seen in the charge density difference plot, which indicates that charge accumulation (red) at the molecule occurs at locations that resemble the shape of the LUMO (Figure 4b, horizontal cut). However, there is also considerable charge depletion (blue) from the molecule, which shows that deeper lying molecular orbitals donate charge to the molecule-substrate bond.³¹ The strong Pauli repulsion between the π electrons of 5A and the electrons of the Ag substrate is represented in the vertical cut in Figure 4b by the charge depletion layer directly above the top-most Ag atoms. The excellent agreement between experimental and calculated WFs for this weakly hybridized molecule-substrate system (Table 1) strongly suggest that the calculation correctly reproduces the effects of charge transfer and push-back in this system.

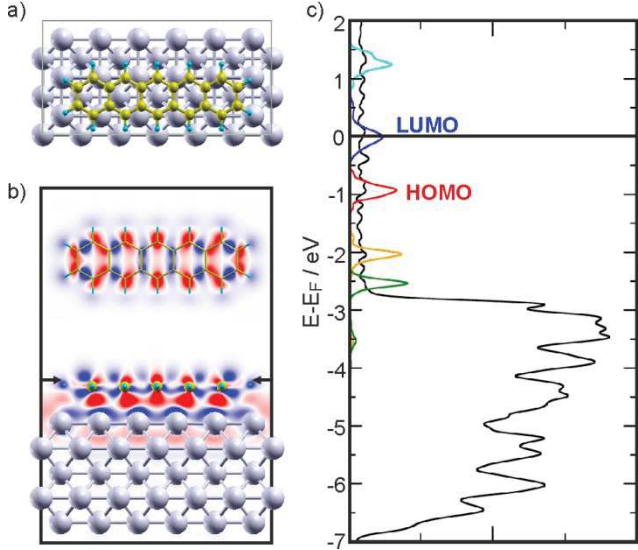


Figure 4. a) Top view of the most stable adsorption configuration of 5A on Ag(001) (Ag: light grey; C: gold; H: light blue). b) Horizontal (top) and vertical two dimensional cuts showing the charge density differences induced by 5A adsorption on the Ag(001) substrate. The arrows indicate where the horizontal cut has been made. Red shows accumulation and blue depletion of charge, respectively. c) Projected DOS obtained for the 5A/Ag(001) interface using the GGA functional. The DOS projected onto the Ag (black) has been reduced for better visibility. In addition the projection on the molecular orbitals are shown for LUMO+1 (cyan), LUMO (blue), HOMO (red), HOMO-1 (orange) and HOMO-2 (dark green).

We now turn to 5A on the 2 ML MgO(001)/Ag(001) films. Here, the most stable adsorption configuration is flat-lying on top of the oxygen rows (Figure 5a). In contrast to the bare Ag(001) surface, where potential barriers <0.1 eV for the lateral movement of 5A have been calculated, the potential barriers are increased by 0.6 eV on the MgO thin film. This immobilization can be understood when considering the calculated charge density differences depicted in Figure 5b. These show an accumulation of charge beneath the benzene rings, directed toward the Mg²⁺ ions beneath the molecule. Thus, there is a strong dipolar contribution to the bonding, and the molecule gets locked into the positions of the cations. Note that this is also reflected in the considerably enhanced adsorption energy of 4.71 eV per molecule compared to 5A/Ag(001) (2.65 eV). The substantially increased diffusion barrier is in accordance with STM observations of reduced mobility of submonolayer coverages of 5A on MgO(001)/Ag(001) compared to Ag(001) (at 77 K).

The charge density difference plot (Figure 5b) also shows a charge accumulation above the molecular backbone, which again resembles the shape of the molecule's LUMO, and naturally suggests charge transfer into the LUMO. Note that the calculated WF change resulting from the charge rearrangement in the system upon 5A adsorption is in good agreement with the experimentally determined WF change (Table 1). In addition, we mention that the presence of the charged 5A molecule induces similar effects in the MgO layer as other charged species, e.g. Au, including the build-up of a polarization in vertical direction (as seen in Figure 5b) and a polaronic distortion of the MgO lattice, which is a necessary factor for the stabilization of charged species above the dielectric film.³²⁻³³

The spin-resolved density of states (DOS) calculated using an HSE functional,³⁴ corresponding to the situation discussed above, is shown in Figure 5c. Clearly, and in contrast to the 5A/Ag(001) system, a distinct spin split of the former LUMO states (blue lines) below and above the Fermi level is observed. Consequently, the two states can be assigned as SOMO and SUMO states. As such, the projected DOS further supports the conclusion, drawn from the experimental results, of charge

transfer into 5A. However, the energy gap of 0.8 eV between the two spin states is undoubtedly underestimated due to the incorrect asymptotic behavior of the HSE potential. Note that this problem is far worse when using a standard GGA functional, which results in the LUMO straddling E_F with an almost imperceptible difference between spin-up and spin-down energies.

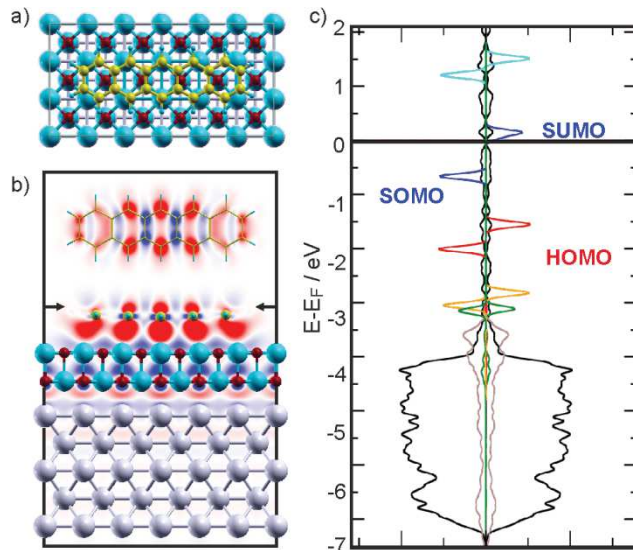


Figure 5. a) Top view of the most stable adsorption configuration of 5A on 2 ML MgO(001)/Ag(001) (Ag: light grey; O: red; Mg: blue; C: gold; H: light blue). b) Horizontal (top) and vertical two dimensional cuts showing the charge density differences induced by 5A adsorption on the 2 ML MgO(001)/Ag(001) substrate. The arrows indicate where the horizontal cut has been made. Red shows accumulation and blue depletion of charge, respectively. c) Spin-resolved projected DOS obtained for the 5A/MgO(001)/Ag(001) interface using the HSE functional. The DOS projected onto the MgO (brown) and Ag (black) has been reduced for better visibility. In addition the projection on the molecular orbitals are shown for LUMO+1 (cyan), LUMO (blue), HOMO (red), HOMO-1 (orange) and HOMO-2 (dark green).

In order to obtain a better estimation for the SOMO-SUMO gap we have calculated the electronic structure of an isolated molecule using an optimally-tuned range-separated hybrid (OT-RSH) functional.³⁵ OT-RSH calculations are known to be useful for correcting the severe underestimation of gaps between occupied and unoccupied states inherent in DFT calculations.³⁵⁻³⁷ For neutral 5A the calculated EA and IP of 1.4 and 6.3 eV (gap 4.9 eV)³⁷⁻³⁸ are in good agreement with gas-phase experimental results of 1.4 and 6.6 eV (gap 5.2 eV). The OT-RSH calculation for the singly charged 5A anion yields a SOMO-SUMO gap of 3.9 eV. Naturally, in the solid state the polarizability of the environment will decrease the IP and increase the EA and thus reduce the band gap,³⁸⁻⁴¹ which can be empirically estimated: As shown further below, the measured IP of the 5A HOMO on the MgO(001)/Ag(001) surface is 5.7 eV, thus 0.9 eV lower than that of the gas phase and, as an increase similar in magnitude can be expected for the EA, a gap reduction of 1.8 eV is estimated. By taking this into account the predicted SOMO-SUMO gap is reduced to 2.1 eV, in closer agreement with the gap measured with STS (1.7 eV).

Quantification of charge transfer. While the STM and DFT results are qualitatively in agreement, the unambiguous identification of the states observed in STM/STS may be problematic owing to a possible influence of the tip, and the questions regarding the degree of charge transfer, and the energy level alignment remain open. Photoemission tomography, the analysis of the angular photoemission distribution within the plane wave final state approximation, has been demonstrated

to be a quantitative tool to identify photoemission features and orbital energy ordering,⁴²⁻⁴³ deduce the molecular orientation and even reconstruct real space orbitals of adsorbed molecules.^{39, 44-45}

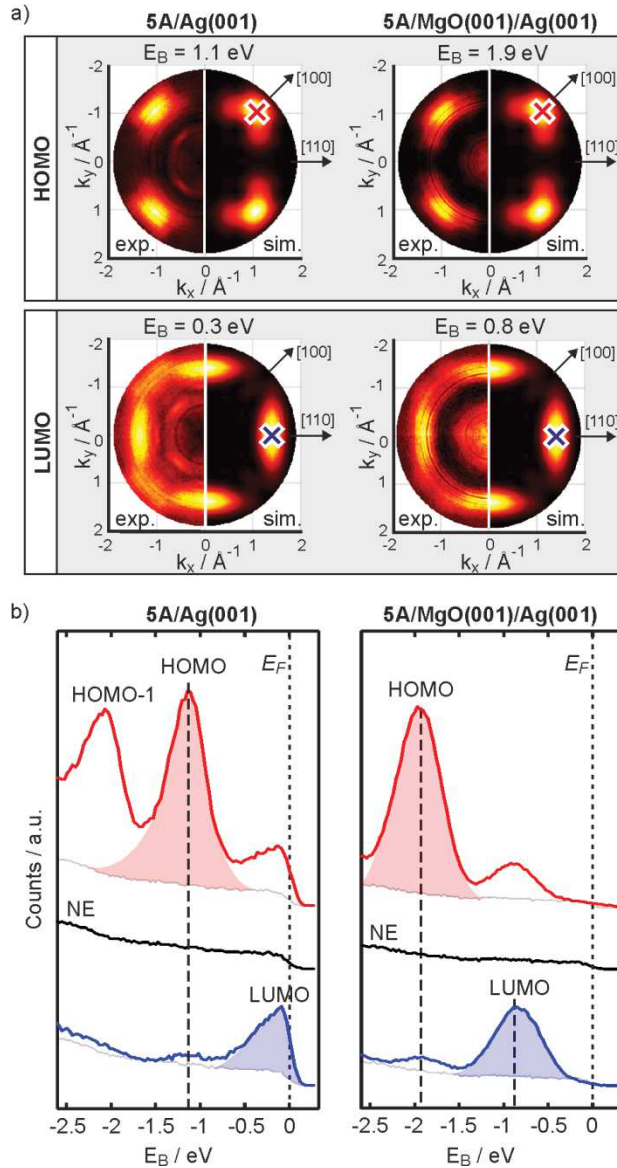


Figure 6. ARPES of 5A ML on Ag(001) (left column) and on 2 MLs of MgO(001) on Ag(001) (right column). (a) Momentum maps of the HOMO (top row) and the LUMO (second row) emission features. Theoretical results for two isolated 5A molecules with perpendicular orientations (right halves of momentum maps) are compared to the experimentally obtained data (left halves of momentum maps) at the stated binding energies, E_B . (b) ARPES spectra of 5A/Ag(001) (left column) and 5A/MgO(001)/Ag(001) (right column) measured at k positions of the HOMO(red)/LUMO(blue) intensity maxima in the momentum maps (depicted as red/blue crosses in panel(a)). Normal emission spectra are shown for comparison (black). The peak areas of the HOMO/LUMO emission features are depicted as red and blue shadings.

The simulations for the photoemission distribution from the HOMO and LUMO of two orthogonally oriented, flat lying 5A molecules are shown in comparison to experimental momentum maps obtained from a ML of 5A on pristine Ag(001) and on 2 ML MgO(001)Ag(001), respectively, at binding energies where the emissions of the molecule-induced states appear (Figure 6a). We first note that in both the resemblance of simulated and measured HOMO and LUMO intensity distributions is clear. Thus, the emissions are identified as HOMO and LUMO states and, in agreement with STM, the molecules are concluded to lie flat and parallel to the [110]/[1-10] azimuths. Furthermore, detection

of the LUMO below E_F ($E_B=0.3$ eV for 5A/Ag and $E_B=0.8$ eV for 5A/MgO(001)/Ag(001)) immediately confirms that charge transfer into the molecule occurs on both substrates.

To better quantify the energies and intensities of the emission features, angle-resolved spectra were obtained with a goniometer-mounted electron spectrometer. Spectra at normal emission ($k_x=k_y=0$) and at the emission directions where the HOMO and LUMO intensities are maximized (red and blue crosses in Figure 6a) are displayed in Figure 6b for 5A/Ag(001) and 5A/MgO(001)/Ag(001), respectively. For 5A on Ag(001), as predicted by the simulation, no molecular features are observed in normal emission and only the Ag(001) Fermi edge is visible. At the geometry of the HOMO emission maximum two peaks are visible corresponding to the HOMO-1 ($E_B = 2.07$ eV) and the HOMO ($E_B = 1.14$ eV), while for the LUMO geometry only an enhancement at the Fermi edge is observed.

For 5A/MgO(001)/Ag(001) again no molecular features are visible in normal emission and the intensity at the Fermi edge is diminished compared to 5A/Ag(001), indicating a well-established MgO interlayer. At emission directions characteristic for the HOMO and LUMO, the HOMO is found at $E_B = 1.94$ eV, shifted down by 0.8 eV relative to 5A on Ag(001), and the LUMO is now a distinct emission feature well below the Fermi edge at $E_B = 0.81$ eV.

Qualitatively, and somewhat counterintuitively, the intensity of the LUMO emission has increased substantially due to the introduction of the MgO dielectric layer. At the emission geometries of Figure 6b the plane wave final state simulations predict a HOMO/LUMO intensity ratio of 1.26 given the orbitals have the same occupation. With the not unreasonable assumption that the HOMO occupancy is 2 electrons, the relative experimental intensities of the emissions (depicted as shaded blue and red areas in Figure 6b) can be used to estimate the LUMO filling. For the 5A/Ag(001) a LUMO occupancy of 0.7 e per molecule is concluded. Fractional charge transfer is also indicated by the truncated appearance of the LUMO emission at E_F in Figure 6b. This indicates hybridization of the molecular LUMO with states of the Ag(001) substrate.

Comparing the measured HOMO/LUMO ratios of several preparations of 5A/MgO(001)/Ag(001) yields a LUMO occupancy of 1.0 ± 0.2 e per molecule. On increasing the 5A exposure from submonolayer to monolayer coverage, the HOMO/LUMO intensity ratio remains constant, while the WF increases essentially linearly with the coverage. As such, there is no evidence for a relation between the amount of charge transfer or the fraction of charged molecules with the packing density in the first layer. This result strongly indicates integer charge transfer to the LUMO, and hence we conclude the observation of a singly occupied molecular orbital (SOMO) for all adsorbed 5A molecules on 2 ML MgO(001)/Ag(001). A scenario where only a fraction of the molecules receive integer charge while others remain uncharged¹⁴ can be excluded since this would lead to the splitting of the HOMO, which is clearly not observed.

Significantly, the observed LUMO binding energy in photoemission is in excellent agreement with the filled state peak position measured with STS. Thus, the obtained STS energy positions reflect a direct tunneling process through the molecular states rather than measurement-induced effects such as charging/discharging, which is often invoked for adsorbates on insulating layers.^{26, 46} Hence, the two peaks observed in the STS (Figure 3c) can be confidently attributed to the SOMO (below E_F) and SUMO (above E_F) of singly-charged 5A on MgO(001)/Ag(001).

Energy level alignment. With the entire set of experimental results, we can now draw a picture of the energy level alignment, including a partitioning into the various factors that influence the alignment (Figure 7). For 5A/Ag(001) (Figure 7a), we start by aligning the HOMO and LUMO levels

with respect to the WF of the system using the experimentally determined ionization potential (IP=6.6 eV) and electron affinity (EA=1.4 eV) of gas-phase 5A. As already mentioned, at the surface the polarizability of the environment will decrease the HOMO-LUMO gap. The decrease of the IP can be empirically estimated by taking the difference of the IPs of the 5A HOMO in the gas phase ($IP_{5A, \text{gas}} = 6.6$ eV) and on the Ag(001) surface ($IP_{5A/\text{Ag}(001)} = \Phi_{5A/\text{Ag}(001)} + E_{B,\text{HOMO}} = 5.0$ eV), which is 1.6 eV. Since for the EA an increase of similar magnitude can be expected, the LUMO level is pushed down, closer to E_F .⁴⁷ However, without a reduction of the WF (vacuum level) the EA is nevertheless not large enough to facilitate charge transfer. From WF measurements we know that the adsorption of 5A reduces the WF by 0.4 eV, which can be understood to result from push-back partly compensated by charge transfer. Since push-back reduces the WF, we estimate its effect to give rise to a 1.2 eV downward shift of all molecular levels, which brings the LUMO close to E_F . As a result, charge transfer between Ag(001) and 5A is facilitated and, while the partially occupied LUMO stays pinned at E_F , the interface dipole created by the charged molecules increases the WF and shifts the HOMO level up. Note that in our analysis of the energy level alignment for the 5A/Ag(001) system, the different contributions of push-back and charge transfer can only indirectly be estimated with the help of the necessary requirement that the LUMO level has to be close to E_F to enable charge transfer. In contrast, a similar analysis of the energy level alignment for the 5A/MgO(001)/Ag(001) system does not require any assumptions because the effects of push-back and charge transfer are separated.

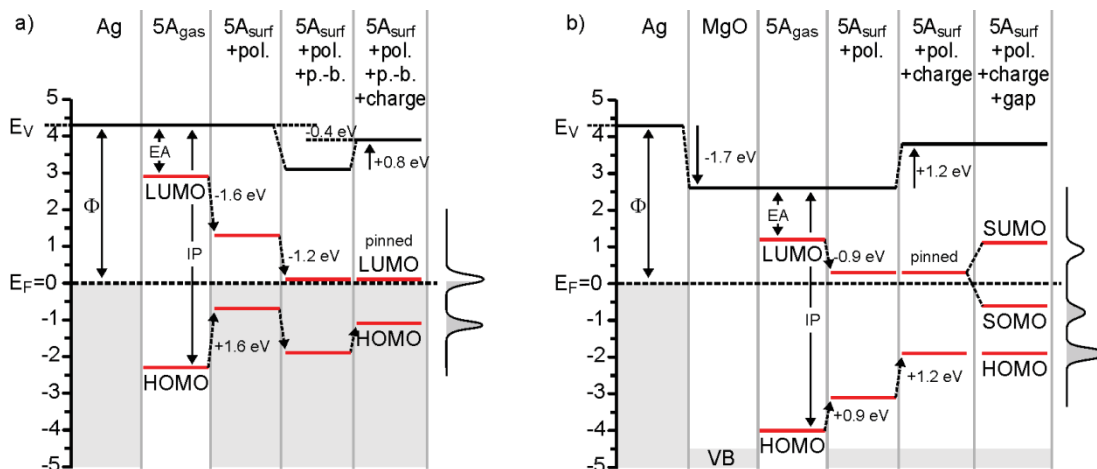


Figure 7. Partitioning of the energy level alignment for a) 5A/Ag(001) and b) 5A/MgO(001)/Ag(001). The orbital energy levels (LUMO, HOMO) of isolated pentacene ($5A_{\text{gas}}$) are aligned to the vacuum levels (E_v) of Ag(001) and MgO(001)/Ag(001), and the contributions of polarization (pol.), push-back (p.-b.), charging (charge) and gap opening (gap, in b only) to the level alignment are added. The curves on the right side of each Figure represent the measured spectra.

For 5A/MgO(001)/Ag(001) (Figure 7b), we again start with the bare Ag(001) surface and the measured WF, which sets the vacuum level (E_v) to 4.3 eV above E_F . The formation of the MgO thin film reduces E_v to 2.6 eV – a 1.7 eV reduction due of the push-back. As in the case of 5A/Ag(001), we align the HOMO and LUMO levels of gas-phase 5A with respect to the E_v of the system and include the effect of the polarizability (determined in the same way as for 5A/Ag(001), using the WF and the energy of the HOMO level of 5A on MgO(001)/Ag(001)), which is naturally smaller than for 5A on Ag(001). This brings the LUMO very close to E_F , enabling charge transfer from the substrate into the molecule. While the LUMO stays pinned at E_F , the interface dipole created by the charging of the molecule leads to an increase of the WF by 1.2 eV and a corresponding shift of the HOMO level by the same magnitude. Because charge transfer through the dielectric barrier occurs by tunneling, the

LUMO is occupied by an integer amount of charge and the resulting singly occupied LUMO is split into a SOMO and a SUMO state separated by a gap of 1.7 eV, as determined by STS.

It is important to note that our experimental approach allows us to determine separately all factors that contribute to the energy level alignment as the molecule interacts with the surface. The consistency of this approach becomes immediately clear when comparing the experimentally measured level energies with those obtained by adding the various contributions of polarizability, push-back and charge transfer to the vacuum level-aligned level energies of gas-phase 5A, as done in Figure 7, which are in perfect agreement with each other.

In addition to addressing the problem of energy level alignment from a very fundamental point of view, our results are significant for the applied field, such as the organic device community. Dielectric interlayers are often used to improve charge injection at contacts.¹² While they undoubtedly can reduce the electron injection barrier by WF reduction, if, as is the case here, the reduction is too great integer charge transfer occurs and a significant gap opens, which renders their use counterproductive.

Conclusion

In conclusion, our study of the adsorption of pentacene (5A) on Ag(001) and Ag(001)-supported MgO(001) thin films provides a clear and comprehensive understanding of charge transfer and energy level alignment at these model inorganic/organic interfaces at a molecular level. Using work function measurements, STM and photoemission imaging and spectroscopy, together with DFT calculations, we show that the molecular LUMO gets pinned to the Fermi level on both substrates, and are able to determine the individual contributions that affect the energy level alignment and lead to charging of the 5A molecule. In particular, the use of MgO(001) as thin dielectric layer enables us to demonstrate the transition from fractional charge transfer at the metal-organic interface to integer charge occupation of the molecular LUMO on an electronically decoupling, low-workfunction substrate. Our study unambiguously identifies the singly occupied (SOMO) and unoccupied (SUMO) molecular orbital of the singly-charged pentacene anion adsorbed on the thin dielectric MgO layer and introduces an approach that permits the quantitative determination of the frontier orbital occupation.

Methods

MgO(100) thin films were grown on clean Ag(001) surfaces following a recipe by J. Pal et al.⁴⁸ The Ag(001) single crystal was cleaned by cycles of Ar⁺ sputtering (1 kV) and successive annealing (773 K, 2 min). Mg was deposited in an oxygen background pressure of 1×10^{-6} mbar at a rate of 0.5 ML/minute. During deposition the Ag(001) crystal was kept at 573 K. The quality of the MgO thin film was checked by LEED and STM/STS. Pentacene was deposited at a sample temperature of $T_{\text{Sample}} = 300$ K. The deposition rates were monitored with a quartz microbalance. STM and STS measurements were performed at 77 K with a *Createc* low-temperature STM attached to a ultrahigh vacuum preparation chamber (base pressure 2×10^{-10} mbar). All stated biases are referring to the sample with respect to the tip. Angle resolved ultra-violet photoemission spectroscopy (ARUPS) measurements were performed using a goniometer mounted VG ADES 400 spectrometer equipped with a helium gas discharge lamp (helium I, $h\nu = 21.2$ eV, angle of incidence $\alpha = 60^\circ$). Workfunctions were obtained from the secondary electron cut-off in normal emission with a sample bias. ARUPS photoemission tomography measurements were performed at the synchrotron radiation facility BESSY II (U125-2NIM beamline, $h\nu = 21$ eV, $\alpha = 40^\circ$) with a toroidal analyzer.⁴⁹ The analyzer collects

the full hemicircle of emission in the plane of incidence and, the momentum maps were obtained by rotating the crystal azimuth in 1° steps.

Density functional theory calculations were performed for the isolated 5A molecule by utilizing NWChem²⁹ and for the full 5A/MgO(001)/Ag(001) and 5A/Ag(001) overlayers, for which the VASP code²⁷⁻²⁸ has been used. The calculations of the isolated molecule were performed using an OT-RSH functional.³⁵ The simulated momentum maps of the HOMO and the LUMO of the isolated 5A molecule are obtained as Fourier transforms of the respective Kohn-Sham orbital as described in Ref. ⁴². The electronic structure calculations for 5A monolayers adsorbed on Ag(001) and MgO(001)/Ag(001) have been carried out using a repeated slab approach. The metallic substrate has been modeled by five metallic layers and the dielectric interface by two layers and a vacuum layer of 15 Å has been added between the slabs. To avoid spurious electrical fields, a dipole layer is inserted in the vacuum region ⁵⁰. Exchange correlation effects were treated either within the GGA ⁵¹ or within the Heyd-Scuseria-Ernzerhof (HSE) hybrid functional ³⁴ with k-point meshes of $4 \times 8 \times 1$ and $2 \times 4 \times 1$, respectively. The projector augmented wave (PAW) ⁵² approach was used allowing for a relatively low kinetic energy cut-off of 500 eV, and a first-order Methfessel-Paxton smearing of 0.1 eV ⁵³. During the geometry optimization, the atomic positions of the molecular layer, the dielectric interlayer and the first two metallic layers were allowed to relax. In order to account for van-der-Waals interactions, we employ the vdW-surf method according to Ruiz et al. ⁵⁴⁻⁵⁵ during the geometry optimization.

Acknowledgment

We acknowledge the Helmholtz-Zentrum Berlin-Electron storage ring BESSY II for provision of synchrotron radiation at beamline U125/2-10mNIM and further acknowledge financial support from Fund FWF (P21330-N20, P27649-N20, P27427). The computational results presented have been achieved using the computing facilities of the University of Graz and the Vienna Scientific Cluster (VSC3).

References

- [1] Pacchioni, G.; Valeri, S. (Eds.), *Oxide Ultrathin Films: Science and Technology*. Vol. Wiley-VCH: Weinheim, 2011.
- [2] Netzer, F. P.; Fortunelli, A. (Eds.), *Oxide Materials at the Two-Dimensional Limit*. Springer Series in Materials Science. Vol. 234, Springer International Publishing: Switzerland, 2016.
- [3] Repp, J.; Meyer, G.; Stojkovic, S. M.; Gourdon, A.; Joachim, C., Molecules on Insulating Films: Scanning-Tunneling Microscopy Imaging of Individual Molecular Orbitals. *Phys. Rev. Lett.* **2005**, 94, 026803.
- [4] Swart, I.; Sonnleitner, T.; Repp, J., Charge State Control of Molecules Reveals Modification of the Tunneling Barrier with Intramolecular Contrast. *Nano Lett.* **2011**, 11 (4), 1580-1584.
- [5] Repp, J.; Meyer, G.; Olsson, F. E.; Persson, M., Controlling the Charge State of Individual Gold Adatoms. *Science* **2004**, 305 (5683), 493-495.
- [6] Rau, I. G.; Baumann, S.; Rusponi, S.; Donati, F.; Stepanow, S.; Gragnaniello, L.; Dreiser, J.; Piamonteze, C.; Nolting, F.; Gangopadhyay, S.; Albertini, O. R.; Macfarlane, R. M.; Lutz, C. P.; Jones, B. A.; Gambardella, P.; Heinrich, A. J.; Brune, H., Reaching the Magnetic Anisotropy Limit of a 3d Metal Atom. *Science* **2014**, 344 (6187), 988-992.
- [7] Pacchioni, G.; Giordano, L.; Baistrocchi, M., Charging of Metal Atoms on Ultrathin MgO/Mo(100) Films. *Phys. Rev. Lett.* **2005**, 94 (22), 226104.

- [8] Sterrer, M.; Risse, T.; Pozzoni, U. M.; Giordano, L.; Heyde, M.; Rust, H. P.; Pacchioni, G.; Freund, H.-J., Control of the Charge State of Metal Atoms on Thin MgO Films. *Phys. Rev. Lett.* **2007**, 98 (9), 096107.
- [9] Sun, Y. N.; Qin, Z. H.; Lewandowski, M.; Carrasco, E.; Sterrer, M.; Shaikhutdinov, S.; Freund, H. J., Monolayer Iron Oxide Film on Platinum Promotes Low Temperature CO Oxidation. *J. Catal.* **2009**, 266 (2), 359-368.
- [10] Sun, Y. N.; Giordano, L.; Goniakowski, J.; Lewandowski, M.; Qin, Z. H.; Noguera, C.; Shaikhutdinov, S.; Pacchioni, G.; Freund, H. J., The Interplay between Structure and CO Oxidation Catalysis on Metal-Supported Ultrathin Oxide Films. *Angew. Chem. Int. Ed.* **2010**, 49 (26), 4418-4421.
- [11] Calaza, F.; Stiehler, C.; Fujimori, Y.; Sterrer, M.; Beeg, S.; Ruiz-Oses, M.; Nilius, N.; Heyde, M.; Parviainen, T.; Honkala, K.; Hakkinen, H.; Freund, H. J., Carbon Dioxide Activation and Reaction Induced by Electron Transfer at an Oxide-Metal Interface. *Angew. Chem. Int. Ed.* **2015**, 54 (42), 12484-12487.
- [12] Greiner, M. T.; Helander, M. G.; Tang, W. M.; Wang, Z. B.; Qiu, J.; Lu, Z. H., Universal Energy-Level Alignment of Molecules on Metal Oxides. *Nat. Mater.* **2012**, 11 (1), 76-81.
- [13] Jönsson, S. K. M.; Salaneck, W. R.; Fahlman, M., Photoemission of AlQ(3) and C-60 Films on Al and LiF/Al Substrates. *J. Appl. Phys.* **2005**, 98 (1), 014901.
- [14] Hofmann, O. T.; Rinke, P.; Scheffler, M.; Heimel, G., Integer versus Fractional Charge Transfer at Metal(/Insulator)/Organic Interfaces: Cu/(NaCl)/TCNE. *ACS Nano* **2015**, 9 (5), 5391-5404.
- [15] Gruenewald, M.; Schirra, L. K.; Winget, P.; Kozlik, M.; Ndione, P. F.; Sigdel, A. K.; Berry, J. J.; Forker, R.; Bredas, J. L.; Fritz, T.; Monti, O. L. A., Integer Charge Transfer and Hybridization at an Organic Semiconductor/Conductive Oxide Interface. *J. Phys. Chem. C* **2015**, 119 (9), 4865-4873.
- [16] Mohn, F.; Repp, J.; Gross, L.; Meyer, G.; Dyer, M. S.; Persson, M., Reversible Bond Formation in a Gold-Atom-Organic-Molecule Complex as a Molecular Switch. *Phys. Rev. Lett.* **2010**, 105 (26), 266102.
- [17] Amsalem, P.; Niederhausen, J.; Wilke, A.; Heimel, G.; Schlesinger, R.; Winkler, S.; Vollmer, A.; Rabe, J. P.; Koch, N., Role of Charge Transfer, Dipole-Dipole Interactions, and Electrostatics in Fermi-Level Pinning at a Molecular Heterojunction on a Metal Surface. *Phys. Rev. B* **2013**, 87 (3), 035440.
- [18] Witte, G.; Lukas, S.; Bagus, P. S.; Wöll, C., Vacuum Level Alignment at Organic/Metal Junctions: "Cushion" Effect and the Interface Dipole. *Appl. Phys. Lett.* **2005**, 87 (26), 263502.
- [19] Gross, L.; Moll, N.; Mohn, F.; Curioni, A.; Meyer, G.; Hanke, F.; Persson, M., High-Resolution Molecular Orbital Imaging Using a p-Wave STM Tip. *Phys. Rev. Lett.* **2011**, 107 (8), 086101.
- [20] Gross, L.; Mohn, F.; Moll, N.; Liljeroth, P.; Meyer, G., The Chemical Structure of a Molecule Resolved by Atomic Force Microscopy. *Science* **2009**, 325 (5944), 1110-1114.
- [21] Soe, W. H.; Manzano, C.; De Sarkar, A.; Chandrasekhar, N.; Joachim, C., Direct Observation of Molecular Orbitals of Pentacene Physisorbed on Au(111) by Scanning Tunneling Microscope. *Phys. Rev. Lett.* **2009**, 102 (17), 176102.
- [22] Jaouen, T.; Jezequel, G.; Delhaye, G.; Lepine, B.; Turban, P.; Schieffer, P., Work Function Shifts, Schottky Barrier Height, and Ionization Potential Determination of Thin MgO Films on Ag(001). *Appl. Phys. Lett.* **2010**, 97 (23), 232104.
- [23] König, T.; Simon, G. H.; Rust, H. P.; Heyde, M., Work Function Measurements of Thin Oxide Films on Metals-MgO on Ag(001). *J. Phys. Chem. C* **2009**, 113 (26), 11301-11305.
- [24] Giordano, L.; Cinquini, F.; Pacchioni, G., Tuning the Surface Metal Work Function by Deposition of Ultrathin Oxide Films: Density Functional Calculations. *Phys. Rev. B* **2006**, 73 (4), 045414.
- [25] Braun, S.; Salaneck, W. R.; Fahlman, M., Energy-Level Alignment at Organic/Metal and Organic/Organic Interfaces. *Adv. Mater.* **2009**, 21 (14-15), 1450-1472.

[26] Repp, J.; Meyer, G.; Paavilainen, S.; Olsson, F. E.; Persson, M., Imaging Bond Formation Between a Gold Atom and Pentacene on an Insulating Surface. *Science* **2006**, *312* (5777), 1196-1199.

[27] Kresse, G.; Hafner, J., Ab-initio Molecular Dynamics for Liquid Metals. *Phys. Rev. B* **1993**, *47* (1), 558-561.

[28] Kresse, G.; Joubert, D., From Ultrasoft Pseudopotentials to the Projector Augmented-Wave Method. *Phys. Rev. B* **1999**, *59* (3), 1758-1775.

[29] Valiev, M.; Bylaska, E. J.; Govind, N.; Kowalski, K.; Straatsma, T. P.; Van Dam, H. J. J.; Wang, D.; Nieplocha, J.; Apra, E.; Windus, T. L.; de Jong, W., NWChem: A Comprehensive and Scalable Open-Source Solution for Large Scale Molecular Simulations. *Comput. Phys. Commun.* **2010**, *181* (9), 1477-1489.

[30] Ules, T.; Lüftner, D.; Reinisch, E. M.; Koller, G.; Puschnig, P.; Ramsey, M. G., Orbital Tomography of Hybridized and Dispersing Molecular Overlayers. *Phys. Rev. B* **2014**, *90* (15), 155430.

[31] Romaner, L.; Nabok, D.; Puschnig, P.; Zojer, E.; Ambrosch-Draxl, C., Theoretical Study of PTCDA Adsorbed on the Coinage Metal Surfaces, Ag(111), Au(111) and Cu(111). *New J. Phys.* **2009**, *11*, 053010.

[32] Honkala, K.; Häkkinen, H., Au Adsorption on Regular and Defected Thin MgO(100) Films Supported by Mo. *J. Phys. Chem. C* **2007**, *111* (11), 4319-4327.

[33] Giordano, L.; Martinez, U.; Sicolo, S.; Pacchioni, G., Observable Consequences of Formation of Au Anions from Deposition of Au Atoms on Ultrathin Oxide Films. *J. Chem. Phys.* **2007**, *127* (14), 144713.

[34] Heyd, J.; Scuseria, G. E.; Ernzerhof, M., Hybrid Functionals Based on a Screened Coulomb Potential (vol 118, pg 8207, 2003). *J. Chem. Phys.* **2006**, *124* (21), 219906.

[35] Kronik, L.; Stein, T.; Refaelly-Abramson, S.; Baer, R., Excitation Gaps of Finite-Sized Systems from Optimally Tuned Range-Separated Hybrid Functionals. *J. Chem. Theory Comput.* **2012**, *8* (5), 1515-1531.

[36] Refaelly-Abramson, S.; Baer, R.; Kronik, L., Fundamental and Excitation Gaps in Molecules of Relevance for Organic Photovoltaics from an Optimally Tuned Range-Separated Hybrid Functional. *Phys. Rev. B* **2011**, *84* (7), 075144.

[37] Refaelly-Abramson, S.; Sharifzadeh, S.; Govind, N.; Autschbach, J.; Neaton, J. B.; Baer, R.; Kronik, L., Quasiparticle Spectra from a Nonempirical Optimally Tuned Range-Separated Hybrid Density Functional. *Phys. Rev. Lett.* **2012**, *109* (22), 226405.

[38] Refaelly-Abramson, S.; Sharifzadeh, S.; Jain, M.; Baer, R.; Neaton, J. B.; Kronik, L., Gap Renormalization of Molecular Crystals from Density-Functional Theory. *Phys. Rev. B* **2013**, *88* (8), 081204.

[39] Lüftner, D.; Milko, M.; Huppmann, S.; Scholz, M.; Ngyuen, N.; Wiessner, M.; Scholl, A.; Reinert, F.; Puschnig, P., CuPc/Au(110): Determination of the Azimuthal Alignment by a Combination of Angle-Resolved Photoemission and Density Functional Theory. *J. Electron Spectrosc. Relat. Phenom.* **2014**, *195*, 293-300.

[40] Liu, Z.-F.; Egger, D. A.; Refaelly-Abramson, S.; Kronik, L.; Neaton, J. B., Energy Level Alignment at Molecule-Metal Interfaces from an Optimally Tuned Range-Separated Hybrid Functional. *J. Chem. Phys.* **2017**, *146* (9), 092326.

[41] Egger, D. A.; Liu, Z. F.; Neaton, J. B.; Kronik, L., Reliable Energy Level Alignment at Physisorbed Molecule-Metal Interfaces from Density Functional Theory. *Nano Lett.* **2015**, *15* (4), 2448-2455.

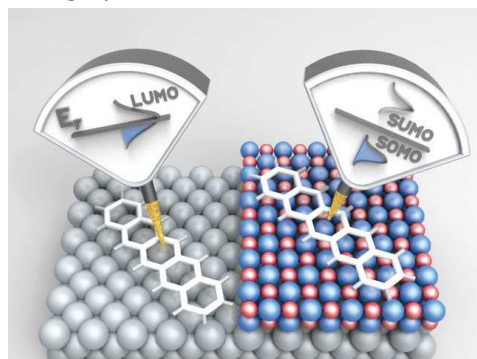
[42] Puschnig, P.; Berkebile, S.; Fleming, A. J.; Koller, G.; Emtsev, K.; Seyller, T.; Riley, J. D.; Ambrosch-Draxl, C.; Netzer, F. P.; Ramsey, M. G., Reconstruction of Molecular Orbital Densities from Photoemission Data. *Science* **2009**, *326* (5953), 702-706.

[43] Ules, T.; Lüftner, D.; Reinisch, E. M.; Koller, G.; Puschnig, P.; Ramsey, M. G., Continuous or Discrete: Tuning the Energy Level Alignment of Organic Layers with Alkali Dopants. *Phys. Rev. B* **2016**, *94* (20), 205405.

[44] Wiessner, M.; Hauschild, D.; Sauer, C.; Feyer, V.; Scholl, A.; Reinert, F., Complete Determination of Molecular Orbitals by Measurement of Phase Symmetry and Electron Density. *Nat. Commun.* **2014**, *5*, 4156.

- [45] Weiss, S.; Lüftner, D.; Ules, T.; Reinisch, E. M.; Kaser, H.; Gottwald, A.; Richter, M.; Soubatch, S.; Koller, G.; Ramsey, M. G.; Tautz, F. S.; Puschnig, P., Exploring Three-Dimensional Orbital Imaging with Energy-Dependent Photoemission Tomography. *Nat. Commun.* **2015**, *6*, 8287.
- [46] Wu, S. W.; Nazin, G. V.; Chen, X.; Qiu, X. H.; Ho, W., Control of Relative Tunneling Rates in Single Molecule Bipolar Electron Transport. *Phys. Rev. Lett.* **2004**, *93* (23), 236802.
- [47] Neaton, J. B.; Hybertsen, M. S.; Louie, S. G., Renormalization of Molecular Electronic Levels at Metal-Molecule Interfaces. *Phys. Rev. Lett.* **2006**, *97* (21), 216405.
- [48] Pal, J.; Smerieri, M.; Celasco, E.; Savio, L.; Vattuone, L.; Rocca, M., Morphology of Monolayer MgO Films on Ag(100): Switching from Corrugated Islands to Extended Flat Terraces. *Phys. Rev. Lett.* **2014**, *112* (12), 126102.
- [49] Broekman, L.; Tadich, A.; Huwald, E.; Riley, J.; Leckey, R.; Seyller, T.; Emtsev, K.; Ley, L., First Results from a Second Generation Toroidal Electron Spectrometer. *J. Electron Spectrosc. Relat. Phenom.* **2005**, *144*, 1001-1004.
- [50] Neugebauer, J.; Scheffler, M., Adsorbate-Substrate and Adsorbate-Adsorbate Interactions of Na and K Adlayers on Al(111). *Phys. Rev. B* **1992**, *46* (24), 16067-16080.
- [51] Perdew, J. P.; Burke, K.; Ernzerhof, M., Generalized Gradient Approximation Made Simple. *Phys. Rev. Lett.* **1996**, *77* (18), 3865-3868.
- [52] Blöchl, P. E., Projector Augmented-Wave Method. *Phys. Rev. B* **1994**, *50* (24), 17953-17979.
- [53] Methfessel, M.; Paxton, A. T., High-Precision Sampling for Brillouin-Zone Integration in Metals. *Phys. Rev. B* **1989**, *40* (6), 3616-3621.
- [54] Tkatchenko, A.; Scheffler, M., Accurate Molecular Van Der Waals Interactions from Ground-State Electron Density and Free-Atom Reference Data. *Phys. Rev. Lett.* **2009**, *102* (7), 073005.
- [55] Ruiz, V. G.; Liu, W.; Zojer, E.; Scheffler, M.; Tkatchenko, A., Density-Functional Theory with Screened van der Waals Interactions for the Modeling of Hybrid Inorganic-Organic Systems. *Phys. Rev. Lett.* **2012**, *108* (14), 146103.

TOC graphic



SUPPORTING INFORMATION

Charge Transfer and Orbital Level Alignment at Inorganic/Organic Interfaces: The Role of Dielectric Interlayers

Michael Hollerer,¹ Daniel Lüftner,¹ Philipp Hurdax,¹ Thomas Ules,¹ Serguei Soubatch,^{2,3} F. Stefan Tautz,^{2,3} Georg Koller,¹ Peter Puschnig,¹ Martin Sterrer,^{1,*} Michael G. Ramsey¹

¹ Institute of Physics, University of Graz, NAWI Graz, Universitätsplatz 5, 8010 Graz, Austria

² Peter Grünberg Institut (PGI-3), Forschungszentrum Jülich, 52425 Jülich, Germany

³ Jülich Aachen Research Alliance (JARA), Fundamentals of Future Information Technology, 52425 Jülich, Germany.

Theoretical estimation of the contribution of static substrate polarizability on HOMO-LUMO gap reduction.

In the main part of the paper, we have demonstrated how to disentangle the various contributions leading to the level alignment based on quantities accessible solely by measurements (compare Fig. 7). In particular, we could estimate the reduction of HOMO-LUMO gap due to the polarizability of the substrate. Here, we present an alternative approach which makes use of electronic structure calculations.^[S1] However, as will be shown below, the two approaches lead to almost identical values within an accuracy of 0.1-0.2 eV.

For determining a theory-based estimate of the gap renormalization of pentacene (5A) gap due to the substrate's polarizability, we proceed according to the following steps:

- 1) Calculate the EA and IP of gas-phase 5A at the same level of theory (semi-local PBE) as is done later for adsorbed 5A.
- 2) Calculate highly accurate values of EA and IP of gas-phase 5A using an optimally-tuned range-separated hybrid (OT-RSH) functional.
- 3) Determine the gas-phase self-energy correction Σ^0 by comparing the EA's and IP's of 1) and 2).
- 4) Calculate 5A adsorbed on the surface using the same semi-local PBE functional as in 1)
- 5) Correct the EA and IP of adsorbed 5A by Σ^0 .
- 6) Compare the corrected EA and IP of surface 5A with the experimentally measured EA and IP and determine the difference Δ between these values which are identified as polarizability effect due to the substrate

The result of this procedure is summarized in Figs. S1 and S2 for 5A on Ag(001) and 5A on MgO(001)/Ag(001), respectively. Thus, we obtain a symmetric gap reduction for 5A/Ag(001) with polarization shifts of $\Delta=1.8$ eV, both for the HOMO and LUMO. This value compares fairly well with our experimental estimate of 1.6 eV (see main text and Table S1). For, 5A/MgO(001)/Ag(001), the computational procedure leads to a polarization shift of $\Delta=1.0$ eV for the HOMO which again compares very well with our experimental estimate of 0.9 eV. Since in our computational procedure, we use a comparison with experiment in the final step 6) and since the LUMO splits into a SOMO and SUMO level, we not unambiguously determine the corresponding polarization shift for the LUMO. Given the symmetric shift found for 5A/Ag(001), the assumption of a symmetric shift also for the 5A/MgO(001)/Ag(001) case seems reasonable, and has therefore been used for Fig. 7b.

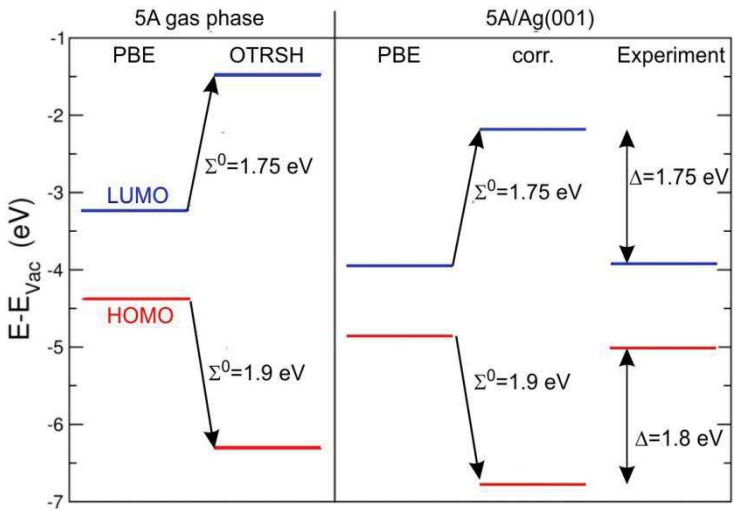


Figure S1. Level alignment for the HOMO (red) and LUMO (blue) for 5A/Ag(001) determined according to the procedure outlined in the text.

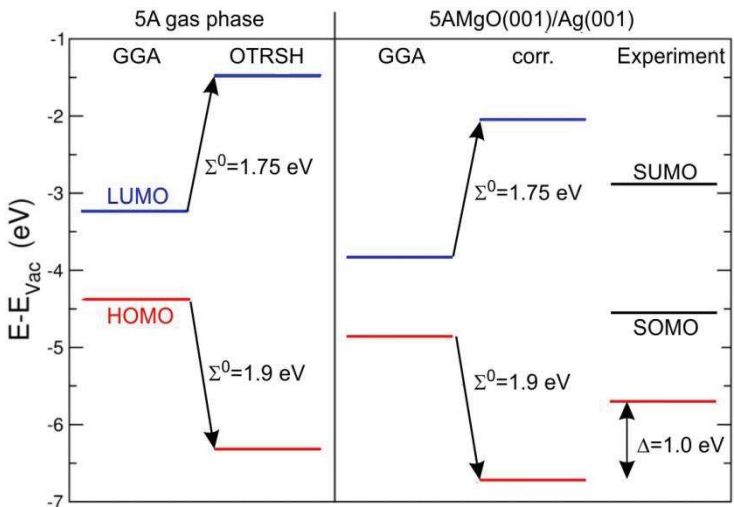


Figure S2. Level alignment for the HOMO (red) and LUMO (blue) for 5A/MgO(001)/Ag(001) determined according to the procedure outlined in the text.

Table S1. Polarization shifts for the HOMO and LUMO for 5A/Ag(001) and 5A/MgO(001)/Ag(001) determined from the experimental and computational procedures outlined in the text.

	5A/Ag(001)		5A/MgO(001)/Ag(001)	
	exp.	calc.	exp.	calc.
Δ_{HOMO}	1.6	1.8	0.9	1.0
Δ_{LUMO}	1.6	1.75	0.9	-

[S1] Khoo, K. H.; Chen, Y.; Li, S.; Quek, S. Y., Length Dependence of Electron Transport Through Molecular Wires – A First Principles Perspective. *Phys. Chem. Chem. Phys.* **2015**, *17*, 77-96.

Growth study of para-sexiphenyl on Ag(001): From single molecule to crystalline film

Michael Hollerer^a, Stefan Pachmayer^b, Daniel Lüftner^a, Boris Butef^a, Eva-Maria Reinisch^a, Peter Puschnig^a, Georg Koller^a, Michael G. Ramsey^a and Martin Sterrer^a

^aInstitute of Physics, University of Graz, NAWI Graz, Universitätsplatz 5, 8010 Graz, Austria

^bInstitute of Solid State Physics, Graz University of Technology, Petersgasse 16, 8010 Graz, Austria

Abstract

In this work we investigate the formation of crystalline organic thin films for p-sexiphenyl (6P) on Ag(001) with a combination of STM, LEED, TPD, SFM, UPS, XRD and DFT. For weakly interacting van-der-Waals-dominated systems of small organic molecules on single crystalline metals we demonstrate the complex epitaxial evolution from sub-monolayer to bulk structure. In the delicate interplay between molecule-substrate and intermolecular interactions we identify the oligo-phenyl's flexibility of central importance for the film growth. We observe a change from a planar to a twisted molecular conformation and, accompanying, a molecular realignment during the formation of a dense monolayer as the result of enhanced 2-dimensional intermolecular interaction. A second molecular realignment occurs collectively for whole domains with the formation of 3-dimensional bilayer structures. Finally the bilayer acts as a template for the epitaxial growth of the molecular thin film, determining the azimuthal orientation and a single contact plane for the organic crystallites.

Declarations of interest: none

Keywords: organic thin film, bilayer, realignment, reorientation, molecular conformation

1. Introduction

Organic electronics offer a vast potential because of the immense diversity of molecule/substrate systems and their room-temperature processibility. Although a variety of organic electronic and opto-electronic devices are already available we are just at the verge of exploiting the immense potential of this technology. In the quest for improved device performance and new applications the focus of research has recently evolved towards ultra-thin organic films and anisotropic molecular crystallites [1,2]. An intriguing new field is also established by the combination of ultrathin molecular films and modern 2D materials, enabling mutual doping of both substrate and the adsorbate film [3,4]. A detailed understanding of the development of molecular wetting layers and the growth of a molecular thin-film on an anisotropic substrate is hence indispensable.

For aromatics generally, in the first monolayer, the atomic structure of the substrate aligns the molecular axis while the strength of the interaction with the substrate will determine the aromatic plane orientation. However, because of the relatively weak interaction of molecule to substrate and molecule to molecule the all-important contact interface may not be immutable and changes may occur during the film growth [5,6]. Para-Sexiphenyl (6P) is an excellent model system for controlled growth studies of flexible, rod-like molecules as it is UHV compatible and an active element in light emitting diodes [7]. For 6P a series of growth studies have already shown epitaxial growth of molecular crystallites on atomically clean substrates, when deposited by physical vapor deposition (PVD) [8,9]. Epitaxial relationships defined by their (low index) contact planes of upright standing molecules (100) and lying molecules {(20-3), (11-1), (11-2) and (21-3)} are frequently obtained and relate to the morphological development of macroscopic platelets and micro-needles respectively [10]. Studies have shown that even large-scale nano-structures can be prepared in a single-crystalline nature [11,12]. The development of a single epitaxial growth mode on a specific substrate is essential for the realization of a well ordered molecular thin-film but highly sensitive to deposition temperature [13–15] and substrate contamination [8,16,17]. Recently also high index contact-planes were observed (62-9) [18], hinting towards a more complex than expected epitaxial relationship, or even towards thin-film polymorphism. Additionally a variety of studies focus on the complex development of the 6P wetting layers on various substrates and indicate epitaxial relations to the molecular thin-film [6,19–21].

It is widely accepted that the formation of epitaxially ordered organic crystallites on surfaces is determined by the symmetry of the substrate surface and the bulk structure of the organic crystallite as well as the substrate/molecule and the intermolecular interaction strengths [9,22–24]. But the actual evolution of the growth, starting from the adsorption of a single molecule up to the development of the

final bulk structure is still poorly understood. Within this work we provide a growth study for the model system of 6P on Ag(001) from sub-monolayers up to device relevant thicknesses. Supported by density functional calculations, we track the complex development of the molecular film, from single molecule to the bilayer, with surface sensitive local (scanning tunneling microscopy, STM) and area-averaging methods (low energy electron diffraction, LEED, angle-resolved ultra violet photoemission spectroscopy, ARUPS) and provide a continuous observation from submonolayer to bulk films with temperature programmed desorption (TPD). The resulting bulk structure is characterized *ex-situ* both morphologically (scanning force microscopy, SFM) and structurally (x-ray diffraction, XRD) and related to the results obtained for the wetting layer. It will be shown that in thin-film formation the flexibility of the oligo-phenyl plays a crucial role in the delicate balance of molecule/substrate and intermolecular interactions leading to a complex, but strictly epitaxial, evolution of the molecular thin film.

2. Experimental

The Ag(001) single crystal was cleaned with cycles of Ar⁺ sputtering (1 kV, 8 µA) and annealing for 5 min. at 773 K. Cleanliness and ordering of the substrate surface was verified by LEED. Deposition of 6P was achieved using evaporation from a home-built Knudsen cell, while monitoring the film thickness with a quartz crystal microbalance. The stated nominal thickness of 6P relates to a density of 1.29 g/cm³. Unless otherwise stated all films were deposited at room temperature (300 K). The background pressure in the UHV systems was 2 x 10⁻¹⁰ mbar.

STM measurements were performed with a *CREATEC* low temperature STM at 7 K using an electrochemically etched tungsten tip. The stated bias voltages U_{Bias} are applied to the sample. Image processing was carried out using *Gwyddion* software [25], including plane subtraction and noise filtering. Additional distortion compensation was carried out using the *Gwyddion* Affine function. UPS was conducted at the BESSY II (Helmholtz-Zentrum Berlin) synchrotron radiation facility. Temperature programmed desorption (TPD) was performed with a temperature rate of approximately 3 K/s while detecting the cracking mass of 152 amu as the molecular mass of 6P with 458 amu was out of range of the employed mass spectrometer. SFM and XRD measurements were performed *ex-situ* on thick films prepared in UHV. AFM was performed under ambient condition using a *NanoSurf EasyScan 2*. XRD was performed with both laboratory and synchrotron X-ray sources.

The samples were investigated by X-ray diffraction using a *Philips* X-ray-texture goniometer equipped with a chromium sealed tube (wavelength $\lambda = 0.229$ nm). The analysis of the preferred growth was performed by obtaining pole figures at various 2θ angles. During the measurements, the samples were

rotated around φ from 0° to 360° and tilted in ψ normal to the beam direction from 0° to 90° in steps of 3° . On the incident beam side, a slit system with an aperture of 4 mm in height and 2 mm in width was chosen, while on the diffracted beam side an antiscatter window of 1.2 mm was used. Intensity was measured using a scintillation counter. Further analysis on the pole figures was done with *STEREOPOLE* [26]. Grazing incidence X-ray diffraction (GIXD) measurements were performed on beamline XRD1 at *Elettra* Sincrotrone (Trieste, Italy). An X-ray energy of 8.86 keV was set and diffracted intensity was collected by a Pilatus 2M detector. The sample was mounted on a moveable stage so that a defined incidence angle, α_i , could be set to 0.5° . Samples were rotated azimuthally and images were taken in two degree steps. Detector calibration and conversion of collected data to reciprocal space representation was done using a custom-written MATLAB program. The data are represented as two dimensional contour

plots with the out-of-plane axis \mathbf{q}_z over the in-plane axis $\mathbf{q}_{xy} = \sqrt{\mathbf{q}_x^2 + \mathbf{q}_y^2}$.

All theoretical results presented in this work are obtained within the framework of density functional theory (DFT). We have conducted periodic boundary calculations, utilizing the VASP code [27,28], for 6P on Ag(001) in the sub-monolayer regime and for a full monolayer using a unit cell as obtained by LEED. We have employed a repeated slab approach, where the Ag substrate has been modeled by five metallic layers and a vacuum layer of about 19 Å has been added between two slabs. In order to avoid spurious electrical fields, a dipole layer is inserted in the vacuum region [29]. For exchange-correlation effects the general gradient approximation (GGA) according to *Perdew, Burke and Ernzerhof* [30] has been utilized. A *Monkhorst-Pack* $3 \times 3 \times 1$ grid of k-points [31] and the projector augmented wave (PAW) [32] approach was used allowing for a relatively low kinetic energy cut-off of about 500 eV. During the geometry optimization the 6P molecules and the two topmost Ag layers were allowed to fully relax. In order to account for van-der-Waals (vdW) interactions, we employ the vdW-surf method according to *Ruiz et al.* [33,34] during the geometry optimization.

3. Results and Discussion

3.1 Thick films

We start with the investigation of thick 6P films deposited at room temperature on atomically clean Ag(001) in UHV. **Figure 1.a-b** show *ex-situ* AFM images obtained for 6P of 30 Å and 300 Å nominal thickness, respectively. The former shows the development of needle-like crystallites featuring heights of 10-20 nm and lengths from 100 nm up to 1 μm. The long needle axis (LNA) shows rough alignment with the <100> directions of Ag(001). A more detailed analysis reveals two distinct maxima of the LNA rotated +/- 11° away from the <100> axis (see **Supplementary Material**). A film with nominal thickness of 300 Å (**Figure 1.b**) gives rise to a peculiar structure of hills and valleys, with height differences of up to 80 nm. The features consist of small crystallites, similar in length to the needles observed in **Figure 1.a**, but with an ill-defined LNA angle distribution. However the LNAs seem to be correlated and arrange in rectangular vortices.

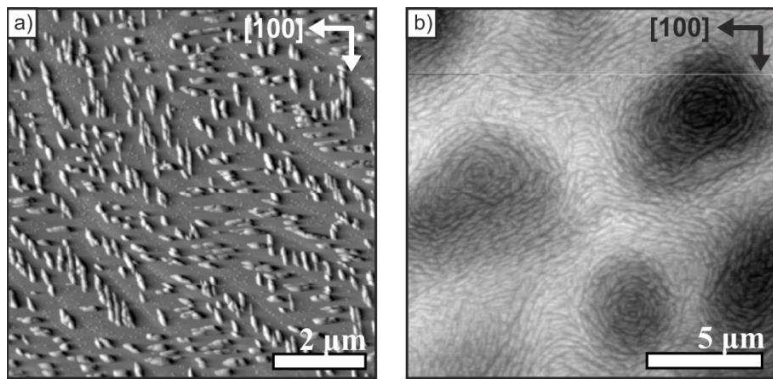


Figure 1: *Ex-situ* AFM images of thick films of 6P on Ag(001) for a nominal coverage of 30 Å (**a**, derivative data) and 300 Å (**b**, topography).

Standard laboratory source 2θ measurements of the 300 Å film of **Figure 1.b** revealed only (21-3) 6P oriented crystallites (data not shown). Assuming the Baker structure of 6P [35], this implies that the long molecular axis of all molecules is perfectly parallel to the substrate surface with alternating layers of molecules with their aromatic planes parallel to the substrate and tilted away from it. More precise grazing-incidence X-ray diffraction (GIXD) measurements with synchrotron radiation were performed on the same film. The corresponding reciprocal space map (RSM) of **Figure 2.a** shows the integrated intensity after the sample was rotated 360°. A (21 10 -28) orientation yields simulated diffraction spots (white indexed circles) that match all observed diffraction peaks (yellow features). The (21 10 -28) plane is very close to the low-index (2 1 -3) contact plane, differing by a slight out-of-plane tilt of the molecules.

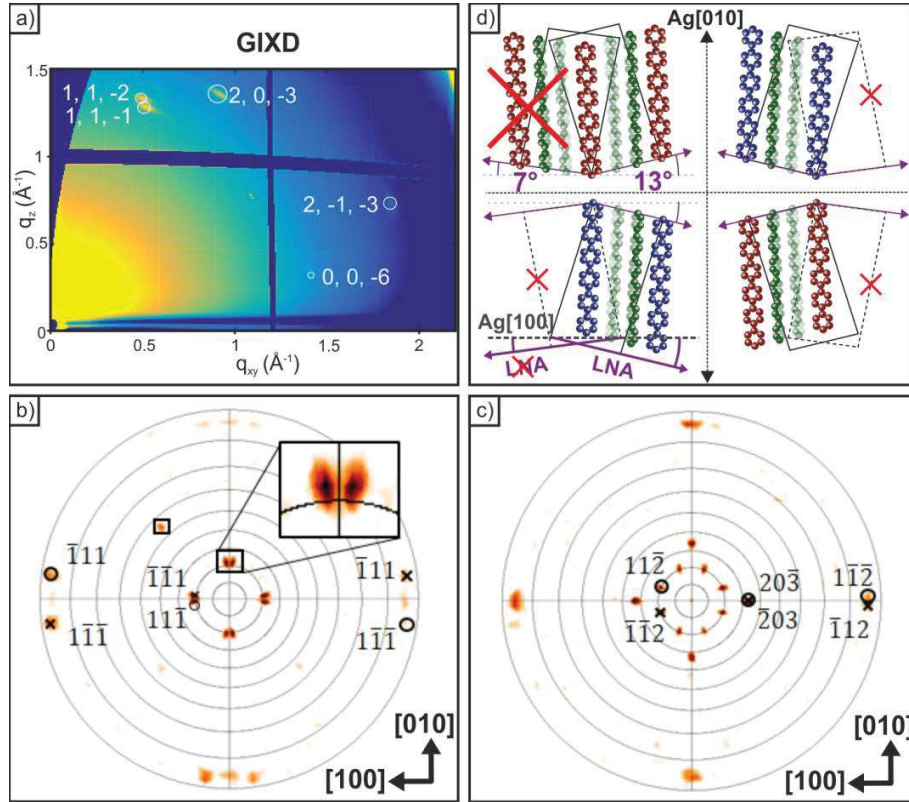


Figure 2: XRD data of the film in **Figure 1.b**: (a) GIXD pattern, indexed spots corresponding to (21 10 -28) contact plane of 6P; (b) XRD pole figure measured at the 11-1 netplane; (c) XRD pole figure measured at the 11-2 and the 20-3 netplane merged together in one image. Peaks from crystallites with a (21 10 -28) contact plane are indexed with o, crystallites with a (-21 -10 28) orientation are indexed with x. (d) Projected surface unit cells of a (21-3) contact plane for the $\langle 010 \rangle \pm 3^\circ$ molecular alignment deduced by XRD (the equivalent $\langle 100 \rangle \pm 3^\circ$ is not shown). The short unit cell vector has the direction of the molecular rows and implies the LNA. The azimuthal orientations that are not observed in the PFs are indicated with red x.

The azimuthal orientation of the molecular crystallites is obtained from XRD pole figure (PF) measurements. In **Figure 2.b** the PF is shown for the 11-1 reflections and measurements for the 11-2 and the 20-3 reflections are merged together in **Figure 2.c**. The sharpness of the pole figures implies that the crystallites are well oriented with respect to substrate azimuths with 8 symmetry equivalent orientations being observed. Around the high symmetry $\langle 100 \rangle$ directions we find reflections displaced by $\pm 4^\circ$ (inset of **Figure 2.b**). As perfectly $\text{Ag}\langle 100 \rangle$ -aligned molecules would exhibit a displacement of $\pm 13^\circ$ a misalignment of the long molecular axis is concluded. A perfect match between simulated spots and diffraction reflexes (see **Figure 2.b** and c) is obtained for an alignment of the long molecular axis of $\text{Ag}\langle 100 \rangle \pm 3^\circ$. With these two molecular alignments 16 symmetry-equivalent azimuthal orientations

could result (**Figure 2.d**), yet only 8 are observed in the PFs. The absence of 8 crystal orientations will be discussed later. The unit cell orientations are naturally reflected in the crystallite shapes, as the fast growth direction of 6P crystallites occurs along the projected low-energy surfaces (herringbone layers) of the bulk structure, defining the crystallites long needle axis (LNA). For the eight observed crystal orientations, the long needle axis can therefore be predicted to enclose an angle of 13° with the Ag<100> high symmetry directions (c.f. **Figure 2.d**), in agreement with the SFM results from **Figure 1.a**.

3.2 Thermal Desorption Spectroscopy

An overview of the 6P film growth is provided by the set of TPD data shown in **Figure 3.a**. Three distinct growth stages can be distinguished for increasing 6P film thicknesses, labeled α , β and γ . The α -peak shows no saturation and a common leading edge, indicating 0-order desorption [36] and is associated with the 6P *multilayer* (or bulk -phase). Desorption starts at ~ 410 K for coverages beyond 4.7 Å. This is in good agreement with the previously reported desorption behavior of a 6P multilayer [24].

Within the β -stage a distinct peak is observed to evolve for nominal coverages between ~ 2 and ~ 4 Å and will hence be denoted as *bilayer*. Desorption starts at ~ 430 K and exhibits a common leading edge, a slightly upward shifting maximum (~ 470 K) and a distinct saturation behavior. Note the shoulder in the 2.3 Å desorption spectrum, marked by an arrow in the inset of **Figure 3.a**, which is present only at the first occurrence of the bilayer but vanishes again with increasing coverage. A similar metastable feature was previously attributed to a mono-/multilayer transition phase [37,38], but is here indicative of a metastable mono-/bilayer transition phase. Finally, the γ -regime desorption stretches over a wide temperature range of 500 - 790 K, indicating a complex *monolayer* development. It exhibits a downward-shifting leading edge and saturates at ~ 2 Å thickness. It should be mentioned that a qualitatively similar TPD coverage series was already observed for 6P on Au(111) [16]. There, the extraordinary width of the monolayer peak is attributed to repulsive intermolecular interactions and the presence of 2 sub-phases in the monolayer regime.

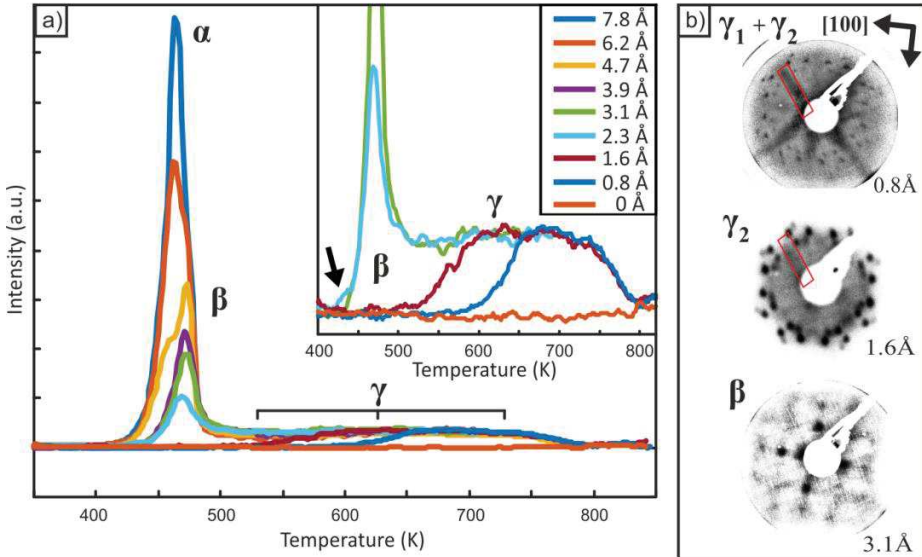


Figure 3: (a) TDS Series for increasing coverages of 6P on Ag(001) deposited at 300 K. The inset shows a magnification of the 0.0 Å to 3.1 Å spectra; (b) LEED patterns for increasing coverages of 6P on Ag(001) ($E_p = 28$ eV)

The complexity of the film growth is also reflected in the coverage-dependent development of LEED patterns as shown in **Figure 3.b**. At low coverage (top panel) the superposition of 2 distinct structures is observed. Faint streaks along the $<100>$ and $<110>$ directions producing a continuous star-shaped pattern appear together with sharp reflexes, marked with a red unit cell. The star-shaped pattern disappears upon increasing the coverage (middle panel) and is thus attributed to a sub-monolayer phase (γ_1). The sharp reflexes prevail and represent the full monolayer, named γ_2 . Increasing the coverage further into the bilayer regime (bottom panel) leads again to an abrupt change to a very different structure (β). We now turn to STM and UPS investigations of 6P/Ag(001) to obtain more detailed information about the molecular alignment during the different stages of the film growth.

3.3 Submonolayer to Monolayer

Figure 4.a shows an STM image for a nominal coverage of 0.4 Å of 6P deposited at 77 K on Ag(001). The 6P molecules appear as rod-like protrusions with their long axis aligned along the principal $<100>$ and $<110>$ substrate directions. At this coverage no long-range ordered structure forms. However, intermolecular repulsion causes a regular intermolecular spacing with nearest neighbor distances of 8-10 Å, which is larger than the vdW-width of 6P (6.7 Å) [39]. Such repulsive interactions have previously been associated with induced localized surface dipoles [40]. The lack of a long-range order and the particular alignment of the molecules is in agreement with the continuous star-shape pattern observed in

LEED (**Figure 3.b**, top panel). Hence the observed structure is attributed to the low-coverage sub-monolayer γ_1 phase.

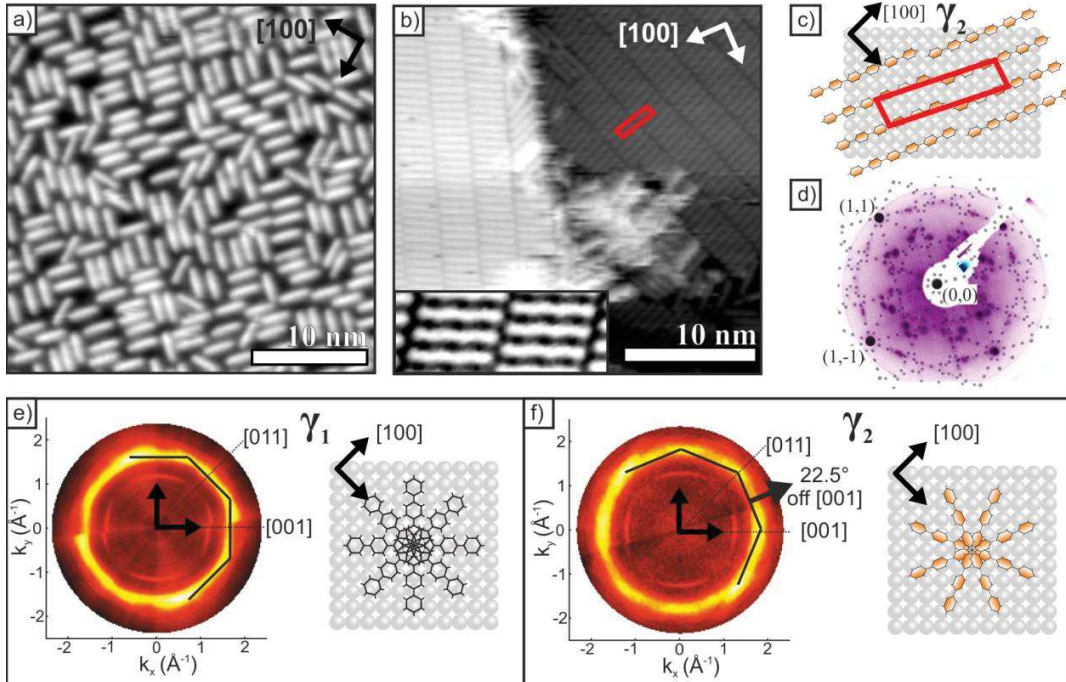


Figure 4: STM images of 6P on Ag(001) for a nominal coverage of (a) 0.4 Å and (b) 0.8 Å (This undistorted image was taken at $T_{\text{STM}} = 77$ K) (c) Model of the unit cell of the γ_2 phase (d) LEED pattern of 1.6 Å of 6P on Ag(001) ($E_{\text{el}} = 55$ eV). (e,f) Photoemission tomography data for two observed phases of 6P on Ag(001). Models for the molecular alignment of 6P with respect to the substrate are illustrated for both phases.

Patches of an ordered structure can be observed in STM upon further increasing the coverage to 0.8 Å (**Figure 4.b**), which is consistent with the γ_2 -pattern observed in LEED in **Figure 3.b**. The molecules form a long-range ordered interdigitated row structure with significantly reduced intermolecular distances of 6.1 Å. Within the ordered regions the long molecular axis has rotated compare to the sub-monolayer γ_1 phase, and is now enclosing an angle of 22.5° to the <100> crystal directions. A model of the 2-dimensional molecular alignment is shown in (**Figure 4.c**). The corresponding unit cell (marked as a red rhomboid) is

$$\begin{pmatrix} 2 & 1 \\ -3 & 9 \end{pmatrix}$$

in accordance with intermolecular distances obtained from the STM image. **Figure 4.d** depicts the simulated diffraction pattern according to the obtained unit cell superimposed onto a LEED image of a preparation with a nominal coverage of 1.6 Å. The good agreement between the simulated and the imaged diffraction pattern confirm the proposed γ_2 unit cell.

The existence of two differently oriented phases has also been observed in photoemission tomography measurements of 6P monolayers on Ag(001). **Figure 4.e** and **f** show the corresponding momentum maps recorded at the binding energy of the 6P HOMO (highest occupied molecular orbital). In both cases the maps are of octagonal shape, which, because of the fourfold symmetry of the Ag(001) substrate, suggests that the molecules acquire two alignments rotated by 45° . In addition, we find the octagons to be rotated by 22.5° . Together with the known directions of the substrate azimuths, this implies that in **Figure 4.e** the molecules are aligned along the principal Ag<100> azimuths (γ_1), while they are rotated by 22.5° with respect to the Ag<100> azimuths (γ_2) in **Figure 4.f**, as schematically shown in the models next to the momentum maps. (Note that the momentum maps were obtained for two preparations of nominally the same coverage, implying that there is a very narrow coverage regime where the phase transition occurs. In addition, we mention that a molecular realignment can also be induced by increasing the substrate temperature as shown in the **Supplementary Material**.) Furthermore, the binding energy of the HOMO in alignment γ_1 is 2.5 eV, whereas it is 2.7 eV in γ_2 , thus showing a difference of 0.2 eV (data not shown). No orbital emissions are observed in the energy region between the HOMO and E_F indicating that no charge transfer to the 6P LUMO (lowest unoccupied molecular orbital) has occurred for both alignments. This suggests a comparatively weak binding for 6P on Ag(001).

The observed molecular realignment from <100> and <110> alignments to <100> +/- 22.5° is always accompanied by a change in the appearance of the molecules in STM from flat, rod-like protrusions to a 3-fold zig-zag shape (inset in **Figure 4.b**). A similar molecular appearance was observed by *Hla et al.* [41] for isolated 6P molecules on Ag(111) and attributed to an alternating twist of the phenyl rings. An intramolecular twist of phenyl rings with torsion angles of 22.7° and 40° was previously shown to be present in 6P bulk and gas-phase, respectively [42,43]. Moreover, it was found that the attractive π - π interactions of phenyl rings facing each other are of long-range electrostatic nature [44]. Hence, we conclude that after overcoming the initial intermolecular repulsion, attractive π - π interactions trigger a twisted molecular conformation in the 6P monolayer and a realignment of the twisted molecular bundle with respect to the substrate.

DFT calculations were performed to further support the proposed twist-mediated realignment. First, we have considered adsorption geometries within the submonolayer with molecules either oriented along the <100> and <110> substrate directions or rotated by 22.5° with respect to these directions and with a long axis separation of ~ 9 Å. For each alignment, four high symmetry adsorption sites for both a flat and a 20° twisted molecular conformation have been considered. We find that the <100> and <110> alignment is energetically preferred over the 22.5° rotated one (by about 200 meV). Furthermore, we observe that the

initially twisted molecules adopt a planar configuration during the geometry optimization. This confirms the experimental finding that the 6P molecules prefer a flat adsorption configuration in the dilute molecular layer with their long molecular axis aligned along the principle azimuths (see **Figure 4.a**). Secondly, we have calculated the full monolayer in the experimentally observed γ_2 overlayer structure, with the molecules rotated 22.5° away from the high symmetry directions. Again, both planar and twisted 6P molecules were used as starting points for the geometry relaxation. In agreement with experiment, we find that the twisted molecular conformation is more stable in the full monolayer. Even when starting from a planar molecular configuration the phenyl rings twist during the structure relaxation giving rise to an angle of 20° between phenyl rings. This confirms that the change in molecular conformation occurs due to the change in molecular density rather than due to the different adsorption directions. The molecular alignment of the planar γ_1 -phase and the twisted γ_2 -phase, is schematically displayed on the right hand-side of **Figure 4.e** and **f**, respectively. Note that the twist of the molecule with respect to the substrate induces a 2D-chirality or pro-chirality of the *per se* achiral 6P molecule [45].

3.4 Monolayer-to-bilayer transition

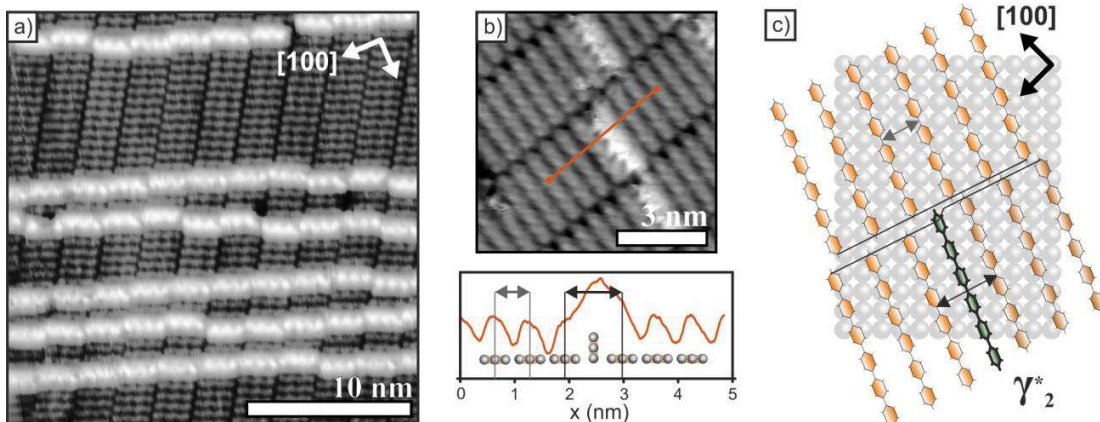


Figure 5: STM images of the saturating monolayer for a coverage of 1.6 Å of 6P on Ag(001) (**a**) Overview ($U_{\text{Bias}} = -187$ mV, $I_{\text{Tunnel}} = 200$ pA). (**b**) Close-up of an ad-on molecule ($U_{\text{Bias}} = -642$ mV, $I_{\text{Tunnel}} = 1500$ pA) with corresponding line scan. Grey and black segments indicate regular and dislocated nearest neighbor distances. (**c**) Model of a single edge-on molecule (green) incorporated into the γ_2 phase. Segments scale to the line-scan derived values. The black lines visualize the molecular row offset which is induced by the introduction of an edge-on molecule.

When increasing the nominal coverage to 1.6 Å, bright strings of molecules appear on top of the monolayer, exhibiting a similar zig-zag shape as the molecules in the γ_2 -phase (**Figure 5.a**). To clarify

whether the strings are ad-molecules on top of the first layer (flat-on) or whether they are molecules incorporated into the monolayer (edge-on [46]), the region around the ad-molecules was looked at in more detail. The higher resolution STM image shown in **Figure 5.b** and the corresponding line scan reveals a dislocation within the molecular row of the γ_2 phase at the position of the ad-molecule. The dislocation (black arrow) has a width of 1.62 regular intermolecular distances (gray arrow). Because a flat ad-molecule would not give rise to a change in the periodicity of the molecular row underneath, we thus conclude that the protrusion can be associated with an incorporated edge-on molecule. In **Figure 5.c** an effort is made to provide an atomic model of the γ_2 row structure with an incorporated edge-on molecule. In order to retain equivalent adsorption sites for the regularly adsorbed 6P molecules next to the dislocation, a slight displacement along the molecular axis is necessary, leading to a decreased (or increased) gap distance between neighboring molecular rows (black line as visual aid). This in turn changes the interdigitated γ_2 row structure to a strained end-on/end-on structure of molecules in neighboring rows. The occurrence of end-on/end-on molecules was already attributed to govern molecular reconstruction processes for 6P on Cu(110) [6]. We argue that the strain is released by the consecutive incorporation of edge-on molecules in neighboring molecular rows, preserving the row-to-row gap distance and resulting in the formation of the observed strings in STM. However, it has to be mentioned that row-to-row gaps with varying gap distance do also occur (**Figure 5.a**). Interestingly, we observe the preservation of twist direction (zig-zag phase) for molecules of neighboring rows separated by short gaps while large gaps are observed to induce twist alternations. The twist direction is obviously strongly correlated with the adsorption site because of the rotated alignment of the molecules with respect to the high-symmetry Ag<100> directions and the associated asymmetric potential (different twist directions (zig-zag phases) give rise to adsorption energy differences of up to 80 meV for the same adsorption site according to DFT). This suggests that molecules are adsorbed at slightly different adsorption sites in neighboring rows separated by large gaps.

Increasing the 6P coverage further results in an increase of incorporated edge-on molecules, until a critical density (1 edge-on per 2 flat-on molecules) is reached at around 2 Å. The abrupt transition in the observed LEED patterns (1.6 Å to 3.1 Å in **Figure 3.b**) together with the observed metastable peak in TDS (2.3 Å, arrow in **Figure 3.a**) strongly indicate that the edge-on/flat-on phase merely acts as a transition phase from the ordered monolayer γ_2 to the bilayer β and will hence be named the γ_2^* transition phase. For the sake of completeness we mention that two additional phases, coexisting with the γ_2 phase, were observed after desorbing a 6P multilayer. A corresponding STM image is shown in the **Supplementary Material**.

3.5 Bilayer

At a nominal thickness of 2.3 Å already large areas of the surface exhibit a well-developed new phase (β phase) in STM (**Figure 6.a**), consisting of vertically stacked molecules forming a 3-dimensional structure with a triangular cross-section. The red and a blue arrows in **Figure 6.a** mark the observed molecular alignments in the β phase, which include an angle of $+/- 2.5^\circ$ with the substrates $<100>$ directions (see model in **Figure 6.b**). This indicates yet another molecular realignment with increasing coverage occurring during the transition from the γ_2^* to the β phase. A zoomed-in STM image (**Figure 6.c**) around a domain boundary reveals important details of the nature of the β phase. We find that the interfacial molecules (observable in the area enclosed by the yellow ellipse) have the same molecular alignment as the second and higher layer molecules, confirming that a realignment of the entire film has occurred. Furthermore, the structure of the compact interfacial layer of the β phase (marked with a red ellipse) is observed to consist of edge-on and flat-on molecules in a 1:1 ratio. A model of this compact interfacial layer is shown in **Figure 6.d**.

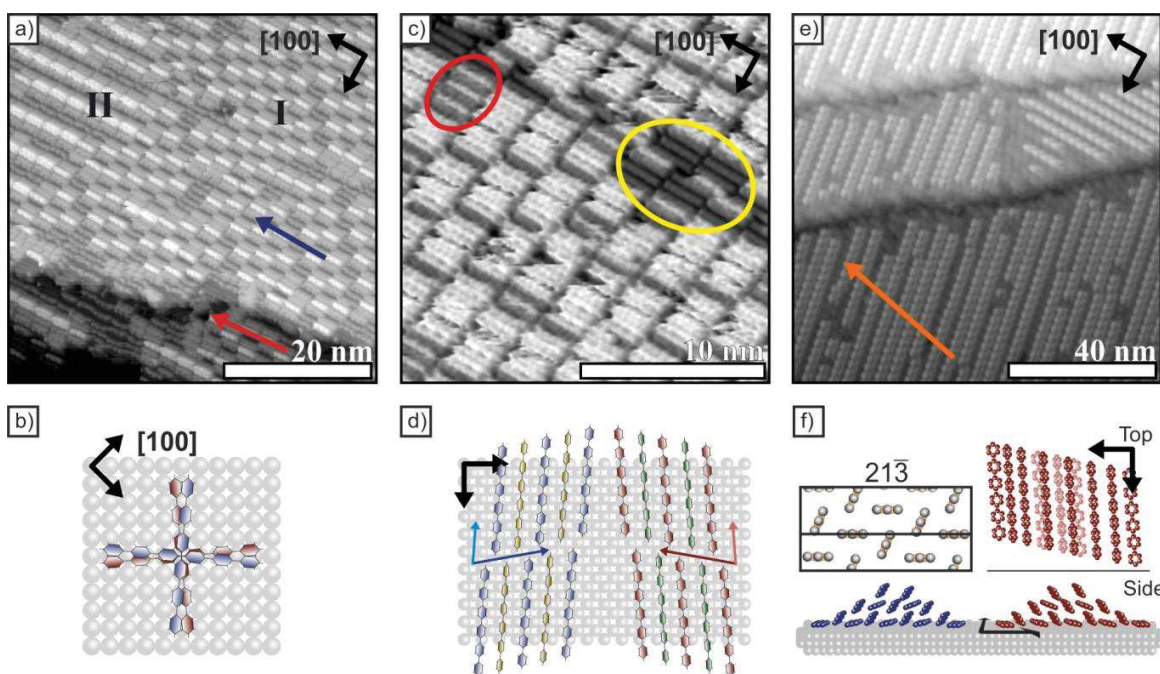


Figure 6: STM images of the bilayer phase (**a,c,e**) (Nominal coverage = [2.3 Å , 2.3 Å , 3.1 Å], $U_{\text{Bias}} = [344, 500, 2024]$ mV, $I_{\text{Tunnel}} = [32, 67, 28]$ pA). (**b**) Alignment scheme of 6P on Ag(001) within the bilayer (**d**) Schematic of the proposed compact interfacial layer upon which the bilayer is growing. The arrows indicate the observed long molecular axis and the direction of the molecular rows for both molecular alignments. (**f**) 3D model of the saturated bilayer (β_{II}) phase.

At closer inspection two distinctive patterns can be distinguished in **Figure 6.a**: (β_1) resembling a checkerboard-like structure and (β_{II}) consisting of bright ridges. Both structures evolve with a similar molecular row direction (in agreement with the proposed interfacial layer) and are topped by one (β_1) or two (β_{II}) molecules of similar apparent height. We propose that the development of this 3D structure (bilayer) causes increased intermolecular forces which in turn trigger the observed second realignment of the entire molecular film, similar to the first 2D realignment in the γ_2 phase (see section 3.3).

Upon increasing the nominal coverage to 3.1 Å, near completion of the bilayer according to TPD, the abundance of the molecular ridge structure (β_{II}) increases at the expense of the checkerboard (β_1) structure (**Figure 6.e**). The majority of the observed ridge structures exhibits a molecular row direction enclosing an angle of +/- 11° to the high symmetry <100> substrate directions (orange arrow in **Figure 6.e**). The β_{II} structure is also obtained from thicker films after desorption of the multilayer at 450 K, indicating that this structure represents the saturated bilayer phase. A model of the proposed internal structure of the β_{II} phase is shown in **Figure 6.f**. Note that the compact interface layer in this model has already strong similarities with the herringbone arrangement of the bulk structure.

We now turn to relate the molecular structure of the saturated bilayer (~4 Å) to the results of the thick film preparation (300 Å) reported in section 3.1. The molecular alignment in the thick film was found to be +/- 3° with respect to the substrates <100> directions according to XRD, which fits perfectly to the molecular alignment of the β_{II} phase as determined from the STM images, confirming that the bilayer is the template for multilayer growth. As such, the molecular row direction in the β_{II} phase is believed to determine the LNA of the crystallites in the thick film. Indeed, as pointed out in section 3.1, only 8 of the 16 crystal orientations possible for the observed molecular alignment are seen in XRD. Those have Ag<100> +/- 13° oriented LNAs, in good agreement with the bilayer row direction, which was determined to be Ag<100> +/- 11°. The slight discrepancy between the observed molecular row direction of the wetting layer and the LNA direction of the bulk structure is presumably related to the development of the more complex (21 10 -28) contact plane and the structure of the observed saturated bilayer phase. The missing 8 orientations would exhibit a LNA of Ag<100> +/- 7°. As no compatible molecular row direction forms in the bilayer, the development of 3-dimensional crystallites with these orientations is not possible.

4. Conclusion

Within this work we applied a multitude of experimental techniques (STM, LEED, TPD, UPS, SFM, XRD) and theoretical calculations (DFT) to investigate the development of the macroscopic bulk phase starting from the adsorption of isolated molecules for 6P on Ag(001).

At sub-monolayer coverage, 6P adsorbs as isolated molecule in a planar conformation. Upon increasing the coverage close to a full monolayer the repulsive forces between the isolated molecules are overcome and the molecules adopt a twisted conformation with increased intermolecular interactions (2D). This is responsible for the first realignment of molecular clusters. For the twisted conformation calculations yield a tilt between neighboring phenyl rings of $\sim 20^\circ$. Further increasing the coverage results in the incorporation of lines of edge-on molecules until a critical density of 2:1 flat-on to edge-on molecules is reached. When continuing the deposition of 6P, a second realignment of the molecules occurs collectively for whole domains, triggered by the increased intermolecular interaction due to the 3D structure of the bilayer. The saturated bilayer is identified as the template for macroscopic crystallites and determines the molecular and crystallite alignment, the contact plane and the orientations of the final organic thin film.

In summary, we could show that a complex growth process involving various stages and including molecular realignment precedes the epitaxial growth of a well-ordered thin film. Understanding the delicate balance between molecule/substrate and intermolecular interactions, further complicated by the flexibility of the organic molecules, is therefore necessary in the quest for designable organic thin-films.

5. Acknowledgement

We thank Helmholtz Zentrum Berlin for the allocation of synchrotron radiation beam time. The research leading to these results has received funding from the European Community's Seventh Framework Programme (FP7/2007-2013) under Grant Agreement No. 312284.

The authors acknowledge the Elettra Sincrotrone Trieste for allocation of synchrotron radiation beamtime. The authors are grateful to Nicola Demitri and Luisa Barba for providing assistance in using beamline XRD1 and Benedikt Schrode and Oliver Werzer for supporting the experiments. D.L. and P.P. acknowledge support from the Austrian Science Fund (FWF) project P27649-N20.

References

- [1] J. Kjelstrup-Hansen, C. Simbrunner, H.-G. Rubahn, Organic surface-grown nanowires for functional devices, *Rep. Prog. Phys.* 76 (12) (2013) 126502.
- [2] H. Klauk, Organic thin-film transistors, *Chem. Soc. Rev.* 39 (7) (2010) 2643–2666.

- [3] M. Kratzer, C. Teichert, Thin film growth of aromatic rod-like molecules on graphene, *Nanotechnology* 27 (29) (2016) 292001.
- [4] A. Matković, M. Kratzer, B. Kaufmann, J. Vujin, R. Gajić, C. Teichert, Probing charge transfer between molecular semiconductors and graphene, *Sci. Rep.* 7 (1) (2017) 9544.
- [5] A.J. Fleming, S. Berkebile, T. Ules, M.G. Ramsey, Pre-nucleation dynamics of organic molecule self-assembly investigated by PEEM, *Physical chemistry chemical physics PCCP* 13 (10) (2011) 4693–4708.
- [6] M. Wagner, S. Berkebile, F.P. Netzer, M.G. Ramsey, Revealing the Buried Metal-Organic Interface: Restructuring of the First Layer by van der Waals Forces, *ACS Nano* 9 (12) (2015) 12070–12078.
- [7] G. Grem, V. Martin, F. Meghdadi, C. Paar, J. Stampfl, J. Sturm, S. Tasch, G. Leising, Stable poly(para-phenylene)s and their application in organic light emitting devices, *Synthetic Met.* 71 (1-3) (1995) 2193–2194.
- [8] R. Resel, Surface induced crystallographic order in sexiphenyl thin films, *J. Phys.: Condens. Matter* 20 (18) (2008) 184009.
- [9] C. Simbrunner, Epitaxial growth of sexi-thiophene and para-hexaphenyl and its implications for the fabrication of self-assembled lasing nano-fibres, *Semicond. Sci. Technol.* 28 (5) (2013) 53001.
- [10] G. Hlawacek, C. Teichert, A.Y. Andreev, H. Sitter, S. Berkebile, G. Koller, M. Ramsey, R. Resel, Self-organization of para-sexiphenyl on crystalline substrates, *Phys. Status Solidi A* 202 (12) (2005) 2376–2385.
- [11] T. Haber, M. Oehzelt, R. Resel, A. Andreev, A. Thierry, H. Sitter, D.-M. Smilgies, B. Schaffer, W. Grogger, Single Crystalline Nature of para-Sexiphenyl Crystallites Grown on KCl(100), *J. Nanosci. Nanotech.* 6 (3) (2006) 698–703.
- [12] H. Kirmse, M. Sparenberg, A. Zykov, S. Sadofev, S. Kowarik, S. Blumstengel, Structure of p - Sexiphenyl Nanocrystallites in ZnO Revealed by High-Resolution Transmission Electron Microscopy, *Cryst. Growth Des.* 16 (5) (2016) 2789–2794.
- [13] T. Haber, S. Muellegger, A. Winkler, R. Resel, Temperature-induced epitaxial growth modes of para-sexiphenyl on Au(111), *Phys. Rev. B* 74 (4) (2006) 2288.
- [14] M. Kratzer, S. Klima, C. Teichert, B. Vasić, A. Matković, U. Ralević, R. Gajić, Temperature dependent growth morphologies of parahexaphenyl on SiO₂ supported exfoliated graphene, *J. Vac. Sci. Technol. B* 31 (4) (2013) 04D114.
- [15] E.J. Kintzel, D.-M. Smilgies, J.G. Skofronick, S.A. Safron, D.H. van Winkle, Effect of temperature on the growth of ultrathin films of p -sexiphenyl on KCl(001), *J. Vac. Sci. Technol. A* 22 (1) (2004) 107–110.
- [16] S. Müllegger, A. Winkler, Hexaphenyl thin films on clean and carbon covered Au(111) studied with TDS and LEED, *Surf. Sci.* 600 (6) (2006) 1290–1299.
- [17] D. Wrana, M. Kratzer, K. Szajna, M. Nikiel, B.R. Jany, M. Korzekwa, C. Teichert, F. Krok, Growth of para -Hexaphenyl Thin Films on Flat, Atomically Clean versus Air-Passivated TiO₂ (110) Surfaces, *J. Phys. Chem. C* 119 (29) (2015) 17004–17015.
- [18] J. Novák, M. Oehzelt, S. Berkebile, M. Koini, T. Ules, G. Koller, T. Haber, R. Resel, M.G. Ramsey, Crystal growth of para-sexiphenyl on clean and oxygen reconstructed Cu(110) surfaces, *Phys. Chem. Chem. Phys.* 13 (32) (2011) 14675–14684.
- [19] W. Chen, H. Huang, A. Thye, S. Wee, Molecular orientation transition of organic thin films on graphite: the effect of intermolecular electrostatic and interfacial dispersion forces, *Chem. Commun.* (36) (2008) 4276–4278.

- [20] L. Sun, S. Berkebile, G. Weidlinger, G. Koller, M. Hohage, F.P. Netzer, M.G. Ramsey, P. Zeppenfeld, Revealing the buried interface: para-sexiphenyl thin films grown on TiO₂(110), *Phys. Chem. Chem. Phys.* 12 (13) (2010) 3141–3144.
- [21] B. Winter, J. Ivanco, F.P. Netzer, M.G. Ramsey, I. Salzmann, R. Resel, Epitaxial growth of sexiphenyl on Al(111): from monolayer to crystalline films, *Langmuir* 20 (18) (2004) 7512–7516.
- [22] D.-M. Smilgies, E.J. Kintzel, Epitaxial orientations of para -sexiphenyl platelets grown on alkali halide (001) surfaces, *Phys. Rev. B* 79 (23) (2009) 53.
- [23] R. Otero, J.M. Gallego, de Parga, Amadeo L. Vázquez, N. Martín, R. Miranda, Molecular Self-Assembly at Solid Surfaces, *Adv. Mater.* 23 (44) (2011) 5148–5176.
- [24] A. Winkler, On the nucleation and initial film growth of rod-like organic molecules, *Surf. Sci.* 652 (2016) 367–377.
- [25] D. Nečas, P. Klapetek, Gwyddion: An open-source software for SPM data analysis, *Open Phys.* 10 (1) (2012).
- [26] I. Salzmann, R. Resel, STEREOPOLE: Software for the analysis of X-ray diffraction pole figures with IDL, *J. Appl. Crystallogr. (Journal of Applied Crystallography)* 37 (6) (2004) 1029–1033.
- [27] G. Kresse, J. Hafner, Ab initio molecule dynamics for liquid metals, *Phys. Rev. B* 47 (1993) 558.
- [28] G. Kresse, D. Joubert, From ultrasoft pseudopotentials to the projector augmented-wave method, *Phys. Rev. B* 59 (1999) 1758.
- [29] J. Neugebauer, M. Scheffler, Adsorbate-substarte and adsorbate-adsorbate interactions of Na and K adlayers on Al(111), *Phys. Rev. B* 46 (1992) 16067.
- [30] J.P. Perdew, K. Burke, M. Ernzerhof, Generalized Gradient Approximation Made Simple, *Phys. Rev. Lett.* 77 (1996) 3865.
- [31] H.J. Monkhorst, J.D. Pack, Special points for Brillouin-zone integrations, *Phys. Rev. B* 13 (1976) 5188.
- [32] P.E. Blöchl, Projector augmented-wave method, *Phys. Rev. B* 50 (1994) 17953.
- [33] A. Tkatchenko, M. Scheffler, Accurate Molecular Van Der Waals Interactions from Ground-State Electron Density and Free-Atom Reference Data, *Phys. Rev. Lett.* 102 (2009) 73005.
- [34] V.G. Ruiz, W. Liu, E. Zojer, M. Scheffler, A. Tkatchenko, Density-Functional Theory with Screened van der Waals Interactions for the Modeling of Hybrid Inorganic-Organic Systems, *Phys. Rev. Lett.* 108 (14) (2012) 146103.
- [35] K.N. Baker, A.V. Fratini, T. Resch, H.C. Knachel, W.W. Adams, E.P. Soccia, B.L. Farmer, Crystal structures, phase transitions and energy calculations of poly(p-phenylene) oligomers, *Polymer* 34 (8) (1993) 1571–1587.
- [36] Richard I. Masel, Principles of adsorption and reaction on solid surfaces, 3rd ed., John Wiley & Sons, 1996.
- [37] P. Jakob, D. Menzel, Benzene multilayers: A model for their anisotropic growth from vibrational spectroscopy and thermal desorption, *Surf. Sci.* 220 (1) (1989) 70–95.
- [38] G. Koller, R.I.R. Blyth, S.A. Sardar, F.P. Netzer, M.G. Ramsey, Growth of ordered bithiophene layers on the p(2x1)O reconstructed Cu(110) surface, *Surface Science* 536 (1-3) (2003) 155–165.
- [39] R. Resel, I. Salzmann, G. Hlawacek, C. Teichert, B. Koppelhuber, B. Winter, J. K. Krenn, J. Ivanco, M. G. Ramsey, Structure and morphology of sexiphenyl thin films grown on aluminium (111), *Org. Electron.* 5 (1-3) (2004) 45–51.
- [40] S. Müllegger, I. Salzmann, R. Resel, G. Hlawacek, C. Teichert, A. Winkler, Growth kinetics, structure, and morphology of para-quaterphenyl thin films on gold(111), *J. Chem. Phys.* 121 (5) (2004) 2272–2277.

- [41] K.-F. Braun, S.-W. Hla, Probing the conformation of physisorbed molecules at the atomic scale using STM manipulation, *Nano Lett.* 5 (1) (2005) 73–76.
- [42] G. Koller, S. Berkebile, M. Oehzelt, P. Puschnig, C. Ambrosch-Draxl, F.P. Netzer, M.G. Ramsey, Intra- and intermolecular band dispersion in an organic crystal, *Science* 317 (5836) (2007) 351–355.
- [43] B. Champagne, D.H. Mosley, J.G. Fripiat, J.-M. André, Ab initio investigation of the electronic properties of planar and twisted polyparaphenylenes, *Phys. Rev. B* 54 (4) (1996) 2381–2389.
- [44] S. Tsuzuki, K. Honda, T. Uchimaru, M. Mikami, K. Tanabe, Origin of Attraction and Directionality of the π/π Interaction: Model Chemistry Calculations of Benzene Dimer Interaction, *J. Am. Chem. Soc.* 124 (1) (2002) 104–112.
- [45] S.M. Barlow, R. Raval, Complex organic molecules at metal surfaces: Bonding, organisation and chirality, *Surf. Sci. Rep.* 50 (6-8) (2003) 201–341.
- [46] C.B. France, B.A. Parkinson, Physical and electronic structure of p -sexiphenyl on Au(111), *Appl. Phys. Lett.* 82 (8) (2003) 1194–1196.

Supplementary Material

a) AFM Analysis

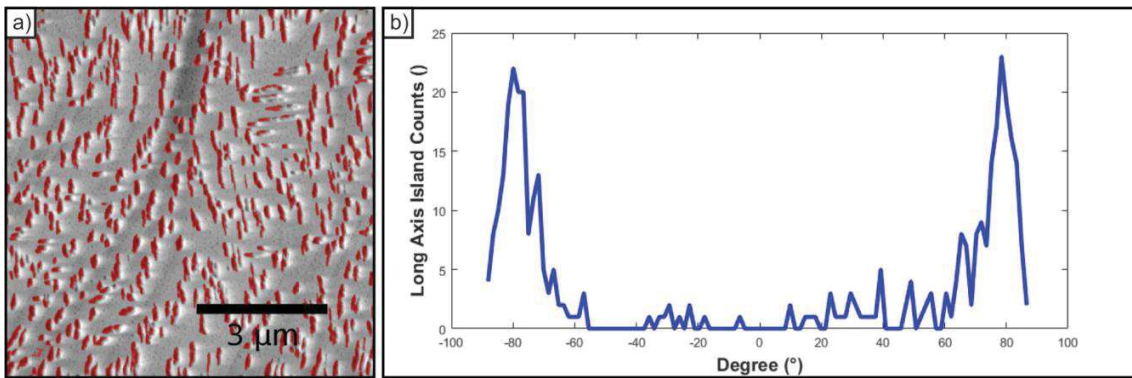


Figure 1: Island analysis of the AFM measurement for the film presented in section **Thick films** for a nominal coverage of 30 Å. Base for the analysis is given on the left side with the considered islands marked by a red mask. Analysis (right image) depicts a histogram of long needle axis orientations.

In **Figure 1** the statistical analysis of the AFM image for the 30 Å preparation of 6P on Ag(001) is shown. The AFM image shows the derivative data of the film topography. Analysis was done with *Gwyddion* software, using automated island recognition and additional filters for minimum island sizes. The Analysis shows a histogram of the long island axis alignment defined as the direction of maximum island dimension. We observe distinct maxima for $[100] \pm 11^\circ$. For the given image few islands are observed along the $[010]$ direction which is also the scanning direction and hence results in poor island statistic.

b) STM Temperature Series

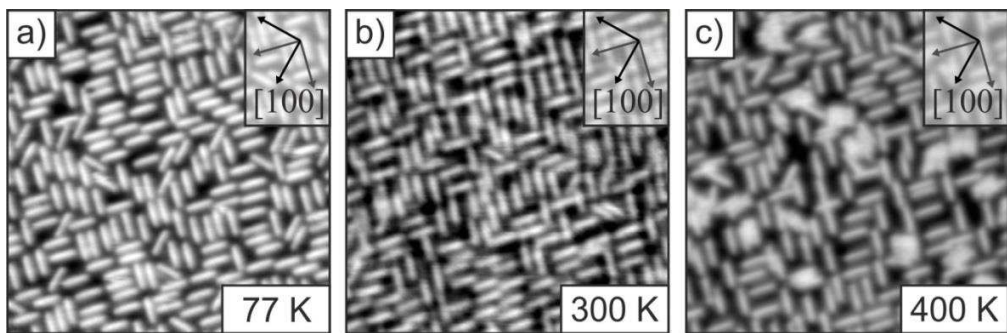


Figure 2: STM - Temperature Series of a nominal coverage of 0.4 Å 6P deposited on Ag(001) at (a) 77 K (658 mV, 42 pA) and after annealing to (b) 300 K (-824mV, 15pA) and (c) 400 K (-390 mV, 40pA).

To investigate the details of the observed reorientation of the molecular layer a STM temperature series for low coverages was conducted. Starting with a nominal deposition of 0.4 Å of 6P on Ag(001) at 77 K and subsequent cooling to 5 K (**Figure 2.a**) the molecules adsorb in the above described γ_1 -phase, aligning along the principal $<100>$ and $<110>$ crystal directions. Flashing of the sample to 300 K (**Figure 2.b**) and subsequent cooling to 5 K results in little change, except for a slight decrease in $<100>$ orientations. When further increasing the flashing temperature to 400 K (**Figure 2.c**) small densely packed clusters are observed in which the molecules have rotated by 22.5° , now resembling the γ_2 -phase. We therefor conclude that the reorientation of the molecules is linked to the formation of molecular clusters by overcoming the initial intermolecular repulsive forces. This can be achieved by either supplying thermal energy or increasing the molecular density.

c) Additionally Observed Monolayer Phases

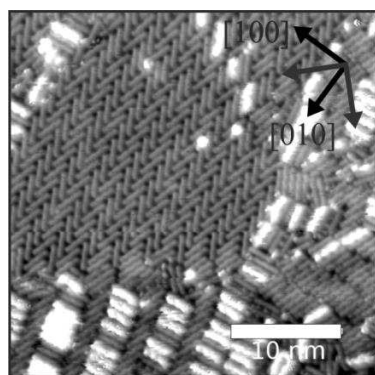


Figure 3: STM image of an additional monolayer phase of 6P on Ag(001) observed after annealing of a multilayer preparation. (-866 mV, 110 pA)

In **Figure 3** an STM image of a multilayer preparation of nominally 4.7 Å is shown after annealing to 500 K. In the upper part of the picture a well-ordered herringbone-like structure (1) is visible. The molecules alternately exhibit a $+22.5^\circ$ and -22.5° orientation with respect to the Ag[010] direction. In the lower left part a different phase (2) is observed. Molecular rows with a $+22.5^\circ$ [010] orientation alternate with molecules of a [100] orientation. Bright molecules indicate the presence of edge-on molecules or even stacked molecules in this orientation. In the lower right part the discussed γ_2 phase is still present. Overall the γ_2 phase and phase 1 were predominantly observed for this preparation.

ACADEMIC CONTRIBUTIONS

List of publications

- 2018 *On the decoupling of molecules at metal surfaces*, X. Yang, I. Krieger, D. Lüftner, S. Weiß, T. Heepenstrick, M. Hollerer, P. Hurdax, G. Koller, M. Sokolowski, P. Puschnig, M. G. Ramsey, F. S. Tautz and S. Soubatch, *Chemical Communications*, DOI: 10.1039/C8CC03334J
- 2018 *Correlation length and dimensional crossover in a quasi-one-dimensional surface system*, S. Dürrbeck, M. Hollerer, C. W. Thurner, J. Redinger, M. Sterrer, and E. Bertel, *Physical Review B*, DOI: 10.1103/PhysRevB.98.035436
- 2018 *Growth study of para-sexiphenyl on Ag(001): From single molecule to bulk*, M. Hollerer, S. Pachmajer, D. Lüftner, B. Butej, E.-M. Reinisch, P. Puschnig, G. Koller, R. Resel, M. Ramsey and M. Sterrer, *Surface Science (SI KH Rieder)*, in press, DOI: 10.1016/j.susc.2018.04.017
- 2017 *Model Systems in Heterogeneous Catalysis: Towards designing and understanding of structure and electronic properties*, Q. Pan, L. Li, S. Shaikhutdinov, Y. Fujimori, M. Hollerer, M. Sterrer and H.-J. Freund, *Faraday Discussions*, DOI: 10.1039/C7FD00209B
- 2017 *Charge Transfer and Orbital Level Alignment at Inorganic/Organic Interfaces: The Role of Dielectric Interlayers*, M. Hollerer, D. Lüftner, P. Hurdax, T. Ules, S. Soubatch, F. S. Tautz, G. Koller, P. Puschnig, M. Sterrer and M. G. Ramsey, *ACS Nano*, DOI: 10.1021/acsnano.7b02449
- 2015 *Optimizing pentacene thin-film transistor performance: Temperature and surface condition induced layer growth modification*, R. Lassnig, M. Hollerer, B. Striedinger, A. Fian, B. Stadlober and A. Winkler, *Organic Electronics*, DOI: 10.1016/j.orgel.2015.08.016
- 2015 *Supports and Modified Nano-particles for Designing Model Catalysts*, C. O'Brien, K.. Dostert, M. Hollerer, C. Stiehler, F. Calaza, S. Schauermann, S. Shaikhutdinov, M. Sterrer and H.J. Freund, *Faraday Discussions*, DOI: 10.1039/C5FD00143A
- 2014 *In situ preparation, electrical and surface analytical characterization of pentacene thin film transistors*, R. Lassnig, B. Striedinger, M. Hollerer, A. Fian, B. Stadlober and A. Winkler, *Journal of Applied Physics*, DOI: 10.1063/1.4895992

Contributions in scientific conferences

2018	ÖPG	Graz, Austria	Talk
2018	ICN+T	Brno, Czech Rep.	Talk
2018	VI San Luis Conference	Santa Fe, Argentina	Talk
2018	GÖCH	Graz, Austria	Poster
2017	Workshop FHI Berlin (CP)	Dölnsee, Germany	Talk
2017	DPG	Dresden, Germany	Talk
2016	ÖPG	Vienna, Austria	Talk
2016	ECOSS 32	Grenoble, France	Talk

8 Acknowledgment

I want to express my deep gratitude to my supervisor Martin Sterrer, for giving me the opportunity to do exciting fundamental research on my own terms in a professional and well supported surrounding. I enjoyed the last four years under his supervision and gained a lot from his support and guidance. I also want to acknowledge Mike Ramsey for his advice and insight within and without the laboratory, as well as Peter Puschnig and Georg Koller for the successful collaboration. Furthermore, I want to thank Margareta Wagner for the introduction into the technical finesse of the LT-STM. You did lay an important foundation for the successful scientific work i could contribute.

A most important contribution is the everyday life within the intense time of the PhD thesis. I therefore genuinely want to express my thanks to all the people who contributed to the good atmosphere within the group, who offered there technical, scientific and personal advice throughout the good and the hard times. To Matthias Blatnik, Sascha Pomp and Peter Seidl, who have been there for me through the most part of my PhD, as well as to Jasmin Abdou, Larissa Egger, Phillip Hurdax, Daniel Lüftner, David Kuhness, Thomas Radlinger, Florian Schwarz, Thomas Ules and all the rest of our group for the shared discussions, laughs and tears. Additionally, lots of help was provided by all the technical and bureaucratic support, by the brilliant workshop of Kurt Ansperger, Robert Holzapfel and Uwe Weilguny, the electronic workshop with Franz Hanauer, by the technical support with their continuous helping hands of Günther Frömmel and Anto Maric and finally by the ever smiling and helpful secretaries, Daniela Gaar and Karin Sorko.

Last but not least, I'm most obliged to my parents, who have nurtured and educated me to the person i have grown to be. To my family, my girlfriend and my friends for their continuous support throughout my life... Thank you!

Bibliography

- [1] F. Calaza, C. Stiehler, Y. Fujimori, M. Sterrer, S. Beeg, M. Ruiz-Oses, N. Nilius, M. Heyde, T. Parviainen, K. Honkala, H. Häkkinen, and H.-J. Freund, “Carbon dioxide activation and reaction induced by electron transfer at an oxide-metal interface,” *Angewandte Chemie (International ed. in English)*, vol. 54, no. 42, pp. 12484–12487, 2015.
- [2] R. Włodarczyk, M. Sierka, K. Kwapień, J. Sauer, E. Carrasco, A. Aumer, J. F. Gomes, M. Sterrer, and H.-J. Freund, “Structures of the ordered water monolayer on mgo(001),” *Journal of Physical Chemistry C*, vol. 115, no. 14, pp. 6764–6774, 2011.
- [3] S. Schintke and W.-D. Schneider, “Insulators at the ultrathin limit: Electronic structure studied by scanning tunnelling microscopy and scanning tunnelling spectroscopy,” *Journal of physics. Condensed matter : an Institute of Physics journal*, vol. 16, no. 4, pp. R49–R81, 2004.
- [4] M. C. Gallagher, M. S. Fyfield, L. A. Bumm, J. P. Cowin, and S. A. Joyce, “Structure of ultrathin mgo films on mo(001),” *Thin Solid Films*, vol. 445, no. 1, pp. 90–95, 2003.
- [5] G. Pacchioni, L. Giordano, and M. Baistrocchi, “Charging of metal atoms on ultrathin mgo/mo(100) films,” *Physical Review Letters*, vol. 94, no. 22, 2005.
- [6] L. Giordano and G. Pacchioni, “Charge transfers at metal/oxide interfaces: A dft study of formation of k δ + and au δ - species on mgo/ag(100) ultra-thin films from deposition of neutral atoms,” *Physical Chemistry Chemical Physics*, vol. 8, no. 28, pp. 3335–3341, 2006.
- [7] L. Giordano, F. Cinquini, and G. Pacchioni, “Tuning the surface metal work function by deposition of ultrathin oxide films: Density functional calculations,” *Physical Review B*, vol. 73, no. 4, 2006.
- [8] M. Sterrer, T. Risze, U. Martinez Pozzoni, L. Giordano, M. Heyde, H.-P. Rust, G. Pacchioni, and H.-J. Freund, “Control of the charge state of metal atoms on thin mgo films,” *Physical Review Letters*, vol. 98, no. 9, 2007.
- [9] D. Ricci, A. Bongiorno, G. Pacchioni, and U. Landman, “Bonding trends and dimensionality crossover of gold nanoclusters on metal-supported mgo thin films,” *Physical Review Letters*, vol. 97, no. 3, 2006.
- [10] M. Sterrer, T. Risze, M. Heyde, H.-P. Rust, and H.-J. Freund, “Crossover from three-dimensional to two-dimensional geometries of au nanostructures on thin

Bibliography

- mgo(001) films: A confirmation of theoretical predictions,” *Physical Review Letters*, vol. 98, no. 20, 2007.
- [11] X. Lin, N. Nilius, M. Sterrer, P. Koskinen, H. Häkkinen, and H.-J. Freund, “Characterizing low-coordinated atoms at the periphery of mgo-supported au islands using scanning tunneling microscopy and electronic structure calculations,” *Physical Review B*, vol. 81, no. 15, 2010.
 - [12] X. Lin, N. Nilius, H.-J. Freund, M. Walter, P. Frondelius, K. Honkala, and H. Häkkinen, “Quantum well states in two-dimensional gold clusters on mgo thin films,” *Physical Review Letters*, vol. 102, no. 20, p. 206801, 2009.
 - [13] D. Braga and G. Horowitz, “High-performance organic field-effect transistors,” *Advanced Materials*, vol. 21, no. 14-15, pp. 1473–1486, 2009.
 - [14] H. Offenbacher, D. Luftner, T. Ules, E. M. Reinisch, G. Koller, P. Puschnig, and M. G. Ramsey, “Orbital tomography: Molecular band maps, momentum maps and the imaging of real space orbitals of adsorbed molecules,” *Journal of Electron Spectroscopy and Related Phenomena*, vol. 204, no. Pt A, pp. 92–101, 2015.
 - [15] H. Ishii, K. Sugiyama, E. Ito, and K. Seki, “Energy level alignment and interfacial electronic structures at organic/metal and organic/organic interfaces,” *Advanced Materials*, vol. 11, no. 8, pp. 605–625, 1999.
 - [16] S. Braun, W. R. Salaneck, and M. Fahlman, “Energy-level alignment at organic/metal and organic/organic interfaces,” *Advanced Materials*, vol. 21, no. 14-15, pp. 1450–1472, 2009.
 - [17] M. T. Greiner, M. G. Helander, W.-M. Tang, Z.-B. Wang, J. Qiu, and Z.-H. Lu, “Universal energy-level alignment of molecules on metal oxides,” *Nature materials*, vol. 11, no. 1, pp. 76–81, 2012.
 - [18] T. Jaouen, P. Aebi, S. Tricot, G. Delhaye, B. Lépine, D. Sébilleau, G. Jézéquel, and P. Schieffer, “Induced work function changes at mg-doped mgo/ag(001) interfaces: Combined auger electron diffraction and density functional study,” *Physical Review B*, vol. 90, no. 12, 2014.
 - [19] J. Schneider, F. Kollhoff, T. Schindler, S. Bichlmaier, J. Bernardi, T. Unruh, J. Libuda, T. Berger, and O. Diwald, “Adsorption, ordering, and metalation of porphyrins on mgo nanocube surfaces: The directional role of carboxylic anchoring groups,” *Journal of Physical Chemistry C*, vol. 120, no. 47, pp. 26879–26888, 2016.
 - [20] G. Di Filippo, A. Classen, R. Pöschel, and T. Fauster, “Interaction of free-base tetraphenylporphyrin with magnesium oxide: Influence of mgo morphology on metalation,” *The Journal of chemical physics*, vol. 146, no. 6, p. 064702, 2017.
 - [21] G. Binnig, H. Rohrer, C. Gerber, and E. Weibel, “Surface studies by scanning tunneling microscopy,” *Physical Review Letters*, vol. 49, no. 1, pp. 57–61, 1982.

- [22] F. J. Giessibl, “High-speed force sensor for force microscopy and profilometry utilizing a quartz tuning fork,” *Applied Physics Letters*, vol. 73, no. 26, pp. 3956–3958, 1998.
- [23] J. Tersoff and D. R. Hamann, “Theory of the scanning tunneling microscope,” *Physical Review B*, vol. 31, no. 2, pp. 805–813, 1985.
- [24] J. Bardeen, “Tunnelling from a many-particle point of view,” *Physical Review Letters*, vol. 6, no. 2, pp. 57–59, 1961.
- [25] R. Wiesendanger and H.-J. Güntherodt, *Scanning Tunneling Microscopy III: Theory of STM and Related Scanning Probe Methods*, vol. 29 of *Springer Series in Surface Sciences*. Berlin and Heidelberg: Springer, second edition ed., 1996.
- [26] A. Selloni, P. Carnevali, E. Tosatti, and C. D. Chen, “Voltage-dependent scanning-tunneling microscopy of a crystal surface: Graphite,” *Physical Review B*, vol. 31, no. 4, pp. 2602–2605, 1985.
- [27] R. J. Hamers, R. M. Tromp, and J. E. Demuth, “Electronic and geometric structure of si(111)-(7 × 7) and si(001) surfaces,” *Surface Science*, vol. 181, no. 1-2, pp. 346–355, 1987.
- [28] B. Q. Pham and M. S. Gordon, “Can orbitals really be observed in scanning tunneling microscopy experiments?,” *The journal of physical chemistry. A*, vol. 121, no. 26, pp. 4851–4852, 2017.
- [29] P. Sautet and C. Joachim, “Calculation of the benzene on rhodium stm images,” *Chemical Physics Letters*, vol. 185, no. 1-2, pp. 23–30, 1991.
- [30] K. W. Hipps, “Scanning tunneling spectroscopy (sts),” in *Handbook of Applied Solid State Spectroscopy* (D. R. Vij, ed.), pp. 305–350, Boston, MA: Springer Science+Business Media LLC, 2006.
- [31] C. Wagner, R. Franke, and T. Fritz, “Evaluation of i(v) curves in scanning tunneling spectroscopy of organic nanolayers,” *Physical Review B*, vol. 75, no. 23, p. 2619, 2007.
- [32] I. Fernández Torrente, K. J. Franke, and J. Ignacio Pascual, “Spectroscopy of c 60 single molecules: the role of screening on energy level alignment,” *Journal of Physics: Condensed Matter*, vol. 20, no. 18, p. 184001, 2008.
- [33] D. A. King, “Thermal desorption from metal surfaces: A review,” *Surface Science*, vol. 47, no. 1, pp. 384–402, 1975.
- [34] S. Pomp, *Adsorption of metals and molecules on metal-supported iron oxide and silica thin films*. Phd thesis, Karl-Franzens-Universität Graz, Graz, 2016.
- [35] P. A. Redhead, “Thermal desorption of gases,” *Vacuum*, vol. 12, no. 4, pp. 203–211, 1962.

Bibliography

- [36] E. Habenschaden and J. Küppers, “Evaluation of flash desorption spectra,” *Surface Science*, vol. 138, no. 1, pp. L147–L150, 1984.
- [37] J. A. W. Elliott and C. A. Ward, “Temperature programmed desorption: A statistical rate theory approach,” *The Journal of Chemical Physics*, vol. 106, no. 13, pp. 5677–5684, 1997.
- [38] V. P. Zhdanov, “Arrhenius parameters for rate processes on solid surfaces,” *Surface Science Reports*, vol. 12, no. 5, pp. 185–242, 1991.
- [39] A. Winkler, “Kinetics of ultra-thin organic film growth.,” in *Encyclopedia of interfacial chemistry: Kinetics of Ultra-Thin Organic Film Growth.* (K. Wandelt, ed.), vol. 3 of *Springer Series in Surface Sciences*, pp. 195–215, Amsterdam, Netherlands and Oxford, UK and Cambridge, USA: Elsevier, 2018.
- [40] S. Zöphel, *Der Aufbau eines Tieftemperatur-Rastertunnelmikroskops und Strukturuntersuchungen auf vicinalen Kupferoberflächen.* PhD Thesis, Deutschland: Freie Universität Berlin, 2000.
- [41] P. Seidel, *Electrochemistry of iron oxide thin lms.* PhD Thesis, Austria: University of Graz, 2017.
- [42] W. P. Davey, “Precision measurements of the lattice constants of twelve common metals,” *Physical Review*, vol. 25, no. 6, pp. 753–761, 1925.
- [43] J. Zemann, “Crystal structures, 2 nd edition. vol. 1 by r. w. g. wyckoff,” *Acta Crystallographica*, vol. 18, no. 1, p. 139, 1965.
- [44] J. Wollschläger, J. Viernow, C. Tegenkamp, D. Erdös, K. Schröder, and H. Pfñür, “Stoichiometry and morphology of mgo films grown reactively on ag(100),” *Applied Surface Science*, vol. 142, no. 1-4, pp. 129–134, 1999.
- [45] J. Pal, M. Smerieri, E. Celasco, L. Savio, L. Vattuone, and M. Rocca, “Morphology of monolayer mgo films on ag(100): Switching from corrugated islands to extended flat terraces,” *Physical Review Letters*, vol. 112, no. 12, 2014.
- [46] S. Kim, P. A. Thiessen, E. E. Bolton, J. Chen, G. Fu, A. Gindulyte, L. Han, J. He, S. He, B. A. Shoemaker, J. Wang, B. Yu, J. Zhang, and S. H. Bryant, “Pubchem substance and compound databases,” *Nucleic acids research*, vol. 44, no. D1, pp. D1202–13, 2016.
- [47] R. Ruiz, D. Choudhary, B. Nickel, T. Toccoli, K.-C. Chang, A. C. Mayer, P. Clancy, J. M. Blakely, R. L. Headrick, S. Iannotta, and G. G. Malliaras, “Pentacene thin film growth,” *Chemistry of Materials*, vol. 16, no. 23, pp. 4497–4508, 2004.
- [48] M. Kitamura and Y. Arakawa, “Pentacene-based organic field-effect transistors,” *Journal of physics. Condensed matter : an Institute of Physics journal*, vol. 20, no. 18, p. 184011, 2008.

- [49] J. Repp, G. Meyer, S. M. Stojkovic, A. Gourdon, and C. Joachim, “Molecules on insulating films: scanning-tunneling microscopy imaging of individual molecular orbitals,” *Physical Review Letters*, vol. 94, no. 2, p. 026803, 2005.
- [50] G. Grem, V. Martin, F. Meghdadi, C. Paar, J. Stampfl, J. Sturm, S. Tasch, and G. Leising, “Stable poly(para-phenylene)s and their application in organic light emitting devices,” *Synthetic Metals*, vol. 71, no. 1-3, pp. 2193–2194, 1995.
- [51] J. Otsuki, “Stm studies on porphyrins,” *Coordination Chemistry Reviews*, vol. 254, no. 19-20, pp. 2311–2341, 2010.
- [52] J. M. Gottfried, “Surface chemistry of porphyrins and phthalocyanines,” *Surface Science Reports*, vol. 70, no. 3, pp. 259–379, 2015.
- [53] G. Sauerbrey, “Verwendung von schwingquarzen zur wägung dünner schichten und zur mikrowägung,” *Zeitschrift für Physik*, vol. 155, no. 2, pp. 206–222, 1959.
- [54] J. D. Meindl, Q. Chen, and J. A. Davis, “Limits on silicon nanoelectronics for terascale integration,” *Science (New York, N.Y.)*, vol. 293, no. 5537, pp. 2044–2049, 2001.
- [55] G. Ertl, H. Knözinger, F. Schüth, and J. Weitkamp, eds., *Handbook of heterogeneous catalysis*. Weinheim: Wiley-VCH, 2., completely rev. and enl. ed. ed., 2008.
- [56] F. Donati, S. Rusponi, S. Stepanow, C. Wackerlin, A. Singha, L. Persichetti, R. Baltic, K. Diller, F. Patthey, E. Fernandes, J. Dreiser, Z. Sljivancanin, K. Kummer, C. Nistor, P. Gambardella, and H. Brune, “Magnetic remanence in single atoms,” *Science (New York, N.Y.)*, vol. 352, no. 6283, pp. 318–321, 2016.
- [57] J. W. Matthews, *Epitaxial Growth*. Burlington: Elsevier Science, 1975.
- [58] K R Lawless, “The oxidation of metals,” *Rep. Prog. Phys.*, no. 37, 1974.
- [59] V. Nicolosi, M. Chhowalla, M. G. Kanatzidis, M. S. Strano, and J. N. Coleman, “Liquid exfoliation of layered materials,” *Journal of Materials Chemistry*, vol. 340, no. 6139, p. 1226419, 2013.
- [60] A. M. Horgan and D. A. King, “Oxygen adsorption, reconstruction, and thin oxide film formation on clean metal surfaces: Ni, fe, w and mo,” *Surface Science*, vol. 23, no. 2, pp. 259–282, 1970.
- [61] K. Nagata, A. Ogura, I. Hirosawa, T. Suwa, A. Teramoto, T. Hattori, and T. Ohmi, “Structural analyses of thin sio 2 films formed by thermal oxidation of atomically flat si surface by using synchrotron radiation x-ray characterization,” *ECS Journal of Solid State Science and Technology*, vol. 4, no. 8, pp. N96–N98, 2015.
- [62] K. S. Novoselov, A. K. Geim, S. V. Morozov, D. Jiang, Y. Zhang, S. V. Dubonos, I. V. Grigorieva, and A. A. Firsov, “Electric field effect in atomically thin carbon films,” *Science (New York, N.Y.)*, vol. 306, no. 5696, pp. 666–669, 2004.

Bibliography

- [63] H. Li, J. Wu, Z. Yin, and H. Zhang, “Preparation and applications of mechanically exfoliated single-layer and multilayer mos₂ and wse₂ nanosheets,” *Accounts of Chemical Research*, vol. 47, no. 4, pp. 1067–1075, 2014.
- [64] L. H. Li, Y. Chen, G. Behan, H. Zhang, M. Petracic, and A. M. Glushenkov, “Large-scale mechanical peeling of boron nitride nanosheets by low-energy ball milling,” *Journal of Materials Chemistry*, vol. 21, no. 32, p. 11862, 2011.
- [65] P. A. Cox and A. A. Williams, “Surface excitons on ionic crystals,” *Surface Science*, vol. 175, no. 2, pp. L782–L786, 1986.
- [66] D. M. Roessler and W. C. Walker, “Electronic spectrum and ultraviolet optical properties of crystalline mgo,” *Physical Review*, vol. 159, no. 3, pp. 733–738, 1967.
- [67] O. E. Taurian, M. Springborg, and N. E. Christensen, “Self-consistent electronic structures of mgo and sro,” *Solid State Communications*, vol. 55, no. 4, pp. 351–355, 1985.
- [68] C. O’Brien, K.-H. Dostert, M. Hollerer, C. Stiehler, F. Calaza, S. Schauermann, S. Shaikhutdinov, M. Sterrer, and H.-J. Freund, “Supports and modified nanoparticles in designing model catalysts,” *Faraday Discussions of the Chemical Society*, 2015.
- [69] B. Yoon, H. Häkkinen, U. Landman, A. S. Wörz, J.-M. Antonietti, S. Abbet, K. Judai, and U. Heiz, “Charging effects on bonding and catalyzed oxidation of co on au8 clusters on mgo,” *Science (New York, N.Y.)*, vol. 307, no. 5708, pp. 403–407, 2005.
- [70] M. Sterrer, M. Yulikov, E. Fischbach, M. Heyde, H.-P. Rust, G. Pacchioni, T. Risse, and H.-J. Freund, “Interaction of gold clusters with color centers on mgo(001) films,” *Angewandte Chemie (International ed. in English)*, vol. 45, no. 16, pp. 2630–2632, 2006.
- [71] Q. Pan, L. Li, S. Shaikhutdinov, Y. Fujimori, M. Hollerer, M. Sterrer, and H.-J. Freund, “Model systems in heterogeneous catalysis: towards the design and understanding of structure and electronic properties,” *Faraday discussions*, vol. 208, no. 0, pp. 307–323, 2018.
- [72] G. Hohlneicher, H. Pulm, and H.-J. Freund, “On the separation of initial and final state effects in photoelectron spectroscopy using an extension of the auger-parameter concept,” *Journal of Electron Spectroscopy and Related Phenomena*, vol. 37, no. 2, pp. 209–224, 1985.
- [73] C. D. Wagner, “Chemical shifts of auger lines, and the auger parameter,” *Faraday Discussions of the Chemical Society*, vol. 60, p. 291, 1975.
- [74] W. E. Kaden, C. Büchner, L. Lichtenstein, S. Stuckenholz, F. Ringleb, M. Heyde, M. Sterrer, H.-J. Freund, L. Giordano, G. Pacchioni, C. J. Nelin, and P. S. Bagus, “Understanding surface core-level shifts using the auger parameter: A study of

- pd atoms adsorbed on ultrathin sio 2 films,” *Physical Review B*, vol. 89, no. 11, 2014.
- [75] A. Bongiorno and U. Landman, “Water-enhanced catalysis of co oxidation on free and supported gold nanoclusters,” *Physical Review Letters*, vol. 95, no. 10, p. 106102, 2005.
- [76] F. Gao, T. E. Wood, and D. W. Goodman, “The effects of water on co oxidation over tio2 supported au catalysts,” *Catalysis Letters*, vol. 1-2, no. 134, pp. 9–12, 2010.
- [77] X. L. Hu, J. Carrasco, J. Klimeš, and A. Michaelides, “Trends in water monomer adsorption and dissociation on flat insulating surfaces,” *Physical chemistry chemical physics : PCCP*, vol. 13, no. 27, pp. 12447–12453, 2011.
- [78] O. Björneholm, M. H. Hansen, A. Hodgson, L.-M. Liu, D. T. Limmer, A. Michaelides, P. Pedevilla, J. Rossmeisl, H. Shen, G. Tocci, E. Tyrode, M.-M. Walz, J. Werner, and H. Bluhm, “Water at interfaces,” *Chemical Reviews*, vol. 116, no. 13, pp. 7698–7726, 2016.
- [79] Z.-T. Wang, Y.-G. Wang, R. Mu, Y. Yoon, A. Dahal, G. K. Schenter, V.-A. Glezakou, R. Rousseau, I. Lyubinetsky, and Z. Dohnálek, “Probing equilibrium of molecular and deprotonated water on tio2(110),” *Proceedings of the National Academy of Sciences of the United States of America*, vol. 114, no. 8, pp. 1801–1805, 2017.
- [80] R. Mu, Z.-J. Zhao, Z. Dohnálek, and J. Gong, “Structural motifs of water on metal oxide surfaces,” *Chemical Society reviews*, vol. 46, no. 7, pp. 1785–1806, 2017.
- [81] B. Meyer, D. Marx, O. Dulub, U. Diebold, M. Kunat, D. Langenberg, and C. Wöll, “Partial dissociation of water leads to stable superstructures on the surface of zinc oxide,” *Angewandte Chemie-International Edition*, vol. 43, no. 48, pp. 6642–6645, 2004.
- [82] M. Wagner, P. Lackner, S. Seiler, A. Brunsch, R. Bliem, S. Gerhold, Z. Wang, J. Osiecki, K. Schulte, L. A. Boatner, M. Schmid, B. Meyer, and U. Diebold, “Resolving the structure of a well-ordered hydroxyl overlayer on in2o3(111): Nanomanipulation and theory,” *ACS nano*, vol. 11, no. 11, pp. 11531–11541, 2017.
- [83] X. Zhao, X. Shao, Y. Fujimori, S. Bhattacharya, L. M. Ghiringhelli, H.-J. Freund, M. Sterrer, N. Nilius, and S. V. Levchenko, “Formation of water chains on cao(001): What drives the 1d growth?,” *The journal of physical chemistry letters*, vol. 6, no. 7, pp. 1204–1208, 2015.
- [84] J. Heidberg, B. Redlich, and D. Wetter, “Adsorption of water vapor on the mgo(100) single crystal surface,” *Berichte der Bunsengesellschaft für physikalische Chemie*, vol. 99, no. 11, pp. 1333–1337, 1995.

Bibliography

- [85] D. Ferry, A. Glebov, V. Senz, J. Suzanne, J. P. Toennies, and H. Weiss, "Observation of the second ordered phase of water on the mgo(100) surface: Low energy electron diffraction and helium atom scattering studies," *The Journal of Chemical Physics*, vol. 105, no. 4, pp. 1697–1701, 1996.
- [86] M.-C. Wu, C. A. Estrada, J. S. Corneille, and D. W. Goodman, "Model surface studies of metal oxides: Adsorption of water and methanol on ultrathin mgo films on mo(100)," *The Journal of Chemical Physics*, vol. 96, no. 5, pp. 3892–3900, 1992.
- [87] M. J. Stirniman, C. Huang, R. Scott Smith, S. A. Joyce, and B. D. Kay, "The adsorption and desorption of water on single crystal mgo(100): The role of surface defects," *The Journal of Chemical Physics*, vol. 105, no. 3, pp. 1295–1298, 1996.
- [88] J. Jung, H.-J. Shin, Y. Kim, and M. Kawai, "Controlling water dissociation on an ultrathin mgo film by tuning film thickness," *Physical Review B*, vol. 82, no. 8, 2010.
- [89] E. Wruss, E. Zojer, and O. T. Hofmann, "Distinguishing between charge-transfer mechanisms at organic/inorganic interfaces employing hybrid functionals," *Journal of Physical Chemistry C*, vol. 122, no. 26, pp. 14640–14653, 2018.
- [90] O. T. Hofmann, P. Rinke, M. Scheffler, and G. Heimel, "Integer versus fractional charge transfer at metal(/insulator)/organic interfaces: Cu(/nacl)/tcne," *ACS Nano*, vol. 9, no. 5, pp. 5391–5404, 2015.
- [91] H. Wang, P. Amsalem, G. Heimel, I. Salzmann, N. Koch, and M. Oehzelt, "Band-bending in organic semiconductors: the role of alkali-halide interlayers," *Advanced Materials*, vol. 26, no. 6, pp. 925–930, 2014.
- [92] J. Bardeen, "Theory of the work function. ii. the surface double layer," *Physical Review*, vol. 49, no. 9, pp. 653–663, 1936.
- [93] H. Vazquez, Y. J. Dappe, J. Ortega, and F. Flores, "Energy level alignment at metal/organic semiconductor interfaces: "pillow" effect, induced density of interface states, and charge neutrality level," *The Journal of Chemical Physics*, vol. 126, no. 14, p. 144703, 2007.
- [94] J. B. Neaton, M. S. Hybertsen, and S. G. Louie, "Renormalization of molecular electronic levels at metal-molecule interfaces," *Physical Review Letters*, vol. 97, no. 21, p. 216405, 2006.
- [95] J. M. Garcia-Lastra, C. Rostgaard, A. Rubio, and K. S. Thygesen, "Polarization-induced renormalization of molecular levels at metallic and semiconducting surfaces," *Physical Review B*, vol. 80, no. 24, 2009.
- [96] M. Bokdam, D. Çakir, and G. Brocks, "Fermi level pinning by integer charge transfer at electrode-organic semiconductor interfaces," *Applied Physics Letters*, vol. 98, no. 11, p. 113303, 2011.

- [97] J K Norsko, “Chemisorption on metal surfaces,” *Rep. Prog. Phys.*, vol. 53, no. 10, p. 1253, 1990.
- [98] T. Ules, D. Lüftner, E. M. Reinisch, G. Koller, P. Puschnig, and M. G. Ramsey, “Continuous or discrete: Tuning the energy level alignment of organic layers with alkali dopants,” *Physical Review B*, vol. 94, no. 20, 2016.
- [99] L. Giordano, U. Martinez, S. Sicolo, and G. Pacchioni, “Observable consequences of formation of au anions from deposition of au atoms on ultrathin oxide films,” *The Journal of chemical physics*, vol. 127, no. 14, p. 144713, 2007.
- [100] J. Goniakowski and C. Noguera, “Polarization and rumpling in oxide monolayers deposited on metallic substrates,” *Physical Review B*, vol. 79, no. 15, 2009.
- [101] L. Sementa, G. Barcaro, F. R. Negreiros, I. O. Thomas, F. P. Netzer, A. M. Ferrari, and A. Fortunelli, “Work function of oxide ultrathin films on the ag(100) surface,” *Journal of chemical theory and computation*, vol. 8, no. 2, pp. 629–638, 2012.
- [102] M. Fahlman, A. Crispin, X. Crispin, S. K. M. Henze, M. P. de Jong, W. Osikowicz, C. Tengstedt, and W. R. Salaneck, “Electronic structure of hybrid interfaces for polymer-based electronics,” *Journal of physics. Condensed matter : an Institute of Physics journal*, vol. 19, no. 18, p. 183202, 2007.
- [103] O. L. A. Monti, “Understanding interfacial electronic structure and charge transfer: An electrostatic perspective,” *Journal of Physical Chemistry Letters*, vol. 3, no. 17, pp. 2342–2351, 2012.
- [104] S. Braun and W. R. Salaneck, “Fermi level pinning at interfaces with tetrafluorotetracyanoquinodimethane (f4-tcnq): The role of integer charge transfer states,” *Chemical Physics Letters*, vol. 438, no. 4-6, pp. 259–262, 2007.
- [105] L. Ley, Y. Smets, C. I. Pakes, and J. Ristein, “Calculating the universal energy-level alignment of organic molecules on metal oxides,” *Advanced Functional Materials*, vol. 23, no. 7, pp. 794–805, 2013.
- [106] J. Schneider, M. Franke, M. Gurrath, M. Rockert, T. Berger, J. Bernardi, B. Meyer, H.-P. Steinruck, O. Lytken, and O. Diwald, “Porphyrin metalation at mgo surfaces: A spectroscopic and quantum mechanical study on complementary model systems,” *Chemistry - A European Journal*, vol. 22, no. 5, pp. 1744–1749, 2016.
- [107] A. J. Fleming, S. Berkebile, T. Ules, and M. G. Ramsey, “Pre-nucleation dynamics of organic molecule self-assembly investigated by peem,” *Physical chemistry chemical physics : PCCP*, vol. 13, no. 10, pp. 4693–4708, 2011.
- [108] M. Wagner, S. Berkebile, F. P. Netzer, and M. G. Ramsey, “Revealing the buried metal-organic interface: Restructuring of the first layer by van der waals forces,” *ACS Nano*, vol. 9, no. 12, pp. 12070–12078, 2015.

Bibliography

- [109] D. J. Gundlach, Y.-Y. Lin, T. N. Jackson, and D. G. Schlom, “Oligophenyl-based organic thin film transistors,” *Applied Physics Letters*, vol. 71, no. 26, pp. 3853–3855, 1997.
- [110] S. Tsuzuki, K. Honda, T. Uchimaru, M. Mikami, and K. Tanabe, “Origin of attraction and directionality of the π/π interaction: Model chemistry calculations of benzene dimer interaction,” *Journal of the American Chemical Society*, vol. 124, no. 1, pp. 104–112, 2002.
- [111] R. Resel, “Surface induced crystallographic order in sexiphenyl thin films,” *Journal of Physics: Condensed Matter*, vol. 20, no. 18, p. 184009, 2008.